Fall 2019

A computational study of sleep and the hemispheres of the brain

Tera Ashley Glaze

Department: Physics

A COMPUTATIONAL STUDY OF SLEEP AND THE HEMISPHERES OF THE BRAIN

by

TERA ASHLEY GLAZE

A DISSERTATION

Presented to the Faculty of the Graduate School of the

UNIVERSITY OF MISSOURI – ST. LOUIS

&

MISSOURI UNIVERSITY OF SCIENCE AND TECHNOLOGY

In Partial Fulfillment of the Requirements for the Degree

DOCTOR OF PHILOSOPHY

in

PHYSICS

2019

Approved by:

Sonya Bahar, Advisor
Ricardo Flores
Paul E. Parris
Alexey Yamilov
Erik Herzog

ABSTRACT

Sleep and sleep cycles have been studied for over a century, and scientists have worked on modeling sleep for nearly as long as computers have existed. Despite this extensive study, sleep still holds many mysteries. Larger and more extensive sleep-wake models have been developed, and the circadian drive has been depicted in numerous fashions, as well as incorporated into scores of studies. With the ever-growing knowledge of sleep comes the need to find more ways to examine, quantify, and define it in the context of the most complex part of the human anatomy – the brain. Presented here is the development of a computational model that explores the activity of individual neurons, modeled with coupled nonlinear ordinary differential equations, in key sleep-related brain regions. The activity patterns of the individual neurons are studied, as well as their synchronization with other neurons within the same region. The model is expanded into two separate interacting hemispheres, whose activity and synchronization reveal chimera-like activity. Multiple different perspectives on jetlag are presented, exploring the impact of circadian rhythm changes. Unihemispheric sleep, the unusual form of sleep exhibited by some ocean creatures and species of birds, is observed, as well as asymmetric sleep, which occurs in human subjects suffering from sleep apnea. These investigations provide a new perspective on the intricate balance between the neural activity in different brain regions that drives the essential phenomenon that is sleep.

ACKNOWLEDGEMENTS

I would like to thank my amazing advisor, Dr. Sonya Bahar, for all her understanding and support. I also acknowledge the NASA-Missouri Space Grant Consortium and thank them for their funding of this research.

And a heartfelt thanks to everyone who agreed to be on my committee:

Dr. Sonya Bahar

Dr. Ricardo Flores

Dr. Paul E. Parris

Dr. Alexey Yamilov

Dr. Erik Herzog

TABLE OF CONTENTS

Page

LIST OF FIGURES

Page

LIST OF ABBREVIATIONS

Abbreviation	Meaning
AMIN	Monoaminergic
ASPD	Advanced sleep phase disorder
BHS	Bihemispheric sleep
CD	Circadian drive
CRSD	Circadian rhythm sleep disorders
DSPD	Delayed sleep phase disorder
DST	Daylight-saving time
EEG	Electroencephalogram
eVLPO	Extended ventrolateral preoptic area
FFI	Fatal familial insomnia
FHN	FitzHugh-Nagumo
FRD	Free-running disorder
GLU	Glutamate
HB	Huber-Braun
HR	Hindmarsh-Rose
ISI	Inter-spike interval
ISWR	Irregular sleep-wake rhythm
IVF	In vitro fertilization
JLD	Jet lag disorder
LC	Locus coeruleus

LHA	Lateral hypothalamic area
MnPO	Median preoptic area
NREM	Non-rapid eye-movement
ORX	Orexin, or hypocretin
REM	Rapid eye-movement
SCN	Suprachiasmatic nucleus
SFI	Sporadic fatal insomnia
SLM	Spatial light modulator
SWD	Shift work disorder
SWS	Slow wave sleep
UHS	Unihemispheric sleep
VLPO	Ventrolateral preoptic area

NOMENCLATURE

Symbol	Description
g_S	Coupling strength from sleep group to wake group
g_W	Coupling strength from wake group to sleep group
g_{CS}	Coupling strength from circadian drive to sleep group
g_{CW}	Coupling strength from circadian drive to wake group
g	Coupling strength within a group or region
g_V	Coupling strength from VLPO region to AMIN region
g_A	Coupling strength from AMIN region to VLPO region
g_{CV}	Coupling strength from circadian drive to VLPO region
g_{CA}	Coupling strength from circadian drive to AMIN region
$g_{V_{LtR}}$	Coupling strength from left hemisphere VLPO to right hemisphere VLPO
$g_{V_{RtL}}$	Coupling strength from right hemisphere VLPO to left hemisphere VLPO
T_S	Temperature of sleep-promoting group neurons (HB)
T_W	Temperature of wake-promoting group neurons (HB)
T_V	Temperature of VLPO region neurons (HB)
T_A	Temperature of AMIN region neurons (HB)
I	Input current (HR)

1. INTRODUCTION TO SLEEP

Everyone sleeps. At least, scientists are well on their way to proving that even creatures we didn't believe had the capacity for it, do indeed sleep. For example, the jellyfish *Cassiopea* was recently discovered by Nath *et al*. (2017) to exhibit a sleep-like state, despite lack of a centralized nervous system. Yet, despite the necessity of sleep and its prevalence in the animal kingdom, many questions remain unanswered as to precisely *why* sleep is so essential, *where* in the brain sleep originates, *which* areas of the brain contribute *what* to the sleep process, and *how* sleep (or the lack thereof) affects processes such as memory consolidation. Research continues to seek answers these questions, with numerous new papers on sleep being published each year. Some basic background and a summary of recent sleep research will be touched upon briefly in this introduction.

1.1. SLEEP IN GENERAL

Sleep has been studied in one form or another for centuries, with published articles about the phenomenon going back at least as far as the 1840s (Ashenheim 1841). There are two distinct sleep states: rapid eye-movement sleep, also known as paradoxical sleep and associated with dreaming; and non-rapid eye-movement sleep.

1.1.1. NREM Sleep. Non-rapid eye-movement (non-REM or NREM) sleep is also known as slow wave sleep, named for the electroencephalogram (EEG) pattern of activity during this state: high amplitude, synchronized, with a frequency in the delta band, between 0.5 and 4 Hz (Krueger *et al*. 2008, de Andres *et al*. 2011). This state of sleep is vital to sleeping creatures – so much so that sleep will *always* reemerge, even after (survivable)

acute damage to regions of the brain that moderate sleep (Krueger *et al*. 2008). Humans spend about 80% of their total sleep time in NREM (Krueger *et al*. 2008), with the rest devoted to REM, to be discussed in the next section.

NREM sleep is broken down into two distinct stages: stage 2 and stage 3-4, the latter of which is now slightly less confusingly called N3 (de Andres *et al*. 2011). Slow wave activity predominates during up to 20% of the duration of stage 2. During the remainder of this sleep state, the EEG exhibits patterns called K-complexes and sleep spindles. K-complexes are brief high amplitude spikes, while sleep spindles are short bursts of higher frequency activity. This stage corresponds to light sleep, where the sleeper is relatively easier to wake. Unlike stage 2, stage N3 consists more heavily of slow wave activity (20% or more) and is considered deep sleep (de Andres *et al*. 2011).

The amount and depth of NREM slow wave activity depends upon the activity of the brain during waking. Brain regions that experience increased activity or stimulation during waking hours experience increased levels of slow wave activity during the following NREM episode, while decreased activity during wake leads to decreased slow wave activity during NREM (Krueger *et al*. 2008, de Andres *et al*. 2011). There is also a distinct decrease in connectivity and signal propagation during NREM. While a signal transmitted in the brain via direct cortical stimulation during waking will propagate to other connected areas of the cortex, when the stimulation occurs during NREM sleep, the signal fades away quickly without much propagation. This appears to be the mechanism underlaying the slow fading of consciousness before and during early stages of sleep (Massimini *et al*. 2005).

1.1.2. REM Sleep. Arguably the more interesting of the two sleep states, rapid eye-movement (REM) sleep was discovered in the 1950s. While eye movement during sleep in humans had been noted previously, Aserinsky and Kleitman were the first to connect this movement to dreaming, publishing their findings in 1953 (Aserinsky & Kleitman 2003, reprint of original 1953 article). Other creatures have subsequently been found to exhibit REM sleep, including cats (Jouvet & Michel 1959), other mammals (Siegel 2001), lizards (Shein-Idelson *et al*. 2016)., and birds (Rattenborg *et al*. 2019).

REM sleep is also called paradoxical sleep; a fitting name, as activity in the brain during this sleep state is similar to that of waking. In fact, not only are multiple areas of the brain, previously quiescent during the descent into NREM, reactivated (Braun *et al*. 1997, Hobson & Pace-Schott 2002), but the brain's energy metabolism during REM is as large as, or even larger than, during wakefulness (Hobson & Pace-Schott 2002). The EEG activity of the brain during REM is reminiscent of waking-state low-amplitude, high-frequency firing. Waking and REM EEG are desynchronized compared to NREM (Peever & Fuller 2017), as inferred from the periodicity and amplitude of EEG recording, though REM has also been found to be the state with the greatest global field synchronization, when compared to NREM and wake (Achermann *et al*. 2016). When the brain shifts from wake to sleep, it always starts in NREM before changing to REM sleep. Over the course of a long sleep, the brain will switch between NREM and REM multiple times (Peever & Fuller 2017).

The wake-like activity of REM sleep still differs from true wakefulness in a few vital ways. When awake, the brain is mainly flooded with aminergic neuromodulators (Hobson & Pace-Schott 2002). After sleep onset, many brain regions, such as the pons and

the thalamus, become quiescent (Braun *et al*. 1997, Hobson & Pace-Schott 2002). Once REM sleep begins, however, these regions become active once again, though this time they are cholinergically modulated (Braun *et al*. 1997, Hobson & Pace-Schott 2002).

Furthermore, after REM onset, the input from the world is blocked, as is any motor output, leading to muscle atonia (Hobson & Pace-Schott 2002), though occasional muscle twitches do occur (Peever & Fuller 2017). This signal blockage is related to REM's most interesting and well-known characteristic – dreaming (Note that while dreaming is associated with REM, it does also sometimes occur during NREM (Peever & Fuller 2017)). In spite of the "sleep paralysis" resulting from muscle atonia, the cerebellum continues to fine-tune the fictive motions performed in dreams (Hobson & Pace-Schott 2002). This production of fictional motions (along with fictional environments and sensory inputs) may be why REM sleep has the highest energy metabolism demands of all sleep states (Hobson & Pace-Schott 2002). Along with dreaming, REM sleep may also have a significant role in memory processing, to be discussed later (Section 1.2.4.1.).

Computational models have been developed to study and simulate REM sleep, both in the context of a larger sleep model (Kumar *et al*. 2012) and as part of a fast-slow process in which fast neuronal firing determines the sleep/wake state, and a slow homeostatic drive regulates the whole system (Booth & Diniz Behn 2012). Various hypotheses have been proposed for the evolutionary benefits of REM sleep (Siegel 2011, 2012, Rial *et al*. 2012).

1.2. SLEEP IN THE BRAIN

Sleep and its relation to neurons, the circadian rhythm, and memory consolidation will be explored in this section. How neurons function and the discovery of the electrical

signal that propagates through them will also be discussed here, followed by a discussion of the circadian rhythm and the benefits of sleep, including memory, emotions, energy, and recovery.

1.2.1. Neuron Review. A neuron's membrane potential (the difference in voltage between inside the membrane and outside) is dependent upon ions that flow in and out of the cell. In its resting state, the interior of the neuron is at a negative potential compared to the extracellular space due to multiple different ions' concentrations.

Signals travel along neurons via action potentials, which consist of three stages: depolarization, repolarization, and hyperpolarization. An action potential begins when an incoming signal pushes the membrane potential above a threshold value. This triggers Na^+ channels to open, allowing sodium ions to flow into the cell due to the electric potential difference and the lower concentration of sodium within the neuron. As more Na^+ flows in, more channels open, allowing sodium to enter the cell in larger quantities. This causes the neuron to "depolarize", corresponding to a sharp rise in the membrane potential. As the increases, K^+ channels begin to open, allowing potassium to flow from the higher concentration inside the cell to the lower concentration outside. Sodium stops flowing into the neuron due to the closing of an inactivation gate on the intracellular side of the Na^+ channels. These events cause the neuron to repolarize, which is seen as the downstroke of the action potential. A brief overshoot of the resting membrane potential results in transient hyperpolarization (Barnett & Larkman 2007).

While the neuron is hyperpolarized, it is in a refractory period, during which it is unable to fire again, regardless of the strength of an applied electric signal. This is called the *absolute refractory period*. For another short time after that, during the *relative*

refractory period, an action potential can be triggered, but it takes a stronger than normal electrical signal. This is due to the recovery of the Na^+ channels preventing passage while the K^+ channels slowly close. The combination of these two refractory periods is what prevents an action potential from propagating back towards the direction of its source (Barnett & Larkman 2007).

1.2.2. Discovery of the Action Potential. Before the mid-18th century, it was believed that muscles and nerves functioned via the four elements (earth, water, air and fire) and via ether. This perspective changed due to the efforts of more than a few important scientists. The history of the action potential's discovery started when Italian physician Luigi Galvani (1737-1798) began studying the effect of electricity on severed frog legs. He found that contact between the leg and some metals, along with an electric spark, cause the contraction of the leg. This action of nerves and muscles he called "animal electricity". Galvani's eventual conclusion that there existed a quantity of positive and negative charge in the muscle and nerves is, in retrospect, eerily accurate (Cajavilca *et al*. 2009, Kazamel & Warren 2017).

Alessandro Volta (1755-1832) at first applauded Galvani's research. As he performed the experiments for himself, however, he came to doubt and publicly contradict all of Galvani's conclusions. Volta believed that Galvani was incorrect about an intrinsic animal energy and that the electricity that caused muscle contraction was a byproduct of using metals to manipulate the frog leg; in essence, heterogeneous contact caused the charge (Piccolino 1997, Kazamel & Warren 2017). Galvani set out to disprove Volta's refutation, and the argument went back and forth for years. In 1797, Galvani undermined all of Volta's contradictions by touching the sciatic nerve of one frog leg to the sciatic

nerve of a second, a homogenous contact, that produced the expected muscle contraction. This definitive experiment went almost completely unnoticed, however, while Volta proceeded to invent the electrical battery in 1800. As a result, the development of electrophysiology and the study of "animal energy" fell by the wayside for nearly three decades (Cajavilca *et al*. 2009).

Carlo Matteucci picked up the thread of Galvani's research in 1838, followed by Emil du Bois-Reymond (1818-1896). In 1843, the latter improved the sensitivity of a galvanometer to the extent that he was able to measure the tiny currents in frog muscles. From this confirmation of Galvani's theory, the field of electrophysiology was born (Finkelstein 2015). The shape of the action potential of a frog's sciatic nerve was captured on an oscilloscope by Joseph Erlanger (1874-1965) and Herbert Gasser (1888-1963) in 1922 (Kazamel & Warren 2017).

Even after the discovery of action potentials, however, many questions had yet to answered about their propagation and signal transmission. In 1937, Alan Lloyd Hodgkin (1914-1998) showed that an active area can excite nearby neurons. He did this by blocking one section of a nerve and measuring the electrical signals that passed beyond the block (Hodgkin 1937). Hodgkin and Andrew Fielding Huxley studied the giant axon of a squid, using their insights to develop a detailed computational model of an action potential, incorporating both conduction and excitation (Hodgkin & Huxley 1952). This model, of course, was the precursor to the model developed by Martin Tobias Huber and Hans Albert Braun (Braun *et al*. 1998) and used in the research presented here, to be discussed in Section 2.1.2.

1.2.3. Circadian Rhythm. Everyone is familiar with the 24-hour cycle of daily life, largely due to one earth day being about equivalent to 24 hours. The reason why humans and other creatures follow the same pattern each day is as much the result of an internal circadian rhythm of the body as it is due to the entrainment with the solar light cycle. Circadian rhythms in plants were observed for the first time by Jean-Jacques Dortous de Mairan in 1729, who noticed the movement of a plant's leaves, which changed depending upon the amount of light, and thus depended upon the time of day. However, this pattern of activity still occurred when the plant was isolated in a dark room, as if it were following its own internal clock. In biological systems, such as the plant, these daily oscillations became known as the circadian rhythm (Pikovsky *et al*. 2001).

The circadian rhythm is generated, and its synchronization maintained, by neurons in the suprachiasmatic nucleus (SCN). This connection was discovered in 1972, when scientists compared the brains of rats kept on the same circadian stimulus with and without lesions in the SCN, each of which was euthanized at different times of day (Moore & Eichler 1972). The neural pathway between the retina and the SCN was demonstrated by the injection of dye into a rat's eye (Moore & Lenn 1972), indicating that external light stimulus does have some effect on the internal circadian rhythm. In the 1990s, the specific role of the SCN was explored, with transplanted SCNs in rats (Ralph *et al*. 1990) and hamsters (Aguilar-Roblero *et al*. 1994) changing their circadian rhythms, SCN lesions in squirrel monkeys changing their daily rhythms of sleep and wake (Edgar *et al*. 1993), and individual neurons removed from the SCN exhibiting daily firing rhythms in vitro (Welsh *et al*. 1995).

The first studies of the circadian rhythm in humans was conducted in the late 1930s by Kleitman, now considered the father of sleep research, who removed external light entrainment by performing studies deep inside of caves, where sunlight was not able to influence the circadian rhythm of subjects (Czeisler & Gooley 2007). Many later studies investigated similar aspects of the human circadian rhythm, including unusual circadian cycle lengths of people living in one of the northernmost inhabitable areas, where the sun does not set over an entire season (Lewis & Lobban 1957).

The SCN moderates a mammal's daily and seasonal rhythms and behaviors, a combination which has been modeled in varying ways and complexities. A robust standard model of SCN neurons, with a 24-hour period, is depicted schematically in Aton & Herzog (2005), with proper anatomical organization. Other models, which focus more on the generated circadian rhythm than the SCN itself, include Daan *et al*. (1984), whose skewed sine wave Process C is used as the circadian drive in many sleep-wake models; a two-oscillator model developed by Strogatz (1987); a square array of SCN oscillators (Kunz & Achermann 2003); and a light-based model with an additional non-photic input (St. Hilaire *et al*. 2007).

A detailed review of the SCN's role in timekeeping and circadian rhythm generation is presented in Anton & Herzog (2005), and a more general review of the circadian rhythm, its history, and its various light-sensitive aspects is given in Czeisler & Gooley (2007).

1.2.4. Benefits of Sleep. Sleep is dangerous. It leaves animals open to predation, takes time away from searching for food, and requires a safe place. Despite that, sleep is a vital component of daily life. If a creature goes without sleep for long enough, it will die.

This has led to animals developing ways of sleeping that improves their chances of survival (Lima *et al*. 2005). An example would be unihemispheric sleep, which will be discussed below (Sections 1.3.2. – 1.3.4.). The benefit of sleep must outweigh the danger and inefficiency of sleep for it to have remained such an important process in living creatures. While sleep deprivation has negative impacts on the body (Schmidt 2014) and on memory (Abel *et al*. 2013), the benefits of sleep are still debated. Some of the more prevalent theories are discussed below.

1.2.4.1. Memory and emotions. Sleep, learning, and memories are connected in the brain (Stickgold *et al*. 2001). Sleep is crucial in the management and storing of memories. Studies have shown that even brief naps can aid memory formation, though the longer the sleep period, the better the memory consolidation (Diekelmann & Born 2010).

Two of the most widespread theories of memory consolidation are the "dual process hypothesis" and the "sequential hypothesis" (Hobson & Pace-Schott 2002). The "dual process hypothesis" states that each stage of sleep performs a different memory process. Specifically, procedural memories are processed during REM episodes, while declarative memories (such as word association) are processed during NREM sleep. In contrast, the "sequential hypothesis" states that memories are simply processed in the order that they happened and are not dependent upon the sleep state (Hobson & Pace-Schott 2002).

Evidence suggests that memories are encoded temporarily in the hippocampus while a subject is awake, and once the subject falls asleep, some of the memories are moved to regions such as the neocortex for longer-term "storage" (Vorster & Born 2015). A detailed moment-by-moment breakdown of the memory consolidation process is covered by Dudai *et al*. (2015).

Emotions are connected to memories, and experiments with human patients have shown that emotions are present during REM sleep (Fosse *et al*. 2001). Emotions during REM seem to be tied to REM's role in processing memories. Besides procedural memory processing, REM also plays a role in emotional memory processing (Diekelmann & Born 2010). This connection between REM and emotional memories has led to the development of therapeutic uses of REM in the treatment of post-traumatic stress disorder (Stickgold 2007).

1.2.4.2. Energy and recovery. Memory encoding relies heavily upon synaptic plasticity as well as sleep (Timofeev & Chauvette 2017). The plasticity of neurons decreases with use, and recovery, or renormalization of synaptic strength, is required to restore this plasticity. This recovery occurs during sleep, according to the synaptic homeostasis hypothesis (Tononi & Cirelli 2014). That sleep is an essential for recovery in the brain is not a new concept (Siegel 2003), and there are prevailing theories that plasticity in the human brain develops in infancy, during REM sleep (Hobson & Pace-Schott 2002).

Beyond plasticity recovery, a part of brain recuperation during sleep includes the clearance of harmful byproducts produced over the course of the day (Xie *et al*. 2013). Energy conservation and distribution for different brain states is also a key aspect of sleep (Schmidt 2014); different stages of sleep provide low-energy consumption states, which helps regulate the amount of energy consumed by the brain.

1.3. SLEEP IN LIVING CREATURES

Animals exhibit a range of unique sleep behaviors. This section will briefly discuss human sleep, as well as sleep in other creatures, specifically cetaceans, seals, and jellyfish.

1.3.1. Humans. Humans have one standard form of sleep: bihemispheric sleep. However, unusual circumstances or illnesses can cause another form of sleep in humans, called asymmetric sleep. Both will be discussed in this section.

1.3.1.1. Bihemispheric sleep (BHS). Humans, like many creatures that sleep, have their entire brain in the same state at any one time: either all awake, or all asleep. This is called bihemispheric sleep (BHS). Those who do not utilize both hemispheres for sleep at the same time undergo what is called unihemispheric sleep (UHS), to be discussed below (Sections 1.3.2 – 1.3.4.).

Scientists initially hypothesized that the corpus callosum, the major pathway for communication between hemispheres, was essential to symmetric sleep between hemispheres, since some other creatures that use UHS, such as birds, do not have a corpus callosum, but instead possess multiple smaller comparable structures (García-Moreno & Molnár 2015). The corpus callosum consists of the bundle of fibers that connect the left and right hemispheres of the human brain (Sperry 1961, Corsi-Cabrera *et al*. 2006). It appears that the corpus callosum is not completely necessary for communication between hemispheres; people with callosal dysgenesis (born without the corpus callosum) still have interhemispheric communication (Tovar-Moll *et al*. 2014), though interhemispheric asymmetries during sleep have been found in acallosal mice (Vyazovskiy *et al*. 2004) and humans (Nielsen *et al*. 1992). People who were born with a corpus callosum and had it surgically severed (partially or completely, to halt the propagation of seizures between hemispheres (Bayne 2008)) have demonstrable difficulty with information transfer (Tovar-Moll *et al*. 2014), as well as interhemispheric asymmetry during sleep, though the latter may recover with time (Corsi-Cabrera *et al*. 2006).

1.3.1.2. Asymmetric sleep. Despite corpus callosum separation and callosal dysgenesis, human sleep is always bihemispheric (Rattenborg *et al*. 2000, Corsi-Cabrera *et al*. 2006), if not necessarily symmetric (interhemispheric coherence was decreased at some frequencies after the corpus callosum was partially or completely severed (Corsi-Cabrera *et al*. 2006)). Although not a very common occurrence, interhemispheric asymmetry has appeared in human sleep (Braun *et al*. 1997). Asymmetry can arise from separation of the hemispheres through surgery, as in Corsi-Cabrera *et al*. (2006), but also appears in humans due to other circumstances. Differences between hemispheres during sleep have been observed in humans with sleep apnea (Abeyratne *et al*. 2010, Rial *et al*. 2013). Sleep apnea was found to be directly related to the magnitude of hemispheric asymmetry; the more severe the apnea, the more distinct the asymmetry (Abeyratne *et al*. 2010). During normal breathing in sleep, apneic patients exhibit this asymmetry. When the patient enters an apneic episode (paused breathing), the hemispheres resynchronize (Rial *et al*. 2013).

Asymmetry between hemispheres during sleep can also occur in healthy humans, as discovered by Tamaki and associates (2016). When humans fall asleep in a new, unfamiliar location, portions of one hemisphere do not sleep as deeply as the other hemisphere, maintaining a heightened awareness of the environment. During this time, unfamiliar sounds will arouse a person more frequently and with faster response time when detected by the more lightly sleeping hemisphere than when detected by the more deeply sleeping hemisphere. This response can be viewed as deriving from a survival mechanism, protecting oneself while resting in an environment that may have unknown dangers. It is

only present during the first night in a novel environment and absent during subsequent nights and is thus called the First Night Effect.

1.3.2. Cetaceans. Unlike humans, Cetaceans (whales, dolphins and porpoises) allow one hemisphere at a time to sleep while the other maintains vigilance, switching multiple times over a period of rest. This form of sleep is called unihemispheric sleep (UHS), characterized by one hemisphere exhibiting an EEG pattern synonymous with NREM sleep (high amplitude and low frequency, or synchronized) while the other hemisphere shows an EEG pattern that indicates wakefulness (low amplitude and high frequency, or desynchronized). The wakeful hemisphere can have intermediate activity, lying in the realm between NREM and wakefulness, without dipping so far into sleep that both hemispheres are considered in the same state (Rattenborg *et al*. 2000).

Other characteristics of UHS include some form of constant movement, such as swimming for cetaceans, and unilateral eye closure, in which the eye associated with the wakeful hemisphere (contralateral (Lyamin *et al*. 2004)) remains open while the other eye is closed (sleeping). It is also important to note that UHS is limited to NREM, or slow wave sleep (SWS). REM is not present during UHS, though experimental studies suggest that REM may still be possible in creatures that exhibit UHS (Rattenborg *et al*. 2000). Later studies, however, suggest that REM has been lost in aquatic mammals due to natural selection as a result of environmental pressures, such as predators, the need to remain at or regularly return to the surface for air, and/or temperature maintenance (Madan & Jha 2012).

This unusual form of sleep was modeled by Kedziora and associates (2012), who adapted a preexisting model to create two hemispheres, which alternately switched between sleep and wake states. Their work formed the inspiration to create a more detailed

model, developed below in this dissertation, with groups of individual neurons in place of single equations that govern entire regions of the brain. UHS is examined in the model presented here, with results discussed in Section 4.2.

1.3.3. Birds. Even before the discovery of UHS, some birds' ability to fly continuously for days at a time was a scientific puzzle. When did the birds sleep? Due to the size mismatch between tiny avian subjects and large experimental recording apparatus, studies have been limited (Rattenborg *et al*. 2000, Rattenborg 2017). Many scientists concluded, through visual observations and indirect studies, that birds may fly using only one hemisphere (UHS) or lock their wings and glide (BHS), supported by the evidence that birds are still capable of flight, even after the connections between the brain and the spinal cord had been severed (Rattenborg *et al*. 2000). Indeed, due to newer tracking capabilities, it has been found that great frigatebirds (*Fregata minor*) do utilize both UHS and BHS while they fly. However, the amount of time they spend sleeping during flight was shockingly small, less than an hour per day (mostly UHS or asymmetric sleep), in contrast to nearly 13 hours of sleep per day while nesting (Rattenborg 2017).

In contrast to studies of birds in flight, birds exhibit UHS conditionally while resting on land. Rattenborg and associates (1999) studied Mallard ducks (*Anas platyrhynchos*) and showed that when sleeping in groups, the ducks show a predilection for sleeping unihemispherically when on the outer edge of the group, with the eye facing away from the group open to watch for predators. Ducks in the center showed no preference for which eye they held open during UHS, while also exhibiting less UHS than those on the outer edge (Rattenborg *et al*. 1999).

1.3.4. Pinnipeds. Seals, members of the suborder Pinnipedia, exhibit UHS like whales and dolphins. However, this is only true of some seals – eared seals have UHS while in the water and BHS on land, while true seals always exhibit BHS, whether in the water or on land. Eared seals use their "awake" side to paddle and keep their face above water to breathe, occasionally switching sides (Rattenborg *et al*. 2000). True seals simply float at the surface or hold their breath and sleep beneath the water (Rattenborg *et al*. 2000, Mascetti 2016). Walruses, also of the suborder Pinnipedia, are like seals in that they exhibit (mostly) BHS on land, and more like true seals in that they hold their breath to sleep underwater, with decreased asymmetries between hemispheres (Mascetti 2016).

1.3.5. Jellyfish. Far less complex than humans, whales, and dolphins, jellyfish lack a central nervous system, instead utilizing a net of neurons, like other members of the phylum Cnidaria (Bosch *et al*. 2017). Despite their distributed nervous system, a species of jellyfish (*Cassiopea* spp.) has been recently observed to exhibit a sleep-like state (Nath *et al*. 2017). Nath and associates determined that *Cassiopea* exhibit a state that satisfies all three accepted behavioral hallmarks of sleep: reduced activity, reduced responsiveness/response time, and homeostatic regulation, or the need to recover (return to that state) if deprived of it (Allada & Siegel 2008). This leads to the question of whether a central nervous system is necessary or sufficient for sleep (Lesku & Ly 2017).

1.4. EFFECTS OF SLEEP DISTURBANCE/DEPRIVATION

The impact of missed sleep has been an area of study since at least the 1920s (Robinson & Herrmann 1922). Lack of sleep can cause many negative effects on the human body, whether the sleep deprivation is caused by shift work, insomnia, disturbances during

sleep, illnesses, disorders, difficult environments, circadian rhythm misalignments, or any number of other things that demand wakefulness or prevent sleep. People who suffer from sleep disorders, including insomnia and narcolepsy, regularly report poor health and low quality of life, especially when compared to people who do not suffer from sleep ailments (Reimer & Flemons 2003). They also spend more time in bed and miss or limit activities more often due to illnesses (Simon & Vonkorff 1997).

The effects of sleep loss are broad and partly dependent upon the amount lost, the frequency, and the how long regular sleep loss occurs. Negative effects associated with regular sleep loss due to disorders, even after treatment, may or may not improve (Reimer & Flemons 2003). Going a full day without sleep, or regular nights with insufficient sleep, causes mental deficiencies and physiological problems. These include difficulty in maintaining attention, slower recollection, difficulty with short-term memory, lower cognitive processing, slower thoughts, and depression. Physiological issues caused by persistent lack of sleep include cardiovascular morbidity, obesity, traffic accidents, accidents at work, and mortality (Banks & Dinges 2007).

Issues are also caused by other inevitable sleep disturbances, such as parents with a newborn, or people working in extreme environments, like astronauts on long or short space missions. Reports indicate that sleep issues such as “circadian misalignment can increase health risks and result in a decreased ability to effectively and efficiently perform tasks” (Guo *et al*. 2014). This can be especially crippling when every task is essential and resources are scarce, as is the case with astronauts in space. While coffee, amongst other caffeinated beverages, is commonly used to attempt to negate some of the negative effects of sleep deprivation, it is not a replacement for sleep. Caffeine’s effect on the brain and its

ability to help improve a sleep-deprived individual's performance varies from person to person. An optimal administration of caffeinated substances and how sleep and wake states are impacted by different dosages taken at different times of day are discussed and modeled in an interesting paper by Puckeridge *et al*. (2011).

1.5. SLEEP DISORDERS

As with any system in a living creature, sleep can be hindered by illnesses and disorders. Along with studying sleep in its natural form, scientists study many different sleep disorders, both to understand the illness and how it impacts sleep, as well as discovering effective ways to treat these disorders.

1.5.1. Narcolepsy and Cataplexy. Narcolepsy, a sleep disorder associated with excessive sleepiness and broken sleep, is somewhat common, affecting around 0.02% – 0.05% of the population (Mahlios *et al*. 2013, Scammell 2015). There are two clinically differentiated types of narcolepsy; loss of orexin/hypocretin-producing neurons in the hypothalamus causes Type 1, while Type 2 is nearly identical to Type 1 but lacks a known cause (Scammell 2015).

Onset of narcolepsy can be sudden or gradual and, unlike other causes of sleepiness, narcoleptic people are not always sleepy. While their sleepiness will emerge every day despite having sufficient sleep, they tend to awaken feeling rested (Scammell 2015). Another characteristic of narcolepsy is the intrusion of REM sleep into waking hours. Narcolepsy's partner condition, cataplexy, is a state where the characteristic loss of muscle tone (atonia) seen in REM occurs while a patient is awake, triggered by intense (usually positive but also occasionally negative) emotions. Cataplexy can cause immobility for up

to two minutes and is most commonly associated with Type 1 narcolepsy (Mahlios *et al*. 2013, Scammell 2015). Hallucinations while transitioning between wake and sleep in either direction are also common in narcolepsy (Scammell 2015).

While it is accepted that damage to, or lack of, orexin/hypocretin producing neurons or receptors causes Type 1 narcolepsy (Mahler *et al*. 2014, Scammell 2015, Branch *et al*. 2016), it has been suggested that narcolepsy may specifically be caused by a subject's own immune system attacking orexin-producing neurons (Mahlios *et al*. 2013).

1.5.2. Insomnia. A common ailment affecting 35% – 50% of the adult population, insomnia is a sleep disorder in which patients have difficulty falling asleep, difficulty staying asleep past a certain time, waking multiple times during the night, not feeling rested after sleeping, or some combination of these symptoms (Buysse 2013). This differs from sleep deprivation in that time and circumstances for sleep are sufficient and not the direct cause of the lack of sleep. Studies on insomnia pathology seem to show signs of hyperarousal, such as high-frequency activity in EEG recordings during NREM (Buysse 2013), a variety of brain regions showing wake-like and sleep-like activity at the same time (Krueger *et al*. 2008), and alpha frequencies during short arousal intervals similar to those observed in restful waking, meaning that the short periods of waking that occur normally during sleep are, in insomniacs, far closer to true wakefulness than in healthy patients (Schwabedal *et al*. 2016).

Whether insomnia is, in any given patient, a primary disorder or a symptom of some other issue, treatments break down into two types: cognitive-behavioral and medicinal. Cognitive-behavioral treatments focus on establishing a schedule to help entrain the circadian rhythm, keeping the bed an area only for sleep, learning techniques for relaxing,

and reducing anxiety (Buysse 2013). These last two approaches reinforce the notion that emotions can play a part in insomnia (Nofzinger *et al*. 2006). Medicinal treatments vary greatly, with many of the drugs prescribed for insomnia primarily used for treatment of other disorders, such as anti-depressants (Buysse 2013).

1.5.3. Fatal Insomnia. Patients with fatal insomnia do not merely find it difficult to fall asleep; they lose the ability to sleep completely. EEG characteristics that define sleep begin to disappear, often starting with sleep spindles. Eventually, the afflicted patient's sleep-wake cycle is altered to the point that true sleep is no longer possible; instead, patients may slide into short infrequent REM episodes directly from wake (Lugaresi *et al.* 1998). Patients become unable to maintain focused attention and will, if lacking stimulation, fall into a vegetative state that becomes more difficult to be roused from as the disease progresses. Cognitive impairments and memory problems commonly manifest as well, growing progressively worse over time (Wu *et al.* 2018). This will, by some complication or other, inevitably end in the death of the patient, often abruptly while they are fully awake and aware, or due to an infection contracted while in a "vegetative state" or coma (Montagna *et al.* 2003). Patients diagnosed with fatal insomnia may have a long or short disease course, with death occurring anywhere between 8 months or 6 years after onset of symptoms (Montagna *et al.* 2003), with an average survival time of 18 months (Khan & Bollu 2018).

Initially studied in an older gentleman by Lugaresi *et al.* (1986), further cases were discovered and documented, with both types of fatal insomnia (familial and sporadic) eventually classified as human prion diseases of different phenotypes (Cortelli *et al.* 1999,

Montagna *et al.* 2003). Both familial and sporadic fatal insomnia will be briefly discussed below.

1.5.3.1. Fatal familial insomnia (FFI). As the name implies, fatal familial insomnia (FFI) is inherited. As of 1999, only 25 different families had been recorded as carrying the gene for FFI (Gambetti & Lugaresi 1998, Cortelli *et al*. 1999). More recently, up to 50 families have been documented (Wu *et al*. 2018). FFI is dominant and is caused by a mutation in the prion gene in the 20th chromosome (Wu *et al*. 2018). Some other prion diseases can manifest in similar ways to FFI, including Creutzfeldt-Jakob disease (more aggressive than FFI, with more widespread neuronal degeneration) and Gerstmann-Straussler-Scheinker syndrome (some cognitive impairment but little sleep disturbance) (Khan & Bollu 2018).

1.5.3.2. Sporadic fatal insomnia (SFI). This phenotype of fatal insomnia is different from FFI in that it spontaneously appears, rather than being inherited (Montagna *et al*. 2003). Sporadic fatal insomnia (SFI) presents symptoms that may be impossible to distinguish from FFI; to differentiate in cases where there is familial history of insomnia, a specific mutation of the prion gene (D178N mutation in PRNP) must be confirmed, as only FFI has this particular mutation (Luo *et al*. 2012).

1.5.4. Circadian Rhythm Sleep Disorders (CRSD). There are two different types of circadian rhythm sleep disorders (CRSD): those with an extrinsic source and those with an intrinsic cause. Disorders primarily caused by outside factors (such as shift work disorder and jet lag disorder) are extrinsic, wherein the circadian drive performs normally under normal circumstances while outside influences cause severe enough disturbances to the circadian rhythm to be considered a disorder (Sack *et al*. 2007A). Then there are those

disorders caused by some intrinsic factors (such as advanced sleep phase disorder, delayed sleep phase disorder, free-running disorder, and irregular sleep-wake rhythm), where the issue lies with the circadian drive (Sack *et al*. 2007B). Also note that there may be cross-over between factors and that any one of these diagnoses may not be purely extrinsic or intrinsic (Sack *et al*. 2007A, B).

1.5.4.1. Shift work disorder (SWD). Due to non-standard work shifts, such as overnight, on-call, early awakenings and changing schedules, a person's circadian rhythm can be perturbed, leading inevitably into sleep deprivation. Shift work disorder (SWD) and its diagnosis are not often utilized in research studies, since the borderline between a normal response to circadian disturbance and an abnormal response is not precise. It can be treated with timed light exposure, prescribed sleep/wake scheduling, timed melatonin administration, hypnotic medication or stimulant medication (Sack *et al*. 2007A).

1.5.4.2. Jet lag disorder (JLD). Much like SWD, jet lag disorder (JLD) is due to an extrinsic cause; in this case, the circadian rhythm is not perturbed so much as misaligned due to a rapid change in time zone. Though usually self-remedying over time, it can also be treated with the same techniques used for SWD (Sack *et al*. 2007A). Disturbances due to changes in the circadian drive, such as jet lag, are explored later, in Section 4.1.

1.5.4.3. Advanced sleep phase disorder (ASPD). An intrinsic CRSD, advanced sleep phase disorder (ASPD) occurs when a patient has difficulty conforming to a certain sleep schedule; specifically, they have a stable, consistent sleep schedule that is several hours earlier than what is desired by the patient. The level of displacement between actual and desired sleep schedules necessary to be diagnosed is not precisely defined, meaning that a diagnosis typically relies more upon the severity of an individual's struggle to shift

their sleep schedules to external requirements. This disorder is usually treated with timed light exposure but may also be treated with phase-advance chronotherapy or timed melatonin administration (Sack *et al*. 2007B).

1.5.4.4. Delayed sleep phase disorder (DSPD). Like ASPD, delayed sleep phase disorder (DSPD) is an intrinsic disorder where a patient's stable sleep schedule is later than what they want or need. Patients have difficulty falling asleep and/or waking up early and tend to sleep longer than those not diagnosed with DSPD. This disorder does not have a defined cause but may be due to an elongated circadian period or a reduced ability to recover from missed sleep. Treatments for DSPD include chronotherapy, where sleep is delayed a little each day until the desired schedule is achieved, timed light exposure, melatonin, and hypnotic or stimulant medication (Sack *et al*. 2007B).

1.5.4.5. Free-running disorder (FRD). This disorder, also known as non-24-hour sleep-wake syndrome, occurs when patients function on a non-24-hour circadian rhythm. Humans have been found to have a natural (outside of any external entrainment) circadian period of slightly longer or shorter than 24 hours, but function on a 24-hour period due to the normal light-dark schedule of the Earth. People with free-running disorder (FRD) appear to either have difficult or failed entrainment to this light-dark schedule, and while more common in completely blind patients, it does occur in sighted patients as well (Sack *et al*. 2007B). For sighted patients, the only effective treatment supported by studies is timed melatonin administration. Blind patients may be treated with timed melatonin administration as well, and some studies have shown prescribed sleep/wake scheduling to be effective (Sack *et al*. 2007B).

1.5.4.6. Irregular sleep-wake rhythm (ISWR). Patients afflicted with irregular sleep-wake rhythm have inconsistent, short periods of sleep distributed throughout the day and night rather than one long sleep bout. Though the cause is unknown, damage to the SCN likely plays a role. Typically afflicting those with mental impairment or older persons with dementia, treatment may consist of timed applications of melatonin or light exposure, or mixed treatments that include increasing time spent in daylight and increasing the amount of daily physical activity (Sack *et al*. 2007B).

1.6. SYNCHRONIZATION

Synchronization is frequently utilized in analysis of neural activity, as it is here. It is also a vital component of brain activity during sleep, as mentioned briefly above. A brief review of synchronization and oscillators is provided here for reference. A comprehensive text on synchronization written by Pikovsky, Rosenblum, and Kurths (2001) covers the scientific history, synchronization in general, and more specific forms of synchronization in specialized systems.

1.6.1. Synchronization in General. Synchronization as a phenomenon was discovered by Christiaan Huygens in the mid-1600s. While improving his invention, the pendulum clock, Huygens observed that two clocks hanging from the same support began swinging in anti-phase synchronization. Each pendulum had 180° difference in phase with the other; in other words, both would hit the lowest point of their swing at the same time, and while one pendulum hit the highest point of its swing on one side (e.g., left), the other hit its highest point on the opposite side (right). Huygens found that the beam that supported the two clocks provided the necessary coupling for them to synchronize.

After this discovery, other forms of synchronization were found. In the mid-1800s, Lord Rayleigh observed a phenomenon called oscillation death between two pipe organs. When placed beside one another and the same note played on both, the sounds would quench each other. Sometimes the quenching was so effective that the organs would smother each other into near silence (Pikovsky *et al*. 2001). In 1920, it was discovered that triode generators could synchronize, a fact expanded upon by Edward Appleton and Balthasar van der Pol, who entrained an oscillator using a weaker external signal with a slightly different period. This demonstrated that an oscillator that is weak can be used to keep a powerful oscillator, such as a power generator, stable and at a specific frequency (Pikovsky *et al*. 2001).

Synchronization, in essence, is an interaction between oscillators that causes them to alter their frequencies and maintain an approximately constant time difference between their phases. The degree of frequency entrainment that can be achieved between two oscillators depends upon the strength of their interactions and the magnitude of the difference between their frequencies (Pikovsky *et al*. 2001). In the case of mutual synchronization, two oscillators experience equal coupling, and both change their frequencies in response (Pikovsky *et al*. 2001).

There are various methods for quantifying the degree of synchronization between two (or more) oscillators. For analysis of neural systems, the most widely used is stochastic phase synchronization, which quantifies the constancy of the phase difference between the oscillators. This is a statistical measure which can be applied to noisy, fluctuating oscillators, including experimental data; importantly, it allows for a definition of

synchronization that includes oscillators which may be out of phase. The mathematical details of this measure will be discussed below Section 2.2.4.1.

1.6.2. Oscillators. Two types of oscillators will be briefly discussed: self-sustained oscillators and relaxation oscillators.

Self-sustained oscillators maintain their periodic motions at frequencies defined by their internal parameters and exhibit three main characteristics: dissipation, stability, and non-linearity. Dissipation occurs when energy is lost (for example, to heat). While purely dissipative systems are unstable, nonlinear dissipative systems may exhibit stable, self-sustained oscillations if they also have some form of internal drive. This stability comes from the feedback between the dissipation and the energy source. If the amplitude of the oscillator increases beyond a threshold, the energy dissipation outstrips the internal power source, causing the amplitude to decrease. If instead the amplitude falls below a certain level, the drive becomes larger than the dissipation, providing the energy necessary for the amplitude to increase again.

Self-sustained oscillators can exhibit chaotic behavior under certain values of internal parameters, as is expected for non-linear systems. When coupled, they maintain their own amplitudes while shifting their frequencies to synchronize. They may also maintain a constant phase difference while synchronized.

Some neurons, under some conditions, can exhibit self-sustained oscillations. The two neural models utilized in this research both produce neurons capable of maintaining oscillations without coupling to other neurons. From this perspective, neural activity can thus be considered a dynamical systems problem.

A subset of self-sustained oscillators are relaxation oscillators. They exhibit the same characteristics described above but with periods of slow and fast change. This pulse occurs when a slowly increasing parameter reaches a threshold and a rapid change, such as a discharge, occurs. An excellent example of this is the neural action potential, where the voltage surpasses a threshold and causes a discharge, as discussed in detail above in Section 1.2.1.

1.7. PURPOSE OF RESEARCH

The author's previous work (Glaze *et al*. 2016) led to the work presented in this dissertation. This progression and the overarching goal of this research are discussed below.

1.7.1. Previous Research. In previously completed research, our group found chimera states in a network of Huber-Braun neurons (Glaze *et al*. 2016). A chimera state is a state in which a group of identical, interacting oscillators divide into two distinct groups – one group of synchronized oscillators and one group of desynchronized oscillators. This has been found in systems of different types of oscillators, including mechanical (Martens *et al*. 2013), optical (Hagerstrom *et al*. 2012), chemical (Tinsley *et al*. 2012), and of course neural (Omelchenko *et al*. 2013, Hizanidis *et al*. 2014, Glaze *et al*. 2016). More information on chimera states will be presented in Section 3.2.

While exploring chimera states in neural groups, we came across the sleep phenomenon known as unihemispheric sleep (discussed in Sections 1.3.2. – 1.3.4. and 4.2.). Comparing chimera states to UHS, we saw that both consisted of two groups (hemispheres) where one was synchronized (asleep) and the other desynchronized (awake),

and that inhibitory connections between the groups produced chimera states (Tinsley *et al*. 2012 and Glaze *et al*. 2016), while inhibitory connections between hemispheres produces UHS in sleep models (Kedziora *et al*. 2012). This led us to ask whether UHS can be modeled as a chimera state, a question which has led to the research presented in this dissertation.

1.7.2. Goal. The purpose of this project is to design a simple, schematic model of sleep dynamics based on the interaction between groups of individual simulated neurons. This approach stands in contrast to other models which describe the activity of brain regions as a whole, rather than arising from the interaction of individual neural oscillators. Using this approach, the interactions between individual neurons both within and between groups can be examined in detail, through the lens of synchronization (Sections 2.2.4. and 2.3.2. – 2.3.4.). The model will also be split into two distinct and interacting hemispheres, providing the opportunity to scrutinize the synchronization of regions within and between halves of a simplified “brain”. The existence of chimera states (Section 3.3.) can then be investigated as a model for asymmetric or unihemispheric sleep (Section 4.2.). Lastly, manipulation of a circadian drive can simulate the effects of jet lag (Section 4.1.).

2. FUNDAMENTAL SLEEP-WAKE MODEL

2.1. BUILDING A BASIC MODEL

The building blocks of a fundamental sleep-wake model, including organization of model elements and utilized neural models, is presented in this section.

2.1.1. Basic Model Organization. The simplest form of a sleep-wake model is comparable to a "flip-flop" switch – a group of neurons for sleep, a group for wake, and, since each state is stable on its own, a driving force that causes the states to switch. This type of model has been explored by other researchers in many flavors; the most common types of model are discussed below.

2.1.1.1. Flip-flop switch. A flip-flop switch is a simple, stable circuit. Essentially, two components mutually inhibit one another, which produces a feedback loop with two stable states. The interactions between sleep-promoting neurons (such as those in the ventrolateral preoptic area (VLPO)) and wake-promoting neurons (such as neurons in the locus coeruleus (LC)) are mutually inhibitive (Saper *et al*. 2001), making the flip-flop switch a good choice to model the switching between non-rapid eye-movement (NREM) sleep and waking.

Many researchers have noted the reciprocal relationship between sleep-promoting and wake-promoting neurons (Gallopin *et al*. 2000, McGinty and Szymusiak 2000, Saper *et al*. 2001, Nakao *et al*. 2007). The flip-flop switch has, for example, been used to model this reciprocal relationship in the model developed by Rempe *et al*. (2010), which utilizes mutual inhibition between wake-promoting and sleep-promoting neurons (along with external inputs) to switch between the stable state of wakefulness and the stable state of

NREM sleep. This reciprocity can also be applied to the switch between NREM and rapid eye-movement (REM) sleep, as explored by Lu *et al*. (2006) and Rempe *et al*. (2010).

Another interesting take on the flip-flop switch was presented by Booth and Diniz Behn (2014), who compared the mutual inhibition between sleep and wake to a hysteresis loop. Essentially, each state – sleep and wake – is stable, and an outside driving force (in this case, the homeostatic drive, or sleep pressure) triggers the switch, by increasing or decreasing beyond a threshold. This increase and decrease, along with the transition between states, forms the hysteresis loop. As Booth and Diniz Behn mention, the activity of this hysteresis loop is comparable to the *two-process model*.

2.1.1.2. Two-process model. The two-process model was developed in 1984 by Daan, Beersma and Borbély. This type of model consists of two separate, interacting processes – a Process C for the circadian drive or rhythm, and a Process S, which represents sleep propensity, or the homeostatic drive. As depicted in Daan *et al*. (1984), the S process increases exponentially during the daytime until it reaches an upper bound H, after which it decreases in the same way until it reaches a lower bound, defined by L. The upper and lower bounds have the periodic behavior of a skewed sine wave, and change according to the circadian process C. The combination of these two processes enables the system to transition between wake and sleep.

This model has been used to simulate sleep numerous times and remains one of the most favored (Nakao *et al*. 2007). Several new models have been developed based on the two-process model (Borbély and Achermann 1992, Phillips and Robinson 2007), and Daan *et al*.'s (1984) is often used as a measure for authors to compare with their own models (Rempe *et al*. 2010).

2.1.1.3. Two-group/two-neuron models. The initial form of the model developed in this dissertation consists of a small group of neurons (typically 8 neurons, unless otherwise specified) active during the wake state, another group of neurons active during the sleep state, and a circadian pacemaker C, which drives the state-switching. While C drives the system, the sleep and wake groups mutually inhibit each other, and the state of the system depends upon the active group.

Similar models have been developed and studied by other groups. Postnova, Voigt and Braun (2009) designed a two-neuron feedback model to simulate sleep-wake cycles, inspired by experimental data. A hypocretin/orexin (ORX) neuron was reciprocally coupled to a glutamate (GLU) neuron with excitatory connections, while also receiving input from the circadian drive, which originates in the suprachiasmatic nucleus (SCN) (Postnova *et al*. 2009). An extended version of this model, including a homeostatic process projecting to the GLU neuron, was used to investigate the impact of noise and diversity of sleep-wake cycling management (Patriarca *et al*. 2012).

A variant of the two-neuron model is the *two-oscillator model* (Nakao *et al*. 2007). Here, two oscillators mutually interact, but do not represent wake and sleep. Rather, one oscillator represents the activity of the SCN, controlling temperature and the circadian pacemaker, while the second mediates the switching between sleep and wake states. The two-neuron model can also be used as a simple way to model the human circadian rhythm (Kronauer *et al*. 1982, Strogatz 1987).

2.1.2. Huber-Braun Neural Model. All neurons in the model presented here utilize either the Hindmarsh-Rose neural model, to be discussed in Section 2.3, or the Huber-Braun model for thermally sensitive neurons (Braun *et al*. 1998). This model was

selected due to the wide range of realistic bursting dynamics it exhibits. The model is described here for reference; for further details, see the original paper.

The Huber-Braun (HB) model is a Hodgkin-Huxley-based (Hodgkin and Huxley 1952) neural model, initially designed to replicate the activity of the facial cold receptors of a cat. It incorporates five different currents – depolarizing, repolarizing, sub-threshold depolarizing, sub-threshold repolarizing, and a leak current. Each of these currents contribute to the change in voltage for each neuron at each timestep. The equation for the change of voltage for each neuron is given by

$$C_M \frac{dV}{dt} = -I_l - I_d - I_r - I_{sd} - I_{sr} - gw + C_i, \tag{2.1}$$

where each *I* represents one of the currents. For the depolarizing (d), repolarizing (r), and sub-threshold depolarizing (sd) currents, $I_i = \rho g_i a_i (V - V_i)$, where $i = d, r, sd$. In this equation, a is the activation variable, whose change over time is given by

$$\frac{da_i}{dt} = \frac{\phi(a_{i\infty} - a_i)}{\tau_i}$$

where

$$a_{i\infty} = \left(1 + \exp\left(-s_i(V - V_{0i})\right)\right)^{-1}.$$

Here, s_i is the steepness, and V_{0i} is the half-activation potential. The model constants are given in Appendix A.

Returning to Equation 2.1, the sub-threshold repolarizing (sr) current is defined as

$$I_{sr} = \rho g_{sr} a_{sr} (V - V_{sr}),$$

with the activation variable given by

$$\frac{da_{sr}}{dt} = \frac{\phi(-\eta I_{sd} - k a_{sr})}{t_{sr}}.$$

Finally, the leak (l) current is given by $I_l = g_l(V - V_l)$. As for the constants, g is the maximum conductance, V_i (where $i = d, r, sd, sr$) is the reversal potential, τ is the time constant, C_M is the membrane capacitance and η and k are scaling factors. There are also temperature-dependent scaling factors, ρ and ϕ, given by

$$\rho = 1.3^{T-T_0/10}$$

and

$$\phi = 3.0^{T-T_0/10}.$$

The final two terms in the original equation (Equation 2.1) are noise and coupling, respectively. Braun *et al*. (1998) used Gaussian white noise as defined in Fox *et al*. (1988),

$$gw = \sqrt{-4\ D\ dt \ln(a)} \cos(2\pi\ b).$$

Here, D is noise amplitude, dt is the numerical integration time step, and a and b are random numbers between 0 and 1, updated independently at each time step for each neuron. The coupling term C_i, not a part of the original model, allows for external input from other neurons, and will be discussed in Section 2.2.

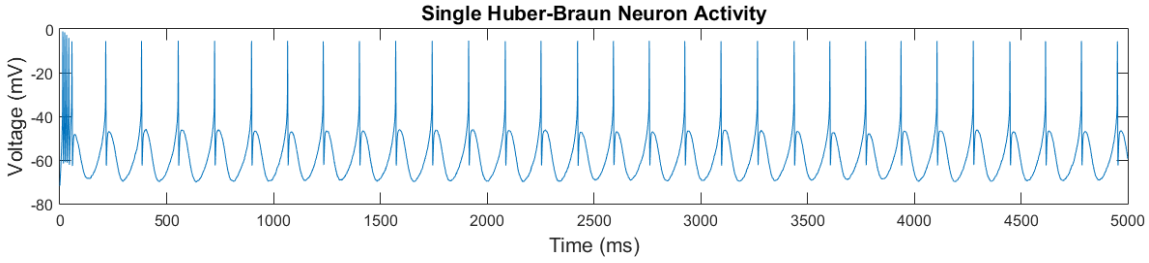

Figure 2.1 – Activity of a Single Uncoupled Huber-Braun Neuron
The firing pattern of a single Huber-Braun neuron, when it is not coupled to anything else. Note the rapid activity during the first few milliseconds of the run. This is transitory behavior as the model settles into its normal behavior.

The activity of a single HB neuron with no external input is shown in Figure 2.1. From 0 to about 75 ms, the voltage of the neuron oscillates rapidly as the model settles into its steady-state behavior. This transient behavior is typically discarded before data analysis. Note that all neurons begin with random, heterogeneous initial voltages, selected from a uniform distribution between 0 to -70 mV.

2.1.3. Circadian Drive. In the model used here, the circadian pacemaker is a skewed sine wave (Figure 2.2), with its peak in the early day and the trough occurring in early night, as defined by Daan *et al*. (1984). The pacemaker function is given as

$$C = 0.97\sin(\omega t) + 0.22\sin(2\omega t) + 0.07\sin(3\omega t) + 0.03\sin(4\omega t) + 0.01\sin(5\omega t). \quad (2.2)$$

It has a range from -1 to 1, with t as the time step dt and $\omega = 2\pi/T$, where the period T is 24 hours.

2.1.4. Time Compression. There is a large discrepancy between the time scale of the HB neurons and the circadian drive. One operates at the scale of milliseconds, while the other changes over the course of hours. To reconcile this difference in time scales we set, unless specified otherwise, one minute of simulation time as equivalent to a 24-hour period. This time compression simplifies the model such that parameter space is easier to explore in a reasonable amount of computational time. However, such a sharp compression may lead to difficulty isolating the transitions between states, as these state switches usually occur on a much smaller time scale than the daily cycles as a whole (Rempe *et al*. 2010); the closer the two time scales are, the harder it will be to differentiate these transitions from the rest of the activity. The time compression is scaled back slightly for some later runs. In future work, this time scaling can be eased further.

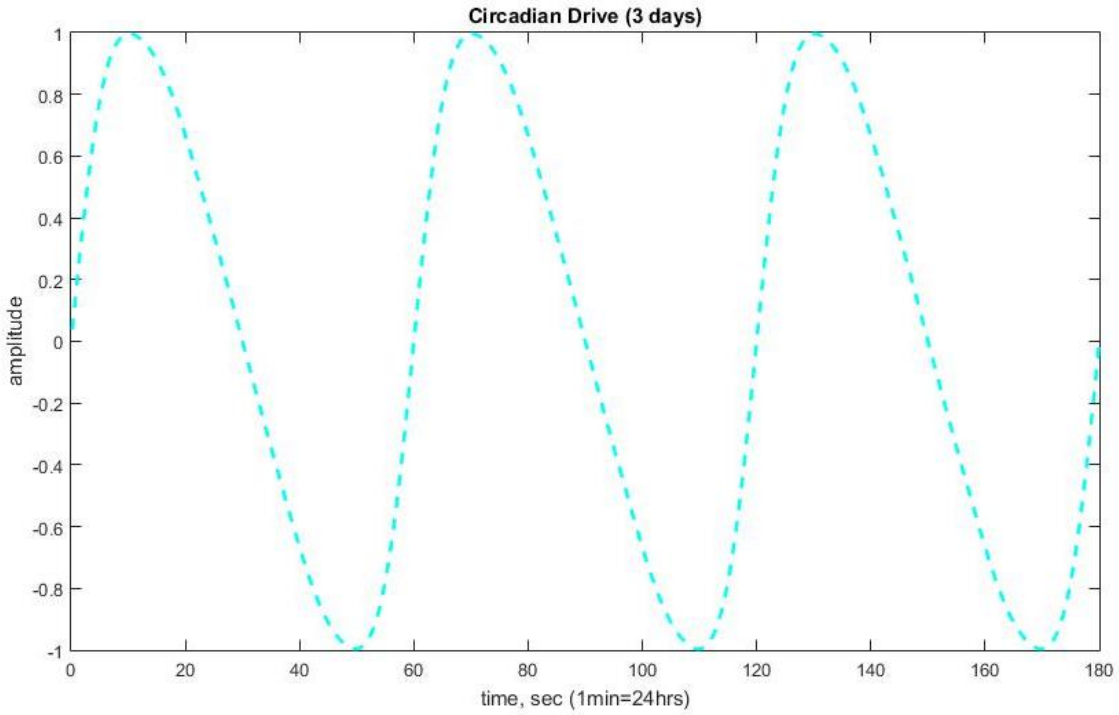

Figure 2.2 – Circadian Drive
Output of the Daan *et al*. (1984) skewed sine wave circadian drive model, for a three-day period.

2.2. ONE-HEMISPHERE MODEL

The model presented here contains individual neurons, like the two-neuron models; however, unlike these models, multiple neurons are utilized to represent each group. This allows investigation of local dynamical changes within and between regions, such as synchronization. Here, the form of the model can be equated to a simple "one-hemisphere" model. A two-hemisphere version is presented in Section 3.1.

The model here, in all its iterations, was run in MATLAB with a custom program using Euler integration and integration time step $dt = 0.01$.

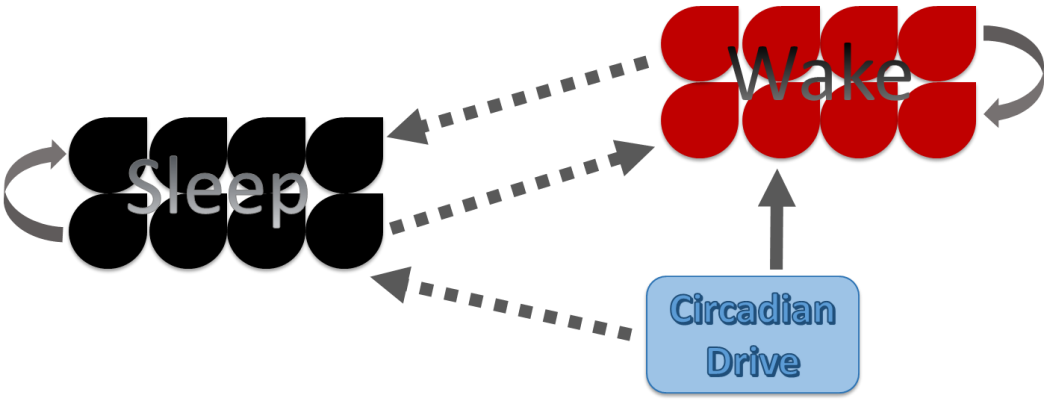

Figure 2.3 – Flow Chart for One-Hemisphere Model.
A representation of the connections between components in the one-hemisphere version of the model. Both the sleep (black) and wake (red) regions consist of 8 neurons (teardrop shapes), which project to other neurons within their region (curved arrows). Each region projects to the other, and the circadian drive (blue box) projects to both regions. Solid lines represent excitatory projections, and dashed lines represent inhibitory projections.

2.2.1. Connections. Each neuron receives input from all other neurons. The model structure is represented schematically in Figure 2.3, where the teardrop shapes are neurons, with black signifying the sleep group and red corresponding to wake, and the circadian drive (CD) is indicated by the light blue rectangle. The arrows represent the projections within and between groups, with solid arrows indicating excitatory connections, and dashed arrows inhibitory connections.

One wake neuron, for example, receives an excitatory stimulus via the mean field of all other neurons in its group, given by

$$V_{Grp} = \left[V_j(t-1) - \frac{\Sigma_{i \neq j} V_i(t-\tau)}{N_{neur} - 1} \right],$$

where V_j is the voltage of the neuron of interest, t is the current timestep, V_i is the voltage of the other neurons in the region, τ is the time delay of the signal from one neuron to another in the same region, and N_{neur} is the number of neurons within a region. Note that the mean field is calculated as the average voltage of neurons in a group at a given time point; for input to a neuron from within its own group, this average is performed over all neurons except the neuron of interest. Each wake neuron is also coupled to the mean field of the sleep group, though this connection is inhibitory. Input from the neurons in a different region is given by

$$V_{Reg} = \left[V_j(t-1) - \frac{\Sigma_{k \neq j} V_k(t-\tau_R)}{N_{neur}}\right].$$

This equation has the same format as the above, with V_k being the voltage of the neurons in another region, and τ_R being the time delay of the signal from one neuron to another in a different region. Each neuron also receives input from the circadian drive.

Coupling strength within a group is represented by g, while projections from the wake group to the sleep group are mediated by the coupling strength g_W, and from sleep to wake by coupling strength g_S. The strength of the projections from the circadian drive to the wake neurons and sleep neurons are given by g_{CW} and g_{CS}, respectively. To make the wake neurons active during the day, at the peak of the circadian drive, and inactive during the night, at the trough of CD, the projection from CD to wake is excitatory. Since the sleep neurons act oppositely to the wake neurons, the projection from CD to sleep is inhibitory. The coupling term C_i from Equation 2.1 can be written as

$$C_i = g\left(V_{Grp}\right) + g_{S/W}(V_{Reg}) + g_{CS/CW}(I_C), \tag{2.3}$$

where I_C is the input from the CD.

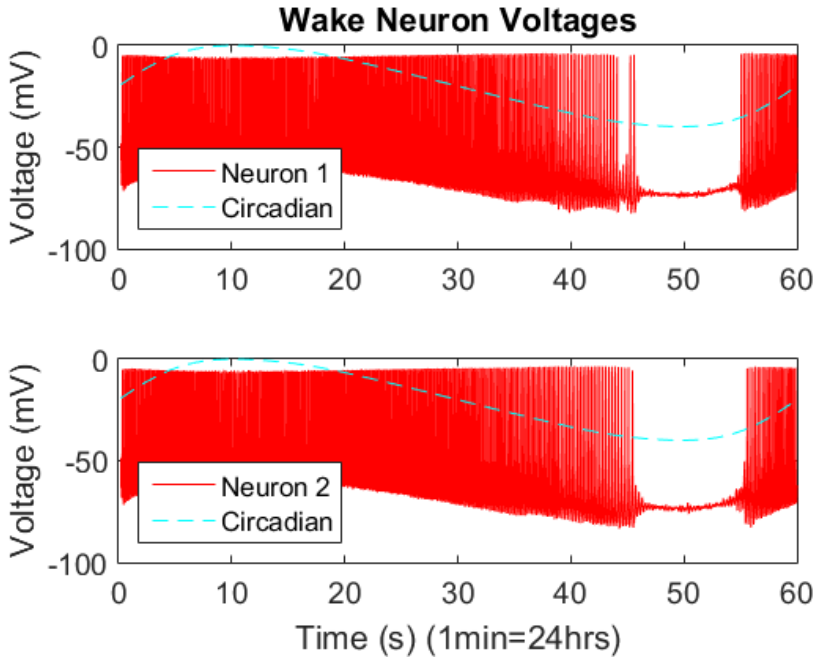

Figure 2.4 – Example of Wake Neuron Voltages
The voltages of two neurons from the wake region. Note how the activity dies out at "night" (the trough of the circadian cycle) and that the firing rate decreases before the onset of "night". The circadian curve is included for reference (light blue dashed line). The parameters were set at $g_W = -0.025$, $g_{CW} = 2.75$, $g = 0.030$, $g_S = -0.005$, and $g_{CS} = -2.75$.

Besides the circadian drive, there is a time delay τ corresponding to the finite time needed for signal transmission. This time delay is shorter for the neurons within a group and is longer between groups. Unless otherwise stated, this delay, given in units of dt, is set at $\tau = 1040$ (corresponding to $10.40\,ms$) for neurons within one group, and $\tau_R = 2100$ (corresponding to $21.00\,ms$) between neurons in different groups.

2.2.2. Results. The system's behavior varies significantly as a function of the coupling constants (g_W, g_S, g_{CW}, and g_{CS}), the number of neurons in each group, and the bursting state of the uncoupled neurons which is governed by the parameter T in the scaling factors ρ and ϕ.

2.2.2.1. Basic results. The wake neurons in this model receive projections from the sleep neurons and the circadian drive, as well as the connections to the other neurons within their group. Note that a negative value for a coupling term corresponds to an inhibitory projection, while a positive term corresponds to an excitatory projection.

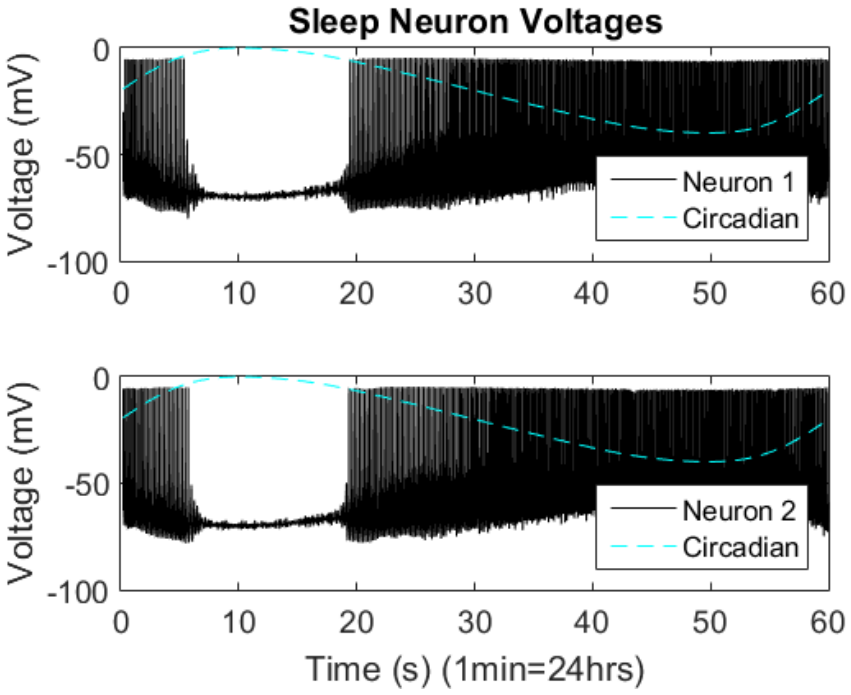

Figure 2.5 – Example of Sleep Neuron Voltages
The voltages of two neurons from the sleep region. Like wake, the activity of the sleep neurons dies out, but during the "day" (the peak of the circadian cycle). The circadian curve is included for reference (light blue dashed line). The parameters were set at $g_W = -0.025$, $g_{CW} = 2.75$, $g = 0.030$, $g_S = -0.005$, and $g_{CS} = -2.75$.

Displayed in Figure 2.4 are the voltages of two of the eight neurons in the wake group. Here, $g = 0.030$, $g_{CW} = 2.75$, and $g_S = -0.005$. Each neuron fires rapidly, with the highest range of voltages occurring with the peak of the circadian drive (the light blue

dashed line). The lower bound of the range of values decreases over the course of the day. As the trough of CD is approached, the firing rate of the neurons decreases, as can be seen from about 40 to 46 seconds on the figure. During the lowest portion of CD, both wake neurons cease firing. At around 55 seconds, the neurons begin firing again, their lower

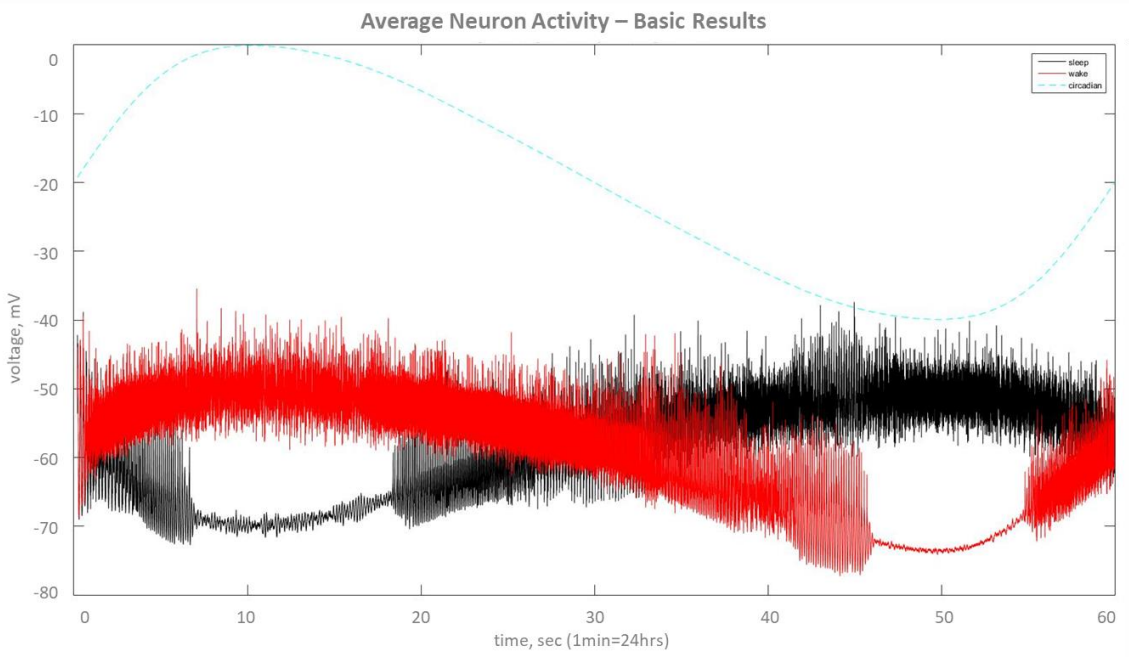

Figure 2.6 – Average Neuron Activity, Initial Results
The average activity of all neurons in the sleep region and the wake region. The peak of activity of one region coincides with the period of inactivity of the other region. Parameters are the same as in Figures 2.4 and 2.5.

bound sharply increasing with CD. The wake neurons' downtime, after time compression, is equivalent to about 3.6 hours of sleep. This is not a sufficient downtime to represent human sleep. Adjustments to parameters to accommodate this fact will be discussed below.

The neurons in the sleep group have projections from the wake neurons and the circadian drive, and connections with the other neurons in their own group. Like the wake group, the sleep group has 8 neurons and internal coupling strength $g = 0.030$; the coupling from wake to sleep is $g_W = -0.025$ and the coupling from the circadian drive is $g_{CS} = -2.75$. With these parameters, the activity of two representative sleep neurons is shown in Figure 2.5.

As expected, the sleep neurons have the greatest activity during the trough of CD and become inactive during the peak. Like the wake neurons, the lower bound of the sleep neurons voltages increases as the day progresses into night and the neurons move to their peak activity; the lower bound then decreases as the night wears on into morning. Unlike the wake neurons, the sleep neurons shift rapidly between active and inactive states, with only a slight gap in the firing as a warning sign (around 6 to 7 seconds in the figure). After time compression, the downtime for the sleep neurons corresponds to ~4.6 hours of wakefulness. This is not sufficient for a system representing a human's sleep-wake cycle, as humans generally are awake for about ⅔ of the day. Changes to parameters to adjust this downtime will be discussed in the next few sections.

The average activity of each group is shown in Figure 2.6. Wake neurons are represented by the red line, and sleep neurons are represented by the black. The circadian drive is included (light blue dashed line) for reference. Each curve has a period of inactivity at its trough, as was seen in Figure 2.4 and Figure 2.5. Each neuron group experiences a decrease in its firing rate before its period of inactivity. There is also an overlap in activity between the two groups (see Section 2.2.4. below for further discussion).

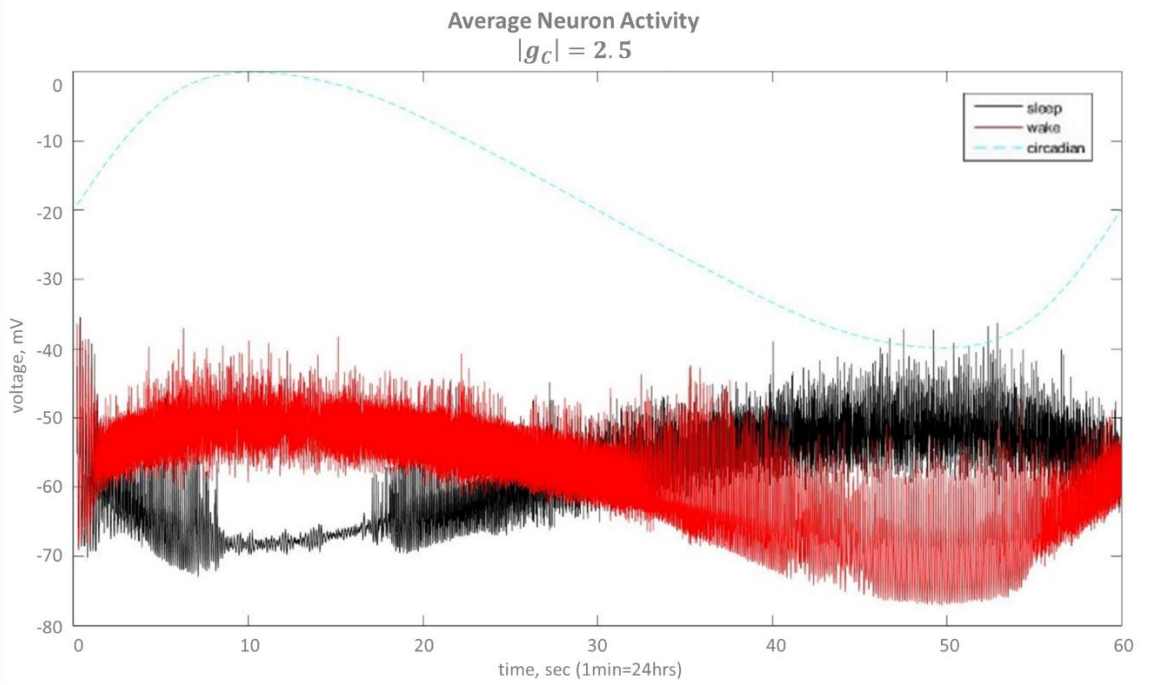

Figure 2.7 – Average Neuron Activity, $|g_C| = 2.5$
Average activity of the wake (red) and sleep (black) neurons when $|g_C| = 2.5$. The circadian drive curve is included for reference. Parameters are $g = 0.030$, $g_W = -0.025$, and $g_S = -0.005$.

2.2.2.2. Changing g_C. The coupling between CD and both the sleep and wake groups has a significant effect on the system dynamics.

The average neural activity for $g = 0.030$, $g_W = -0.025$, $g_S = -0.005$, $g_{CS} = -2.5$, and $g_{CW} = 2.5$ is shown in Figure 2.7. Comparing this figure to the average activity figure from the previous section (2.2.2.1., Figure 2.6, $|g_C| = 2.75$), it is easy to see that the activity each group is significantly affected by the change in the circadian coupling. In Figure 2.7, the wake neuron group does not cease firing during the entire run, unlike in Figure 2.6. Though the firing does not stop in Figure 2.7, it decreases during the expected period of "sleep". As a result of decreasing CD input to the wake neurons, there is

insufficient inhibitory input to inactivate the wake region. In contrast, the sleep region displays more subtle changes. For the sleep and wake regions, both the length of the downtime and the amplitude of the hyperpolarization increase with g_C (Figures 2.8 and 2.9).

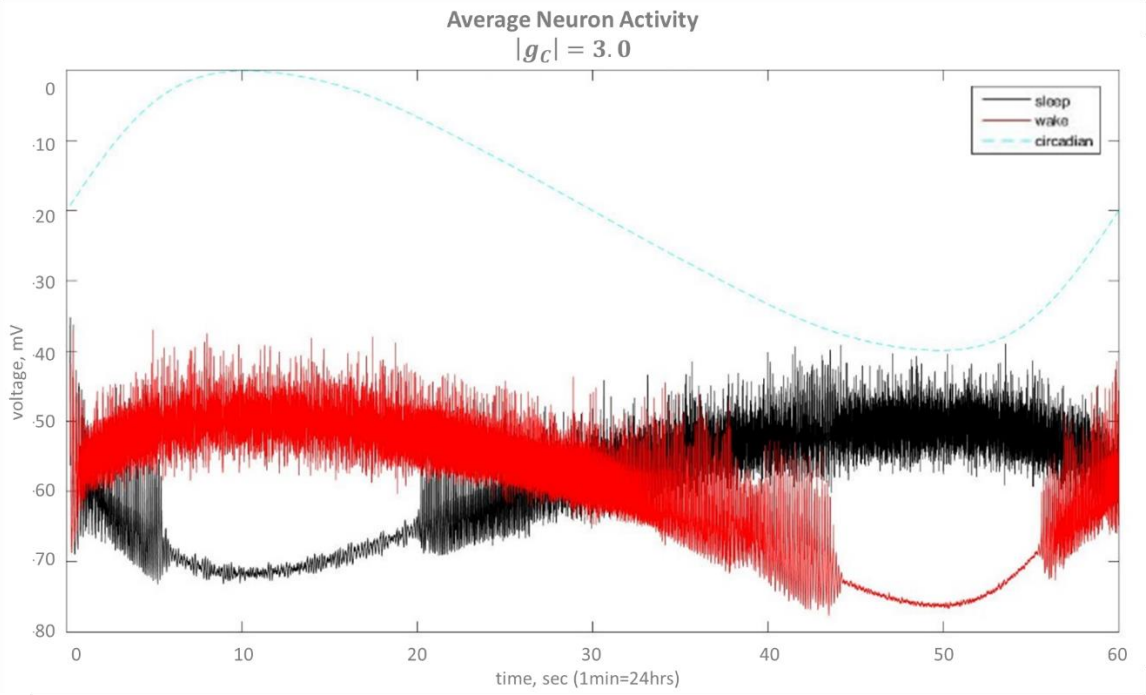

Figure 2.8 – Average Neuron Activity, $|g_C| = 3.0$
Average activity of the wake (red) and sleep (black) neurons when $|g_C| = 3.0$. The circadian drive curve is included for reference. The wake neuron activity stops during the trough of the circadian drive, and sleep has a longer period of inactivity than in Figure 2.7. Parameters are $g = 0.030$, $g_W = -0.025$, and $g_S = -0.005$.

2.2.2.3. Changing g_S/g_W. The connections between regions are as essential as the input from the circadian drive. With $|g_C| = 2.75$, $g = 0.03$, and $g_S = g_W = -0.012$, the

model produces results seen in Figure 2.10A. Similar to previous results, there is downtime for each region at the trough of its average activity curves, which correlates with the trough and peak of CD for wake and sleep, respectively. When g_S (coupling strength from sleep to wake) and g_W (coupling strength from wake to sleep) are doubled, the results change slightly, as can be seen in Figure 2.10B. The downtime for each region occurs at the same time, while the length has increased. The amplitude of the hyper polarization has also decreased.

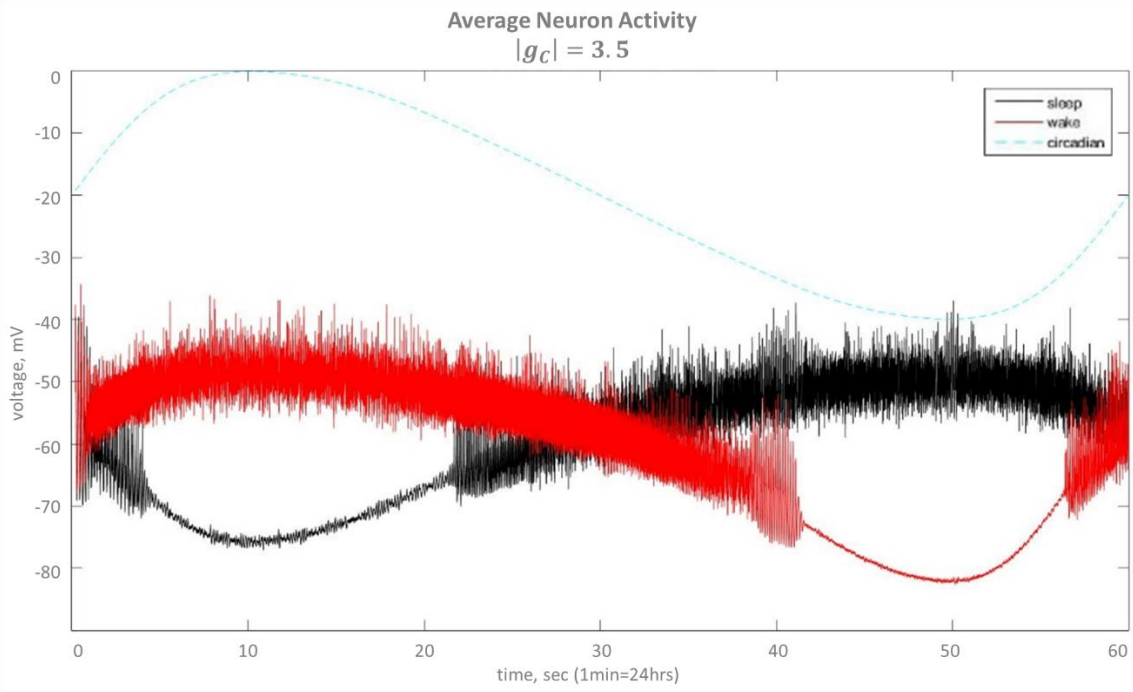

Figure 2.9 – Average Neuron Activity, $|g_C| = 3.5$

Average activity of the wake (red) and sleep (black) neurons when $|g_C| = 3.5$. The circadian drive curve is included for reference. The wake activity stops during the trough of the circadian drive, becoming hyperpolarized. Sleep has a longer period of inactivity than in Figures 2.7 and 2.8. Parameters are $g = 0.030$, $g_W = -0.025$, and $g_S = -0.005$.

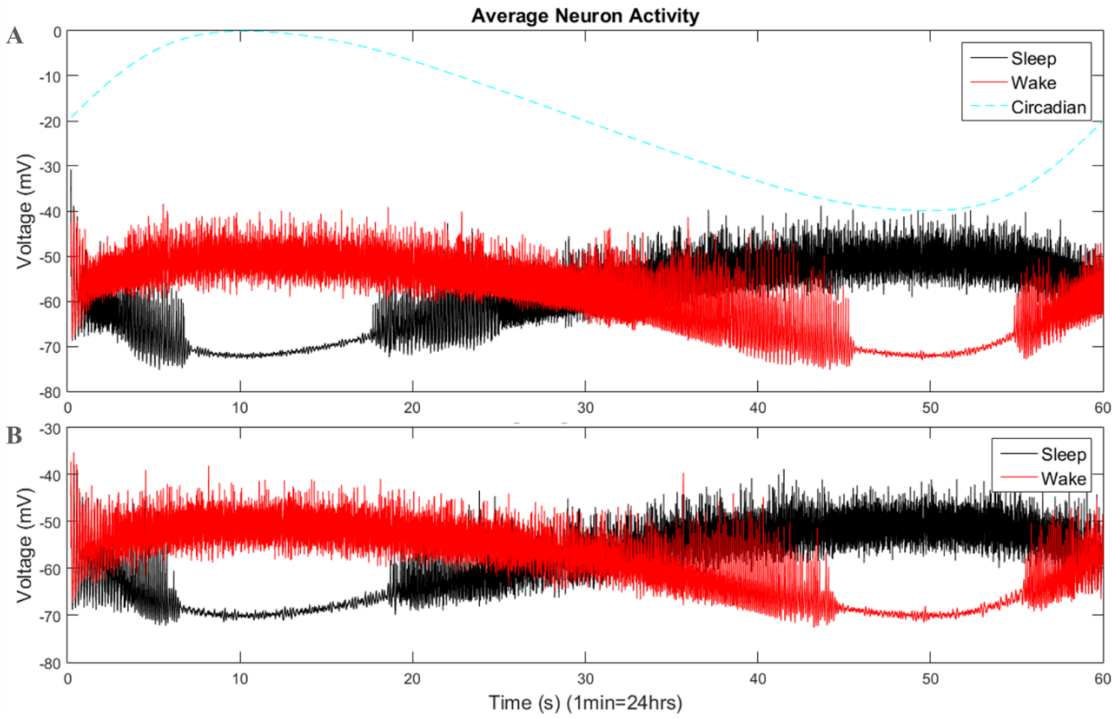

Figure 2.10 – Average Neuron Activity, Changing g_S and g_W
Average activity of sleep and wake neural groups with different values of coupling between groups. Parameter values common to all parts of the figure are $|g_C| = 2.75$ and $g = 0.03$.Circadian drive curve included for reference. (A) $g_S = g_W = -0.012$. Note the periods of inactivity at the peak (sleep) and trough (wake) of the circadian drive, which hyperpolarize each region. (B) $g_S = g_W = -0.025$. Periods of inactivity are longer, and the hyperpolarization is smaller in amplitude.

Much like increasing g_C, increasing g_S and/or g_W will increase the downtime of a region. In contrast to increasing g_C, however, increasing the coupling between the regions decreases the amplitude of the hyperpolarization.

2.2.2.4. Changing number of neurons. Most nonlinear dynamical systems exhibit so-called size effects, where the number of oscillators affects the outcome of the dynamics (data not shown). In order to investigate the size effects in the present model, the number of neurons per region was increased from 8 to 10 and 12.

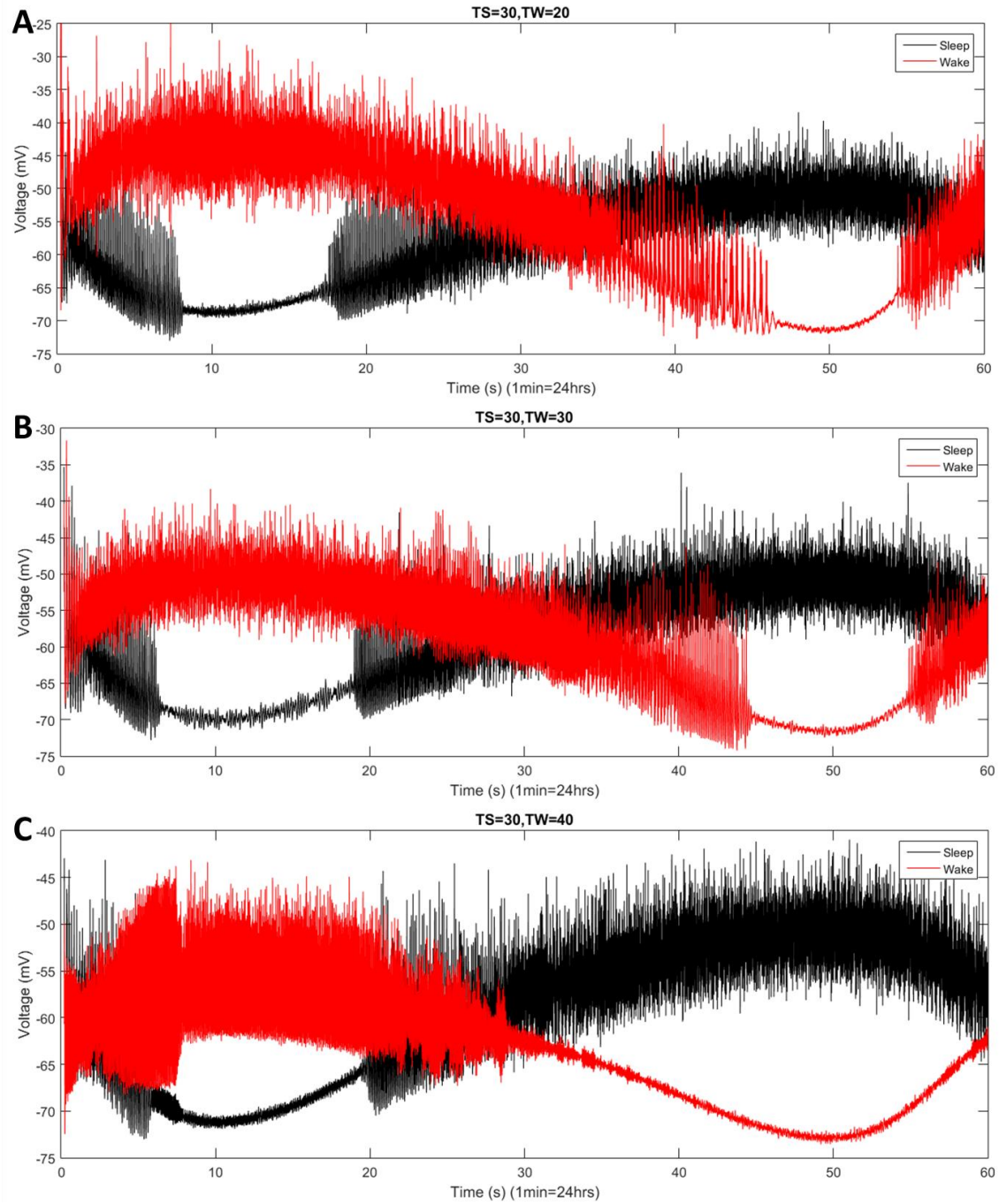

Figure 2.11 – Average Neuron Activity, Changing T_W

Average activity of sleep and wake regions with changing T_W. For all panels, $g = 0.030$, $g_W = -0.025$, $g_S = -0.015$, $g_{CW} = 2.75$, $g_{CS} = -2.75$, and $T_S = 30\ °C$. The standard temperature at which all neurons were set was $30\ °C$. In (B), both regions are set at this standard temperature. (A) $T_W = 20\ °C$. Note that the wake amplitude has increased from B, while the downtime has decreased. (C) $T_W = 40\ °C$. Note that the wake amplitude has decreased slightly from B, and the downtime has significantly increased.

Despite this increase of up to 50% of the original value, no discernible changes to activity were observed. This may be due to the simplicity of this form of the model. If so, then a more complex version may yield different results. A much larger increase in the number of neurons may also be needed in order to obtain discernable size effects. Variations of the system size will be revisited in Section 2.2.4.3.

2.2.2.5. Changing temperature. The Huber-Braun neural model used here is based on temperature-sensitive neurons, as mentioned above (Section 2.1.2.). This means that the behavior of the model can change with the temperature parameter. Here, the temperature parameter will be used not to represent the temperature of the environment or the neurons, but rather to modulate the behavior of the neurons. For all previous runs, all neurons in both regions had the same temperature of $30° C$, a value for which the uncoupled oscillators fire repetitive single spikes without bursting. To examine the effect of changing the temperature parameter, the temperature of the wake neurons was varied while the temperature of the sleep neurons was held constant. The average activity of each group at varying temperatures is shown in Figure 2.11.

In Figure 2.11, the parameters are $g = 0.030$, $g_W = -0.025$, $g_S = -0.015$, $g_{CW} = 2.75$, and $g_{CS} = -2.75$. Both T_W (wake neuron temperature) and T_S (sleep neuron temperature) are set to the standard $30° C$ in Figure 2.11B; the shape of the average activity curves and behavior of the neurons in this figure are akin to other previous figures, such as Figure 2.6. Decreasing T_W to $20 °C$ (a value for which the uncoupled oscillators fire triplets, or triple spikes) while maintaining T_S at $30 °C$ produces average activity curves such as those in Figure 2.11A. The amplitude of the wake curve increases with the decrease in temperature. In contrast, the sleep neuron group amplitude did not change appreciably.

When the temperature for the wake group was increased to $40° C$ (a value for which the uncoupled neurons do not fire, but undergo rapid, subthreshold oscillations), the average activity for each region changed more significantly, as can be seen in Figure 2.11C.

These results suggest that the mean field amplitude is inversely proportional to temperature and positively correlated with the bursting activity. As the temperature is decreased (still above the homoclinic bifurcation threshold at $10.7° C$, where the neuron ceases firing (Feudel *et al*. 2000, Finke *et al*. 2011)), the uncoupled neurons fire bursts with an increasing number of spikes. The duration of the downtime of each region has a positive correlation with the temperature and a negative correlation with the bursting activity. As the temperature is increased above $30° C$, the uncoupled neurons begin to fire irregularly, skipping spikes (Braun *et al*. 1998). This less frequent firing decreases the excitatory impact from other wake neurons, giving the inhibitory sleep neurons the opportunity to drive the wake region into its downtime sooner, and for a longer duration.

2.2.3. Specifying Regions. The sleep and wake groups of neurons can be associated with specific regions of the brain. For this model, the sleep region is specified as the ventrolateral preoptic area (VLPO). The wake region is specified as monoaminergic (AMIN) neurons from the locus coeruleus (LC).

2.2.3.1. Sleep and VLPO. The VLPO is located in the hypothalamic preoptic area. Its role in sleep regulation was first recognized in 1946, when Walle Nauta experimentally demonstrated that insomnia occurred in rats whose hypothalamic preoptic area had been lesioned (Nauta 1946). That the VLPO specifically contains sleep-promoting neurons was not discovered, however, until 1996 (Sherin *et al*. 1996). Soon afterward, it was noted that VLPO activity is correlated with the fostering of sleep rather than the tiredness of the

subject (Szymusiak *et al*. 1998). Furthermore, the extended ventrolateral preoptic area (eVLPO) is strongly associated with the production of REM sleep, as will be discussed in Section 5.3.2.

A close correlation between the VLPO and the amount of NREM sleep has been observed, along with a strong reciprocal inhibitory relationship with the wake promoting regions of the hypothalamus, leading to use of the VLPO in flip-flop switch models (Gallopin *et al*. 2000, McGinty and Szymusiak 2000, Saper *et al*. 2001, Saper and Lowell 2014). VLPO activity has also been simulated in more complex models of sleep-wake dynamics, including Phillips and Robinson's model (2007), which has been utilized in many other models and papers since its introduction; a model developed to replicate mouse sleep-wake behavior (Diniz Behn *et al*. 2007); a complex model by Rempe *et al*. (2010) based on a flip-flop switch with a removable REM-NREM switch; a physiologically-based model including the circadian rhythm (Phillips *et al*. 2013); and a two-hemisphere sleep-wake model developed specifically to simulate unihemispheric sleep (Kedziora *et al*. 2012).

2.2.3.2. Wake and AMIN. The neural group that promotes wake can be equated to the wake-promoting monoaminergic neurons in the locus coeruleus. Monoaminergic neurons promote waking and are located in several regions of the brain. There are serotoninergic neurons in the dorsal and median raphe nuclei, dopaminergic neurons near the dorsal raphe nuclei, and most notably, noradrenergic neurons in the LC (Saper *et al*. 2010).

The LC and VLPO have reciprocal inhibitory connections (Saper *et al*. 2001, Saper *et al*. 2010), making AMIN neurons a prime choice to pair with the VLPO for flip-flop

switch models. AMIN neurons are also frequently used in other sleep models to represent a group or region that promotes waking. The models discussed previously (Section 2.2.3.1.) utilize an AMIN group to represent the wake-promoting region, with Phillips and Robinson (2007) and Diniz Behn *et al*. (2007) specifying their use of AMIN neurons from the LC.

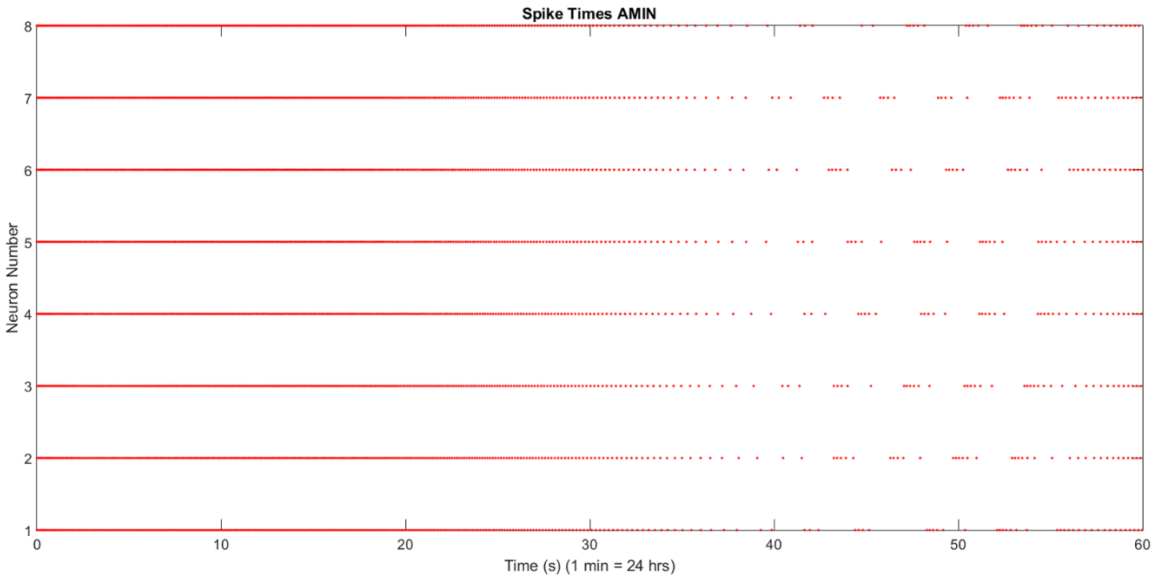

Figure 2.12 – Spike Times Plot for AMIN Neurons
A raster plot of the spike times for all the neurons in the AMIN region. Parameters are $g_A = -4.25x10^{-5}$, $g_V = -3.75x10^{-5}$, $g = 4.5x10^{-5}$, $|g_C| = 0.95$, $T_A = 5\,°C$, and $T_V = 15\,°C$, with the threshold at $-28\,mV$.

2.2.4. Synchronization Analysis. Henceforth, parameters g_S, T_S, and g_{CS}, are replaced by g_V, T_V, and g_{CV}, respectively, in order to emphasize the association between the sleep neurons and the VLPO region. Likewise, we emphasize the association between the wake neurons and the AMIN region by replacing g_W, T_W, and g_{CW} with g_A, T_A, and g_{CA}.

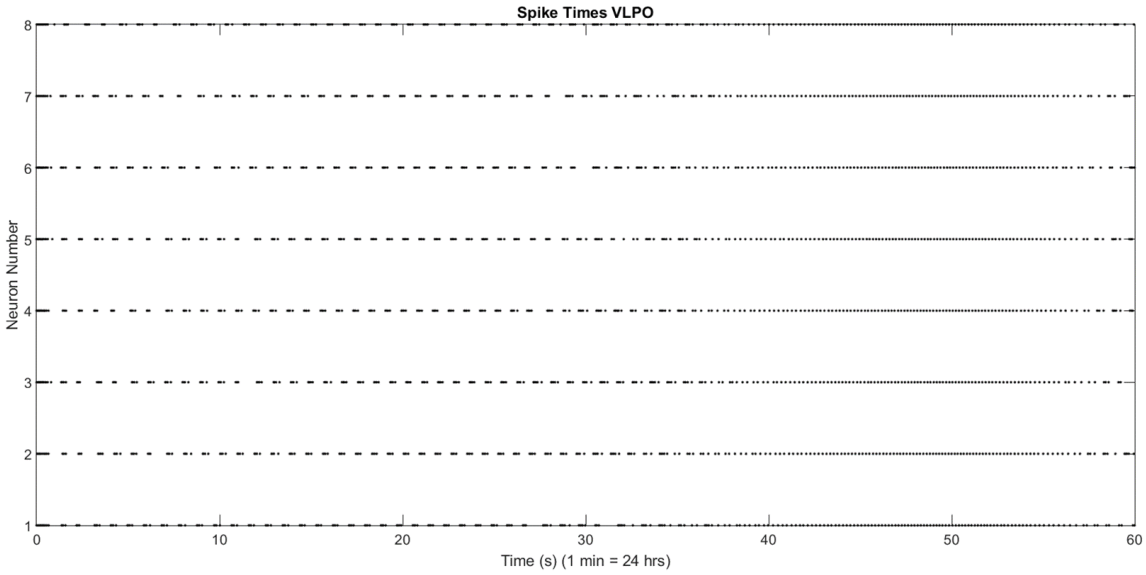

Figure 2.13 – Spike Times Plot for VLPO Neurons
A raster plot of the spike times for all the neurons in the VLPO region. Parameters are $g_A = -4.25x10^{-5}$, $g_V = -3.75x10^{-5}$, $g = 4.5x10^{-5}$, $|g_C| = 0.95$, $T_A = 5\ °C$, and $T_V = 15\ °C$, with the threshold at $-28\ mV$.

2.2.4.1. Spike times and phase synchronization. Two oscillators, such as neurons, are considered synchronized if their phase difference φ changes very little over time. The phase difference between two neurons, i and k, is defined as

$$\varphi_{ik}(t_i) = 2\pi\,(t_i - t_k)/(t_{k+1} - t_k),$$

where neuron i spikes at time t_i, while t_k and t_{k+1} are two sequential spike times for neuron k. The condition $t_k < t_i < t_{k+1}$ must be satisfied for the calculation. The more φ changes, the less synchronized the neurons are. Synchronization can be quantified using the synchronization index

$$\gamma_{ik}{}^2 = \langle\cos(\varphi_{ik}(t_i))\rangle^2 + \langle\sin(\varphi_{ik}(t_i))\rangle^2.$$

If γ is equal to 1, a pair of oscillators is considered perfectly synchronized, while if it is equal to 0, they are completely desynchronized (Pikovsky *et al*. 2001).

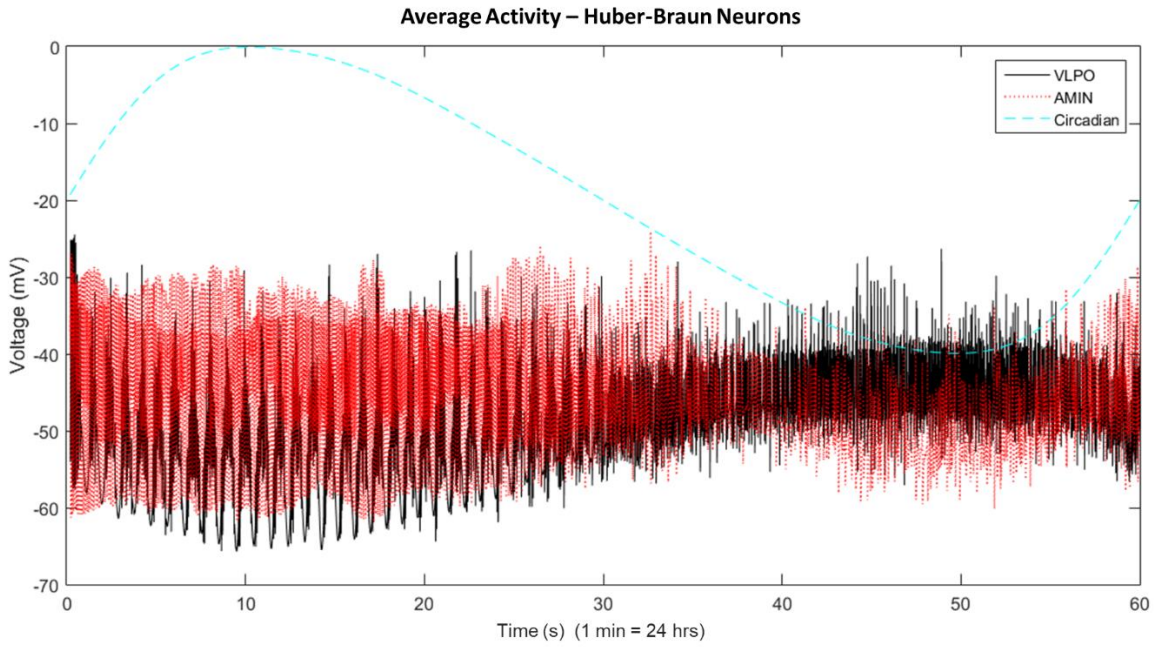

Figure 2.14 – Average Activity, Huber-Braun
With more exploration in parameter space and 8 neurons per region, the average activity of the HB version of the model experienced a change in behavior compared to the average activity plot shown earlier. Rather than periods of inactivity for the downtimes for each region, they exhibit clustered, low frequency activity, corresponding to bursting. Parameters are $g_A = -0.00004$, $g_{CA} = 0.95$, $g = 0.000045$, $g_V = -0.000035$, $g_{CV} = -0.95$, $T_A = 5\ °C$, and $T_V = 15\ °C$, with 8 neurons per region.

In order to investigate the synchronization of neurons during the transitions between sleeping and waking states, the timing of spikes for each neuron was found for every run. These spikes can be graphed in a raster plot, an example of which is given in Figure 2.12. Each dot on the plot is a spike, and each row of dots represents one neuron. A spike is counted each time the voltage of a neuron surpasses a threshold (as described in detail in Section 1.2.1.). For all runs here, the threshold is $-28\ mV$. In Figure 2.12, it can be seen that the AMIN neurons fire rapidly for about the first half of the day, slowing down as the system transitions from wake to sleep (around 35 seconds). During the AMIN neuron

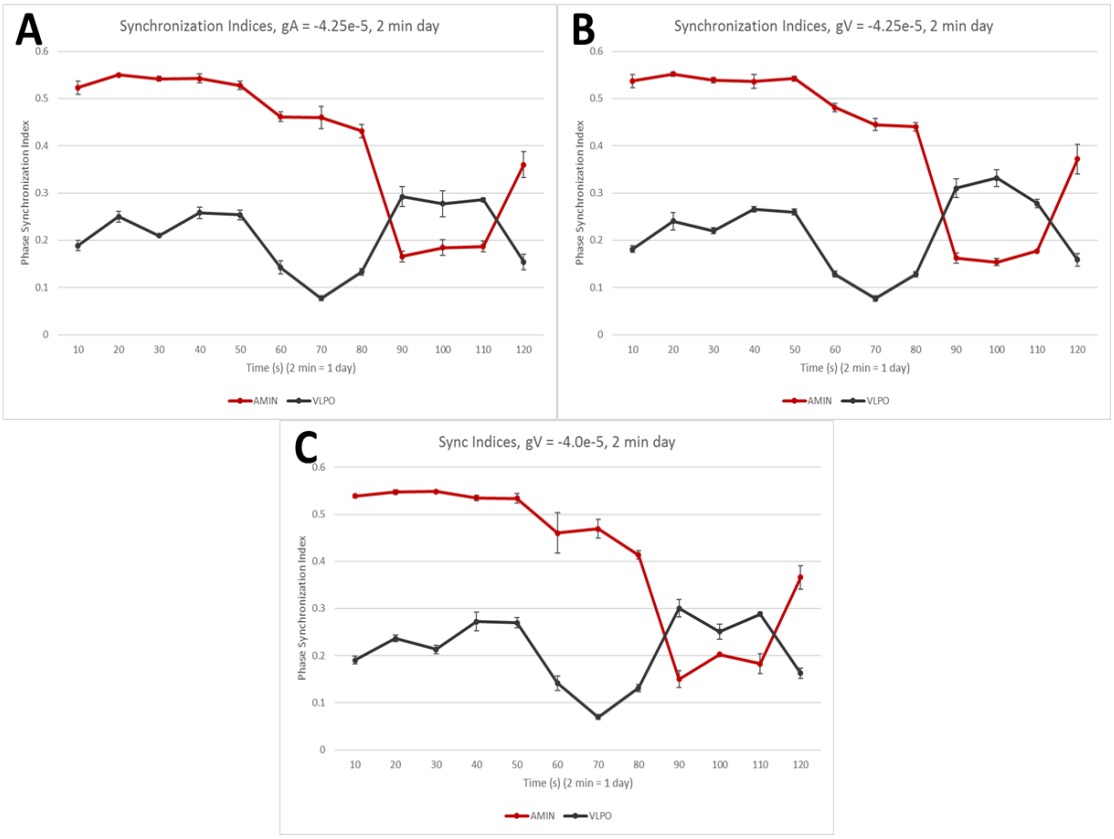

Figure 2.15 – Synchronization Indices with 2 Minutes = 1 Day
Phase synchronization indices for each 10-second period in a two-minute day. The red line represents the AMIN neurons, while the black line represents the VLPO neurons. Each data point indicates the average of the synchronization index over each 10-second period, over all values of the varied parameter. The error bars denote the standard deviation. For all panels, parameters were set as $g = 4.5x10^{-5}$, $|g_C| = 0.95$, $T_A = 5\ °C$, and $T_V = 15\ °C$. g_V or g_A took values from $-3.75x10^{-6}$ to $-4.25x10^{-5}$ in increments of $2.5x10^{-6}$. (A) $g_A = -4.25x10^{-5}$, with g_V varying. (B) $g_V = -4.25x10^{-5}$, with g_A varying. The curve has minor differences from A. (C) $g_V = -4.0x10^{-5}$, with g_A varying. This panel shows more differences from A and B, but remains overall the same, showing that the synchronization does not exhibit large changes with the change in coupling strength at this resolution.

downtime (the sleep state), which lasts about 20 seconds, each neuron fires in bursts, from 3 to 5 or more spikes in quick succession, with longer periods of inactivity between bursts.

The firing rate increases before a transition into another state. This pattern repeats every 60 seconds, or 1 day, for a multiple day run (data not shown).

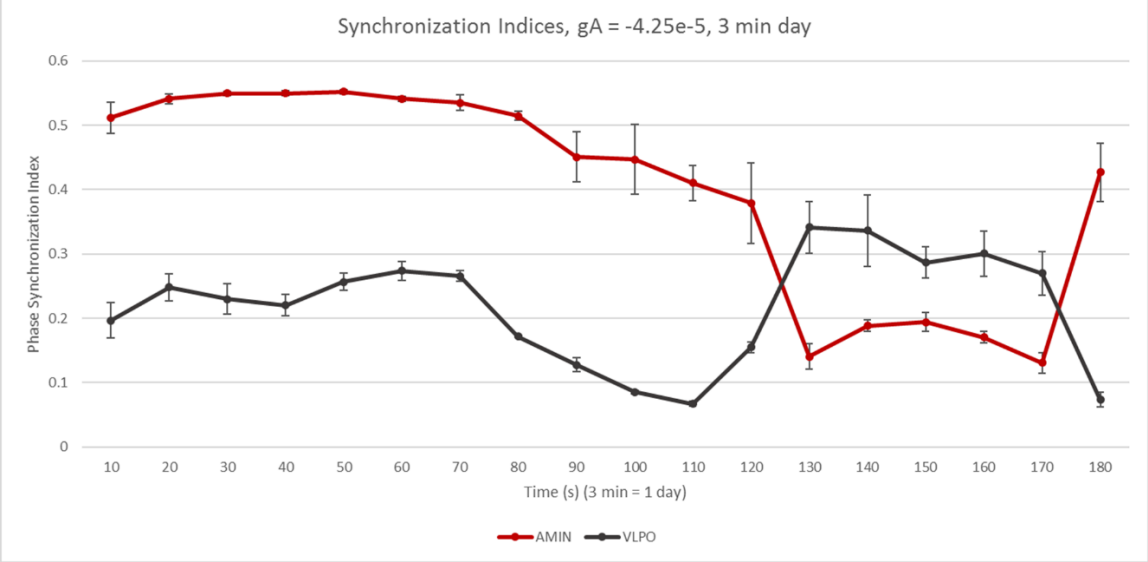

Figure 2.16 – Synchronization Indices with Constant g_A and 3 Minutes = 1 Day
Phase synchronization indices for each 10-second period in a three-minute day. The red line represents the AMIN neurons, while the black line represents the VLPO neurons. Each data point indicates the average of the synchronization index over each 10-second period, over all values of g_V. The error bars denote the standard deviation. Note how the shape of each curve is reminiscent of the 2-minute day runs but with more detail. Parameters were set as $g_A = -4.25x10^{-5}$, $g = 4.5x10^{-5}$, $|g_C| = 0.95$, $T_A = 5\,°C$, and $T_V = 15\,°C$. g_V took values from $-3.75x10^{-6}$ to $-4.25x10^{-5}$ in increments of $2.5x10^{-6}$.

The raster plot for the VLPO neurons, with the same parameters, is given in Figure 2.13. In direct contrast to the AMIN neurons, the VLPO neurons fire more rapidly at night, between about 37 to 57 seconds. They have a similar pattern of behavior during their downtime (day or wake state), firing in bursts. Unlike AMIN, however, the VLPO neurons

fire in much tighter clusters of 3 to 5 spikes. The decrease in firing rate during the transition from sleep to wake and the increase in firing rate when shifting from wake to sleep are comparable to the behavior of the AMIN neurons.

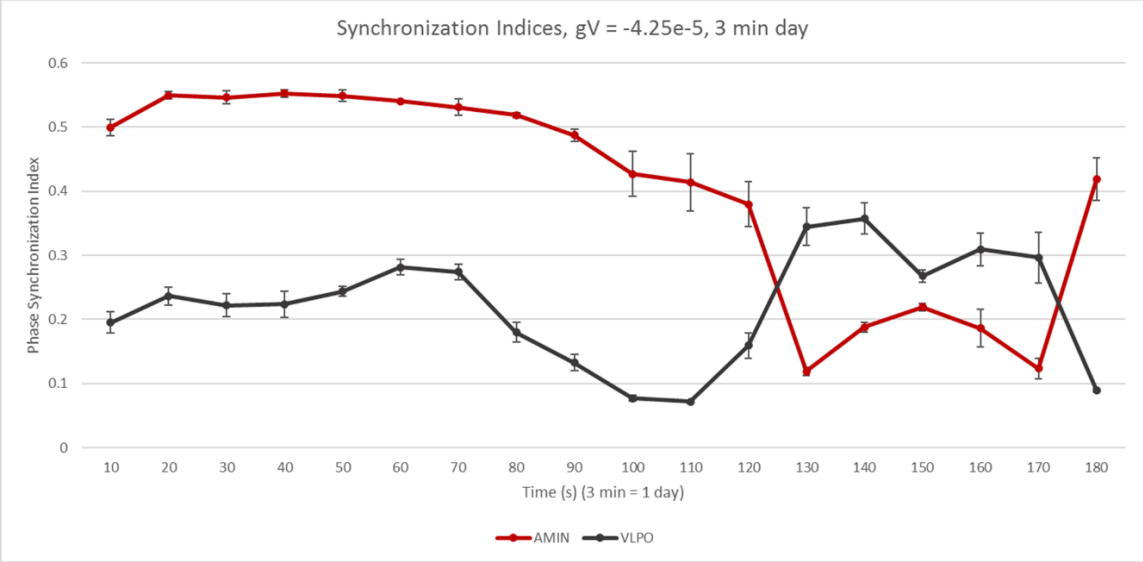

Figure 2.17 – Synchronization Indices with Constant g_V and 3 Minutes = 1 Day
Phase synchronization indices for each 10-second period in a three-minute day. The red line represents the AMIN neurons, while the black line represents the VLPO neurons. Each data point indicates the average of the synchronization index over each 10-second period, over all values of g_A. The error bars denote the standard deviation. Note the similarities between this figure and Figure 2.16. Parameters are $g_V = -4.25x10^{-5}$, $g = 4.5x10^{-5}$, $|g_C| = 0.95$, $T_A = 5\ °C$, and $T_V = 15\ °C$. g_A took values from $-3.75x10^{-6}$ to $-4.25x10^{-5}$ in increments of $2.5x10^{-6}$.

An example of the average activity produced by neurons in this region of parameter space is given in Figure 2.14. As seen in the raster plots, each region fires continuously throughout the simulation. Synchronization analysis of the data shown in this figure will be discussed below in Section 2.3.4.

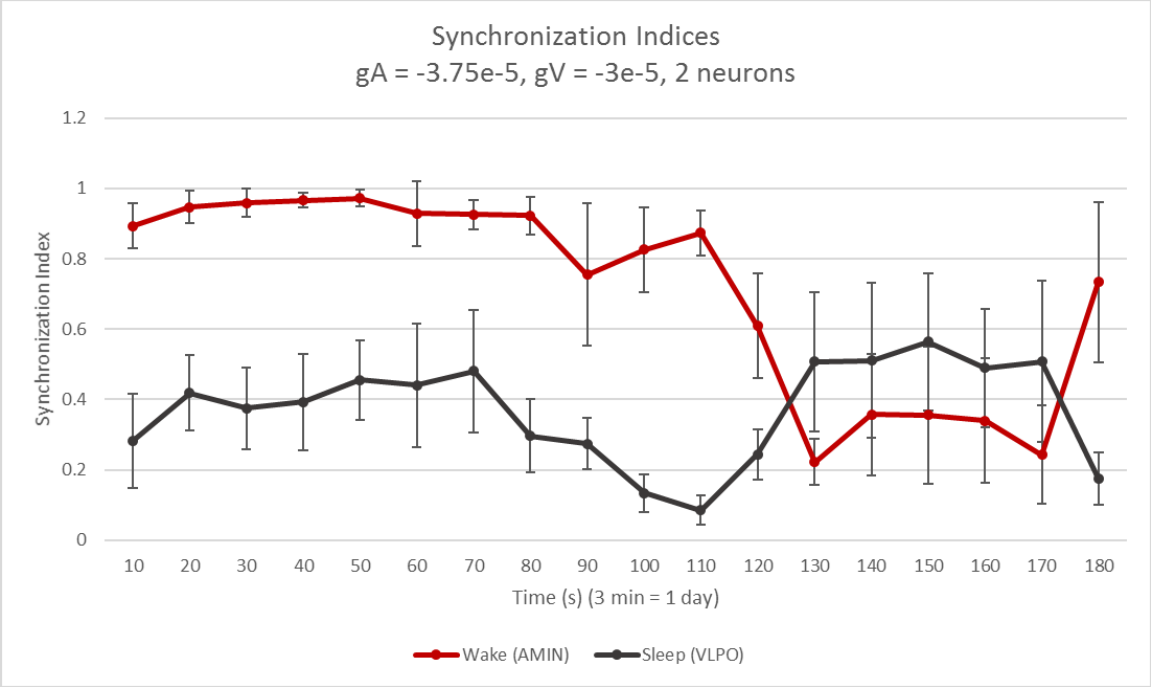

Figure 2.18 – Synchronization Indices for 10 Runs, 2 Neurons per Region
Phase synchronization indices for each 10-second period in a three-minute day. The red line represents the AMIN neurons, while the black line represents the VLPO neurons. Each data point indicates the average of the synchronization index over each 10-second period, from 10 runs with identical parameters. The error bars denote the standard deviation. This figure is comparable to Figures 2.19 and 2.20, which have the same parameters but a different number of neurons per region. Parameters are $g_V = -3x10^{-5}$, $g_A = -3.75x10^{-5}$, $g = 4.5x10^{-5}$, $|g_C| = 0.95$, $T_A = 5\,°C$, and $T_V = 15\,°C$, with two neurons per region.

2.2.4.2. Two- and three-minute runs. In order to demonstrate the impact of the coupling constants g_V and g_A on the system dynamics, we systematically changed each one with the remaining parameters held constant at $T_V = 15\,°C$, $T_A = 5\,°C$, $g = 0.000045$, $g_{CV} = -0.95$, and $g_{CA} = 0.95$. For one run, g_A is held constant while g_V is varied from $-3.75x10^{-5}$ to $-4.25x10^{-5}$ in increments of $2.5x10^{-6}$. Afterward, g_A is varied over the same range.

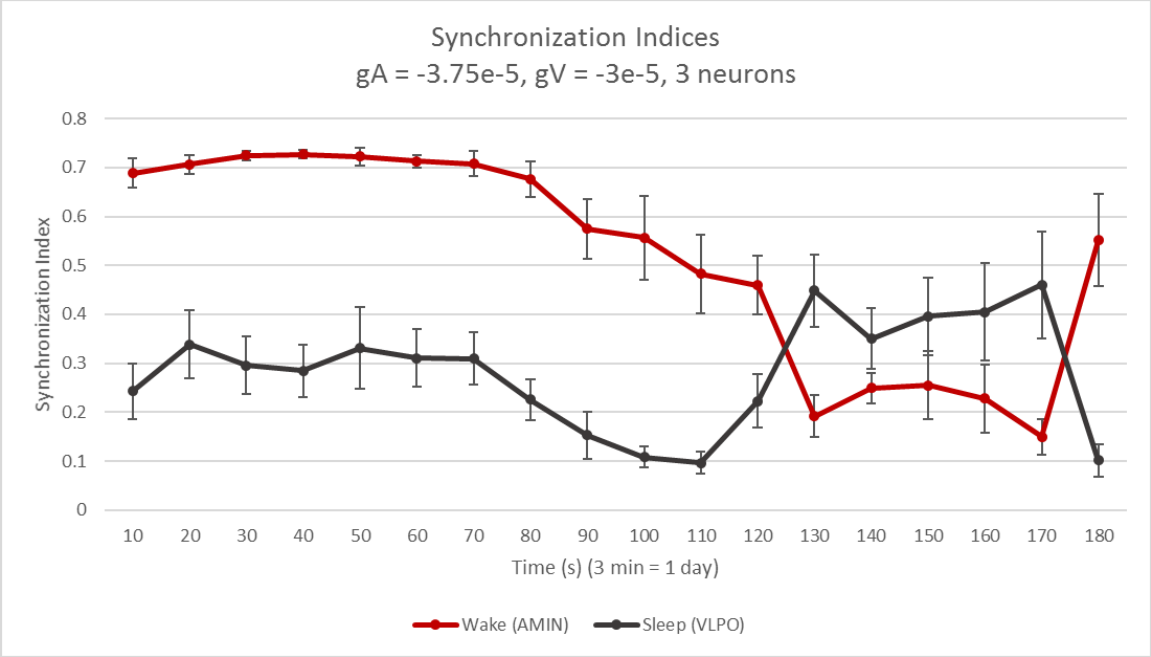

Figure 2.19 – Synchronization Indices for 10 Runs, 3 Neurons per Region
Phase synchronization indices for each 10-second period in a three-minute day. The red line represents the AMIN neurons, while the black line represents the VLPO neurons. Each data point indicates the average of the synchronization index over each 10-second period, from 10 runs with identical parameters. The error bars denote the standard deviation. Note the smaller range of values for the synchronization index and the smaller error bars compared to Figure 2.18. Parameters were set as $g_V = -3x10^{-5}$, $g_A = -3.75x10^{-5}$, $g = 4.5x10^{-5}$, $|g_C| = 0.95$, $T_A = 5\ °C$, and $T_V = 15\ °C$, with three neurons per region.

For a more detailed representation of a full day, one simulated "day" was decompressed from 1 minute to 2 and 3 minutes. With this decompression, the model was run with the parameters listed above. The phase synchronization index was determined for the range of values of g_A and g_V. Since the phase synchronization of the neurons in each region changes over time, the 120 (180) second day was divided into twelve (eighteen) 10-second periods, and the phase synchronization index was calculated for each of these

periods. Smaller intervals are not used, since they might contain too few spikes to obtain a reliable synchronization index value.

While one parameter (such as g_A) is held constant, the synchronization index for the first 10 seconds of the run is averaged over each value of g_V. These average values are plotted vs. time, with error bars that represent the standard deviation. Displaying the data in this fashion provides insight into the impact of changing one of the inter-region coupling strengths (g_A and g_V). With one coupling strength held constant and the other varied over a range of values, the error bars indicate the magnitude of variation possible for the graph in that range of parameter values.

Figure 2.15A shows the phase synchronization indices changing over a 2-minute day, with $g_A = -4.25x10^{-5}$. VLPO activity is shown with the black line, and AMIN activity is indicated by the red line. Note that the synchronization increases whenever a region enters its active period and decreases when a region shifts into its downtime. The synchronization indices for both VLPO and AMIN exhibit complex and gradual changes.

In Figure 2.15B, g_V was held at $-4.25x10^{-5}$ and g_A was varied from $-3.75x10^{-6}$ to $-4.25x10^{-5}$ in increments of $2.5x10^{-6}$. With consistently small error bars compared to Figure 2.15A, this figure shows that variation in g_A has less impact on the system synchronization than variation in g_V over a similar range. Similar results with a different value of g_V are shown in Figure 2.15C.

The time compression was eased further, decompressing a “simulated” day to 3 minutes. The parameters and ranges are the same as above. The results of holding g_A constant at $-4.25x10^{-5}$ while varying g_V are shown in Figure 2.16. This expanded time compression reveals more detail of the change in synchronization index over time for both

AMIN and VLPO. However, both these time courses retain the same general shape as they had in the 2-minute day figures, suggesting that further expansion of the time compression would not reveal anything significant for the model in its current form. The companion figure to Figure 2.16 is Figure 2.17, where g_V was held constant at $-4.25x10^{-5}$ and g_A was changed. This figure still holds the same general shape as previous figures.

Further study on g_V and g_A for this form of the model may include expanding the parameter ranges for the two-minute day and three-minute day runs, along with changing the magnitude of the noise in the neural model to determine its effect on the activity of this model.

2.2.4.3. 10-run averages. In order to determine the reproducibility of the synchronization behavior, 10 simulations were performed with all parameters held constant at $g_A = -0.0000375$, $g_{CA} = 0.95$, $g = 0.000045$, $g_V = -0.00003$, $g_{CV} = -0.95$, $T_A = 5\ ^\circ C$, and $T_V = 15\ ^\circ C$. Results are shown in Figures 2.18 to 2.20 for various system sizes.

For Figure 2.18, there were 2 neurons per region for all runs, marking the smallest number of neurons a region can have and still be analyzed via synchronization. The impact of the small number of neurons shows in the broad range of the synchronization index and the large error bars, which denote the standard deviation over the 10 runs. Figure 2.19 shows another set of 10 runs with 3 neurons per region, and Figure 2.20 shows 10 runs with 4 neurons per region. One and two extra neurons per region provide a visible change in the behavior of the system, smoothing out the overall behavior and decreasing the variability between runs. The error bars are smaller and the range of values for the synchronization index has decreased. The reciprocal behavior of the synchronization indices for each region over the course of the day is maintained, as in prior figures. This

implies that an increase in the number of neurons, while not providing any perceptible difference in the average activity of the model (see Section 2.2.2.4.), does impact the synchronization of the neurons and the reliability of their activity patterns.

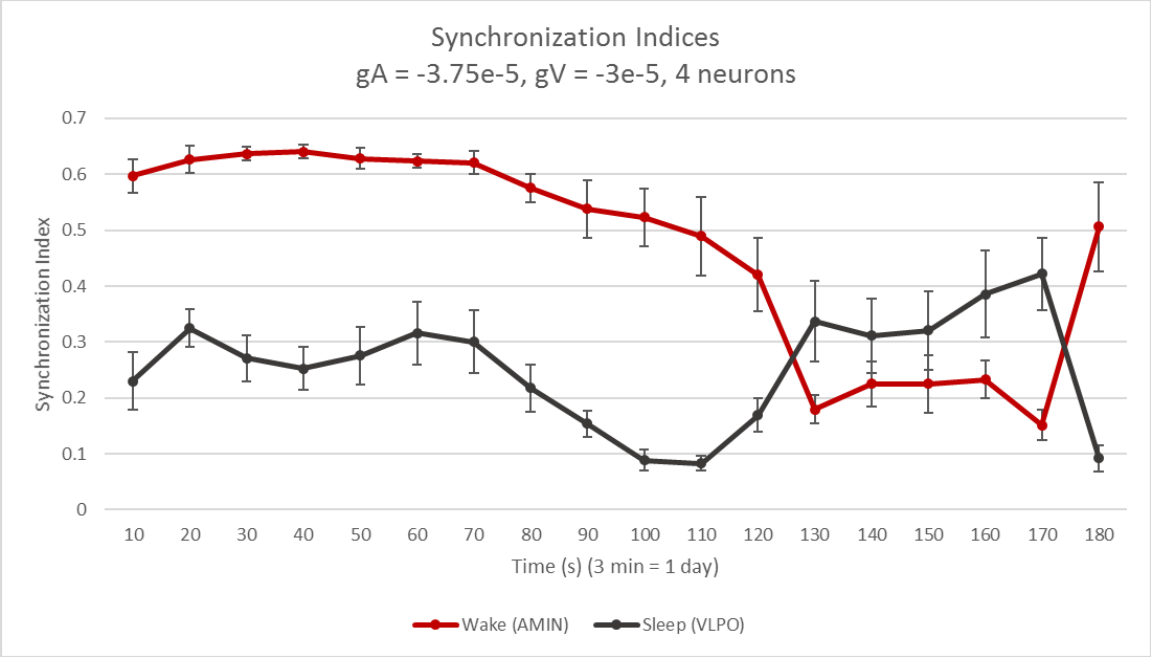

Figure 2.20 – Synchronization Indices for 10 Runs, 4 Neurons per Region
Phase synchronization indices for each 10-second period in a three-minute day. The red line represents the AMIN neurons, while the black line represents the VLPO neurons. Each data point indicates the average of the synchronization index over each 10-second period, from 10 runs with identical parameters. The error bars denote the standard deviation. Parameters are $g_V = -3x10^{-5}$, $g_A = -3.75x10^{-5}$, $g = 4.5x10^{-5}$, $|g_C| = 0.95$, $T_A = 5\ °C$, and $T_V = 15\ °C$, with 4 neurons per region.

2.3. ALTERNATE NEURAL MODEL

An alternative neural model was implemented in place of Huber-Braun, as discussed below.

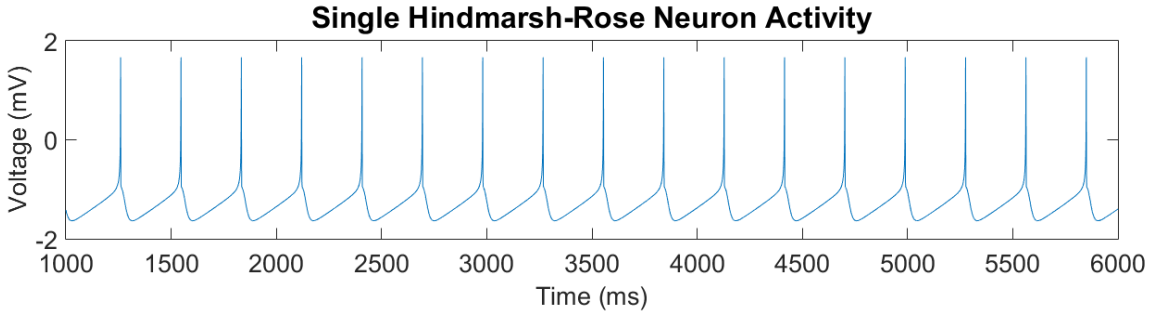

Figure 2.21 – Activity of a Single Uncoupled Hindmarsh-Rose Neuron
The firing pattern of a single Hindmarsh-Rose neuron, when uncoupled. Note that the transient activity was removed. This neuron was set in the non-bursting regime.

2.3.1. Hindmarsh-Rose. Similarly capable of complex behavior such as bursting but less biologically realistic than the Huber-Braun model, the Hindmarsh-Rose (HR) model was developed from to studies of a neuron in *Lymnaea*, a type of pond snail. What was interesting about this neuron was its behavior after a perturbation. The neuron did not fire until it received a depolarizing stimulus, after which it began bursting and maintained that bursting far longer than the input lasted. In an effort to understand this behavior, Hindmarsh and Rose developed a neural model that utilized two first-order differential equations (Hindmarsh & Rose 1982). Further study of *Lymnaea* revealed that the cell would eventually cease firing after the removal of the stimulus. To reproduce this, Hindmarsh and Rose added a third first-order differential equation to their previous model (Hindmarsh & Rose 1984). This three-dimensional version of the model is used below as an alternative to Huber-Braun neurons and is described here for reference.

Briefly, the three-dimensional version of the Hindmarsh-Rose neural model (Hindmarsh & Rose 1984) consists of three coupled nonlinear differential equations:

$$\dot{x} = y - ax^3 + bx^2 + I - z\ - gw + C_i$$

$$\dot{y} = c - \mathrm{d}x^2 - y \tag{2.4}$$

$$\dot{z} = r(s(x - x_1) - z).$$

Here, x is the membrane potential or voltage of the neuron, y is the recovery variable, and z is the adaptation current. I is the applied or external current and directly influences the

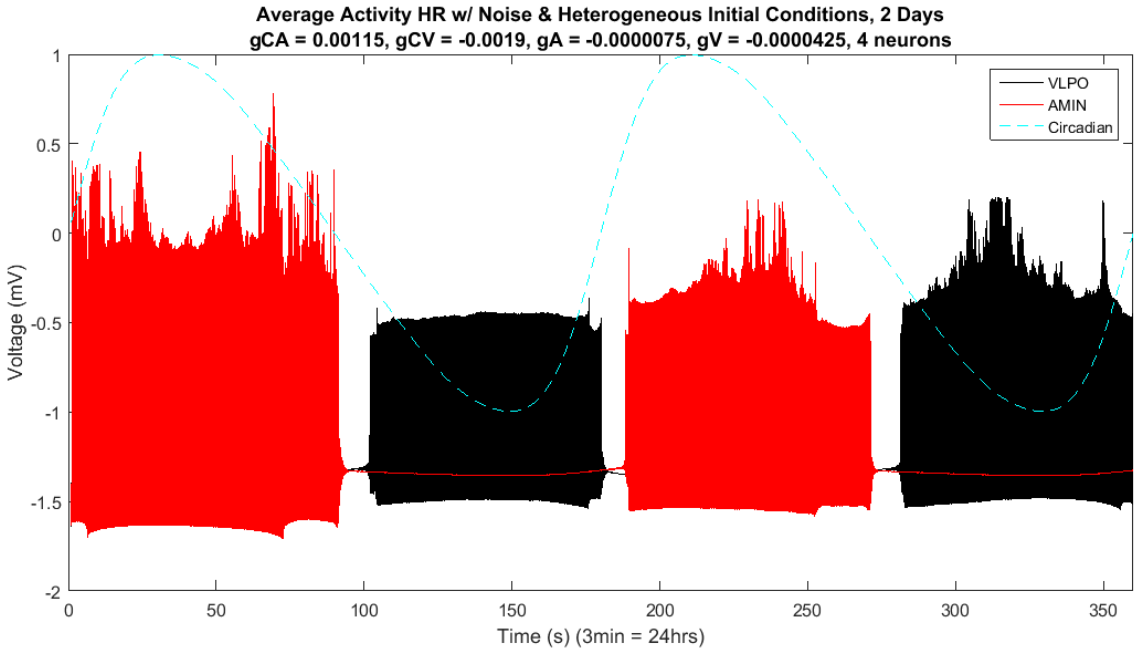

Figure 2.22 – Average Neuron Activity, 2 Day Run, Hindmarsh-Rose
VLPO (black) and AMIN (red) activity over a two-day period. Note the gaps between the active periods. Parameters are $g_A = -7.5x10^{-6}$, $g_V = -4.25x10^{-5}$, $I = 1.28$, $g_{CA} = 1.15x10^{-3}$, and $g_{CV} = -0.0019$, with 4 neurons per region.

behavior of the neuron. The final two terms in the $\dot{x}$ equation are the same Gaussian white noise term and coupling term from the Huber-Braun version of the model, discussed in Sections 2.1.2. and 2.2.1., respectively. Constants are given in Appendix B.

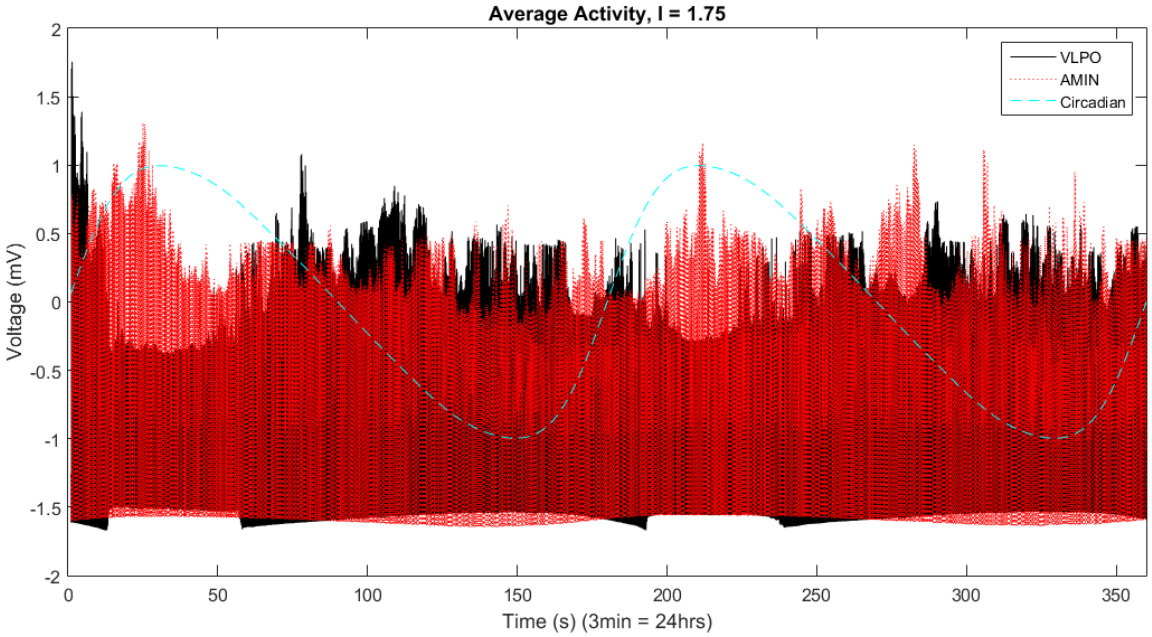

Figure 2.23 – Average Activity in Bursting Regime, $I = 1.75$, Hindmarsh-Rose
Average activity in the bursting regime using Hindmarsh-Rose neurons and two 3-minute days. Parameters are $g_A = -7.5x10^{-6}$, $g_V = -4.25x10^{-5}$, $I = 1.75$, $g_{CA} = 1.15x10^{-3}$, and $g_{CV} = -0.0019$, with 4 neurons per region.

An example of the firing pattern of a single, uncoupled Hindmarsh-Rose neuron is shown in Figure 2.21. Note that this single neuron is not in the bursting regime, hence the single spikes. It is also important to note is the range of values for the "voltage". Unlike the more realistic range of values portrayed by Huber-Braun neurons, Hindmarsh-Rose neurons have a range from about -2 to +2. This is due to the variable x, which is a merely schematic representation of the membrane potential of the neuron. For consistency with the Huber-Braun figures, however, the vertical axis for figures with Hindmarsh-Rose neural activity will be labeled "Voltage (mV)". The sleep model using Hindmarsh-Rose neurons is structured identically to that using Huber-Braun neurons, with the same connections, circadian drive, and mean field equations.

2.3.2. Results. Using the model schematic depicted in Figure 2.3, all neurons were replaced with Hindmarsh-Rose neurons. Results from this version of the model are discussed below.

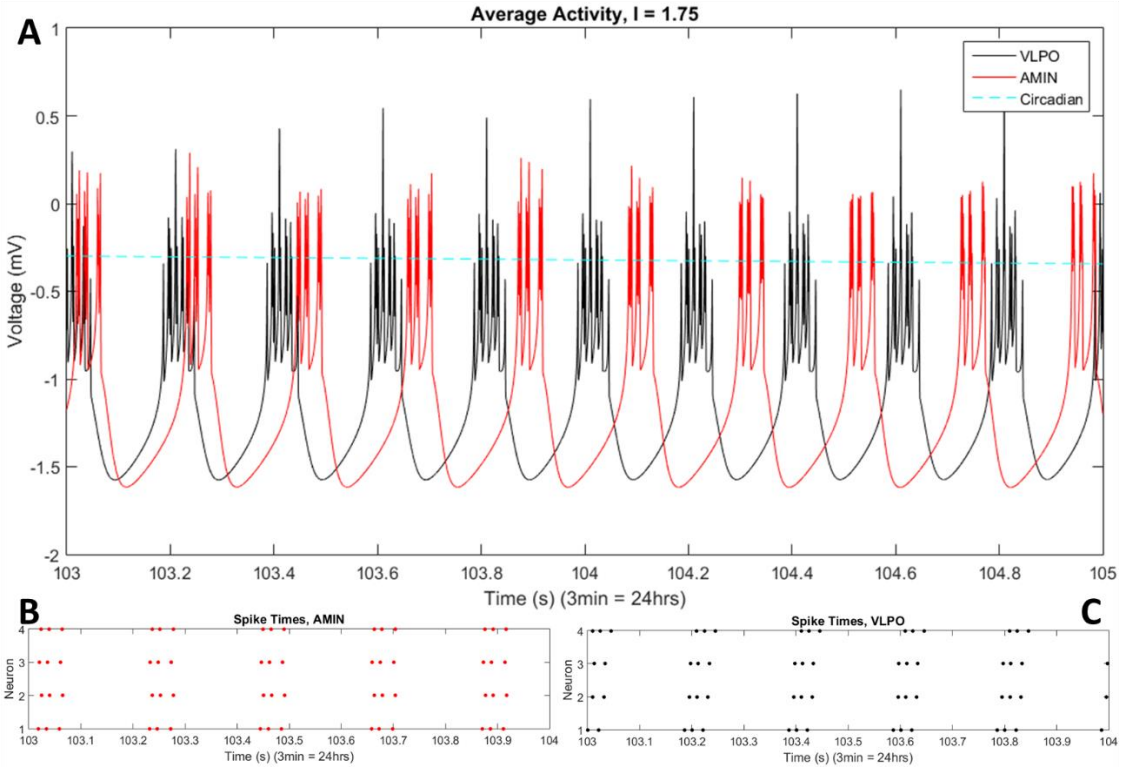

Figure 2.24 – Average Activity in Bursting Regime, HR, Day 1
Close up of Figure 2.23 from 103 to 105 seconds. (A) Average activity. (B) Spike times, AMIN. Note each neuron is firing triplets. (C) Spike times, VLPO. Each neuron is firing triplets. Parameters are $g_A = -7.5x10^{-6}$, $g_V = -4.25x10^{-5}$, $I = 1.75$, $g_{CA} = 1.15x10^{-3}$, and $g_{CV} = -0.0019$, with 4 neurons per region.

2.3.2.1. Spiking regime. After replacing the Huber-Braun neurons with Hindmarsh-Rose, simulations were performed with $g_A = -7.5x10^{-6}$, $g_V = -4.25x10^{-5}$, $I = 1.28$, $g_{CA} = 1.15x10^{-3}$, $g_{CV} = -0.0019$, and 4 neurons per region. The average

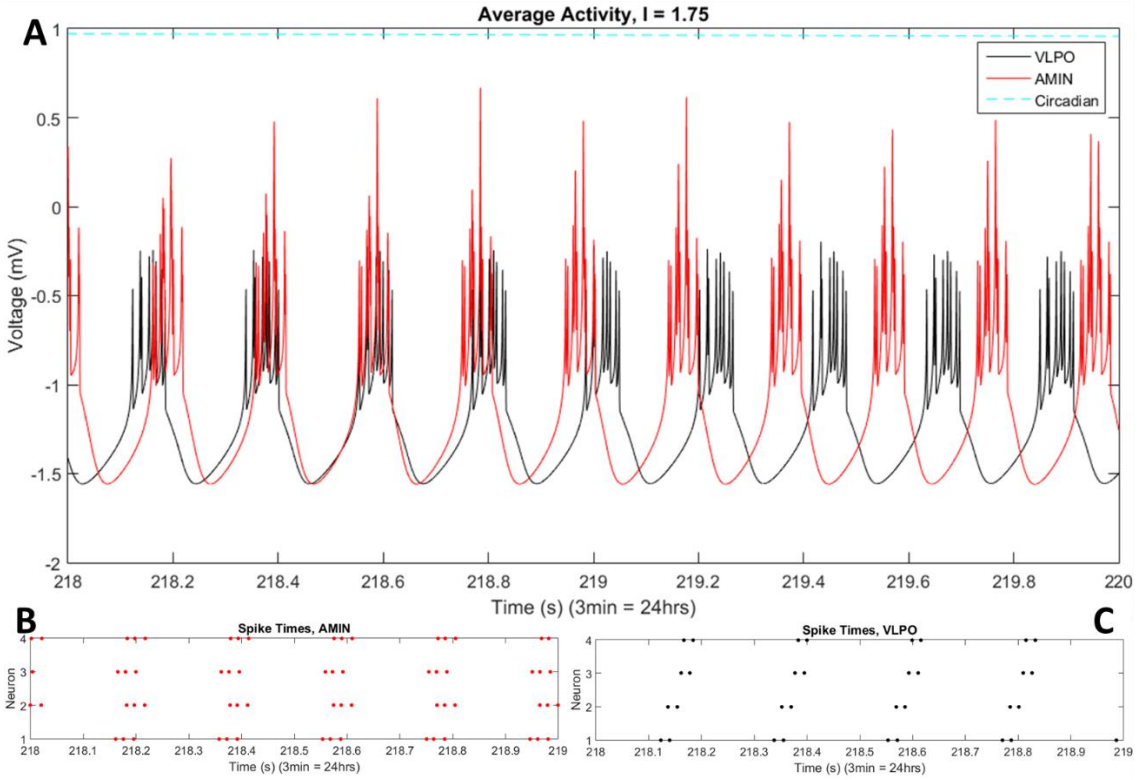

Figure 2.25 – Average Activity in Bursting Regime, HR, Day 2
Close up of Figure 2.23 from 218 to 220 seconds. (A) Average activity. (B) Spike times, AMIN. Note that each neuron is firing triplets, with neurons 1 and 3 slightly out of phase from neurons 2 and 4. (C) Spike times, VLPO. Each neuron is firing doublets with a small phase shift from one another. Parameters are $g_A = -7.5x10^{-6}$, $g_V = -4.25x10^{-5}$, $I = 1.75$, $g_{CA} = 1.15x10^{-3}$, and $g_{CV} = -0.0019$, with 4 neurons per region.

activity of each region in the model is shown in Figure 2.22. Note that the value of I for this run is in the non-bursting regime. Mean field activity of the AMIN region is shown in red, and mean field activity of the VLPO region is shown in black. Each region ceases firing during its downtime (night for AMIN and day for VLPO), and an overlap of these downtimes causes a small gap between periods of activity. The first period of high activity for VLPO is smooth and level compared to the AMIN activity. The increased variability

during the second activity period may be due to the noise built into the model, or due to neurons firing in or out of phase; the former results in high peaks in the average activity while the latter results in lower peaks and/or an evenness to the average activity.

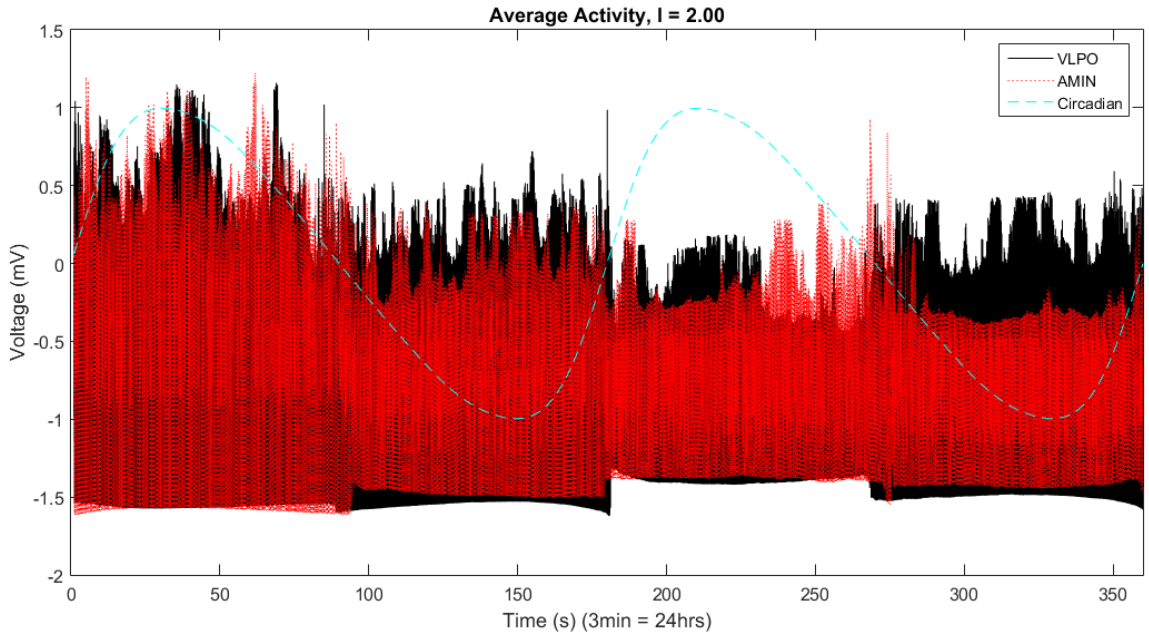

Figure 2.26 – Average Activity in Bursting Regime, $I = 2.00$, Hindmarsh-Rose
Average activity in the bursting regime using Hindmarsh-Rose neurons and two 3-minute days. As in Figure 2.23, the neurons continue firing over the entire day. Parameters are $g_A = -7.5x10^{-6}$, $g_V = -4.25x10^{-5}$, $I = 2.00$, $g_{CA} = 1.15x10^{-3}$, and $g_{CV} = -0.0019$, with 4 neurons per region.

2.3.2.2. Bursting regime. Changing the input current *I* changes the bursting state of the Hindmarsh-Rose neurons. When *I* is increased to 1.75, well into the bursting regime, the activity of each region in the model becomes continuous throughout the entire day, as can be seen in Figure 2.23. With parameters set at $g_A = -7.5x10^{-6}$, $g_V = -4.25x10^{-5}$,

$I = 1.75$, $g_{CA} = 1.15x10^{-3}$, $g_{CV} = -0.0019$, and 4 neurons per region, Figure 2.23 shows the average activity of both AMIN and VLPO for two three-minute days. While the

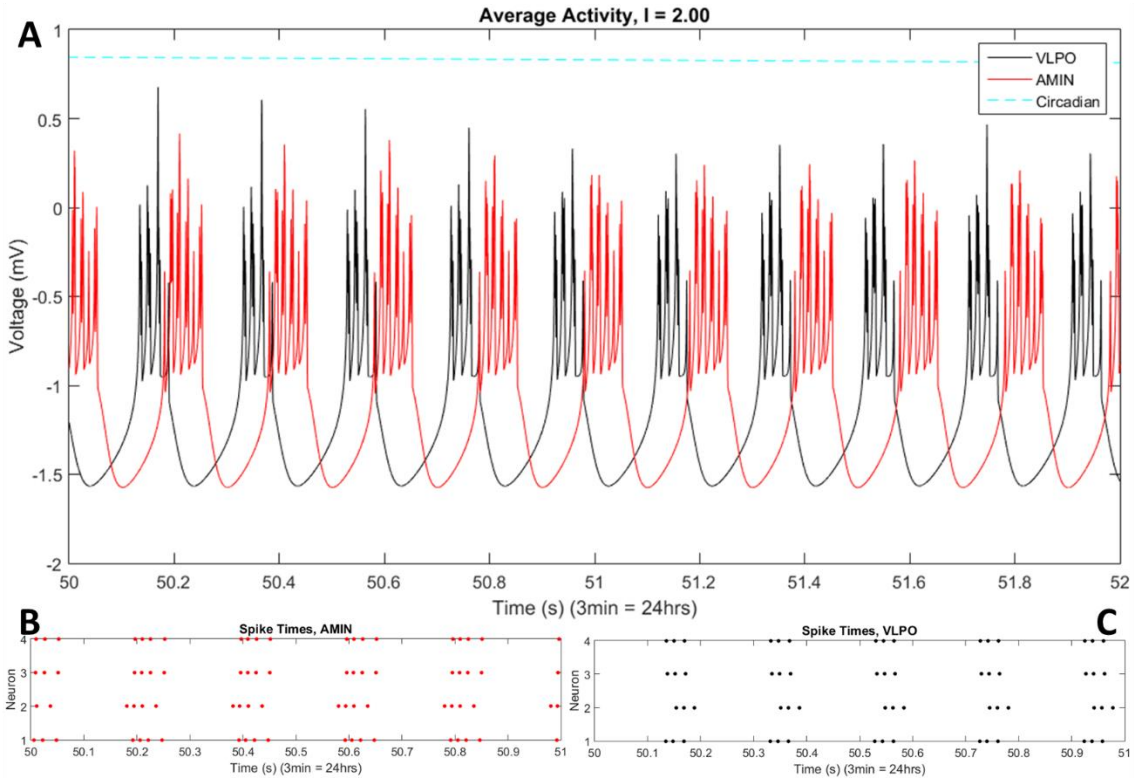

Figure 2.27 – Average Activity in Bursting Regime, HR, Day 1
Close up of Figure 2.26 from 50 to 52 seconds. (A) Average activity. (B) Spike times, AMIN. Note each neuron is firing quadruplets. (C) Spike times, VLPO. Each neuron is firing triplets. Parameters are $g_A = -7.5x10^{-6}$, $g_V = -4.25x10^{-5}$, $I = 2.00$, $g_{CA} = 1.15x10^{-3}$, and $g_{CV} = -0.0019$, with 4 neurons per region.

constant activity of both regions makes it impossible to identify separate sleep and wake states, average activity of AMIN has a higher magnitude than VLPO at the peak of the circadian drive cycle.

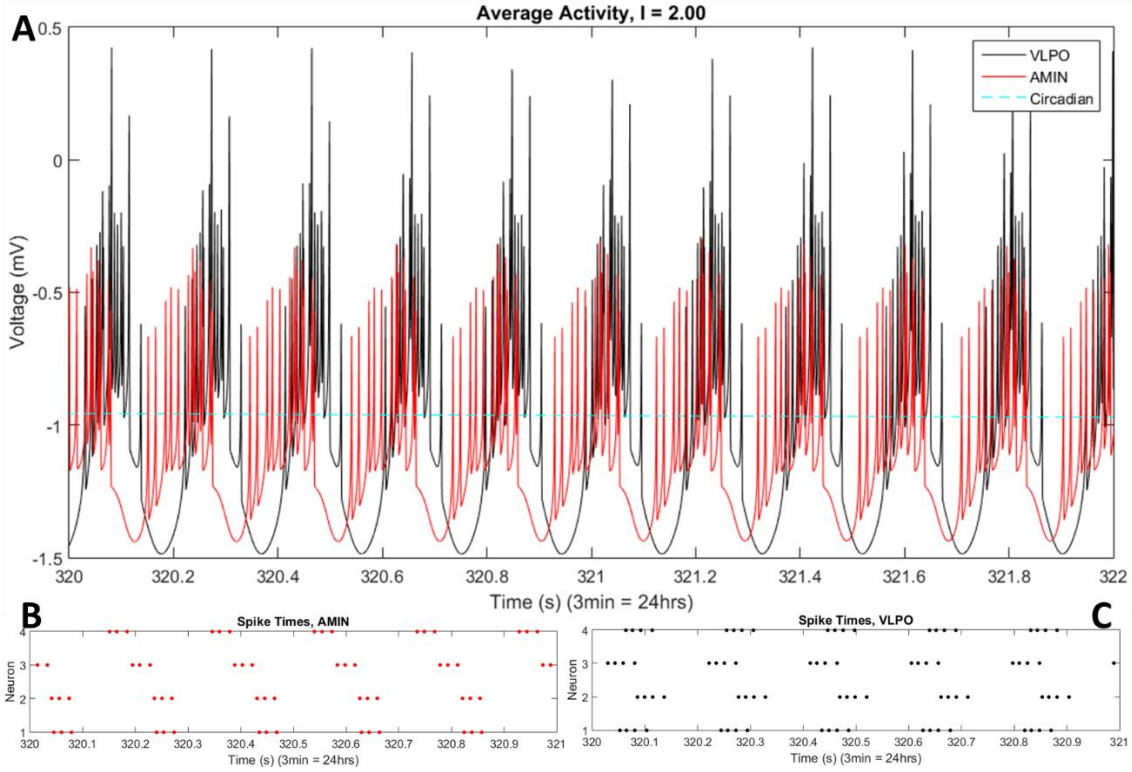

Figure 2.28 – Average Activity in Bursting Regime, HR, Day 2
Close up of Figure 2.26 from 320 to 322 seconds. (A) Average activity. Unlike the tight bundles of activity in Figure 2.27, the bursting activity of AMIN and, to a lesser extent, VLPO is spread out over time. (B) Spike times, AMIN. The neurons are firing triplets. (C) Spike times, VLPO. Each neuron is firing quadruplets. Parameters are $g_A = -7.5x10^{-6}$, $g_V = -4.25x10^{-5}$, $I = 2.00$, $g_{CA} = 1.15x10^{-3}$, and $g_{CV} = -0.0019$, with 4 neurons per region.

Figure 2.24 shows a close-up view of an interval from Figure 2.23 (103 to 105 seconds). This corresponds to a time period where VLPO has higher activity than AMIN. The activity of both regions, shown in Figure 2.24A, is initially almost synchronized before slowly drifting out of phase, with VLPO firing more frequently than AMIN. Each region's neurons are firing with triple spikes, as can be seen in Figures 2.24B and 2.24C. Both regions exhibiting the same bursting behavior and CD's moderate value during this time of day suggests that this time interval is a neutral time between switching states, where

each region is firing the same number of spikes per burst. The higher VLPO mean field amplitude indicates that the system is shifting toward sleep.

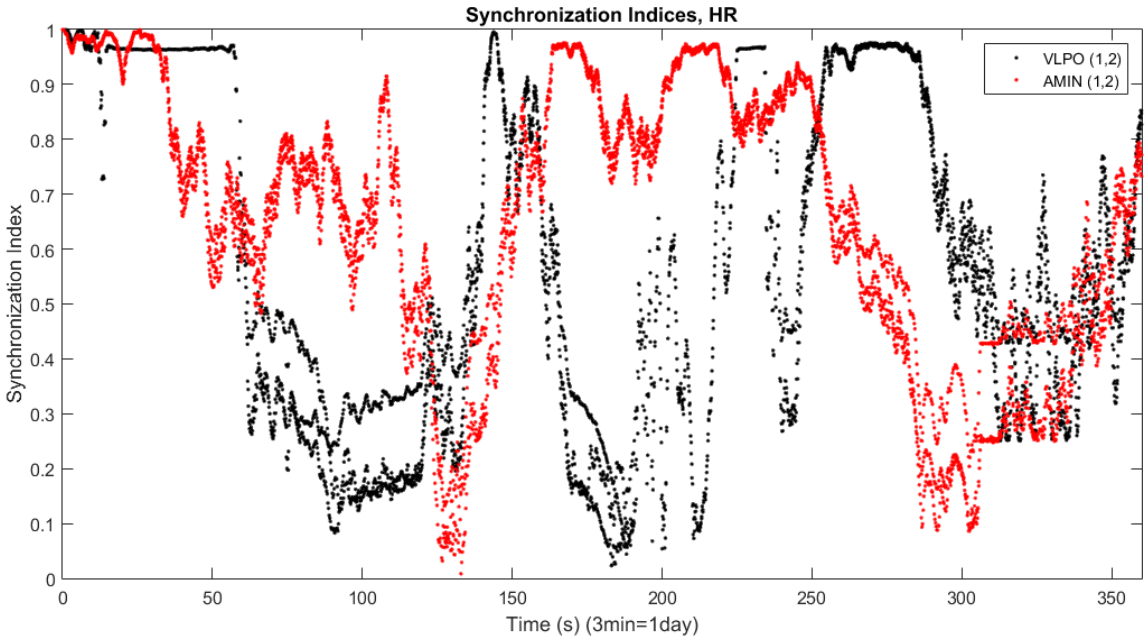

Figure 2.29 – Synchronization Indices of Neurons 1 & 2, $I = 1.75$, HR
Synchronization index of neurons 1 and 2 from each region calculated with a sliding window. Calculated from data in Figure 2.23. VLPO appears to rapidly increase synchronization around the time AMIN's synchronization drops. Consistency is low while looking at one neural pair's synchronization index. Parameters are the same as Figure 2.23.

Figure 2.25 shows a different time interval from Figure 2.24 (218 to 220 seconds), when AMIN's activity is higher than VLPO's. This is reflected in AMIN's higher amplitude in Figure 2.25A. Here, VLPO is firing with a slightly higher frequency than AMIN, though it displays similar clustering behavior. In Figure 2.25B, the spike times of the neurons in the AMIN region are shown to be firing triplets, as in Figure 2.24B. The

VLPO region, however, is firing doublets (Figure 2.25C). This change in bursting behavior seems to indicate a change in state for the model, where the more active region – AMIN in this case, as this time interval corresponds to daytime – bursts with more spikes than the less active region (VLPO).

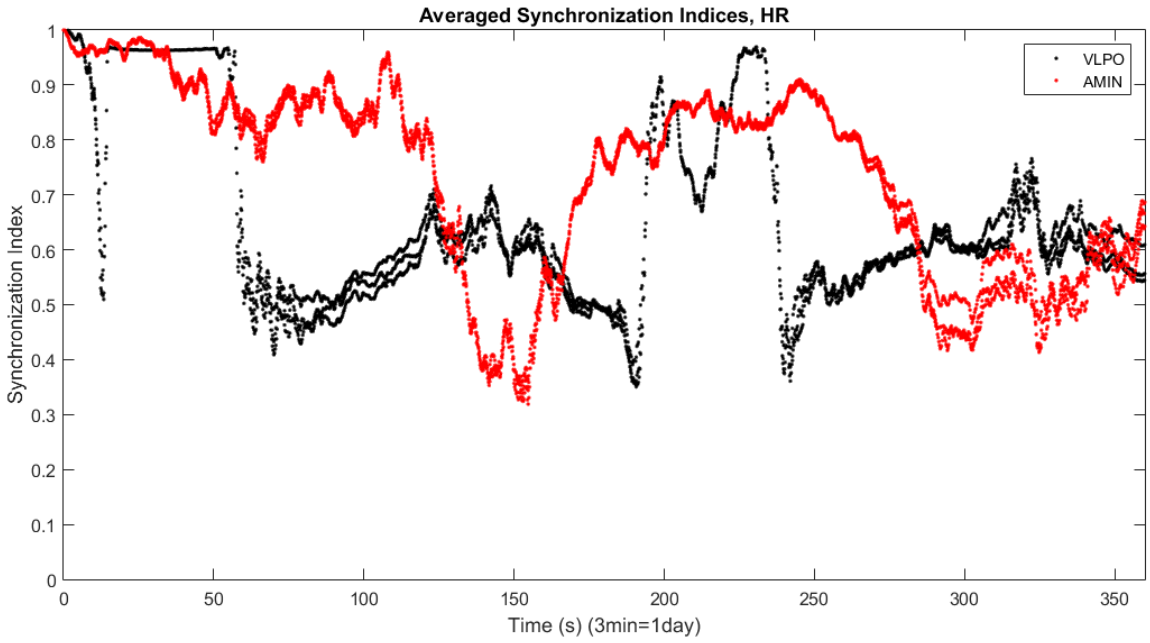

Figure 2.30 – Averaged Synchronization Indices, $I = 1.75$, Hindmarsh-Rose
Synchronization indices averaged over all unique pairs of neurons in each region using a sliding synchronization window. The range of indices for all unique pairs is smaller than the range of indices from a single pair of neurons seen in Figure 2.29. Parameters are the same as Figure 2.23.

Changing the value of I from 1.75 to 2.00 puts the behavior of Hindmarsh-Rose neurons farther into the bursting regime. Figure 2.26, with $g_A = -7.5x10^{-6}$, $g_V =$

$-4.25x10^{-5}$, $I = 2.00$, $g_{CA} = 1.15x10^{-3}$, $g_{CV} = -0.0019$, and 4 neurons per region, shows the average activity of each region over two three-minute days.

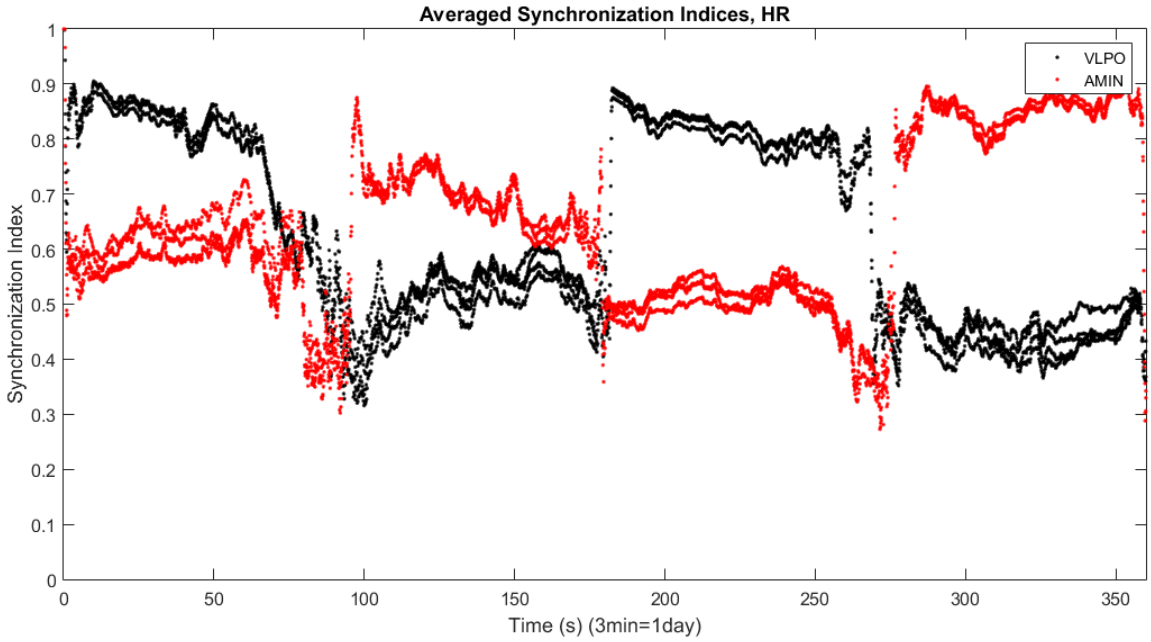

Figure 2.31 – Averaged Synchronization Indices, $I = 2.00$, Hindmarsh-Rose Synchronization indices averaged over all unique pairs of neurons in each region using a 10-spike sliding synchronization window. Note the distinct transitions between day and night. Parameters are the same as Figure 2.26.

Figure 2.27 displays a two-second time interval from Figure 2.26 (50 to 52 seconds). The average activity during this time period is shown in Figure 2.27A. In Figure 2.27B, the spike times of AMIN show that the wake-promoting neurons are firing quadruplets, while the VLPO neurons are firing triplets (Figure 2.27C).

A different two-second portion (320 to 322 seconds) of Figure 2.26 is presented in Figure 2.28, showing irregular mean field activity (Figure 2.28A), due to the cascades of burst firing in both regions (Figures 2.28B and 2.28C). These results support the conclusion

that the more active region fires more spikes per burst than the less active region. The effect of coupling strengths on the behavior of individual HB neurons has been previously shown to cause tonic-firing neurons to burst, and even induce firing in neurons that are normally quiescent at certain parameter values (Weihberger & Bahar 2007). A similar shift in behavior in coupled HR neurons is seen here.

2.3.3. Synchronization. To analyze the activity of the model with Hindmarsh-Rose neurons, the phase synchronization index is used once more. Some of the following analysis was calculated as described in Section 2.2.4., with the synchronization index calculated for 10-second intervals over the entire duration of each simulation. However, the synchronization index is also calculated using a sliding window.

2.3.3.1. Sliding synchronization window. A sliding synchronization window allows a detailed look at the change in the synchronization index over time. The index is calculated over a small window (10 sequential spikes fired by a single neuron), and then the window is shifted forward by one spike and the index is calculated again. This process is repeated until there are not enough spikes left to form another window. The equation for the synchronization index is the same as described in Section 2.2.4.1.

An example of the sliding synchronization window can be seen in Figure 2.29. Here, the synchronization index for two neurons in each region is shown for parameter values corresponding to the average activity from Figure 2.23. The index ranges over all values from 0 to 1, with significant fluctuations over time. A few interesting notes can be taken from Figure 2.29, such as the dip in synchronization in AMIN around the time the circadian drive dips (about mid-late afternoon), accompanied by a near-simultaneous spike in VLPO synchronization.

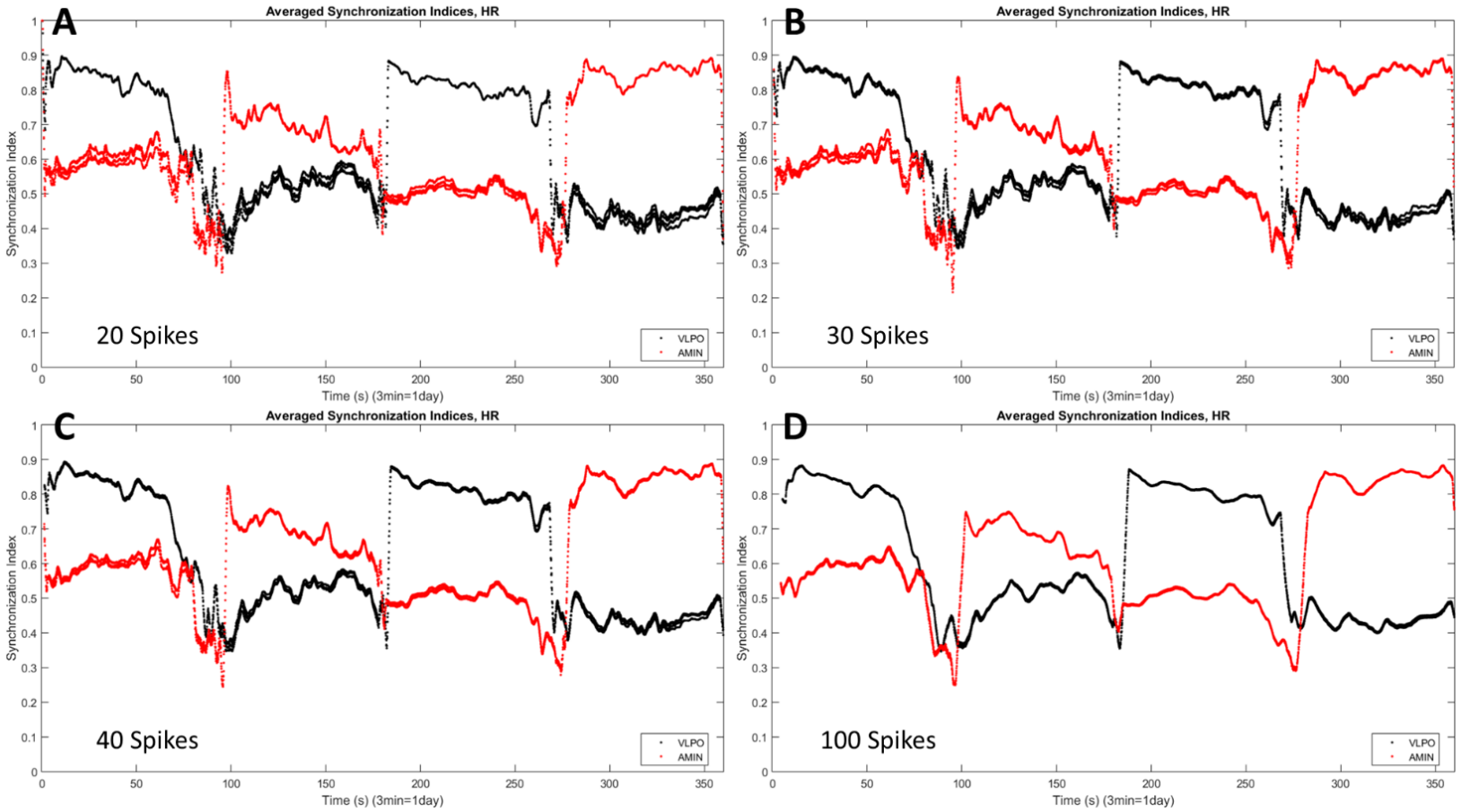

Figure 2.32 – Sliding Window Synchronization, HR, Varied Window Sizes
Synchronization indices averaged over all unique pairs of neurons in each region using sliding synchronization windows of various sizes. Calculated from data in Figure 2.26 ($I = 2.00$). (A) 20 spikes per window. (B) 30 spikes per window. (C) 40 spikes per window. (D) 100 spikes per window.

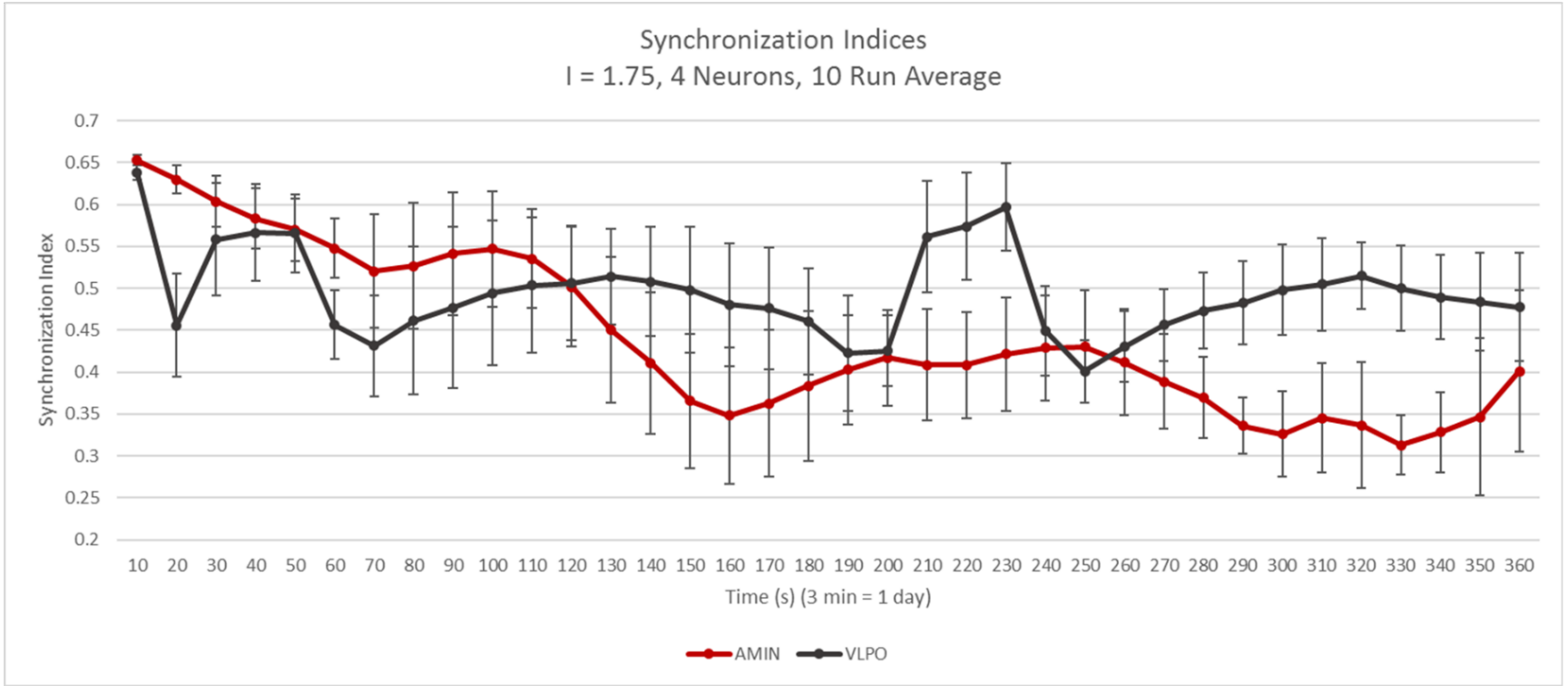

Figure 2.33 – 10-Run Average Synchronization, $I = 1.75$, HR, 10-Second Intervals
Synchronization indices averaged over 10 runs, calculated over 10-second intervals. Error bars denote the standard deviation across all runs. The pattern of change in synchronization from a single run with these parameters is shown in Figure 2.30. The parameters are $g_A = -7.5x10^{-6}$, $g_V = -4.25x10^{-5}$, $I = 1.75$, $g_{CA} = 1.15x10^{-3}$, and $g_{CV} = -0.0019$, with 4 neurons per region.

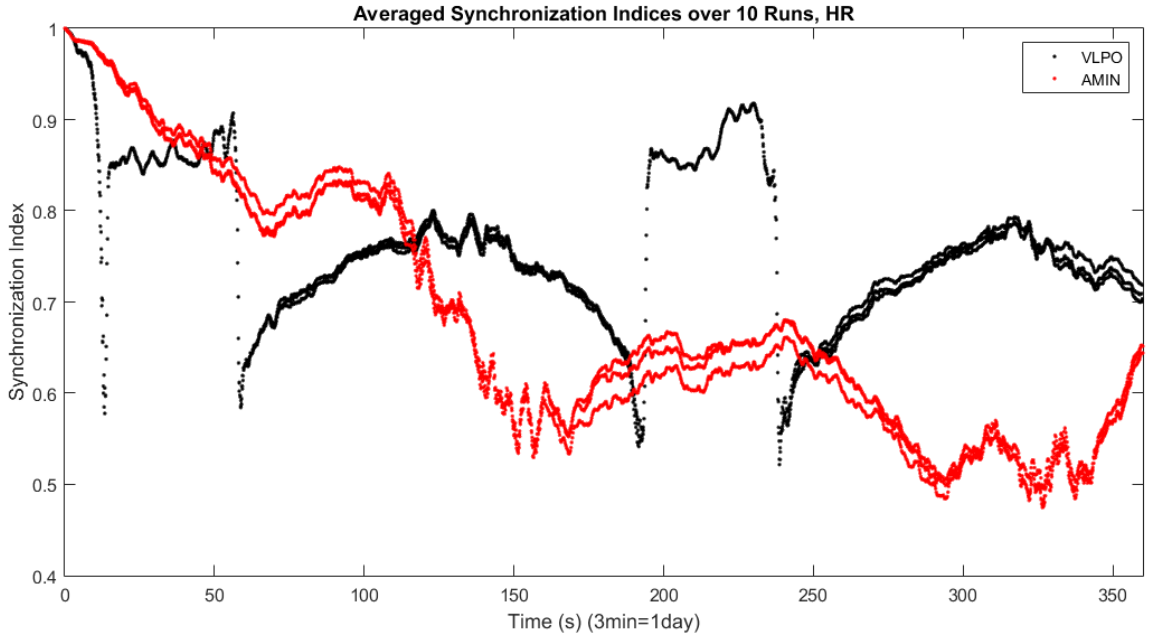

Figure 2.34 – 10-Run Average Synchronization, $I = 1.75$, HR, Sliding Window
Synchronization indices averaged over 10 runs, calculated using a 10-spike sliding window. Parameters are $g_A = -7.5x10^{-6}$, $g_V = -4.25x10^{-5}$, $I = 1.75$, $g_{CA} = 1.15x10^{-3}$, and $g_{CV} = -0.0019$, with 4 neurons per region.

Figure 2.30 shows the averaged synchronization indices for all unique pairs of neurons in each region, for the data shown in Figure 2.23. Note the varying levels of synchronization of each region and the time of day. AMIN has higher synchronization during the daytime before dipping during the nighttime. VLPO does the same, though it remains for a longer time with lower synchronization, and the transitions are more distinct. Also of note is the multiplicity of the VLPO lines around the 100-second mark. The number of lines reflects the number of spikes per burst (in this case, the neurons are firing triplets, as can be seen in Figure 2.24C). This is explored further in the next two figures.

Increasing the value of I from 1.75 to 2.00, the synchronization of the activity in Figure 2.26 is plotted in Figure 2.31. The relationship between time of day and relative

synchronization is clear here; AMIN has higher synchronization during the night while VLPO has higher synchronization during the day. A reciprocal relationship between AMIN and VLPO synchronization was also seen in the Huber-Braun version of the model. Note that the multiple lines indicating burst-firing are averaged out when the width of the sliding window is increased (Figure 2.32).

2.3.3.2. 10-run averages. To investigate the consistency of the model's behavior multiple simulations were performed at various parameter values. The synchronization index was calculated for each run and then averaged for a given set of parameter values. The synchronization index was calculated with both non-overlapping 10-second intervals and with a sliding window.

Using the same parameters as Figure 2.23, with $g_A = -7.5x10^{-6}$, $g_V = -4.25x10^{-5}$, $I = 1.75$, $g_{CA} = 1.15x10^{-3}$, $g_{CV} = -0.0019$, and 4 neurons per region, 10 runs were completed. The 10-second non-overlapping interval method results are shown in Figure 2.33. Both the AMIN and VLPO regions show fluctuating synchronization indices, with frequent switches between which group is more highly synchronized.

The corresponding sliding-window results are shown in Figure 2.34. The VLPO and AMIN regions again show fluctuations and switch between which region is more highly synchronized. However, the results reveal the number of spikes per burst, and the synchronization changes are much more abrupt. Averaging over 10 runs did not cause the multiplicity of the lines to merge or become smeared, which speaks to the consistency of the bursting behavior over numerous runs.

Both Figures 2.33 and 2.34 indicate that VLPO has higher synchronization during the early day, with a lower, varying synchronization over the afternoon and night. AMIN,

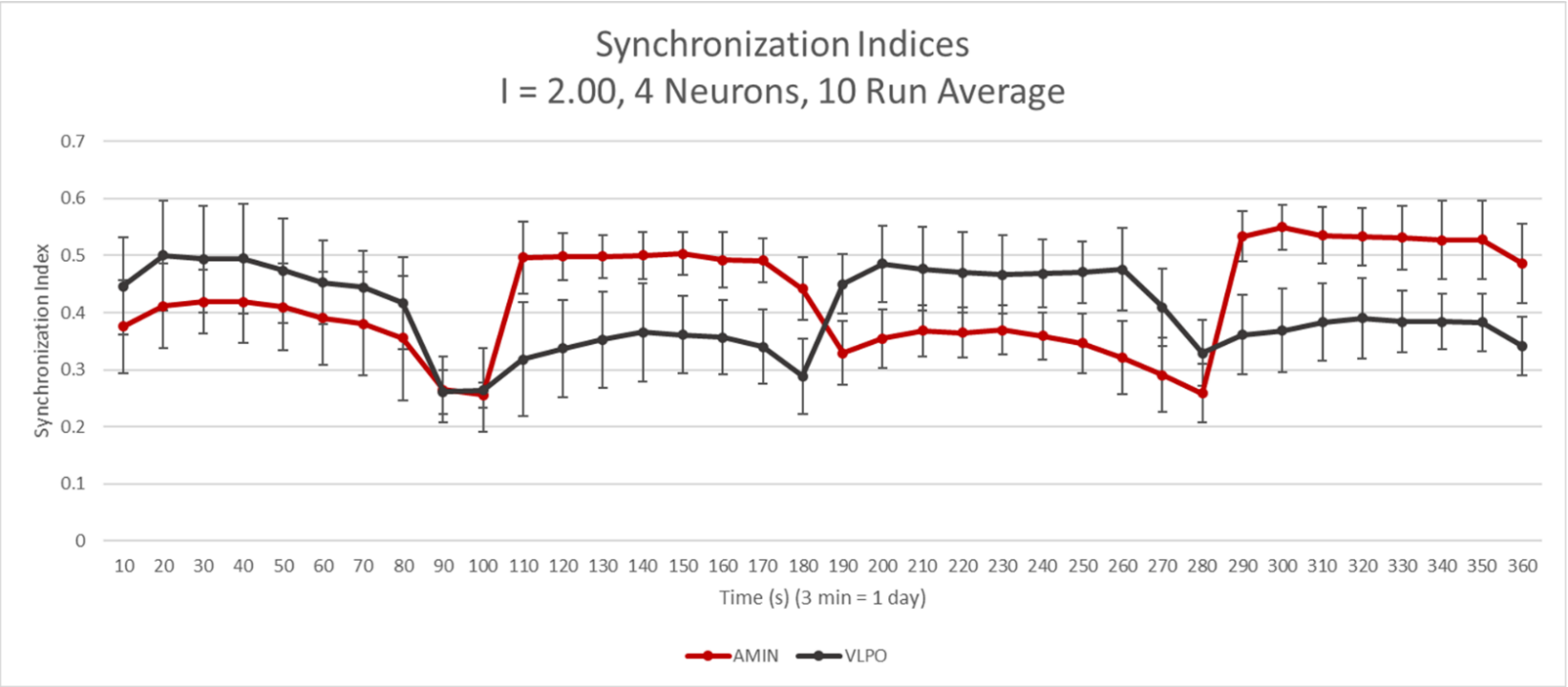

Figure 2.35 – 10-Run Average Synchronization, $I = 2.00$, HR, 10-Second Intervals
Synchronization indices averaged over 10 runs, calculated over 10-second intervals. Error bars denote the standard deviation across all runs. The pattern of change in synchronization from a single run with these parameters is shown in Figure 2.31. Parameters are $g_A = -7.5x10^{-6}$, $g_V = -4.25x10^{-5}$, $I = 2.00$, $g_{CA} = 1.15x10^{-3}$, and $g_{CV} = -0.0019$, with 4 neurons per region.

on the other hand, has higher synchronization during the day with a more gradual decrease to nighttime minimums. The separation between the multiple lines for both AMIN and VLPO may indicate changes in the bursting behavior, with more space separating the lines during active times (day for AMIN, night for VLPO) and less separation during downtimes.

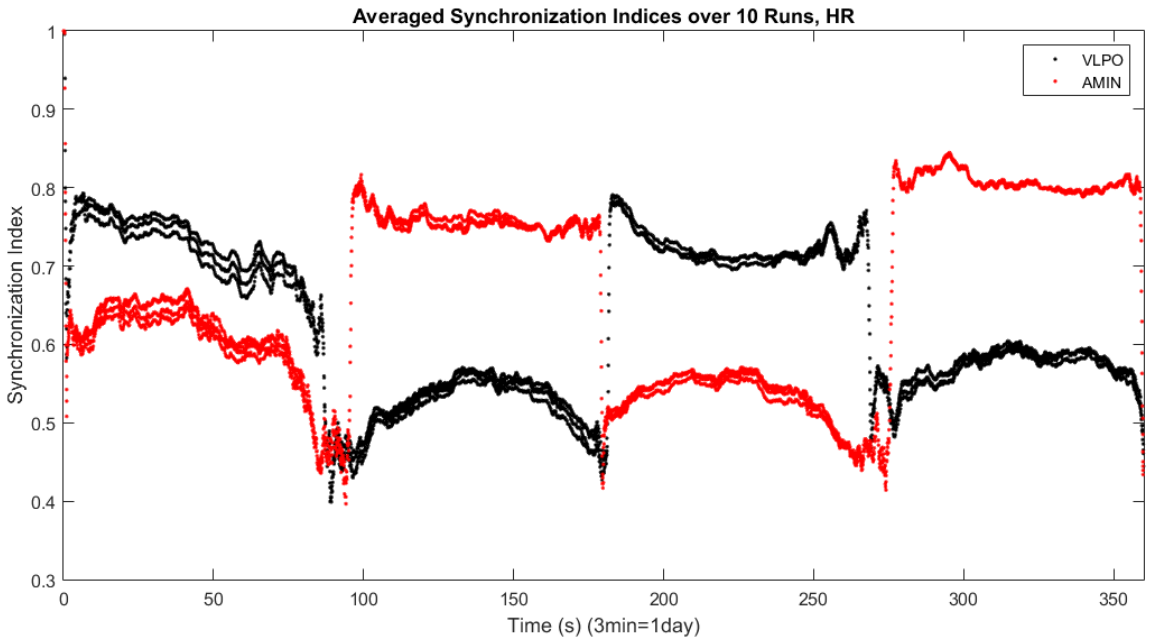

Figure 2.36 – 10-Run Average Synchronization, $I = 2.00$, HR, Sliding Window
Synchronization indices averaged over 10 runs, calculated with a 10-spike sliding window. Parameters are $g_A = -7.5x10^{-6}$, $g_V = -4.25x10^{-5}$, $I = 2.00$, $g_{CA} = 1.15x10^{-3}$,and $g_{CV} = -0.0019$, with 4 neurons per region.

Results for different parameter values, shown in Figure 2.35, exhibit a clearer reciprocal relationship between VLPO and AMIN's synchronization values, similar to that previously observed in the Huber-Braun version of the model (see Figure 2.20). In the Hindmarsh-Rose version of the model, however, this relation has been reversed. AMIN

now consistently has higher synchronization than VLPO during the night, and VLPO is more synchronized than AMIN during the day. These results can be compared to what is known about actual synchronization in the human brain during sleep and wake states. As discussed in Section 1.3.2., EEG recordings suggest that human brain activity is more synchronized while sleeping than while it is awake (Krueger *et al*. 2008, de Andrés et *al*. 2011, Schwartz & Kilduff 2015). This leads to the generalization that "sleep = synchronized activity" and "wake = desynchronized activity". Keeping this in mind, the reciprocal relationship between AMIN and VLPO may be related to their state of activity during different times of the day. During the daytime, the sleep-promoting neurons in the VLPO may be considered as "resting", which would correspond to a synchronized state, while the AMIN neurons would be in a "wake", or desynchronized state; these states would switch during the nighttime, with the VLPO neurons more active (less synchronized). These states of rest and activity thus correspond roughly to the levels of synchronization seen in Figure 2.35. This interpretation of the results explains the reciprocal relation of VLPO and AMIN's synchronization in the HR results, but does not suitably explain the HB version of the results.

Figure 2.36, which shows the sliding window synchronization, retains the relationships between VLPO and AMIN shown in Figure 2.35, though with a higher and wider range of indices, multiple lines indicative of burst firing, and sharper transitions. Small changes in the index over periods of relative stability are also visible, likely an effect of the noise in the system.

For comparison, the sliding window synchronization index approach was also applied to the Huber-Braun model. Figure 2.37 shows the synchronization index calculated

with a sliding window for the same data shown in Figure 2.20. The reciprocal relationship between synchronization indices for VLPO and AMIN is present, and like its 10-second non-overlapping interval counterpart, VLPO has some local maxima during the day and a dip before nighttime.

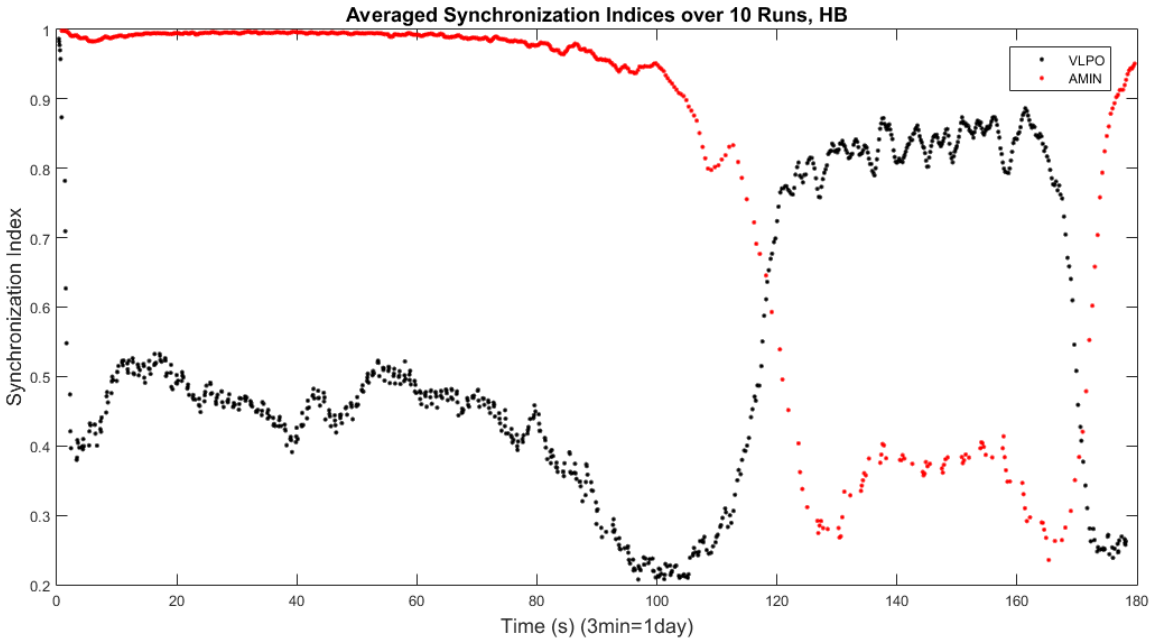

Figure 2.37 – Average Synchronization, 10-Run, Huber-Braun
The 10-spike sliding window analysis of the HB 10-run data shown in Figure 2.20. As before, parameters are $g_V = -3x10^{-5}$, $g_A = -3.75x10^{-5}$, $g = 4.5x10^{-5}$, $|g_C| = 0.95$, $T_A = 5\ °C$, and $T_V = 15\ °C$, with 4 neurons per region.

As mentioned in Section 2.3.3.2., the reciprocal relationship between VLPO and AMIN synchronization in runs using HB neurons is the opposite of the relationship seen in runs with HR neurons. While the reciprocal relationship in the HR results can be explained using the argument presented above, the HB simulations are inconsistent with

this interpretation. More detailed comparisons between HR and HB dynamics can shed light on this inconsistency, as discussed in the following section.

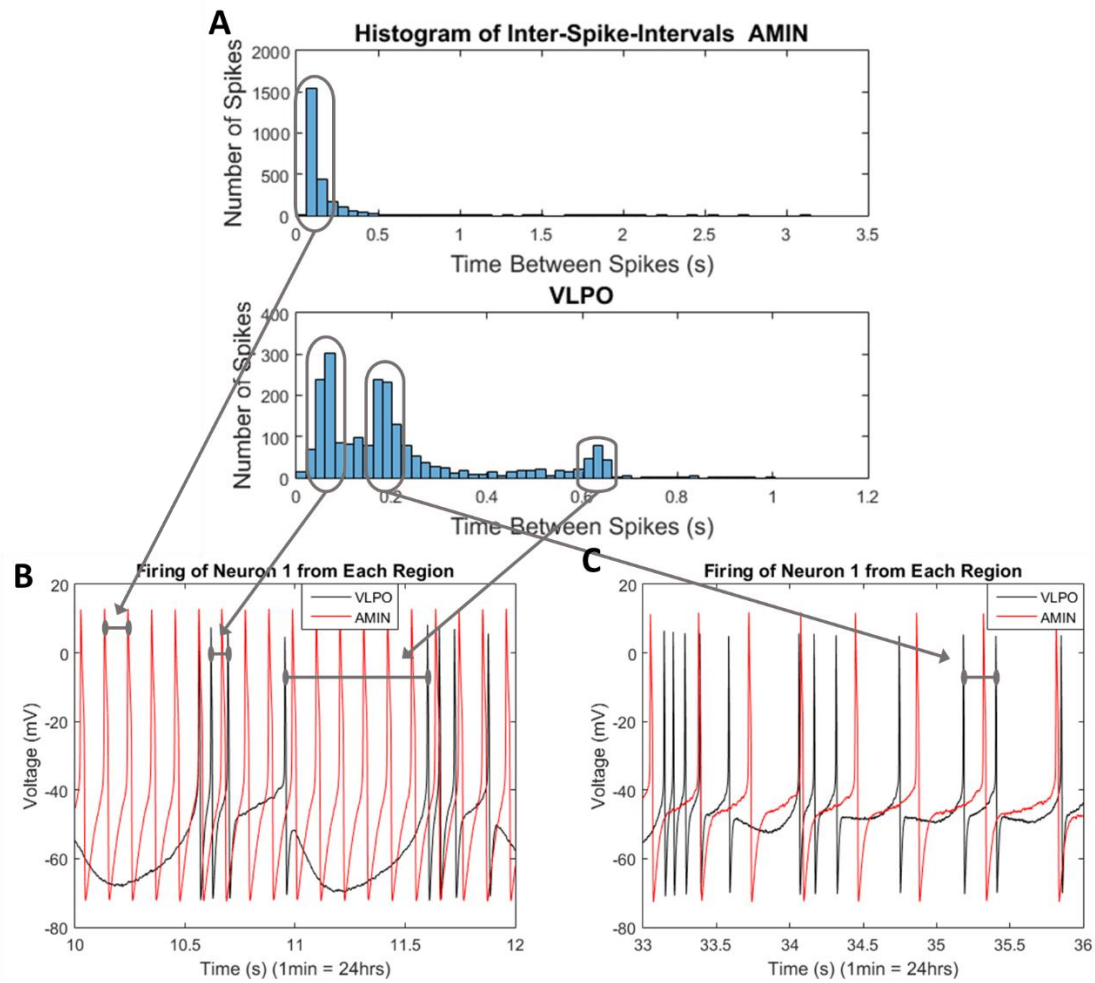

Figure 2.38 – Inter-Spike Interval Histograms, Huber-Braun
Inter-spike interval histogram and corresponding firing patterns for HB neuron activity in Figure 2.14. (A) The single peak in the ISI histogram for AMIN indicates that the neurons are predominantly firing single spikes. In contrast, the histogram for the VLPO neurons shows three distinct peaks, indicating that the firing pattern is predominantly bursting. (B,C) Example firing from neuron 1 of each region. AMIN's rapid single spikes correspond to the single peak in the AMIN ISI histogram (see leftmost arrow). VLPO's highest ISI peaks correspond to intra-burst and inter-burst intervals, as indicated by the arrows.

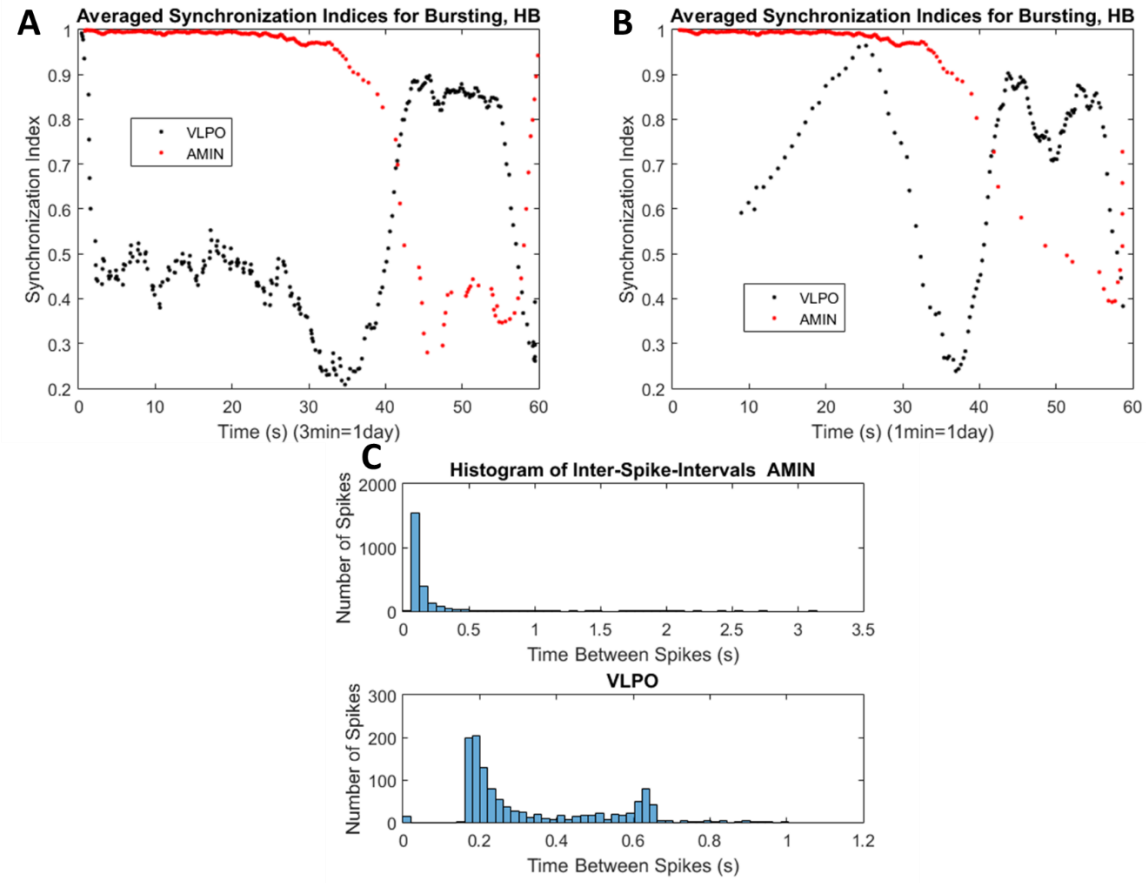

Figure 2.39 – Burst Synchronization, Huber-Braun
Synchronization indices corresponding to Figure 2.14. (A) Sliding window synchronization index based on spike times, showing the HB reciprocal relationship between VLPO and AMIN synchronization indices. (B) Sliding window synchronization index based on burst times. For VLPO, the minimum ISI threshold used to determine the first spike in a burst was 0.2 s for times before 38 s and after 57 s and 0.16 s for times in between. For AMIN, there was no threshold for times before 40 s and after 56 s and 0.52 s for times in between. Note the increase in VLPO's synchronization during the day and its dip at night, along with AMIN's slight increase in synchronization at night. (C) ISI histogram with the burst synchronization thresholds applied. Compared to Figure 2.38A, VLPO's smallest ISI value has been removed. The peak at 0.2s is the inter-burst interval during VLPO's active time overnight.

2.3.4. Huber-Braun Comparison. Both HR and HB neurons exhibit bursting behavior, as seen in Figures 2.24-2.28 for HR and Figures 2.12 and 2.13 for HB. Despite

this, the sliding synchronization window provides different results for HB and HR; specifically, the reciprocal relationship between VLPO and AMIN's synchronization indices, where one has higher synchronization during the day and the other during the night. This may be because HR neurons shift between various bursting patterns during the course of the day, while HB neurons shift between rapid, single spikes to bursting. This results in a broad range of inter-spike intervals (ISIs), as shown in Figure 2.38A.

The large single peak in the top panel of Figure 2.38A indicates that the neurons in the AMIN region are primarily firing single spikes, as can be seen in Figure 2.38B and C. In contrast, the ISI histogram for the VLPO neurons shows two peaks at short ISIs and one at a much longer interval, indicating bursting behavior. The shorter ISI values (the two larger peaks to the left) are the intra-burst intervals, or the time between spikes within a burst, and the longer ISI corresponds to the inter-burst interval. The relationship between the histogram peaks and the time-course of neural firing is shown by the arrows in Figure 3.28.

The ISI histogram suggests that the apparent lack of daytime synchronization in the VLPO may be due to variation in the intra-burst intervals. The bursts themselves may be more synchronized than previously indicated by the synchronization index, which treated every spike independently. To test this hypothesis, synchronization is measured between bursts alone. Burst times were identified by selecting the first spike in each burst, i.e., selecting only those spikes preceded by a specified spike-free time interval.

Figure 2.39 shows the impact of quantifying burst synchronization alone. The sliding window burst synchronization corresponding to the data in Figure 2.14 is shown in panel B; compared to the sliding window spike synchronization shown in panel A, the burst

synchronization demonstrates that the levels of synchronization are indeed impacted by the bursting activity. VLPO shows higher synchronization during the day when assessed by burst synchronization rather that spike synchronization, in contrast to the low synchronization previously shown by the HB results. Varying thresholds were utilized to account for the drastic changes in the inter- and intra-burst intervals (values and times in caption).

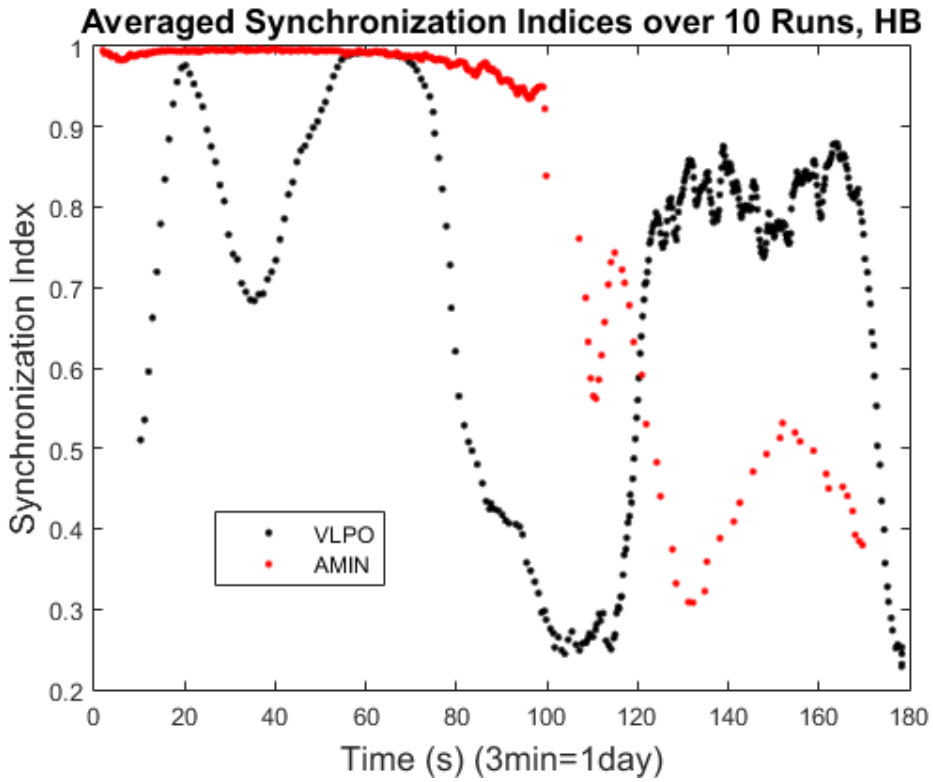

Figure 2.40 – Burst Synchronization, Huber-Braun, 10 Runs
Burst synchronization indices for 10 Huber-Braun runs, using same data from Figure 2.37. Comparing this figure to Figure 2.37, VLPO shows a marked increase in synchronization during the day, consistent with the change seen between Figures 2.39A and 2.39B. Parameters were the same as Figure 2.37, and the burst synchronization thresholds are the same as Figure 2.39.

Burst synchronization (Figure 2.39B) reveals much greater daytime VLPO synchronization than when the synchronization index is calculated based on every neural spike (Figure 2.39A). Also, AMIN synchronization does not decrease as much during the nighttime as it did in the non-burst synchronization figure. Interestingly, there is still a large dip in synchronization for VLPO as it transitions into nighttime. This dip is remarkably consistent, showing up in some form in every HB synchronization figure.

The ISI histogram for the burst synchronization is shown in Figure 2.39C. AMIN has a single peak as it did for the non-burst synchronization; however, VLPO has one fewer peaks than before (Figure 2.38A, bottom panel). This shows that the shorter intra-burst interval has been removed, leaving the inter-burst and the larger intra-burst intervals. The second inter-burst interval peak (at about 0.2) is due to the lower threshold during the VLPO region's active time overnight, when the ISIs are shorter.

The levels of synchronization and the time of day may be related to the average activity of each region. When the average activity is low, such as during the daytime for VLPO, it may be due to the change in the behavior of the neurons, which shift from continuous firing to bursting (Figure 2.13). This bursting occurs at the time when the neurons fall out of synchronization, leading to the lower synchronization index during the day. A similar occurrence happens to the AMIN region, where the lower synchronization values correspond with the time where AMIN shifts from continuous firing to bursting (Figure 2.12). In Figure 2.40, burst synchronization is calculated for 10 separate realizations of the HB model at the same parameter values. The results above remain consistent with those shown in Figure 2.39.

While there is evidence that the single spike synchronization index may not be revealing the whole picture, the burst synchronization analysis does not completely resolve the discrepancy between the HR and HB reciprocal relationships of the synchronization indices for VLPO and AMIN. This suggests that this discrepancy between the HR and HB results may simply be due to the inherent differences between the two neural models. There is no consistent, simple 1-to-1 mapping that connects these two models. They represent the same types of activity, but HB uses equations for each current while HR uses three coupled nonlinear differential equations to represent all of a neuron's activity. There might be other regions of parameter space where HR and HB neurons exhibit behaviors that are directly comparable. Future work covering other regions of parameter space and more values of coupling strengths may yield an answer to this question, as well as a more precise dynamical explanation for the differences in synchronization between the two cases.

2.4. CONCLUSIONS

Huber-Braun neurons provide a more realistic representation of the activity of a neuron and are used in a wide range of applications and programs. Hindmarsh-Rose is also utilized often, and though it is not as biologically realistic as HB, it also is less computationally expensive than HB. This means when the sleep-wake model presented here switched from HB to HR, options to add more neurons and expand the time compression further became available. Both versions of the model using HB or HR gave qualitatively similar results, except for the opposite relationship in the reciprocal synchronization switching between AMIN and VLPO. From this point forward, HR will be the neural model utilized.

2.4.1. Huber-Braun. While the activity of each region does not stop during their respective downtimes, the average activity decreases, suggesting a system state change between wakefulness and sleep. The synchronization of each region changes over the course of the day. AMIN has higher synchronization during the daytime (first two-thirds of the day) than it has at nighttime (last third of the day), while VLPO has higher synchronization during the nighttime than it does during the daytime. AMIN and VLPO also have a reciprocal relationship in synchronization. When AMIN has high synchronization, it is higher than VLPO (daytime), and when VLPO's synchronization is high, it is higher than AMIN (nighttime). These switches occur approximately when daytime turns to nighttime, and when the day ends.

The daytime synchronization index for VLPO increases significantly when burst synchronization is applied. The system exhibits size effects in that the synchronization indices vary more smoothly for larger system sizes (Figures 2.18-2.20).

2.4.2. Hindmarsh-Rose. As the external input current increases, the neurons go from no activity during downtime to continuously firing through the entire day. While firing continuously, the neurons of each region may change their firing patterns depending on the time of day, such as VLPO firing doublets (Figure 2.25) or triplets in the morning and triplets or quadruplets at night (Figure 2.28).

Synchronization analysis of the Hindmarsh-Rose version of the program revealed a relationship between AMIN and VLPO opposite to that observed in the HB model. With HR, AMIN has the highest synchronization at night, while VLPO has its highest synchronization during the day (Figures 2.35 and 2.36). While these results may be

interpreted in terms of greater synchronization in less active brain regions, the opposite results for the HB model remains to be explained.

2.4.3. Comparison. The HB neural model has the benefit of being more biologically realistic, though computationally more expensive. On the other hand, the HR neural model is somewhat simplistic in comparison yet yields similarly complex results. While the HB neurons change behavior from single spikes to bursting and back during the course of a day (See Figure 2.38), HR neurons maintain bursting behavior (at larger values of I) with varying numbers of spikes. This behavioral shift in HB appears to influence the synchronization relationship, as discussed in Section 2.3.4. It does not fully explain the discrepancy, however. It may be that the HB neurons, whose bursting behavior is sensitive to temperature and coupling (Weihberger & Bahar 2007), may simply be in a different dynamical regime than the HR neurons for the parameter space explored in this dissertation. Due to the complexity differences between HR and HB, they are not directly comparable. The differences in the HR and HB reciprocal synchronization relationship may be explored in future research.

3. TWO-HEMISPHERE MODEL

The Hindmarsh-Rose version of the one-hemisphere model showed reciprocal activation of AMIN and VLPO regions during wake and sleep, accompanied by synchronization changes. This model, however, is incomplete. Here, a two-hemisphere model, which exhibits chimera-like behavior reminiscent of asymmetric sleep, will be presented.

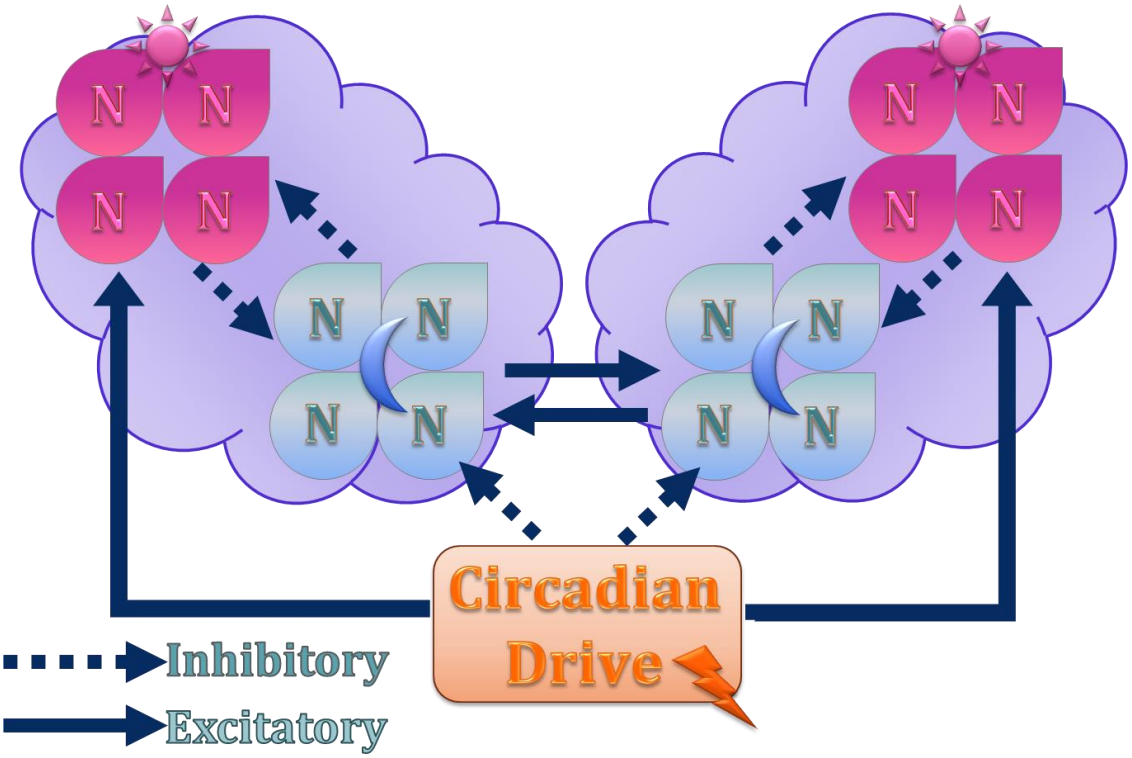

Figure 3.1 – Two-Hemisphere Model
A schematic representation of the two-hemisphere version of the model. Note how each hemisphere consists of the same elements – a VLPO sleep-promoting region (blue with moon) and an AMIN wake-promoting region (pink with sun) – and shares a single circadian drive. The connection between hemispheres is represented by the excitatory connection (solid arrows) between the VLPO regions in each hemisphere.

3.1. MODEL ORGANIZATION

To expand the model into two separate interacting hemispheres, the regions from the one-hemisphere model were duplicated. Each hemisphere (left and right) has its own VLPO region and AMIN region, each consisting of individual neurons. The circadian drive from the original model is retained, projecting to each of the VLPO and AMIN regions in the same fashion as in Figure 2.3. This is displayed schematically in Figure 3.1. The hemispheres communicate via excitatory connections (solid arrows) between the VLPO regions. This form of the model was inspired by the two-hemisphere sleep-wake model designed by Kedziora *et al*. (2012).

The coupling strength between neurons in the same region is given by g, and is the same for each region. Each of the other connection strengths between regions and between the circadian drive and each region remain the same as in Section 2.2.1., summarized here for reference. Projections from AMIN to VLPO are mediated by the coupling strength g_A, and from VLPO to AMIN the coupling strength is g_V. The projections from the circadian drive to AMIN and VLPO are g_{CA} and g_{CV}, respectively. For the new connection from VLPO in the left hemisphere to VLPO in the right hemisphere, the coupling strength is g_{VLtR}, and for the opposite direction it is g_{VRtL}.

3.2. CHIMERA REVIEW

As will be seen below, the two-hemisphere model exhibits so-called chimera states. Here, I will briefly review dynamical chimera states and prior observations of chimeras in neural systems. Further details are also provided in the author's Master's thesis (Glaze 2015).

3.2.1. Chimeras in General. The term "chimera" originated in ancient Greece. It referred to a mythical fire-breathing beast – a lion with a goat's head growing out of its back and a snake for a tail. From this, the word chimera became associated with incongruity, or connected parts that seem mismatched. Many different types of chimeras have been discovered and/or created by science since then, with a few notable examples briefly examined below.

3.2.1.1. Gene chimeras. A gene chimera operates at the level of DNA, occurring naturally but also reproducible experimentally. A gene chimera occurs when a portion of a gene is cut, removed, and replaced with a portion of a different gene. This can occur naturally during DNA recombination or can be performed using gene editing tools in a laboratory. When this process occurs in genes, the product can result in an entirely new phenotype. While such procedures have been performed experimentally since the 1970s (Berg *et al*. 1974), there are still many unknown factors and possible side effects of such gene splicing. A genetically altered pet called GloFish was developed for sale, becoming available to the public in 2003. This caused unease and a mild uproar among biologists and watchdog groups, who worried that these transgenic fish might end up in the wild and lead the way for other, potentially harmful transgenic creatures (Knight 2003). There is a brighter side to the study of creating gene chimeras, however – developing gene therapies for those with genetic disorders. One such disorder is Angelman Syndrome, where a small microdeletion of several bands from one gene causes a slew of mental and physical disabilities. While still preliminary, gene therapies are being developed to lessen the negative impact of this (Meng *et al*. 2015) and other genetic disorders.

3.2.1.2. Genetic chimeras. Very similar to gene chimeras but on a larger scale are genetic chimeras. Rather than a spliced single gene, a genetic chimera is a combination of larger portions of different DNAs. A prominent example of an experimentally-created genetic chimera is the "geep". By combining the embryonic cells of a goat and a sheep, a single creature with the genetics of both species was created (Fehilly *et al*. 1984). This has been repeated and studied in the lab (Polzin *et al*. 1987) and a natural occurrence has been observed, though the chimera did not survive to term (Lühken *et al*. 2009). Another natural genetic chimera occurs when two embryos of the same species merge and become one creature. A striking (and adorable) example of this are cat chimeras, such as "Venus the Chimera Cat", who looks like a "black cat with green eye" on one side of her face and "orange tabby with blue eye" on the other side (Andreassi 2012). This is not uncommon, as the numerous pictures on Google can attest, though the blue eye is a trait typically only seen in white or mostly white cats.

Genetic chimeras can also occur with humans, both naturally and via experimental intervention. Sometimes twin embryos merge and become a single embryo naturally, which is called a fusion chimera, or sometimes the process of in vitro fertilization (IVF) can create a fusion chimera, as multiple embryos are usually implanted to improve the chances that one or more will survive to term. Specifically, in the case of IVF, multiple fetuses may be observed in early ultrasounds only to decrease in later ultrasounds, termed "vanished twin syndrome". One or more of the fetuses "vanishes", either through death and reabsorption, or through fusion with its twin. This occurs in ~18% of IVF pregnancies (Wenk 2018). Most human chimeras remain undetected.

Besides human and animal chimeras, scientists have been investigating human-animal chimeras to find an optimal model for studying human disease (Levine & Grabel 2017, De Los Angeles *et al*. 2019) and for growing human organs inside of these chimeras for use in transplantation (Levine & Grabel 2017, Hagan-Brown *et al.* 2017). These chimeras, which would be created by inserting human stem cells into monkey or pig embryos, have raised ethical issues regarding both experimentation on animals and the creation of human-animal hybrids (Hagan-Brown *et al.* 2017, Levine & Grabel 2017, De Los Angeles *et al*. 2019).

3.2.2. Dynamical Chimeras. A dynamical chimera state occurs when an array of identical oscillators divides into two groups with different activity – one group is synchronized, while the other is desynchronized. Variants of this state, such as phase-cluster chimeras and partial phase-cluster chimeras, are discussed below (Section 3.2.2.1.). As mentioned previously in Section 1.7.1., dynamical chimeras can occur in many different types of systems, including mechanical (Martens *et al*. 2013), optical (Hagerstrom *et al*. 2012), chemical (Tinsley *et al*. 2012), and neural (Omelchenko *et al*. 2013, Hizanidis *et al*. 2014, Glaze *et al*. 2016).

3.2.2.1. Variants of the chimera state. In a phase-cluster chimera, instead of one group of desynchronized and one group of synchronized oscillators, both groups are synchronized but with different behavior. For example, one group of oscillators (neurons, in this case) may be firing single spikes while the other group fires double spikes. Partial phase-cluster chimera states can also occur in cases where the groups of oscillators are predefined (see Tinsley *et al*. 2012 and Glaze *et al*. 2016). Like the phase-cluster state, each group is predominately synchronized with different activity, though a few neurons

may exhibit synchronization not with the group in which they reside, but instead with the other group.

These variants, along with the standard chimera state, have been found in systems using different media. A few notable cases, such as mechanical, optical, and chemical oscillators are described below; neural chimeras are discussed in Section 3.2.3.

3.2.2.2. Mechanical chimeras. In a large-scale physical experiment, Martens *et al*. (2013) utilized groups of metronomes as oscillators to simulate a chimera state in a mechanical medium. Two swings, each containing N metronomes, were connected by a spring with tunable spring constant κ. The metronomes were all set to the same frequency. As they beat together on the swing, the motion of the swing provided the coupling between the metronomes, which became synchronized over time. This coupling scheme is known as Abrams-Strogatz coupling, which will be discussed in more detail below (Section 3.2.4.1.).

Martens *et al*. (2013) observed synchronized in-phase motion of the metronomes from both swings when κ was large. When κ was small, however, all the metronomes exhibited anti-phase synchronization, meaning that there was a 180° phase difference between the metronomes on one swing and those on the other. Chimera states appeared when κ had an intermediate value. They also consistently appeared with a specific initial condition: one swing was allowed to synchronize before being coupled to the other swing. This showed that chimera states were not simply a side effect of heterogeneous initial conditions. These chimera states lasted for the duration of the experiments, leaving the question of the possibly transient nature of chimera states (Wolfrum & Omel'chenko 2011) unanswered in this instance. To further study their chimeric metronomes, Martens *et al*.

(2013) performed simulations of their experimental system. This allowed the exploration of different configurations and parameters not possible in the lab. Their computational results agreed with their experimental results.

The mechanical configuration reviewed here, essentially an expansion of Huygens' famous clock experiment, demonstrated that chimera states can occur in simple systems of oscillators. That chimera states can appear in systems so elegantly uncomplicated speaks to the idea that chimera states are a naturally-occurring phenomenon.

3.2.2.3. Optical chimeras. Dynamical chimera states were explored in optical systems by Hagerstrom *et al*. (2012). They employed a coupled map lattice which made use of a spatial light modulator (SLM). The SLM, which altered the polarization of an optical input, was divided into a matrix of square elements with periodic boundary conditions and coupling that decreased with distance. Light from an LED passed through a beam splitter before striking the SLM and a camera, and the camera's input was routed through a computer, which applied the coupling before the signal was fed into the SLM. The variable of importance was the phase of each element, which depended upon the light striking it and was also affected by the input from the camera, which was in turn influenced by the light via the coupling term.

Optical chimeras in this system, which was also computationally modeled by Hagerstrom *et al*. (2012), are characterized by groups of elements exhibiting coherent, intense light, separated by thinner regions of incoherence. Like the mechanical chimera described above, optical chimeras were found at intermediate coupling strengths, with high values producing a completely synchronized system and low values producing a desynchronized system.

3.2.2.4. Chemical chimeras. Tinsley *et al*. (2012) investigated chimera states in chemical oscillators using two subgroups with strong coupling within each group and weaker coupling between groups. These coupling strengths were based upon the phase of an oscillator and the phase of every oscillator coupled to it, meaning that the overall strength of the coupling varied with time.

The oscillators, based on the photosensitive Belousov-Zhabotinsky reaction, began with heterogeneous initial conditions. N oscillators, divided into two equal subgroups A and B, communicated via light intensity. Subgroup A remained synchronized, while subgroup B exhibited a range of different behaviors, including complete synchronization with A, chimera states, phase-cluster chimera states, and semi-synchronization. Full synchronization between both subgroups always occurred with homogenous initial conditions, but also arose for some parameter values with heterogeneous initial conditions. Chimera states exhibited by this system consisted of full synchronization for subgroup A and complete desynchronization for subgroup B that typically lasted for the duration of the experiment. The phase-cluster chimera states, as described earlier (Section 3.2.2.1.), occurred when A and B were both synchronized, but with B exhibiting different synchronization patterns, such as double or triple spikes. As for the semi-synchronization states, each group has a different frequency, causing B to repeatedly fall into and out of synchronization with A.

The coupling within each group influenced the system's dynamics. Keeping the within-group coupling the same for both groups, and with weaker, symmetrical between-group coupling, Tinsley *et al*. (2012) found that the chimera states often occurred when coupling within a group was small, and almost always when the coupling between groups

was negative, or inhibitory. However, a small region of excitatory inter-group coupling values also produced chimera states. Other states, such as phase-cluster and fully synchronized states, occurred more frequently for stronger within-group coupling.

Simulations performed by Tinsley *et al*. (2012) were consistent with their experimental observations and allowed an expansion of the parameter space. With larger group sizes, chimera states appeared more frequently and lasted longer. While this does not definitely answer the question of whether chimera states are transient, it shows that the duration of the chimera state can increase with system size. Other experiments have been performed with chemical oscillators (Wickramasinghe & Kiss 2013, 2014), where different connectivity networks and coupling strengths were explored.

3.2.3. Neural Chimeras. As non-linear dynamical oscillators, neurons provide an ideal substrate for the investigation of chimera states. The time delay between coupled oscillators has been shown to have an effect on the establishment of chimera states (Sethia *et al*. 2008, Tinsley *et al*. 2012, Hagerstrom *et al*. 2012, Bick *et al*. 2017). Time delays represent more realistic signal propagation, such as in systems of oscillators like neurons and chemical reactions (Sethia *et al*. 2008). Clusters of alternating synchronized and desynchronized groups have been found in optical and neural chimera states (Hagerstrom *et al*. 2012, Glaze *et al*. 2016). These results are reminiscent of some neural processes, such as UHS (discussed in Sections 1.3.2 – 1.3.4. and 4.2., Majhi *et al*. 2019) and multiple brain disorders, including epilepsy and brain tumors (Uhlhaas & Singer 2006).

Several different neural models have been shown to produce chimera states, including leaky integrate-and-fire, FitzHugh-Nagumo, Hindmarsh-Rose, and Huber-Braun. The last of these was covered by the author's previous research and will be reviewed

later in Section 3.2.4. FitzHugh-Nagumo and Hindmarsh-Rose chimera states will be discussed below.

3.2.3.1. FitzHugh-Nagumo. FitzHugh-Nagumo (FHN) oscillators are used in neuroscience, among other disciplines. Chimera states in systems of FHN oscillators were explored by Omelchenko *et al*. (2013). Using a ring of N locally coupled FHN oscillators with heterogeneous initial conditions and positive (excitatory) coupling, chimera states were observed for small coupling strength. For larger values of coupling strength, the behavior of the system reflected what Omelchenko *et al*. (2013) called multichimera states. Rather than a single desynchronized group, multiple desynchronized groups were separated by groups of synchronized oscillators. Similar results were observed by Sethia *et al*. (2008) and Hagerstrom *et al*. (2012).

3.2.3.2. Hindmarsh-Rose. A different approach was taken by Hizanidis *et al*. (2014). Using N Hindmarsh-Rose oscillators, a 2-dimensional array and a 3-dimensional array were created. For the 2-D array, the 2-D version of the Hindmarsh-Rose neural model was used; this version of HR is essentially the 3-D version described in Section 2.3.1., though without the final z equation and the z term in the x equation. Starting with heterogeneous initial conditions, Hizanidis *et al*. (2014) observed chimera states and a configuration they called mixed oscillatory states. These mixed oscillatory states had desynchronized neurons like the chimera state, but the desynchronized neurons were not situated in bands or clusters. Rather, these neurons were distributed evenly among the synchronized neurons. They also found that the system's state changed with the variation of the coupling strength.

For the 3-D array, the 3-D version of the HR model was used (see Section 2.3.1.). Unlike the 2-D model, the 3-D HR model is capable of firing in bursts. Like the 2-D array, the 3-D array produced both chimera states and mixed oscillatory states, with the coupling strength being the driver of state changes in the system.

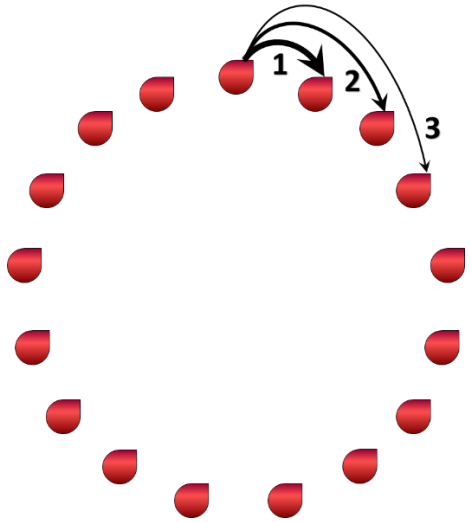

Figure 3.2 – Kuramoto Coupling Scheme
A schematic representation of Kuramoto coupling. A ring of inter-connected oscillators impact one another with a strength that decreases exponentially with distance.

3.2.4. Previous Research Results. The author's master's thesis research and first peer-reviewed paper centered on chimera states in the Huber-Braun model of thermally sensitive neurons with two different coupling schemes (Glaze 2015, Glaze *et al*. 2016). In this system of HB neurons, chimera states were found, along with two other variants of the chimera state. Each of the used coupling schemes will be briefly described here, followed

by the key results. For details beyond those reviewed below, see Glaze 2015 and Glaze *et al*. 2016.

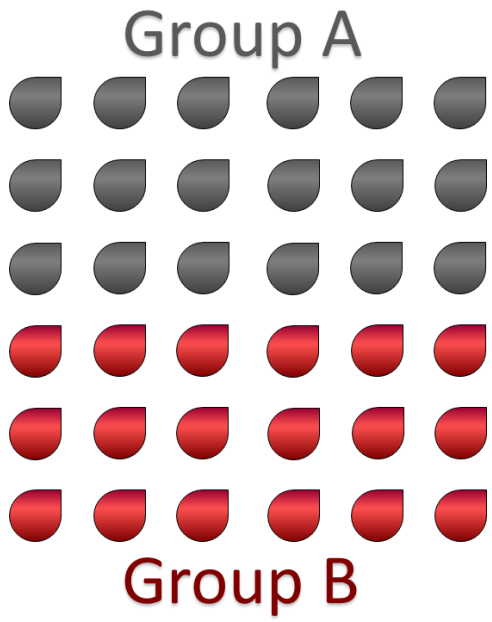

Figure 3.3 – Abrams-Strogatz Coupling Scheme
A schematic representation of Abrams-Strogatz coupling. A large group of oscillators is divided into two subgroups, with intra-group coupling and a weaker inter-group coupling.

3.2.4.1. Coupling schemes. Common coupling schemes utilized in generating chimera states are the Kuramoto and Abrams-Strogatz coupling schemes.

Kuramoto and colleagues (2002) developed a dynamical coupling scheme, using it in their discovery of the coexistence of synchronized and unsynchronized activity in coupled nonlinear oscillators. In other words, they discovered the chimera state. The Kuramoto coupling scheme consists of N oscillators, arranged in a ring, as shown in Figure 3.2. This allows periodic boundary conditions, with the strength of coupling between

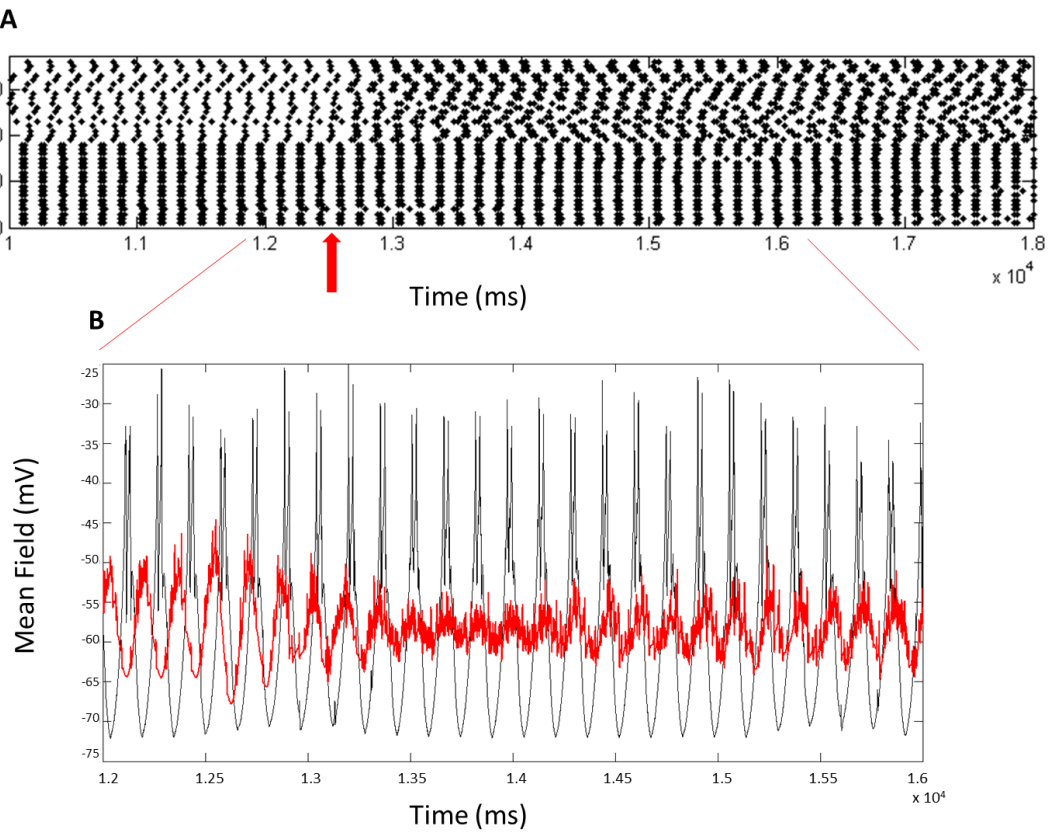

Figure 3.4 – Chimera State in Abrams-Strogatz Configuration
A dynamical chimera state found in the Abrams-Strogatz coupling scheme using Huber-Braun neurons, with weak inhibitory inter-group coupling and stronger, excitatory intra-group coupling. The red arrow indicates when the intra-group coupling for B and inter-group coupling was turned on. (A) A raster plot of all neurons in the configuration, with the bottom 18 neurons making up group A, and the top 18 neurons group B. The synchronized group A neurons simultaneously fire double spikes, in contrast to the desynchronized firing pattern of group B. (B) Mean field voltage, or average activity for groups A (black) and B (red). Reproduced from Glaze *et al*. 2016 with permission from AIP Publishing.

neurons decreasing exponentially with distance. Though Kuramoto *et al*. (2002) utilized simple phase oscillators in their model, any oscillator can be substituted, such as neurons. As the oscillators fire and interact, they will begin to form groups of synchronized oscillators, separated by desynchronized oscillators.

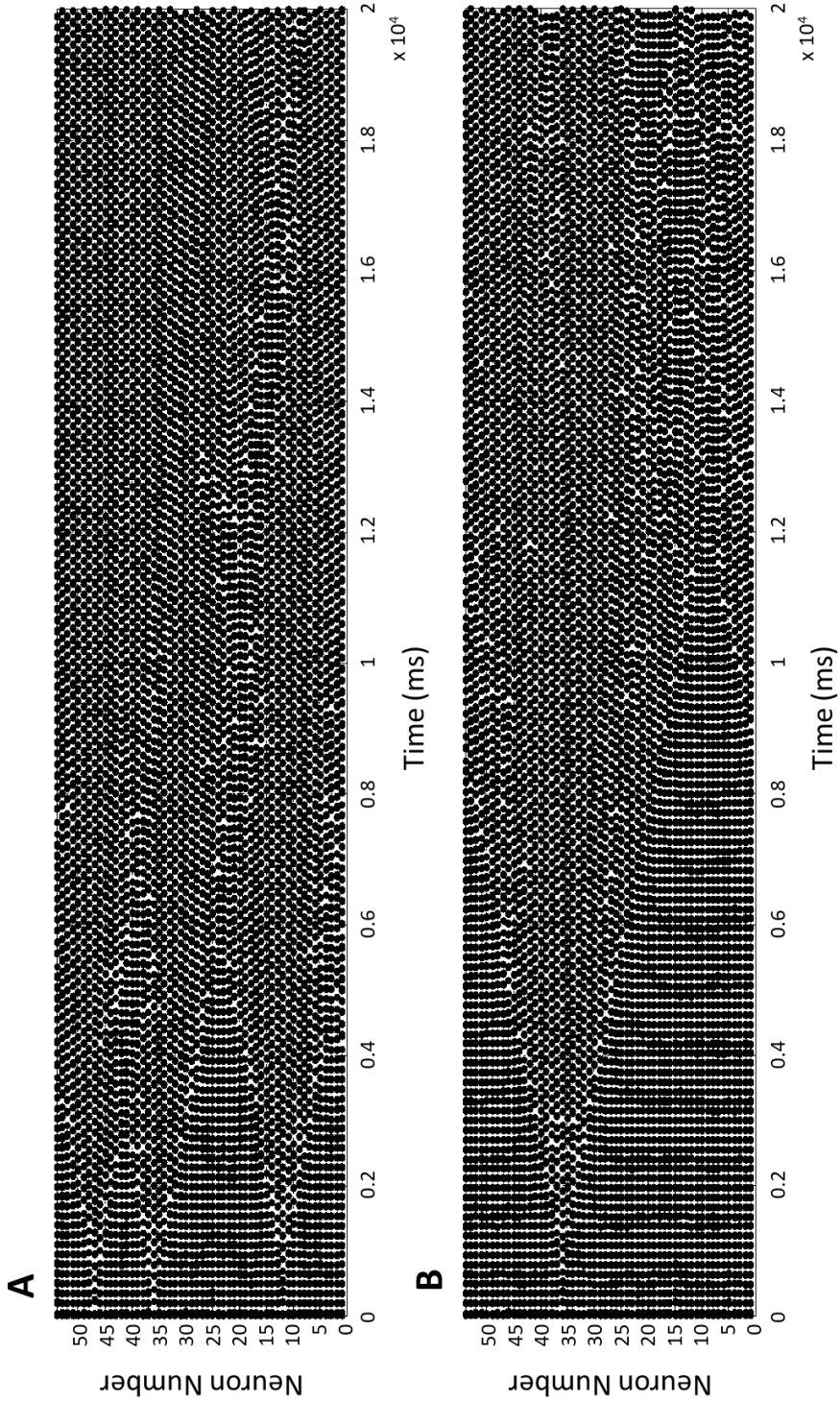

Figure 3.5 – Chimera State in Kuramoto Configuration

Raster plot for neurons in the Kuramoto coupling scheme. (A) All neurons begin in a synchronized state, with multiple desynchronized regions forming and spreading over time. Small bands of synchronized neurons are eventually snuffed out, with a single band lasting to the end of the simulation. (B) With a slightly larger coupling strength than part A, a single desynchronized region appears, widening over time. Later in the simulation, synchronized groups spontaneously reappear. Reproduced from Glaze *et al*. 2016 with permission from AIP Publishing.

Abrams and Strogatz began exploring chimera states shortly after Kuramoto *et al*.'s 2002 discovery. In their 2004 paper (Abrams & Strogatz 2004), they found both stable and unstable chimera states in the Kuramoto coupling scheme. Subsequently, they investigated chimera states using a different coupling scheme (Abrams *et al*. 2008). This coupling scheme, known as Abrams-Strogatz coupling, splits a group of identical oscillators into two equal subgroups (A and B), as shown in Figure 3.3; see the description of chemical chimeras in the work of Tinsley *et al*. (2012) above for an example of an experimental realization of Abrams-Strogatz coupling. There is coupling within and between groups, meaning a neuron in group A will feel the impact of all the neurons from group A, as well as the impact of all neurons in group B. The coupling strength within each group is stronger than the inter-group coupling, with the intra-group coupling for A and B being equal. The authors describe this system as "the simplest model that supports chimera states".

3.2.4.2. Chimera state. In Glaze (2015) and Glaze *et al*. (2016), chimera states were found for Huber-Braun neurons in both the Abrams-Strogatz and Kuramoto configurations. For the Abrams-Strogatz coupling scheme, an example chimera state is given in Figure 3.4. Figure 3.4A is a raster plot (or spike times plot) for all the neurons in the simulation. The bottom 18 neurons are group A, and the top 18 neurons are group B. The neurons in group A fire simultaneously (aside from a few occasional outliers, due to the noise in the model). Thus, group A is synchronized. The raster plot reveals that the neurons in group B fire at different times and in no discernable pattern, meaning that group B is desynchronized. These observations clearly meet the definition of a chimera state.

Figure 3.4B shows the mean field voltage, or the average activity, of each group, where the black line represents the activity of group A and the red line that of group B. The

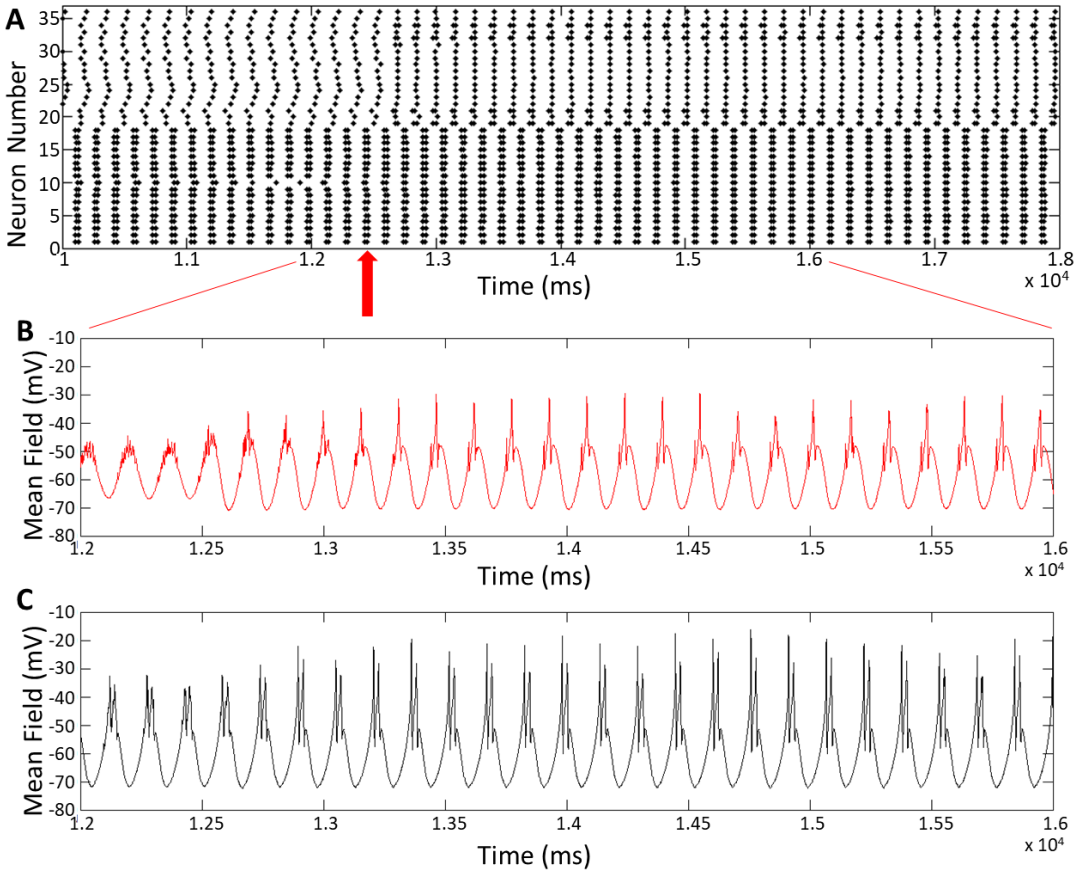

Figure 3.6 – Phase-Cluster Chimera State in Abrams-Strogatz Configuration
A phase-cluster chimera state found in the Abrams-Strogatz coupling scheme. The red arrow indicates when the intra-group coupling for B and inter-group coupling was turned on. (A) The raster plot for all neurons in the simulation reveals that group A (bottom 18 neurons) is firing synchronized double spikes, while group B (top 18 neurons) is firing synchronized single spikes. (B) Mean field voltage for group B. (C) Mean field voltage for group A. The inter-group coupling strength was about 10 times the value from Figure 3.4. Reproduced from Glaze *et al*. 2016 with permission from AIP Publishing.

voltage for group A has a high amplitude and shows double spikes, which confirms that group A is synchronized (the two dots for the double spikes on the raster plot are too close to be easily discerned by eye at the level of resolution of the figure). As for group B, the low amplitude and disordered oscillation of the mean voltage confirms that group B is

desynchronized. This chimera state occurred with weak, inhibitory coupling between groups and stronger, excitatory coupling within each group. For Abrams-Strogatz coupling, Glaze *et al*. (2016) found that chimera states occurred most often with inhibitory coupling between groups, with a few instances of chimera states occurring with excitatory coupling between groups.

A chimera state for the Kuramoto coupling scheme is shown in Figure 3.5. Unlike the Abrams-Strogatz configuration, in the Kuramoto configuration, groups of synchronized and desynchronized oscillators emerge spontaneously along the ring. This is seen in Figure 3.5A, where all the neurons are initially synchronized, and three regions of desynchronized activity emerge. The desynchronized regions spread around the ring until there are only narrow bands of synchronized neurons remaining. Some of these bands end before the simulation, while one stretches out until the end of the simulation. Note that this band of synchronized neurons travels around the ring; specifically, the middle band originally consisted of neurons around number 25, and by the end of the simulation consists of neurons around number 12. The coupling between neurons in this simulation was excitatory.

A chimera state for a slightly larger value of coupling strength is shown in Figure 3.5B. A single desynchronization region is seen to spread from one neuron. Note that other bands of synchronization emerge from the larger region of desynchronization starting around 1.4×10^4 ms.

3.2.4.3. Phase-cluster chimera state. A phase-cluster chimera state is similar to a typical chimera state in that there are two interacting groups, but different in that both groups are synchronized with different activity, such as those found by Tinsley *et al*. (2012)

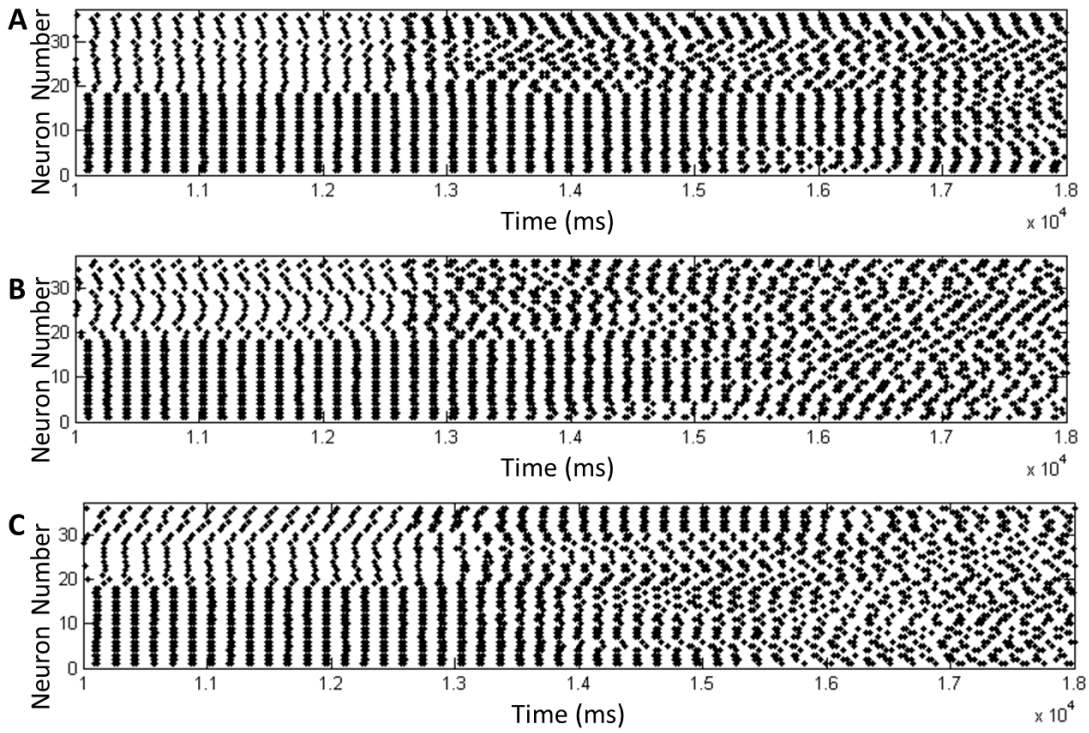

Figure 3.7 – Temporal Variation of Chimera State in Abrams-Strogatz Configuration Chimera states in a system of 36 neurons in the Abrams-Strogatz configuration with varying coupling strength between groups. (A) The phase-cluster chimera state starts with group A synchronized firing double spikes and group B synchronized firing single spikes. Over time, group B becomes desynchronized, becoming a general chimera state. Further along, group A begins losing its synchronization, until all the neurons are desynchronized by the end of the simulation. There is weak, inhibitory coupling between groups. (B) Similar to part A, the neurons go from a phase-cluster chimera state to a more traditional chimera state before dissolving into complete desynchronization. This occurs more rapidly than it did in part A. The weak, inhibitory inter-group coupling was increased slightly from part A. (C) The phase-cluster state barely begins transitioning into a chimera state before all neurons become desynchronized, occurring faster than parts A and B. The inter-group coupling here is slightly increased from part B and is double the value from part A. Reproduced from Glaze *et al*. 2016 with permission from AIP Publishing.

with their chemical chimeras (Section 3.2.2.4). An example of a phase-cluster state in the Huber-Braun model is shown in Figure 3.6. In Figure 3.6A, the bottom 16 neurons in the raster plot (group A) are synchronized and firing double spikes, while the neurons in group

B are synchronized and firing single spikes. This is also seen in the high amplitude of the mean field oscillations in Figures 3.6B and 3.6C. Note the single-spike mean field oscillations in 3.6B and the double spikes in 3.6C, consistent with the results from the raster plot.

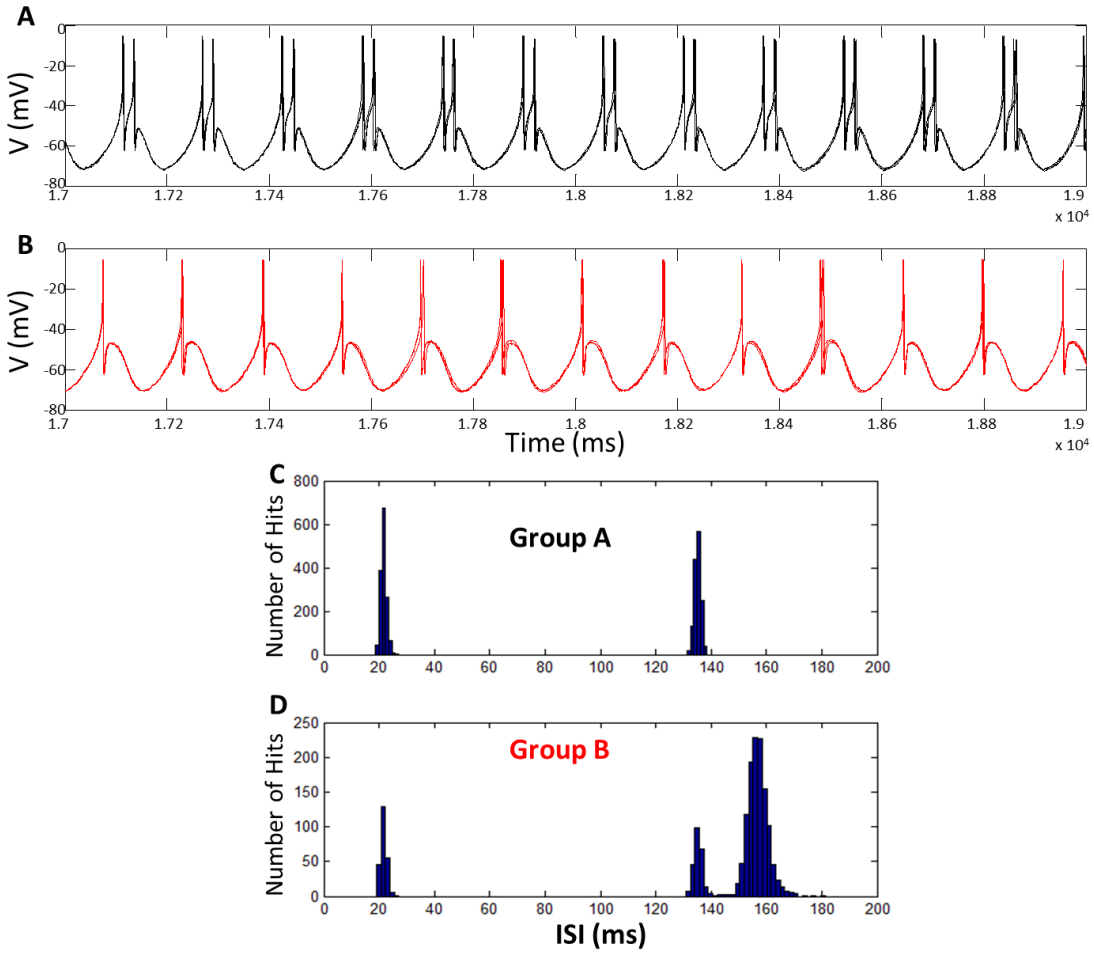

Figure 3.8 – Partial Phase-Cluster Chimera State in Abrams-Strogatz Configuration
An example of a partial phase-cluster chimera state in the Abrams-Strogatz coupling configuration. (A) The firing pattern of three neurons from group A, showing doublets. (B) The firing pattern of three neurons from group B, showing singlets. (C) ISI histogram for group A. (D) ISI Histogram for group B. Reproduced from Glaze 2015.

The chimera state, whether phase-cluster or typical chimera state, may be transient. Different parameters produce different lengths of chimera states, indicating that chimera states may have shifting stability. This is shown in Figure 3.7. There are three raster plots, all with 36 neurons and identical parameters, save for the inhibitory inter-group coupling. These panels all show transitions between phase-cluster states, chimera states, and desynchronization, consistent with the suggestion (Wolfrum & Omel'chenko 2011) that chimera states are transients.

3.2.4.4. Partial phase-cluster chimera state. A partial phase-cluster chimera state is a specific form of the phase-cluster chimera state. Rather than each group being synchronized with different activity, a few neurons of one group are synchronized with the other group. An example of this is shown in Figure 3.8. The firing patterns of three neurons from group A are shown in Figure 3.8A. It is clear that the neurons are firing double spikes, as has been seen previously. This is confirmed by the histogram in Figure 3.8C, where the inter-spike intervals (ISI) for group A are displayed. Two high peaks here mean that the neurons are firing double spikes, with the smaller ISI values corresponding to the intra-burst interval, or the time between spikes in a burst, and the larger ISI values corresponding to the time between bursts, or the inter-burst interval.

Figure 3.8B shows the firing patterns for three neurons from group B, which are firing single spikes. However, this is not representative of all neurons from group B, as Figure 3.8D can attest. The larger peak on the right corresponds to the single spike inter-spike interval, while the other two peaks, at the same ISI values as those in Figure 3.8C show that some of the neurons from group B are firing double spikes like group A. This

mixture of activity patterns in group B differentiates this partial phase-cluster chimera from a typical phase-cluster chimera.

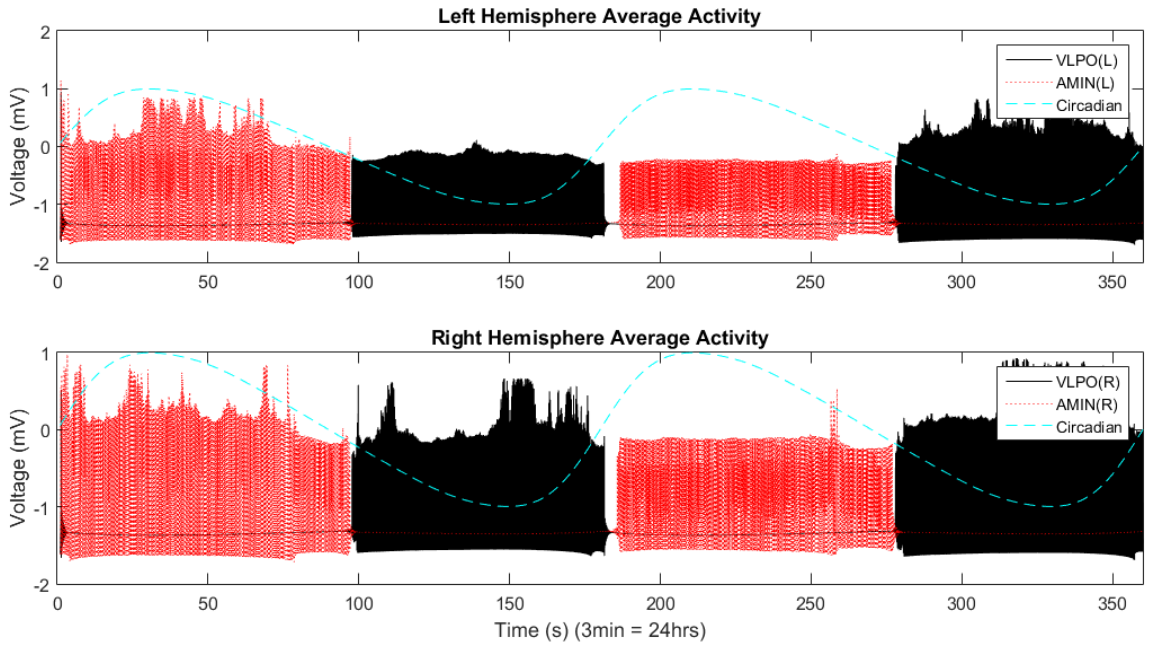

Figure 3.9 – Two-Hemisphere Activity, HR
The average activity of the left (top panel) and right (bottom panel) hemispheres of a Hindmarsh-Rose neuron run. Note how the hemispheres have different levels of activity, despite their coupling and identical connectivity. Parameters were set as $g_A = -0.0000075$, $g_{CA} = 0.00115$, $g = 0.000045$, $g_V = -0.0000425$, $g_{CV} = -0.0019$, $g_{V_{LtR}} = 0.00002$, $g_{V_{RtL}} = 0.00002$, and $I = 1.295$, with 4 neurons per region.

These three versions of the chimera state found in Glaze 2015 and Glaze *et al*. 2016 show some of the dynamic range of Huber-Braun neurons, as well as the multi-medium capabilities of the chimera state. The chimera state can be quantified using measures derived from the synchronization index and used to map the regions of parameter space for which chimera states occur (Glaze 2015, Glaze *et al*. 2016).

Unihemispheric sleep has been likened to the chimera state, with its mixture of synchronized and desynchronized activity (see Sections 1.3.2.-1.3.4. and 4.2.). Searching for UHS in the present two-hemisphere sleep model resulted in the identification of chimera states, discussed below. More specific models of unihemispheric sleep itself are discussed in Section 4.2.

3.3. RESULTS

The two-hemisphere version of the model can generate chimera states in which the two hemispheres exhibit radically different dynamical behaviors.

3.3.1. Two-Hemisphere Results. The average activity for each hemisphere is shown in Figure 3.9, for parameters identical to those in Figure 2.22 except for the input current, which is set at $I = 1.295$. Much like Figure 2.22, the wake-promoting region AMIN is only active during the daytime, while the sleep-promoting region VLPO is only active during the night. However, in Figure 3.9, each hemisphere has its own sleep-promoting and wake-promoting regions, with the left hemisphere's average activity shown in the top panel and the right hemisphere's average activity shown in the bottom panel.

Despite all the neurons having identical parameters (and random uniform distribution of initial voltages), each hemisphere exhibits variations in its level of activity. This can be clearly seen in the direct comparison between the activity of VLPO in each hemisphere over the first night. While the left hemisphere's VLPO region has relatively constant activity, remaining almost entirely beneath 0 mV, the right hemisphere's VLPO region has multiple spikes in activity that reach above 0.5 mV. This interhemispheric

asymmetry can also be seen in the different timing of spikes of AMIN activity in each hemisphere over the first day.

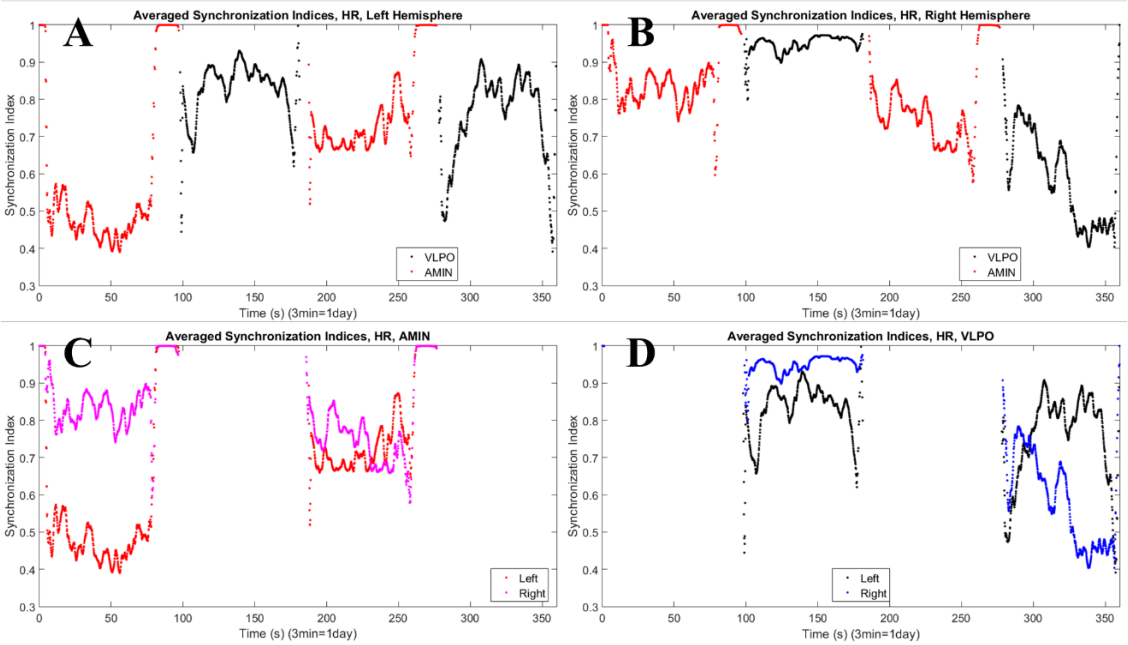

Figure 3.10 – Synchronization Indices for Non-Bursting Run, HR
Synchronization indices for each region in each hemisphere for the data displayed in Figure 3.9. (A) Synchronization indices for the VLPO and AMIN regions of the left hemisphere. (B) Synchronization indices for the VLPO and AMIN regions of the right hemisphere. (C) Synchronization indices for AMIN region from the left (red) and right (pink) hemispheres. (D) Synchronization indices for the VLPO region from the left (black) and right (blue) hemispheres. Parameters are $g_A = -0.0000075$, $g_{CA} = 0.00115$, $g = 0.000045$, $g_V = -0.0000425$, $g_{CV} = -0.0019$, $g_{V_{LtR}} = 0.00002$, $g_{V_{RtL}} = 0.00002$, and $I = 1.295$, with 4 neurons per region.

The synchronization indices for Figure 3.9 are shown in Figure 3.10. Synchronization indices for the left and right hemispheres are shown in Figures 3.10A (left hemisphere) and 3.10B (right hemisphere). As is expected from the average activity, there

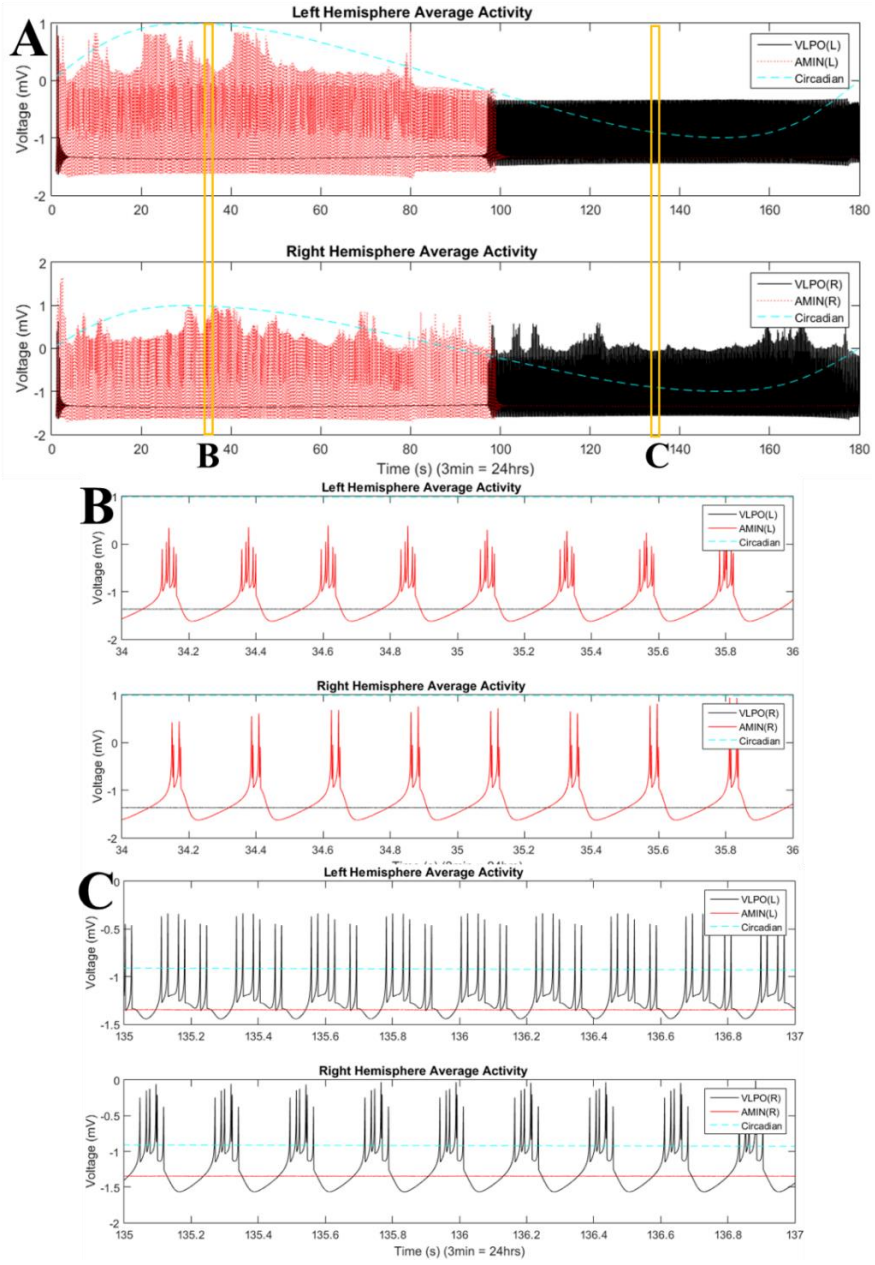

Figure 3.11 – Phase-Cluster Chimera State in Non-Bursting Regime, HR

Average activity of the two-hemisphere version of the model with HR neurons in the non-bursting regime, showing a phase-cluster chimera state. (A) Average activity of left (top panel) and right (bottom panel) hemispheres over the entire simulation. (B) Magnification of A, 34-36s. The left hemisphere AMIN is bursting in tight clusters, and the right is firing synchronized doublets. (C) Magnification of A, 135-137s. The right hemisphere VLPO shows tight, clustered firing while the left has cascading doublets. This difference in behavior is a phase-cluster chimera state. Parameters are $g_A = -0.0000075$, $g_{CA} = 0.00115$, $g = 0.000045$, $g_V = -0.0000425$, $g_{CV} = -0.0019$, $g_{V_{LtR}} = 0.00002$, $g_{V_{RtL}} = 0.00002$, and $I = 1.30$, with 3 neurons per region.

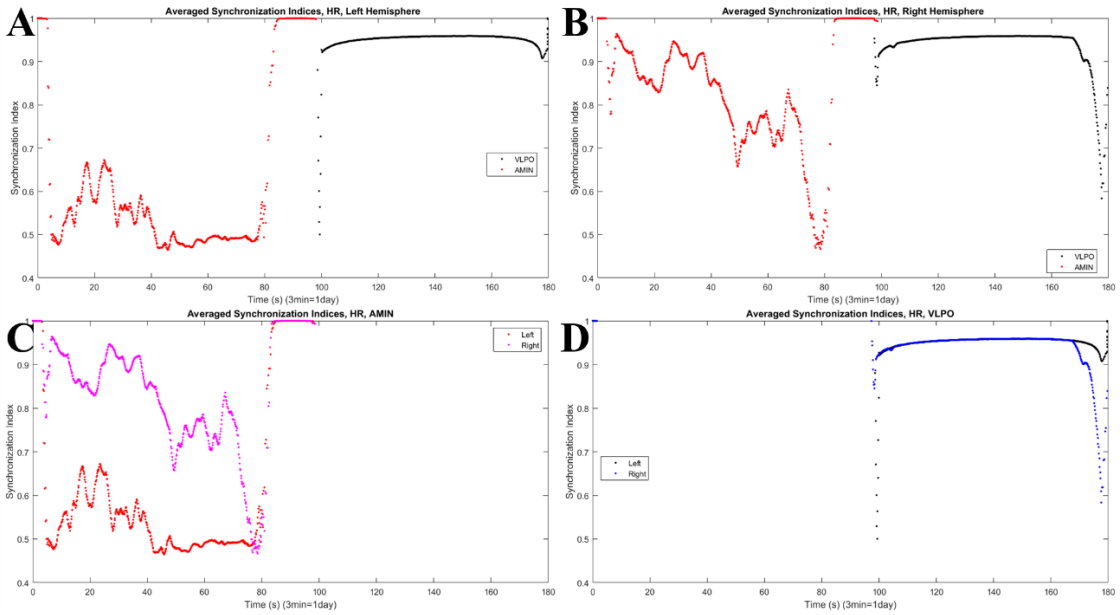

Figure 3.12 – Two-Hemisphere Non-Bursting Synchronization
Synchronization indices for each hemisphere, from data shown in Figure 3.11. (A) Left hemisphere synchronization for AMIN (red line) and VLPO (black line). (B) Right hemisphere synchronization for AMIN and VLPO. (C) AMIN regions synchronization for left (red line) and right (magenta line) hemispheres. Note the large difference between the hemispheres. This suggests a chimera state; the AMIN regions do not directly interact with each other, and therefore does not fit the classical description of a chimera state. (D) VLPO regions synchronization for left (black line) and right (blue line) hemispheres. Though showing different activity (Figure 3.11C), the VLPO regions are highly synchronized both within and with each other. Parameters were set as $g_A = -0.0000075$, $g_{CA} = 0.00115$, $g = 0.000045$, $g_V = -0.0000425$, $g_{CV} = -0.0019$, $g_{V_{LtR}} = 0.00002$, $g_{V_{RtL}} = 0.00002$, and $I = 1.30$, with 3 neurons per region.

are only indices for AMIN during the daytime, and indices for VLPO during the nighttime. Direct comparisons between AMIN and VLPO from each hemisphere are displayed in Figures 3.10C and 3.10D, respectively. In Figure 3.10C, the right hemisphere is much more synchronized than the left during the first day, while during the second day, the left hemisphere becomes more synchronized. As for the VLPO direct comparison in Figure 3.9D, the right hemisphere is more synchronized during the first night, while during the

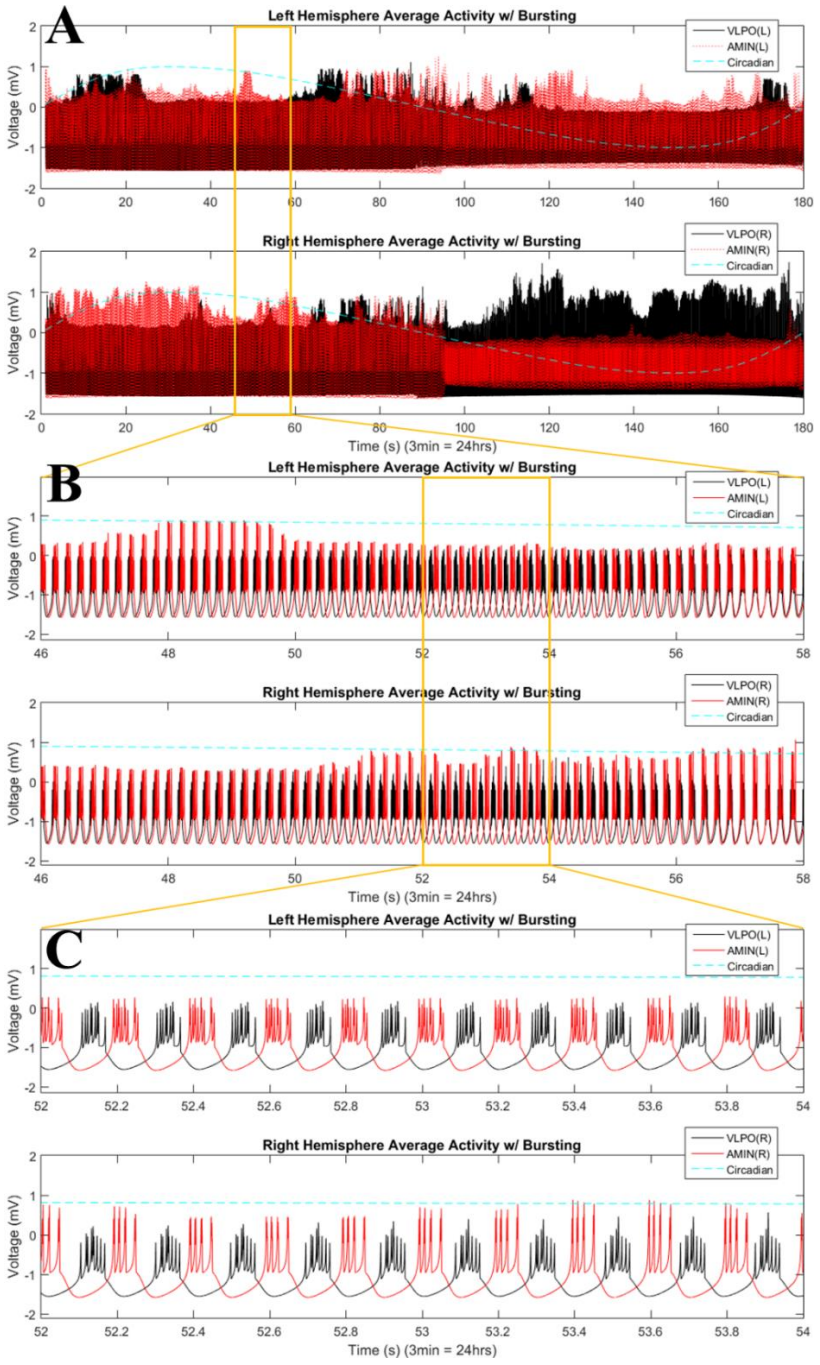

Figure 3.13 – Average Activity in Bursting Regime, HR
Average activity of the two-hemisphere version of the model with HR neurons in the bursting regime. (A) Average activity for the left (top panel) and right (bottom panel) hemispheres. (B) Magnification of A, 46-58s. VLPO and AMIN regions in each hemisphere move in and out of phase. (C) Magnification of B, 52-54s. Each region exhibits clustering behavior. Parameters are $g_A = -0.0000075$, $g_{CA} = 0.00115$, $g = 0.000045$, $g_V = -0.0000425$, $g_{CV} = -0.0019$, $g_{V_{LtR}} = 0.00002$, $g_{V_{RtL}} = 0.00002$, and $I = 2.00$, with 3 neurons per region.

second night the left hemisphere becomes more highly synchronized. This suggests that this gap may indicate some specific behavior, as having different synchronization in two coupled groups may indicate a chimera state, or the possibility of unihemispheric sleep (to be discussed in Section 4.2.).

3.3.2. Non-Bursting. The average activity of the VLPO and AMIN for $I = 1.30$ is shown in Figure 3.11A. Each hemisphere exhibits variances in behavior, creating some interhemispheric asymmetries; this is most clear for the VLPO region at night. The left hemisphere's VLPO (top panel) displays constant, even firing over the entire time it is active, unlike the right hemisphere (bottom panel), whose VLPO firing has more variability, like the AMIN regions.

Magnification of the average activity for each region is shown in Figures 3.11B and 3.11C. In Figure 3.11B, the left hemisphere AMIN exhibits tight clusters of multi-spike burst-firing, while the right hemisphere shows double spikes, indicating that all the neurons are firing at the same time, and all firing doublets. This difference in behavior between coupled identical groups is a phase-cluster chimera state. In Figure 3.11C, VLPO exhibits a similar phase-cluster chimera state, with tight, clustered firing in the right hemisphere, and nearly evenly-spaced cascades of spike pairs in the left hemisphere.

The identification of chimera states is further confirmed by examination of the corresponding synchronization indices, displayed in Figure 3.12. The left and right hemispheres' synchronization indices are given in Figures 3.12A and 3.12B, respectively. The AMIN synchronization is clearly significantly different between the two hemispheres, as shown in Figure 3.12C. this suggests a chimera state; however, since the AMIN regions do not directly interact with each other, their interactions do not fit the canonical

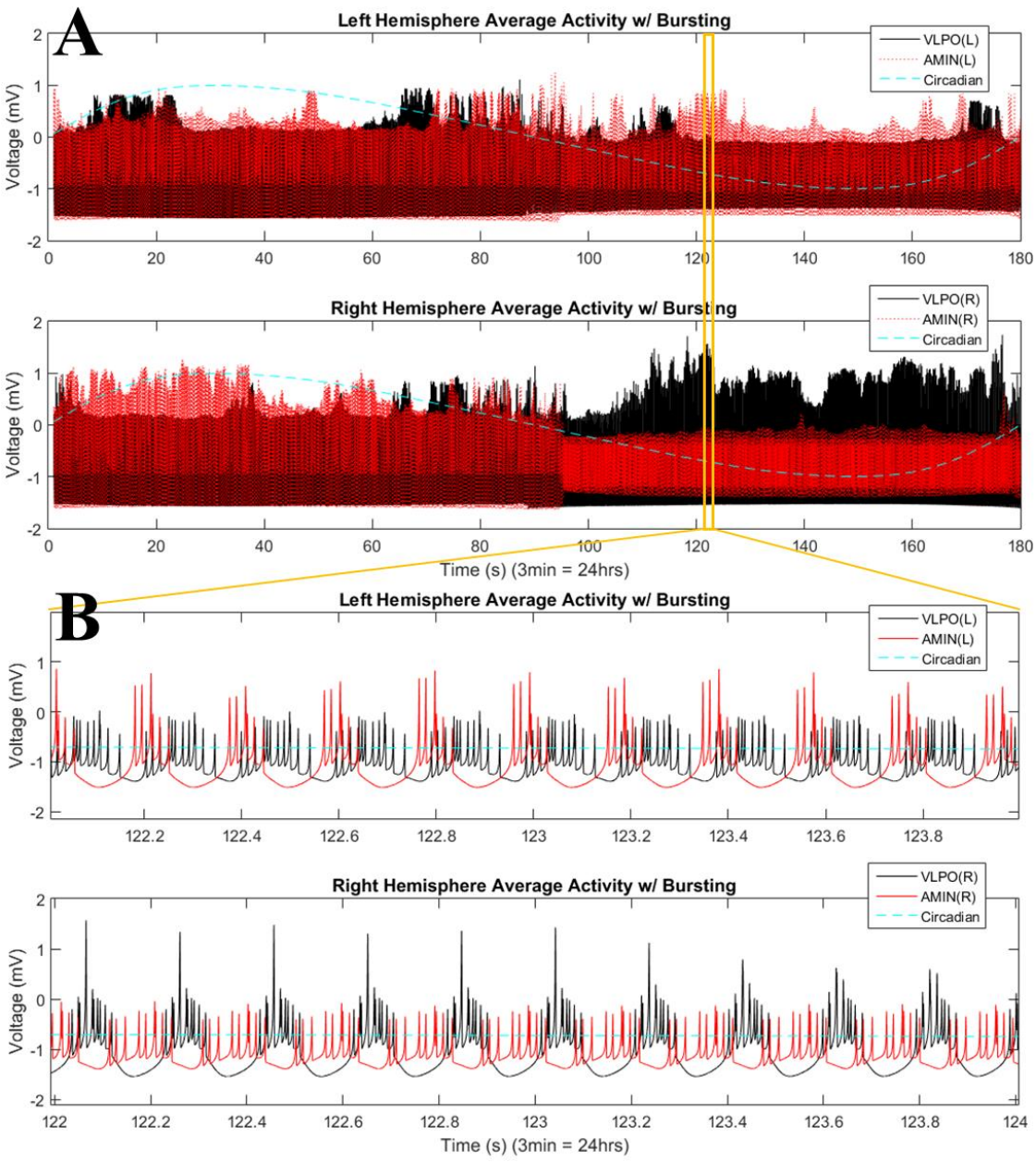

Figure 3.14 – Phase-Cluster Chimera State in Bursting Regime, HR
Average activity of the two-hemisphere version of the model with HR neurons in the bursting regime, showing a phase-cluster chimera state. Uses the same data as Figure 3.13. (A) Average activity for the left (top panel) and right (bottom panel) hemispheres. (B) Magnification of A, 122-124s. Parameters are $g_A = -0.0000075$, $g_{CA} = 0.00115$, $g = 0.000045$, $g_V = -0.0000425$, $g_{CV} = -0.0019$, $g_{V_{LtR}} = 0.00002$, $g_{V_{RtL}} = 0.00002$, and $I = 2.00$, with 3 neurons per region.

description of Kuramoto or Abrams-Strogatz coupling. The VLPO regions, though exhibiting different dynamical behaviors in Figure 3.11C, reveal themselves to be similarly highly synchronized (Figure 3.12D).

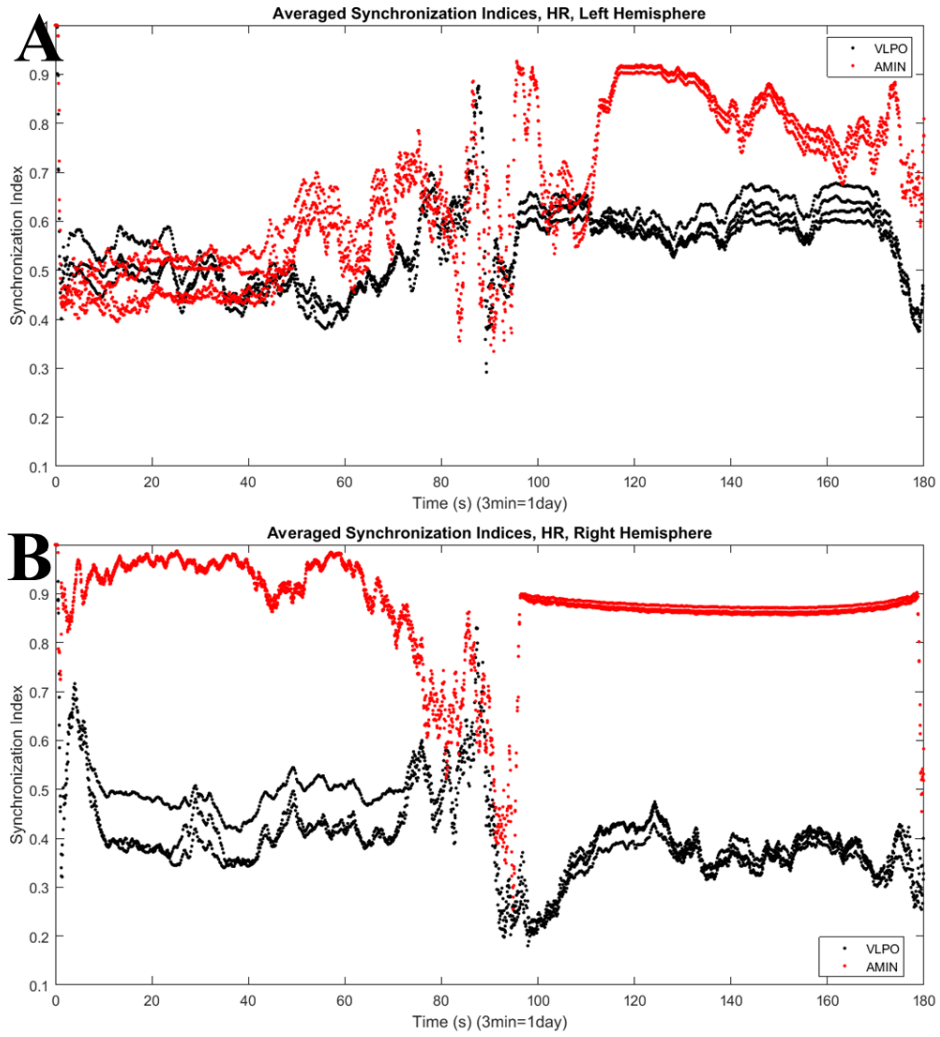

Figure 3.15 – Two-Hemisphere Bursting Synchronization
Synchronization indices for each hemisphere, from data shown in Figure 3.13. (A) Left hemisphere synchronization for AMIN (red line) and VLPO (black line). (B) Right hemisphere synchronization for AMIN and VLPO. Parameters are $g_A = -0.0000075$, $g_{CA} = 0.00115$, $g = 0.000045$, $g_V = -0.0000425$, $g_{CV} = -0.0019$, $g_{V_{LtR}} = 0.00002$, $g_{V_{RtL}} = 0.00002$, and $I = 2.00$, with 3 neurons per region.

3.3.3. Bursting. Moving into the bursting regime, with $I = 2.00$, the neurons of all regions fire over the entire day, as seen in Figure 3.13A. Interhemispheric asymmetry is immediately apparent, in the morning (AMIN more active in the right hemisphere and VLPO in the left) and at night (VLPO more active in the right hemisphere and AMIN in the left). Zooming in on the daytime activity (46 to 58 s), it is clear that the regions within each hemisphere are moving in and out of phase (Figure 3.13B). Zooming in further (from 52 to 54 s), each region exhibits the same clustering behavior, though the right hemisphere AMIN has a slightly higher amplitude than the left (Figure 3.13C).

Figure 3.14B shows the average activity from Figure 3.13A (shown again as Figure 3.14A) at a different time of day (from 122 to 124 s). The behavior displayed here is significantly different, with tight, clustered firing for AMIN in the left and VLPO in the right hemisphere, and a cascading firing pattern for VLPO in the left and AMIN in the right hemisphere. This different behavior for both regions across hemispheres is evidence of a phase-cluster chimera state. The synchronization indices (Figure 3.15) confirm this, showing significantly different levels of synchronization in the left and right hemispheres. The VLPO synchronization indices for the left hemisphere change from three to four lines, indicating that neurons change from firing triple spikes during the day to quadruple spikes at night; the transition to quadruplets is less evident for the right hemisphere. The AMIN synchronization index values are higher and more stable for the right hemisphere.

Note that the VLPO regions have similar synchronization during the day, but the left hemisphere VLPO is significantly more synchronized at night. This implies that the VLPO regions, which can be classified as exhibiting a phase-cluster chimera state based

on the bursting state differences shown in Figure 3.14B, could also be described as exhibiting a classical dynamical chimera state at night.

3.4. CONCLUSIONS

The two-hemisphere version of the sleep model presented here demonstrates clear evidence of chimera states. This can be seen in the gap in synchronization between the VLPO region in the left and right hemispheres, as seen in Figure 3.10D and Figure 3.15. This gap varies in magnitude, not only dependent upon the input current I, but also over the course of a single night in one simulation. It remains to be determined whether the observed chimera states are ever stable rather than transient. In other cases, such as those shown in Figures 3.11, 3.13 and 3.14, the interhemispheric differences in dynamical behavior indicate phase-cluster chimeras.

The observation of chimera states can serve as a schematic model for UHS, as mentioned earlier, due to their shared characteristic of mixed synchronized and desynchronized behavior. The difference in synchronization of VLPO for each hemisphere shows a definitive chimera state (Figures 3.10D and 3.15) but might also be interpreted as either UHS or asymmetric sleep. Asymmetric sleep, as discussed in Section 1.3.1.2., is a state where both hemispheres of the brain are asleep, but one more deeply than the other (and hence presumably more synchronized). This can occur in humans, unlike UHS, where one hemisphere is awake and desynchronized and the other is asleep and synchronized. While these two sleep states will both display a synchronization difference between hemispheres, asymmetric sleep requires both hemispheres to be in a sleep state, and UHS obviously requires one hemisphere to be in a wake state while the other is in a sleep state.

Since this model can generate chimera states, it is reasonable to ask whether it may also generate asymmetric sleep and UHS.

The “first night effect”, discussed in Section 1.3.1.2., is a form of asymmetric sleep in humans, and occurs when sleeping for the first time in a novel environment. Travel itself also has an impact on sleep, usually in the form of jet lag. In the next section, jet lag, asymmetric sleep, and UHS are simulated in the sleep model.

4. JETLAG AND UNIHEMISPHERIC SLEEP

Here, the effect of changes in the circadian drive, or jet lag, is discussed, along with simulations of unihemispheric sleep (UHS).

4.1. JET LAG

Jet lag is a syndrome caused by desynchronization between the body's circadian rhythm and the rhythm of light in a locale, typically due to long flights that cross multiple time zones (Herxheimer 2014). Also known as Jet Lag Disorder (JLD, Section 1.5.4.2.), its symptoms include difficulty sleeping and fatigue, among others, such as the side effects associated with both sleep deprivation (Section 1.4.) and travel fatigue. Jet lag qualifies as a form of partial sleep deprivation, or sleep restriction, where sleep duration is shortened (Banks & Dinges 2007). Another type of jet lag, or "social jet lag", is caused by a combination of artificial lights disrupting natural circadian rhythms and social constraints that require early rising, such as work and school (Skeldon *et al*. 2017).

To simulate jet lag, the circadian drive is altered in four different ways, and its impact on the synchronization of each region investigated using Hindmarsh-Rose (HR) neurons. The one-hemisphere version of the model was used here. For all runs, the parameters were set at $g_A = -0.0000075$, $g_{CA} = 0.00115$, $g = 0.000045$, $g_V = -0.0000425$, $g_{CV} = -0.0019$, and $I = 2.00$, with 3 neurons per region.

4.1.1. Period of Constant CD. A period of constant circadian drive (CD) amplitude was inserted in the first day of two-day runs to interrupt the normal periodicity of the circadian drive.

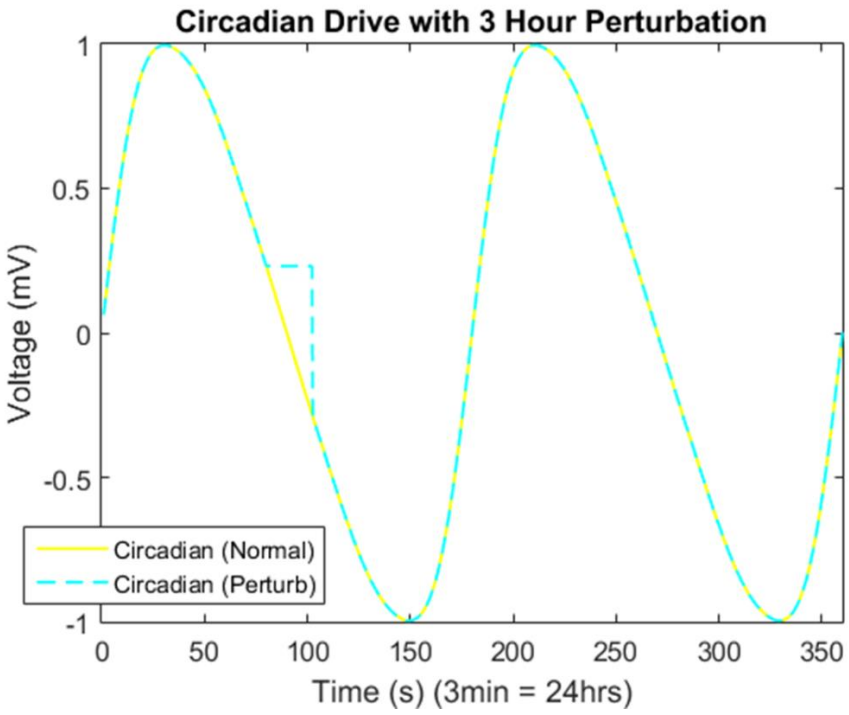

Figure 4.1 – Circadian Drive with Perturbation
An example of a circadian drive with (dashed light blue line) and without (yellow line) a 3-hour perturbation. Note that after the perturbation ends, the circadian drive returns to the value it would have had without the perturbation.

4.1.1.1. Perturbation. Here, a period of constant CD is used to cause a perturbation. At a set time of day, the circadian drive is held at its current value for a set duration. At the end of the perturbation, the value of CD jumps to the value it would be if it had not been perturbed. An example of such a perturbation is shown in Figure 4.1 and would be roughly equivalent to staying in a room with a constant light level for a set number of hours before exiting outside, where the light entrainment (the value of CD) had continued changing. In other words, like a grad student studying all evening in their room, emerging to find it is not night but early morning. Basically, the circadian drive is perturbed and afterward returns to its proper value for the time of day. Multiple simulations were

performed in the one-hemisphere version of the model for 1, 3, 6, and 9-hour perturbations occurring at 600, 1100, 1600, and 2100 hours (corresponding to 6 A.M., 11 A.M., 4 P.M., and 9 P.M.) on the first day of two-day runs.

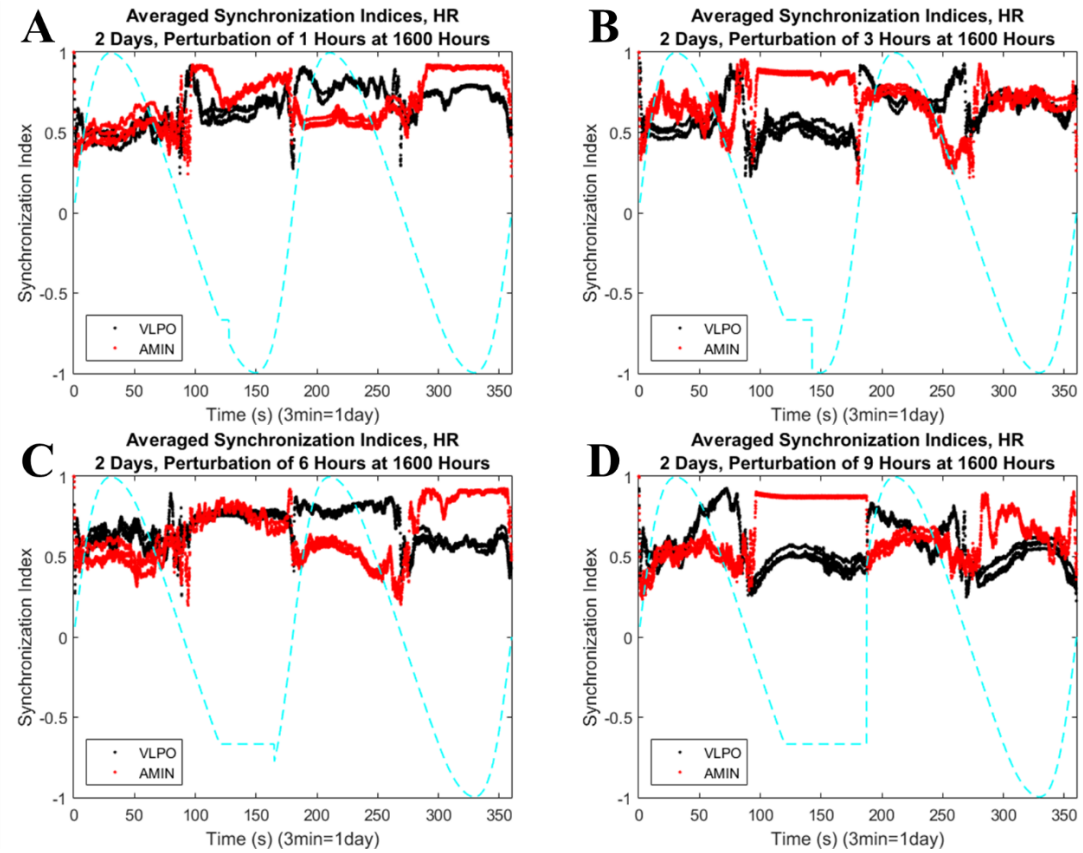

Figure 4.2 – Circadian Drive with Perturbations at 1600 Hours
Synchronization indices of AMIN and VLPO after different lengths of circadian perturbation at 1600 hours. (A) 1-hour. The small perturbation had neither a large nor a lasting impact. (B) 3-hour. The perturbation heavily impacted the second day, obscuring the reciprocal relationship of synchronization in AMIN and VLPO. (C) 6-hour. The synchronization indices for each region are pushed together during the perturbation, but the reciprocal relationship is clear immediately after. (D) 9-hour. The AMIN and VLPO synchronization relationship during the perturbation is the usual for nighttime but departs from the typical behavior following the removal of the perturbation.

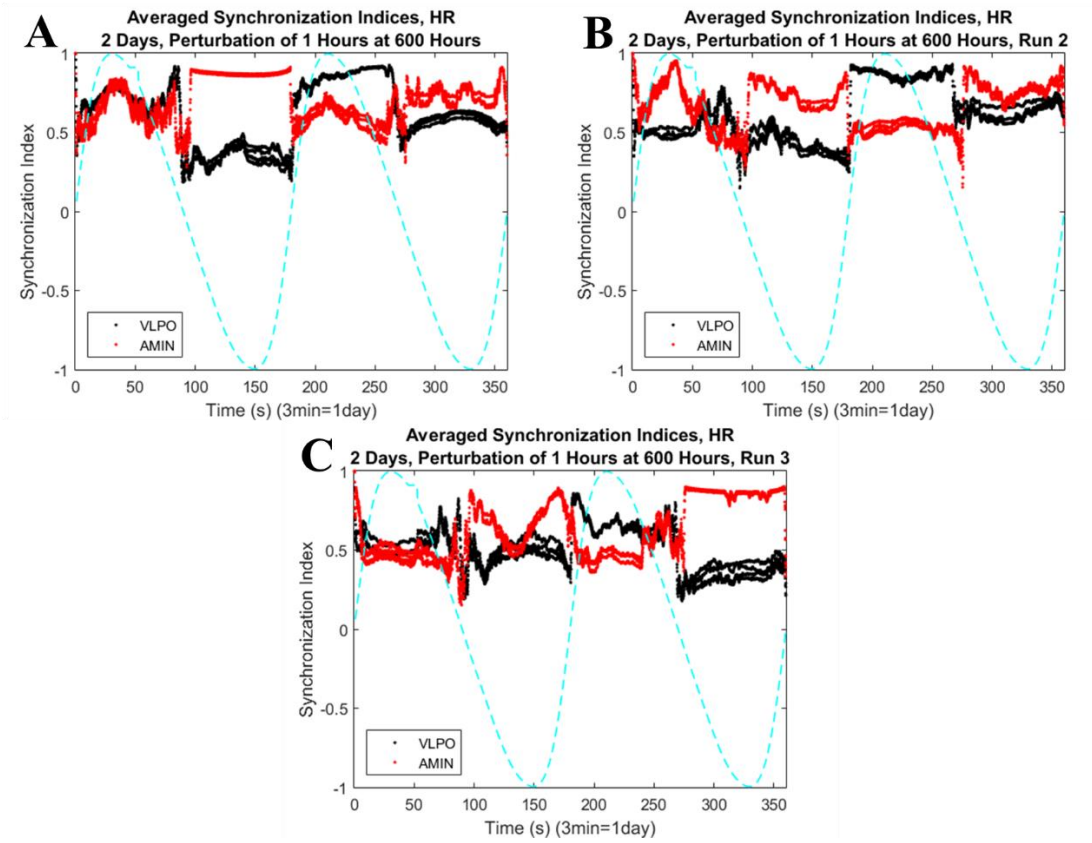

Figure 4.3 – Circadian Perturbation, 1 Hour at 600 Hours
Synchronization indices for AMIN and VLPO after circadian perturbation of 1 hour at 600 hours, 3 runs. (A) Run 1. A small perturbation causes minimal change in synchronization with respect to the control conditions shown in Figure 2.36. (B) Run 2. Like run 1, little to no change in synchronization. (C) Run 3. The reciprocal synchronization relationship between the AMIN and VLPO regions is preserved.

The synchronization indices for parameters used here (Section 4.1.) were previously shown, without any circadian drive perturbation, in Figure 2.36, with 4 neurons per region. In that figure, the activity of AMIN and VLPO neural groups display a reciprocal relationship, discussed in more detail in Section 2.3.3.2., that will be considered the control behavior against which to compare the jet lag results presented below. Specifically, in this control case, when AMIN exhibits high synchronization and VLPO

has low synchronization, the system is asleep, and when VLPO has high synchronization and AMIN low synchronization, the system is awake.

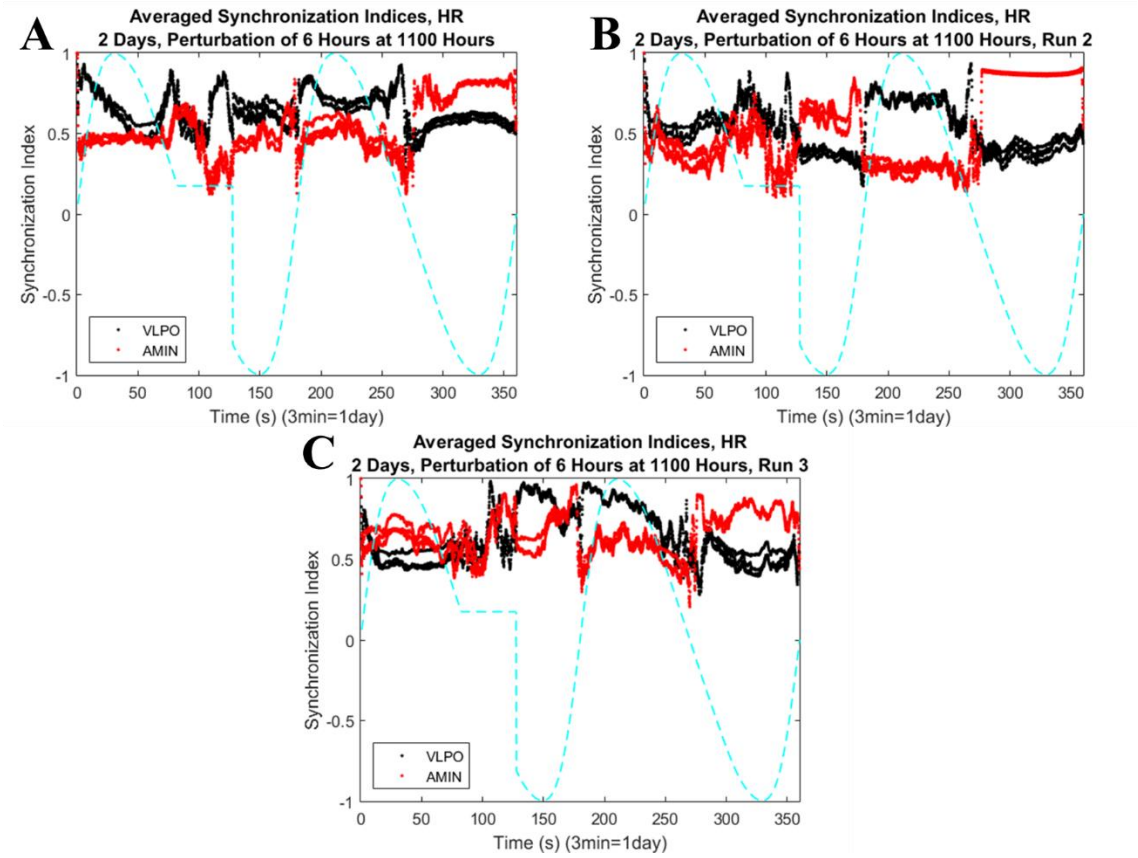

Figure 4.4 – Circadian Perturbation, 6 Hours at 1100 Hours
Synchronization indices for AMIN and VLPO after circadian perturbation of 6 hours at 1100 hours, 3 runs. (A) Run 1. After the perturbation, the system remains awake almost all night before returning to the reciprocal relationship. (B) Run 2. The system settles into its reciprocal behavior immediately after the perturbation. (C) Run 3. This run exhibits similar behavior to run 1, but with more oscillations and irregularities.

The length of the perturbation differently impacts the synchronization of both regions, as seen in Figure 4.2. A small perturbation of 1 hour at 1600 hours has little effect,

as Figure 4.2A shows the reciprocal synchronization pattern seen previously for HR neurons when I = 2.00 (Figure 2.36). This relationship begins to break down with a larger perturbation, as seen in Figures 4.2B and 4.2D (3-hour and 9-hour perturbations, respectively). A perturbation of 6 hours had little effect. It could be hypothesized that this

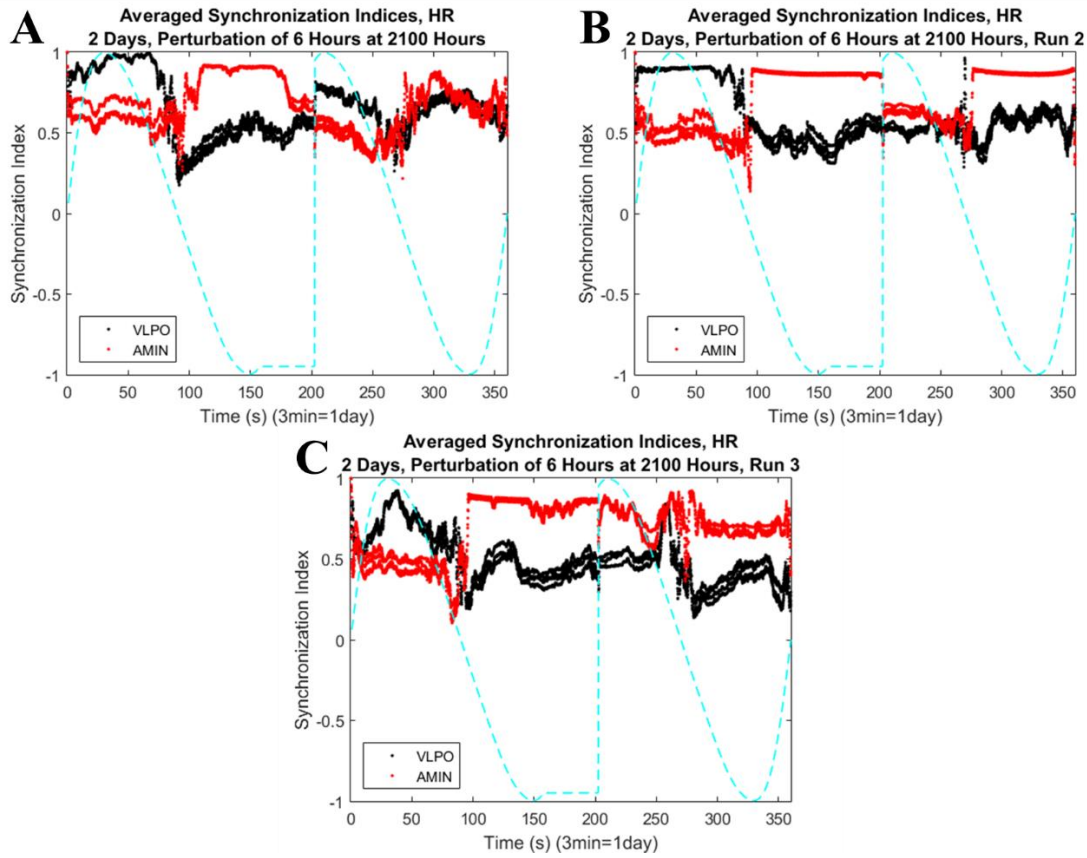

Figure 4.5 – Circadian Perturbation, 6 Hours at 2100 Hours
Synchronization indices for AMIN and VLPO after circadian perturbation of 6 hours at 2100 hours, 3 runs. (A) Run 1. In this run, the reciprocal behavior returns after the perturbation, but fails to properly switch states the second night. (B) Run 2. Here, during and after the perturbation, the system remains asleep, unable to change states the second day. (C) Run 3. Like run 2, the system is unable to switch from sleep to wake. Though the system attempts to shift to waking at the end of day two, it is foiled by the advancing of night.

perturbation length promotes the system, settling into AMIN and VLPO's reciprocal relationship, which may be easier to do during a period of constant CD rather than during CD's continuous change. This hypothesis is consistent with two of the three runs for a 6-hour perturbation at 1600 hours (data not shown), though further experiments will needed to determine whether there is in fact such a causal connection.

To investigate the variability of the perturbation effect, simulations were performed in triplicate for each combination of perturbation conditions. In some cases, the perturbation does not greatly impact the simulation, as seen in Figure 4.3. A perturbation of one hour at 600 hours has minimal impact, as might be expected. Run 1 and run 2 (Figures 4.3A and 4.3B, respectively) each exhibit HR's distinct reciprocal relationship (for $I = 2.00$), while run 3 (Figure 4.3C) demonstrates some irregularities, such as the dip in AMIN's synchronization in the middle of the first night.

Variation between runs can be seen in Figure 4.4, which shows a 6-hour delay at 1100 hours. This perturbation could be considered equivalent to a subject staying up past their usual bedtime; either they fall asleep easily and settle right back into their sleep/wake rhythm (run 2), or they have difficulty falling asleep, which is reflected in the jagged synchronization the next day (runs 1 and 3).

Perturbations of 6 hours occurring at 2100 hours have another significant effect on the synchronization of regions in the model, as seen in Figure 4.5. This may be likened to sleeping in a bit (run 1) or sleeping in very late, waking up for a few hours, then going back to bed (runs 2 and 3, which I have done after particularly exhausting days).

4.1.1.2. Delay. In this section, a period of constant circadian drive amplitude was inserted in the first day of two-day runs to create a delay in the normal periodicity of the

circadian drive. At the specified time of day, the value of CD was held constant at its current value for the chosen duration. After the delay, CD continued its normal course from the delay value. An example of this delay is given in Figure 4.6. This case is roughly equivalent to a subject boarding a flight, traveling for a set number of hours (at a constant

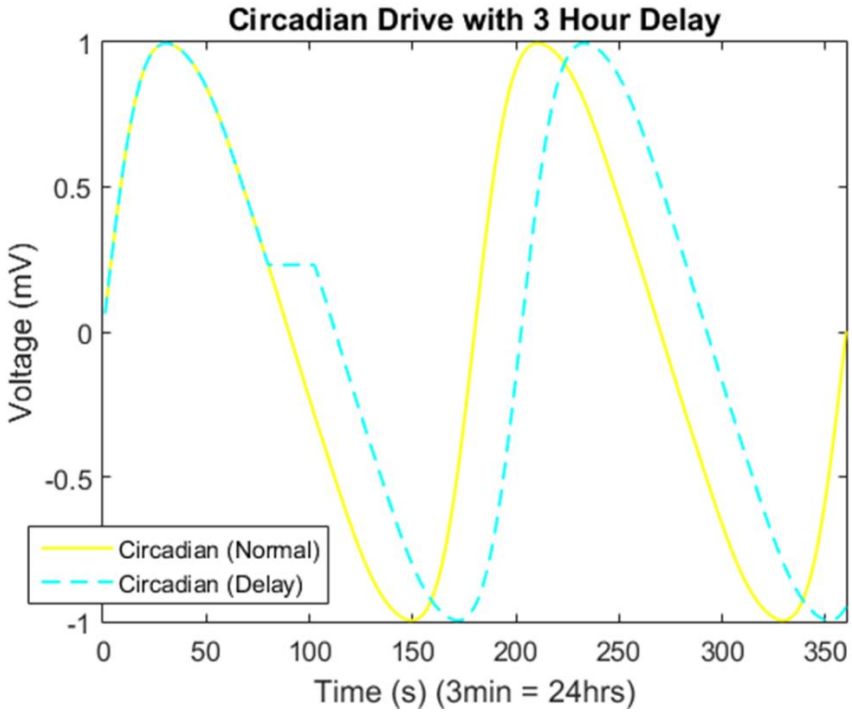

Figure 4.6 – Circadian Drive with Delay
An example of a circadian drive with (dashed light blue line) and without (yellow line) a 3-hour delay. This delay "pauses" the circadian drive.

light value, or constant CD), and landing at a location that has the same light entrainment (or value of CD) as the place they had left, at the time they had left. Essentially, this acts like a pause in the circadian drive. Multiple simulations were performed in the one-

hemisphere version of the model for a 1, 3, 6, and 9-hour delay occurring at 600, 1100, 1600, and 2100 hours (corresponding to 6 A.M., 11 A.M., 4 P.M., and 9 P.M.) on the first day of two-day runs.

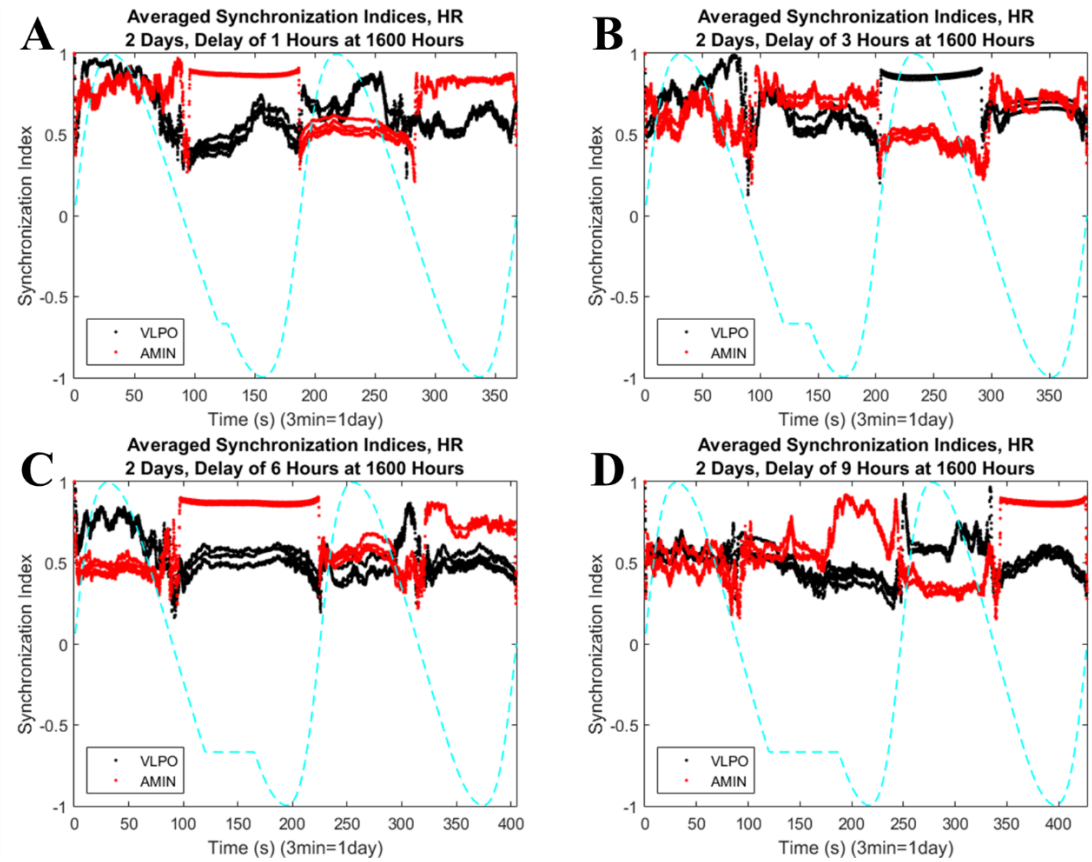

Figure 4.7 – Circadian Drive with Delays at 1600 Hours
Synchronization indices of AMIN and VLPO after different lengths of circadian delay at 1600 hours. (A) 1-Hour. The reciprocal synchronization relationship between the two regions remains intact, with a brief overlapping during day two. (B) 3-Hour. Though there is increased overlap between the synchronization indices of the different regions, the increase and decease in synchronization for each region is still present, along with the reciprocal relationship. (C) 6-Hour. The system's ability to shift states is disrupted, causing a sleep state for most of day two. (D) 9-Hour. During the delay, the system settles into the reciprocal synchronization relationship of VLPO and AMIN.

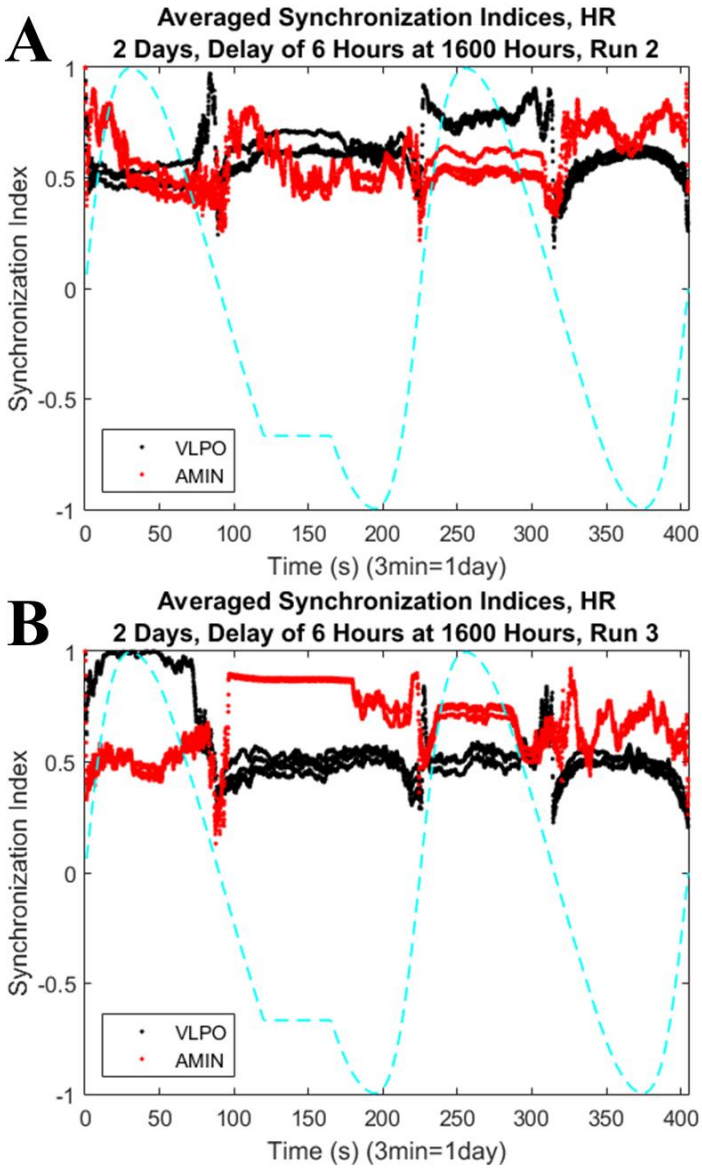

Figure 4.8 – Circadian Delay, 6 Hours at 1600 Hours
Synchronization indices for AMIN and VLPO after circadian delay of 6 hours at 1600 hours, 3 runs. Run 1 was displayed as Figure 4.7C. (A) Run 2. During the delay, the system switches to wakefulness when it would normally be asleep, which persists until the next night. (B) Run 3. After the delay, the system is unable to wake, remaining in the sleep state for the rest of the simulation.

Despite the fact that the circadian delay and the perturbation discussed above both have intervals of constant CD, the delay has a less disruptive impact on the synchronization

of the AMIN and VLPO regions than the perturbation shown in Figures 4.1 to 4.5. This can be seen in Figure 4.7, which shows delays of various lengths at 1600 hours. This situation could be considered roughly analogous for an increased amount of sleep, with a subsequent forward shift in bedtime and wake time.

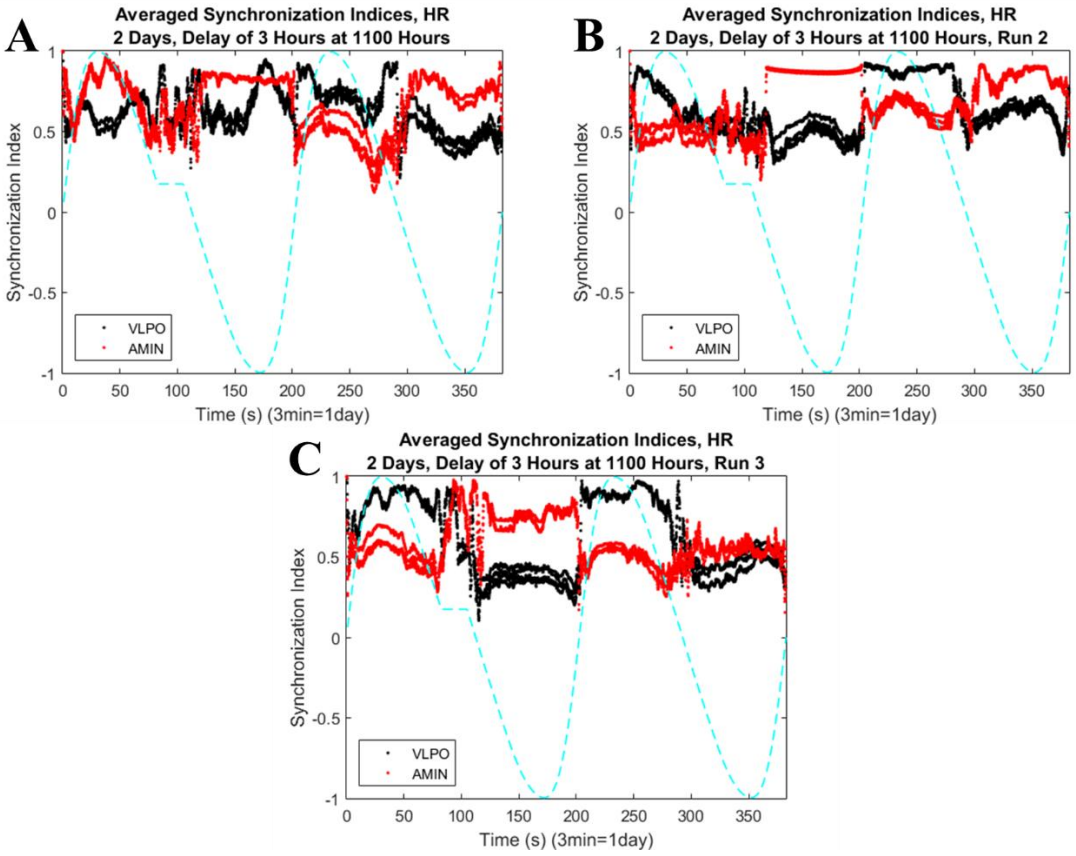

Figure 4.9 – Circadian Delay, 3 Hours at 1100 Hours
Synchronization indices for AMIN and VLPO after circadian delay of 3 hours at 1100 hours, 3 runs. (A) Run 1. Immediately after the delay, the system settled into the usual reciprocal behavior, with a brief wake period in night one. (B) Run 2. No detrimental impact from the delay is discernable. (C) Run 3. The delay does not impact the model immediately but may be the cause of the overlap in night two.

Two more runs for the 6-hour delay at 1600 hours are displayed in Figure 4.8. Like the first run, run 2 (Figure 4.8A) is unable to properly switch states, particularly after the delay, where the system is awake when it should be asleep. This is particularly visible in Figure 4.8B, which shows a perpetual sleep state after the circadian delay. Disruptions in state switching only occurred in one run of the 3-hour delay at 1600 hours and was not present in any of the other delay runs at this time of day (data not shown).

A 3-hour circadian delay applied at 1100 hours has minimal effect, as seen in Figure 4.9. Each run clearly shows the familiar reciprocal relationship, though with some irregularities. The delay appears to correlate with maintenance of the reciprocal behavior. This may be an indication that a longer simulation time with a less compressed time scale will stabilize the model, giving it more opportunity to settle in each state before switching. Future work quantifying the length of time needed to settle into a given state, and comparison of settling times between perturbed and unperturbed states will allow a rigorous determination of whether the perturbation has a significant effect on this process.

Interestingly, a delay of 9 hours at 2100 hours (Figure 4.10) does not have a substantial disturbing force on the model. A delay of this length at this late time of day may be construed as an extra-long night, or extra hours of sleep, which have little negative effect on the system.

4.1.2. Phase-Shifted CD. Here, the circadian drive is phase-shifted forward or backward during the first day of two-day runs, shifting the entire skewed sine wave. This skips (forward shift) or repeats (backward shift) a segment of the circadian drive, then continues as normal.

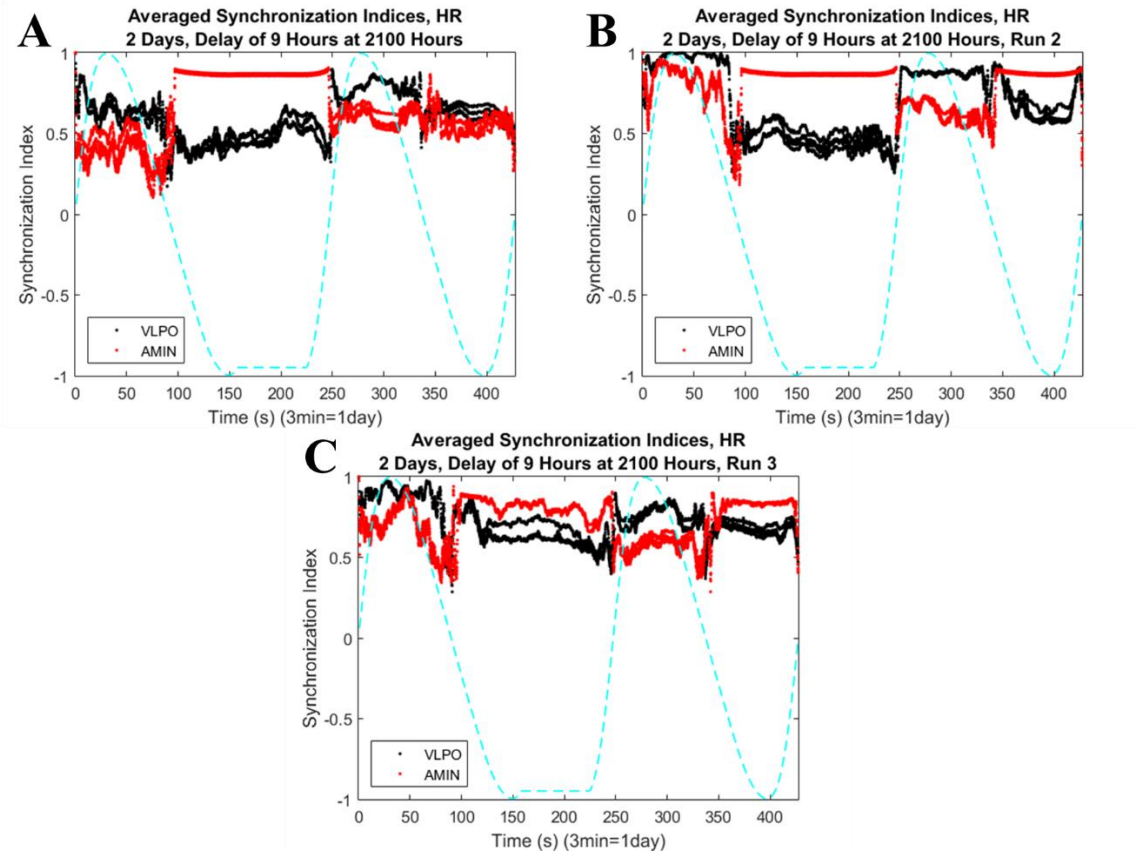

Figure 4.10 – Circadian Delay, 9 Hours at 2100 Hours
Synchronization indices for AMIN and VLPO after circadian delay of 9 hours at 2100 hours, 3 runs. (A) Run 1. The delay did not affect the system immediately, but note the synchronization overlap in night two. (B) Run 2. No impact from the delay is discernable. (C) Run 3. Note the distinct but narrow gap between the regions' synchronization indices.

4.1.2.1. Backward phase shift. To phase shift the circadian drive, a time of day was chosen, and the value of CD shifted back a set number of hours, then allowed to continue as normal (Figure 4.11). A backward phase shift of one hour at 2 A.M. can be likened to the end of daylight-saving time (DST) in the autumn; the clock is shifted backward one hour. A longer shift, or a shift occurring at a different time of day, would be equivalent to instantly traveling from one time zone to another further West.

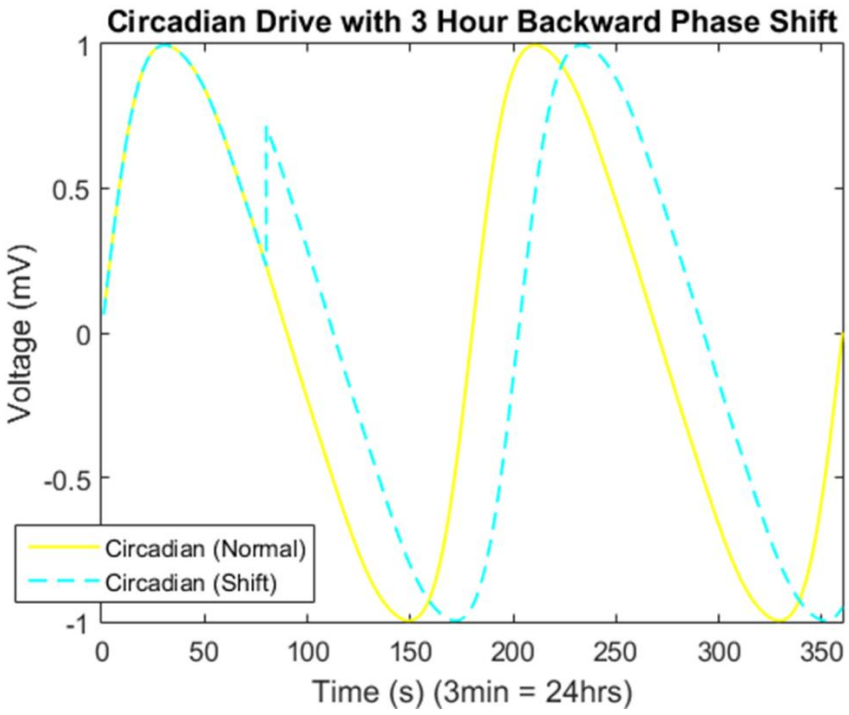

Figure 4.11 – Circadian Drive with Backward Phase Shift
An example of a circadian drive with (dashed light blue line) and without (yellow line) a 3-hour backward phase shift. This sets the clock backward three hours.

Multiple simulations were performed in the one-hemisphere version of the model for a 1, 3, 6, and 9-hour backward phase shift occurring at 200, 600, 1100, 1600, and 2100 hours (corresponding to 2 A.M., 6 A.M., 11 A.M., 4 P.M., and 9 P.M.) on the first day of two-day runs. Phase shifts that would revert to a time before 12 A.M. of day one were not performed (for example, 3-hour backward phase shift at 2 A.M.).

A backwards phase shift of 1 hour at 200 hours simulates the “fall back”, or end of DST in the autumn, shown in Figure 4.12. These results can be likened to the various reactions to the end of DST, such as no effect (run 2), a rough time adjusting during the

day but easy nights (run 1), or a person's sleep-wake schedule being absolutely shredded and unable to recover for a several days (run 3). This last case may happen to people who

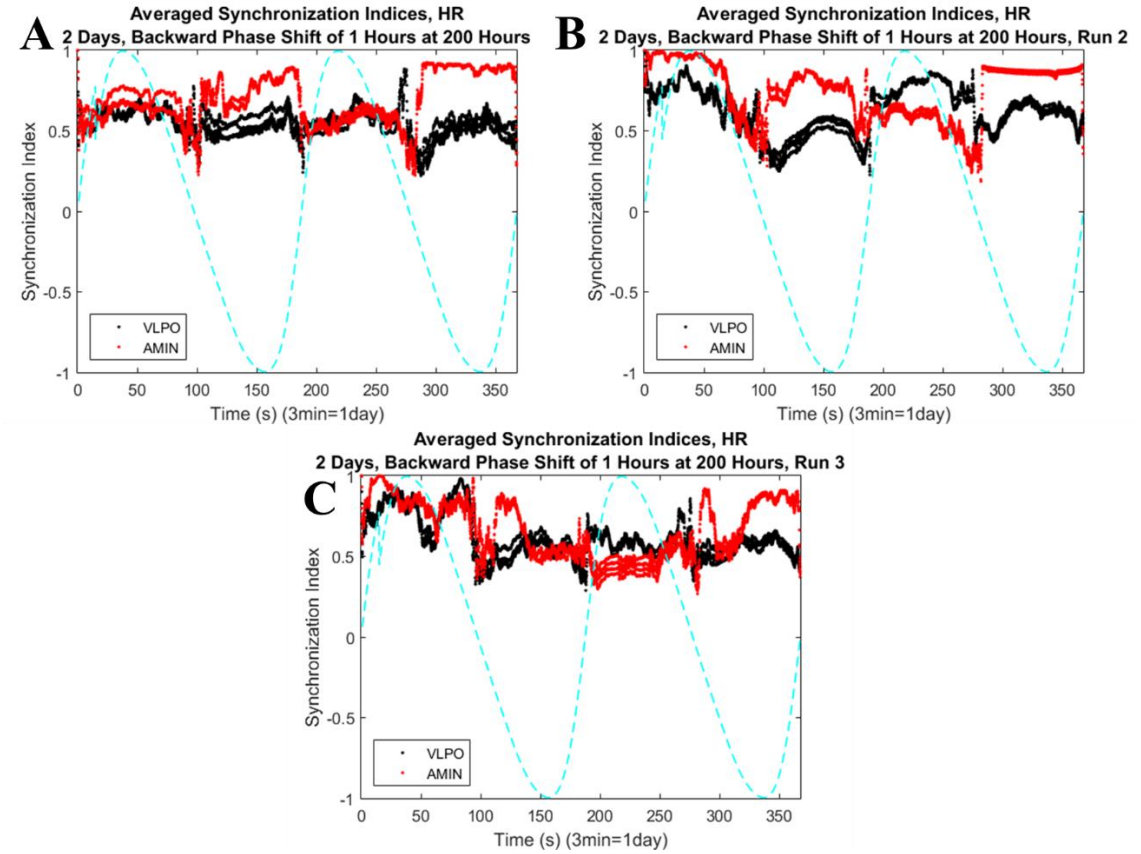

Figure 4.12 – Circadian Backward Phase Shift, DST End
Synchronization indices for AMIN and VLPO after circadian backward phase shift of 1 hour at 200 hours, 3 runs. This is equivalent to the end of DST in the autumn. (A) Run 1. There is an overlap in synchronization for both regions during the daytime both days, while the nights remain unchanged with respect to control. (B) Run 2. The system begins with AMIN more synchronized but settles into its proper reciprocal relationship by the start of night one. (C) Run 3. After the phase shift, there is a significant amount of overlap in synchronization, as well as state switching, leaving the state indeterminate until near the end of the simulation.

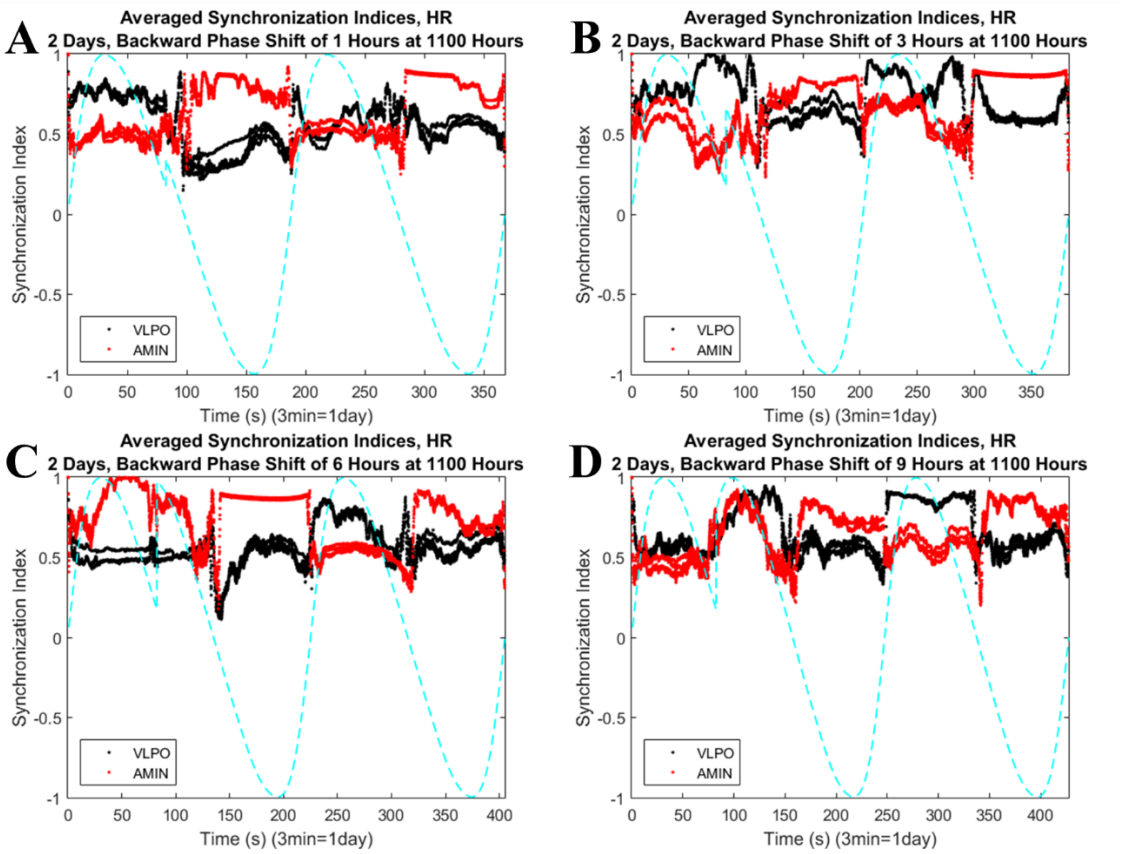

Figure 4.13 – Circadian Drive with Backward Phase Shifts at 1600 Hours
Synchronization indices for AMIN and VLPO after different lengths of circadian backward phase shifts at 1100 hours. (A) 1-Hour. Overlap in synchronization indices is observed during night two. Runs 2 and 3 exhibit clear reciprocal behavior (not pictured). (B) 3-Hour. Synchronization indices behave similarly to the control case, with the exception of a few overlaps between indices. The remaining two runs show similar results (not pictured). (C) 6-Hour. Recovery from the shift occurs by night one. Run 2 was similar with more overlap and run 3 remained asleep after the shift (not pictured). (D) 9-Hour. Normal behavior returns by night one; results are similar for runs 2 and 3 (not pictured).

have difficulty adjusting their circadian rhythms, such as those who have an intrinsic circadian rhythm sleep disorder (Sections 1.5.4.3. – 1.5.4.6.). These detrimental effects on synchronization and state switching are notable considering the observed negative side effects of the autumn DST shift. While some studies have found that there is no significant

increase or decrease in the number of heart attacks following the backward shift (Janszky *et al*. 2012), others have found that the risk of heart attacks does increase, though to a lesser extent than following the spring shift forward (Manfredini *et al*. 2019). An increased risk of stroke was found to be present for both shifts, however (Sipilä *et al*. 2016).

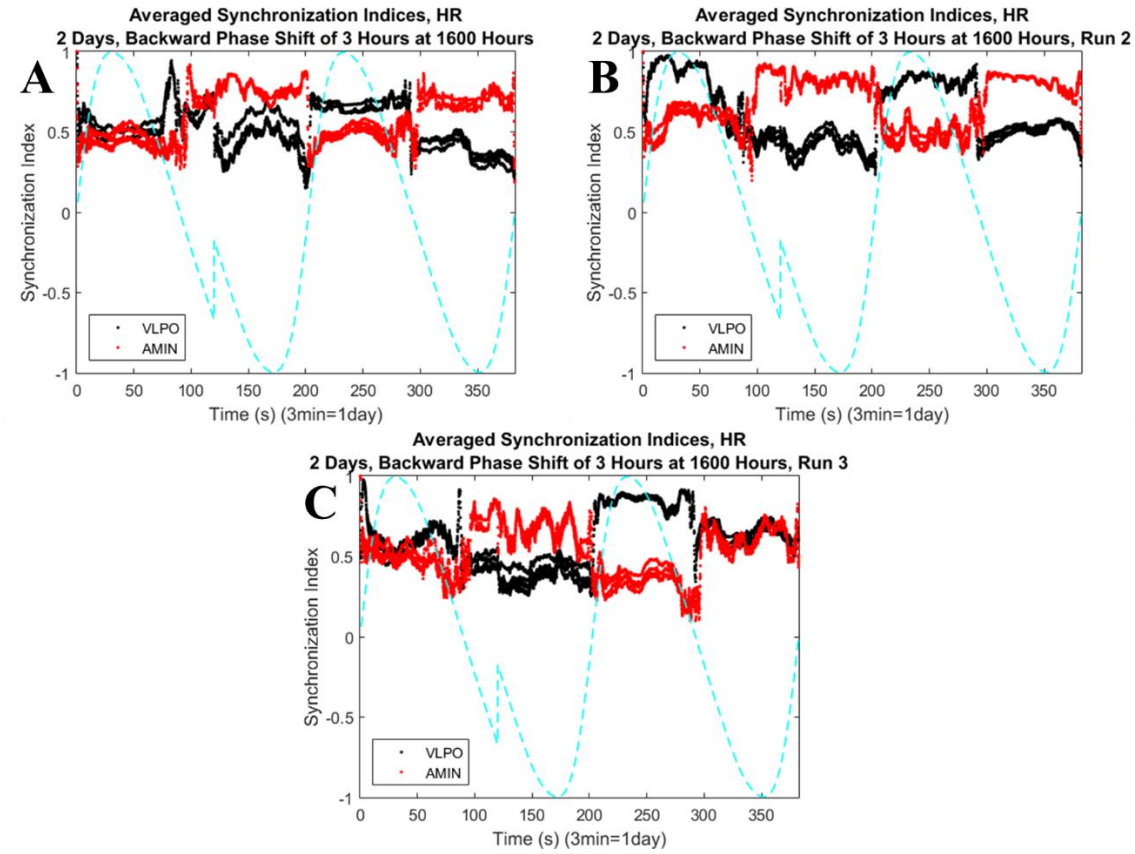

Figure 4.14 – Circadian Backward Shift, 3 Hours at 1600 Hours
Synchronization indices for AMIN and VLPO after circadian backward phase shift of 3 hours at 1600 hours, 3 runs. (A) Run 1. The expected reciprocal relationship is unperturbed by the phase shift. (B) Run 2. Like run 1, the system remains unperturbed. (C) Run 3. The effect of the phase shift is delayed, causing an overlap in synchronization indices during night two.

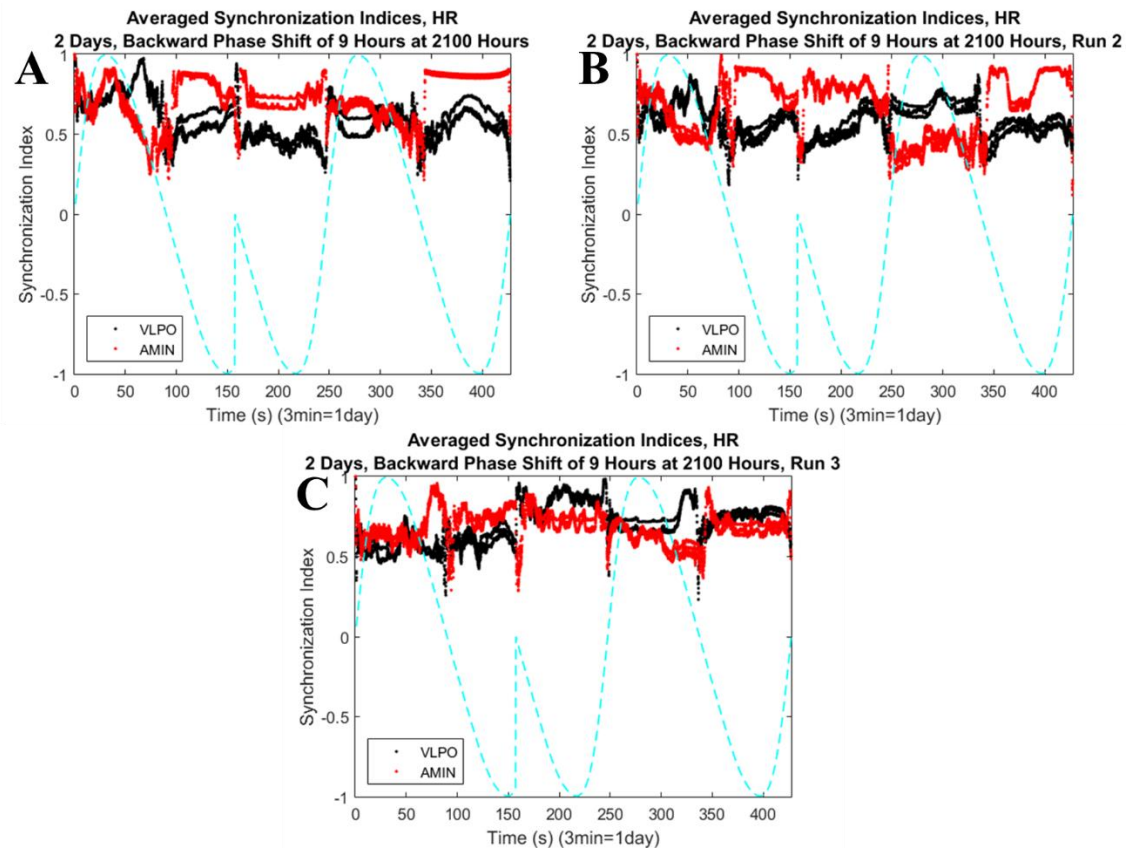

Figure 4.15 – Circadian Backward Shift, 9 Hours at 2100 Hours
Synchronization indices for AMIN and VLPO after circadian backward phase shift of 9 hours at 2100 hours, 3 runs. (A) Run 1. The system remains asleep after the phase shift, with a synchronization overlap during day two. (B) Run 2. The system was unperturbed by the phase shift. (C) Run 3. After the phase shift, the system changes to wake for the repeated night, remaining awake for the remainder of the simulation.

The impact of backward phase shifts of varying lengths on the system at 1100 hours is shown in Figure 4.13. Though all of these results exhibited irregularities, they all maintained their reciprocal synchronization relationship, showing that backward phase shifts at this hour has little negative impact on the synchronization of the system. The 1 and 3-hour delays can be considered equivalent to staying up a few extra hours, which would not be expected to have significant impact. However, the results for 6 and 9-hour

shifts are inconsistent with what would be expected in a biological system, since these results imply that staying awake for two days in a row would have no major negative impact (see Section 1.4.). More realistic versions of the present model are likely to be needed in order to accurately simulate the response to such phase shifts. Sleep studies conducted on people living in the Arctic Circle have found that their season-long days and nights cause seasonal changes in their circadian rhythms (Lewis & Lobban 1957, Friborg *et al*. 2014).

A more complex and realistic version of a sleep model would be expected to reproduce such results as well.

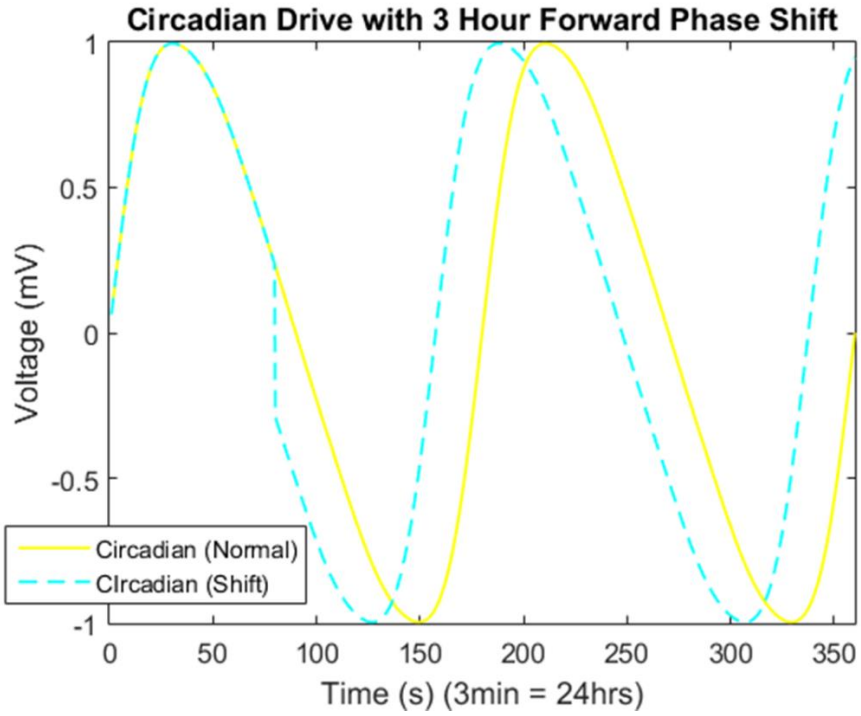

Figure 4.16 – Circadian Drive with Forward Phase Shift
An example of a circadian drive with (dashed light blue line) and without (yellow line) a 3-hour forward phase shift. This sets the clock forward three hours.

Consistently stable results are also exhibited by backwards circadian phase shifts, shown in Figure 4.14. When the circadian drive is shifted back 3 hours at 1600 hours, the reciprocal relationship observed in the control case remains intact, suggesting that this phase shift length at this time of day has little impact on the system.

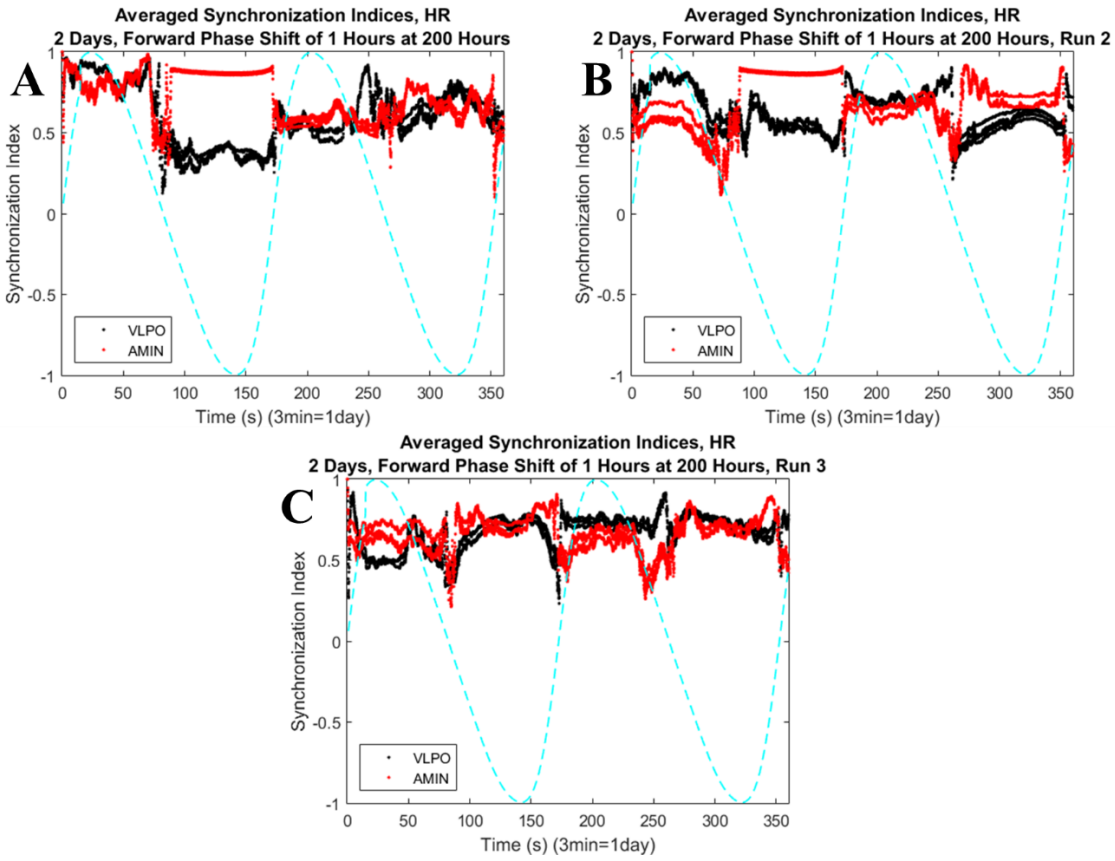

Figure 4.17 – Circadian Forward Phase Shift, DST Start
Synchronization indices for AMIN and VLPO after circadian forward phase shift of 1 hour at 200 hours, 3 runs. This is equivalent to the beginning of DST in the spring. (A) Run 1 shows synchronization overlap and numerous state switches after the first night. (B) Run 2. Despite the phase shift, the reciprocal relationship remains intact, with some synchronization overlap. (C) Run 3. After the phase shift, there is significant synchronization overlap, to the point that the sleep/wake state is difficult to determine.

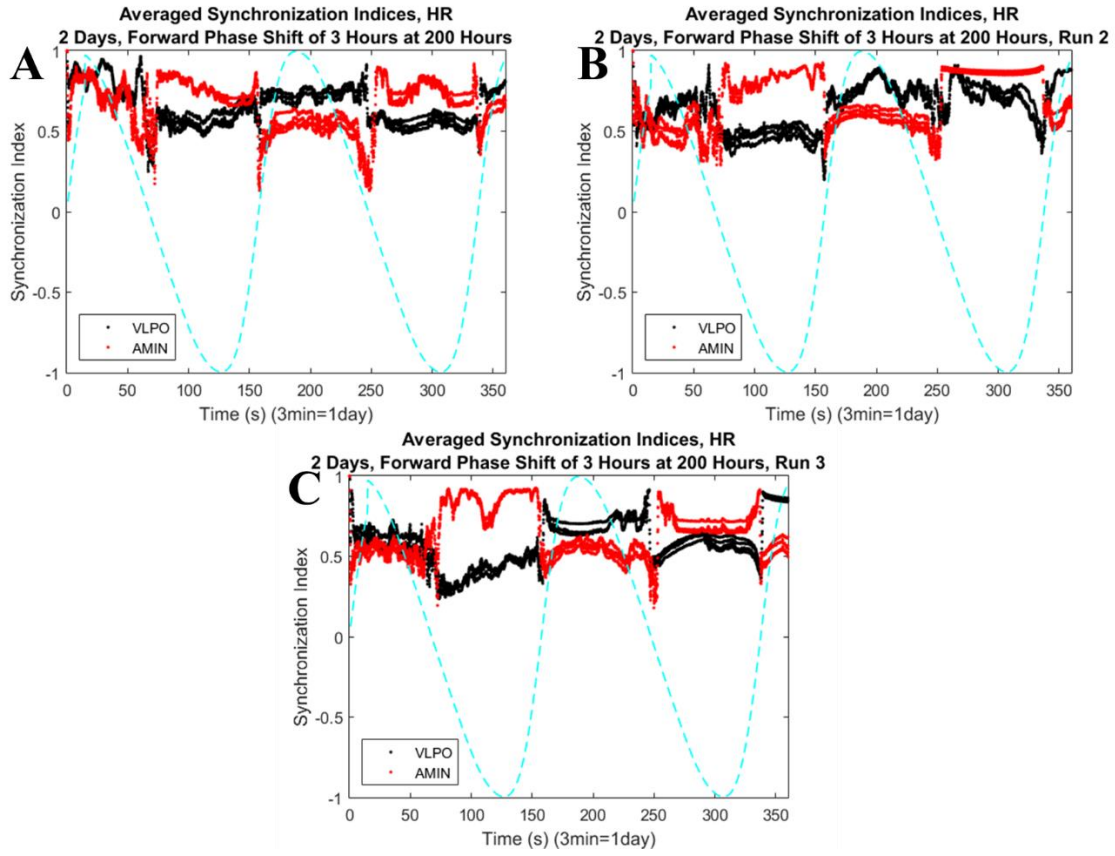

Figure 4.18 – Circadian Forward Shift, 3 Hours at 200 Hours
Synchronization indices for AMIN and VLPO after circadian forward phase shift of 3 hours at 200 hours, 3 runs. (A) Run 1. The reciprocal relationship is unimpeded by the phase shift. (B) Run 2. Besides the briefest of synchronization overlaps during night two, the reciprocal relationship is intact. (C) Run 3. Though the synchronization indices bend close to each other, the relationship is still clear. The inward bends are also seen in the original figure with no circadian disturbances, Figure 2.36.

In contrast to Figure 4.14, the longer phase shift implemented in Figure 4.15 shows some of the wide variability caused by backwards phase shifts in the model. Here, the backward shift takes the CD from late night (low CD) back to the point of state change (C = 0). Sometimes the system can recover from the backward shift (4.15B), and other times it causes the system to become unstable (4.15C). Whether or not the system can recover

from this instability may be determined with simulations extended over multiple circadian cycles.

4.1.2.2. Forward phase shift. Here, the circadian drive is phase-shifted forward during the first day of two-day runs, shifting the entire skewed sine wave. This removes a segment of the circadian drive, bringing a later point in the wave forward. Like the backwards phase shift, the forward phase shift occurs at a set time of day, changing the current value of C to its value a defined number of hours ahead. The drive then continues as normal. An example of a forward phase shift is shown in Figure 4.16. A forward phase shift of one hour at 2 A.M. is equivalent to DST beginning in the spring. Any shift of greater magnitude and/or different time of day would be equivalent to instantly traveling to a time zone further East.

Multiple simulations were performed in the one-hemisphere version of the model for a 1, 3, 6, and 9-hour forward phase shift occurring at 200, 600, 1100, 1600, and 2100 hours (corresponding to 2 A.M., 6 A.M., 11 A.M., 4 P.M., and 9 P.M.) on the first day of two-day runs.

A forward phase shift of 1 hour at 200 hours was used to simulate the beginning of DST, as shown in Figure 4.17. Some runs display persistent synchronization overlap and state ambiguity (runs 1 and 3), with others had relatively few irregularities (run 2). This is particularly interesting, as the “spring forward” start of DST has been connected to a coinciding rise in heart attacks, traffic accidents, and ischemic strokes, among other negative effects (Janszky *et al*. 2012, Harrison 2013, Sipilä *et al*. 2016, Manfredini *et al*. 2019). Changes this severe from a short phase shift may indicate that this model has the capability to simulate the negative impacts on synchronization caused by DST, though

more simulations, and development of a measure to quantify the degree of sleep disruption, are needed to confirm these results.

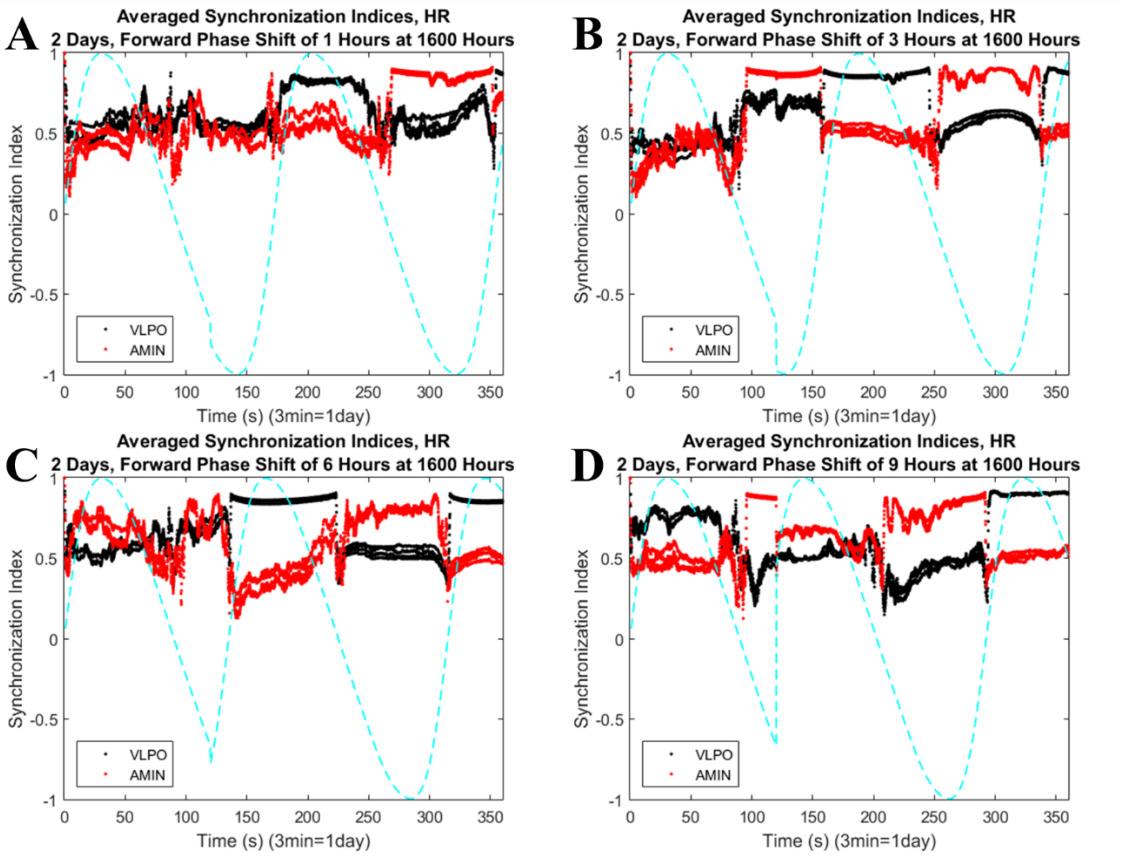

Figure 4.19 – Circadian Drive with Forward Phase Shifts at 1600 Hours
Synchronization indices of AMIN and VLPO after different lengths of circadian forward phase shifts at 1600 hours. (A) 1-Hour. The system recovers the reciprocal behavior after the start of day two. Similar irregularities plague the other two runs, though at different times (not pictured). (B) 3-Hour. A small dip in synchronization is experienced when the phase shift occurs, but the reciprocal behavior is not negatively impacted. This is consistent for all three runs (not pictured). (C) 6-Hour. The simulation begins roughly but recovers by the start of day two. This is not seen in the other two runs, which experience mainly synchronization overlapping after the phase shift. (D) 9-Hour. After the shift, the system experiences difficulty waking up, sleeping through all of day two. The remaining runs are shown in Figure 4.20.

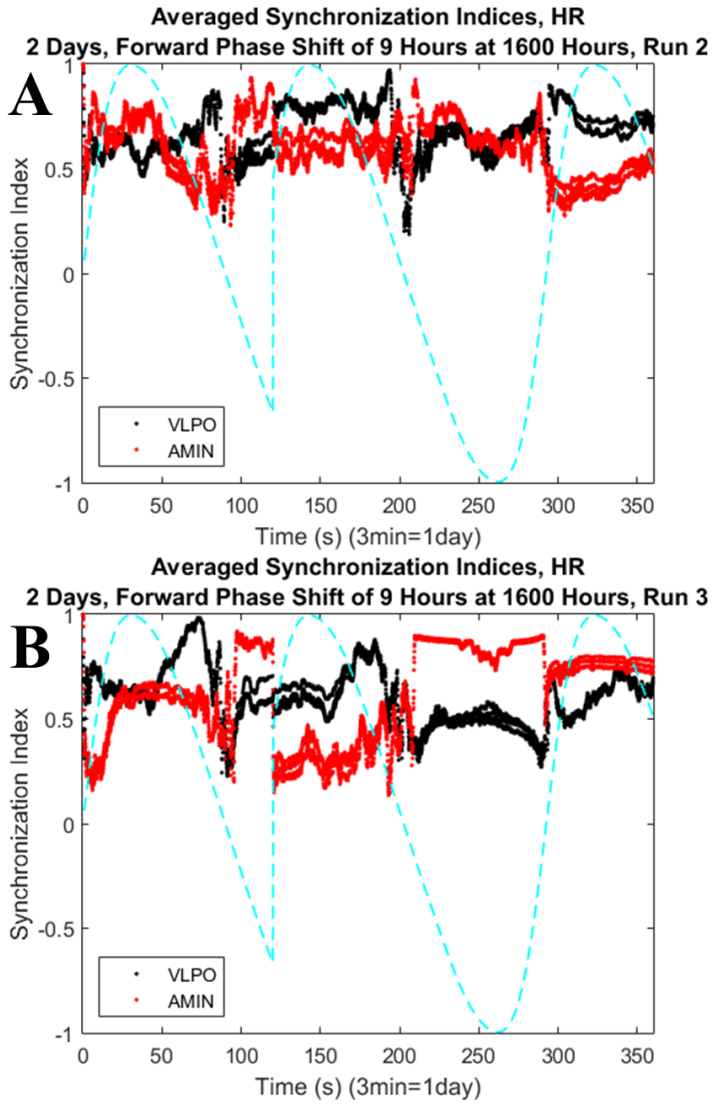

Figure 4.20 – Circadian Forward Shift, 9 Hours at 1600 Hours
Synchronization indices for AMIN and VLPO after circadian forward phase shift of 9 hours at 1600 hours, 3 runs. Run 1 was displayed as Figure 4.19D. (A) Run 2. Immediately following the phase shift, the system returns to a wake state. Over the second night, however, the system remains in an indeterminate state. (B) Run 3. There are no perturbations in synchronization at the phase shift, though the system fails to wake up during day three.

In contrast to the 1-hour phase shift, a 3-hour phase shift at 200 hours did little to influence the synchronization, as shown in Figure 4.18. All the runs maintain the reciprocal

behavior of the synchronization indices previously observed for these parameter values (Figure 2.36). A 9-hour phase shift at this time (data not pictured) also had minimal effect on the system's synchronization. Additional simulations, as well as quantification of the effect of the circadian disturbance, will be needed in order to determine whether these results are robust or simply a result of small sample size.

The effect of varied lengths of forward phase shifts at 1600 hours is presented in Figure 4.19. The sequence of panels shows an increasing amount of sleep loss, from an hour lost to a large portion of the night. While the shorter shifts (the first three panels) all exhibit some irregularities, they each seem to recover their reciprocal synchronization relationship. Following the severe sleep loss represented by the 9-hour shift, however, the system having difficulty returning to wake during the second day. Additional runs (Figure 4.20) show what may be considered alternative biological reactions to the short night, with one having a restless sleep the following night (top panel) and the other sleeping for additional time the next night (bottom panel).

The variability in outcome for a 9-hour shift at 1600 hours contrasts strongly with the lack of variability among the simulations of a 9-hour shift at 200 hours. Anomalies like this may indicate the system's sensitivity to the timing of a circadian shift. Further study and simulations may shed light on the role of perturbation timing in disrupting the sleep cycle.

4.2. UNIHEMISPHERIC SLEEP

Unihemispheric sleep (UHS) is a form of sleep where one hemisphere remains awake to monitor for predators or other dangers, and to maintain breathing and/or motion,

while the other hemisphere sleeps. This was discussed earlier in Sections 1.3.2.-1.3.4. The mixture of various types of dynamical activity in UHS is reminiscent of the chimera state. UHS and chimera states are also linked by the prevalence of inhibitory connections, which are necessary for the production of UHS in a computational model (Kedziora *et al*. 2012) and are more likely than excitatory connections to produce chimera states (Tinsley *et al*. 2012, Glaze *et al*. 2016). Preliminary results show that UHS can be generated in the present sleep model for both excitatory and inhibitory interhemispheric connections.

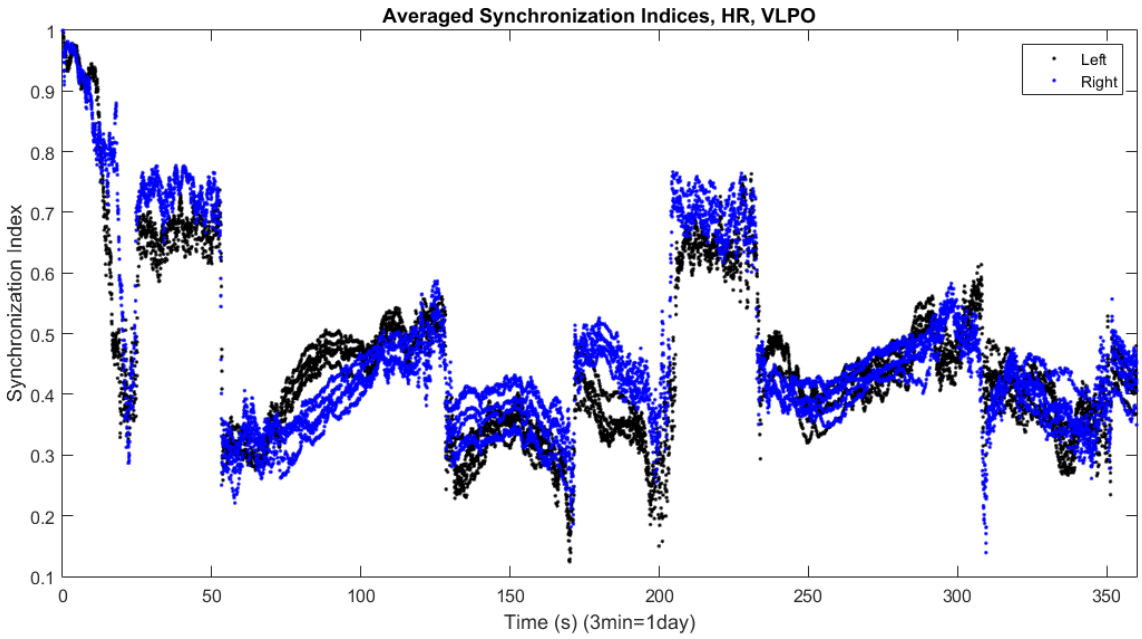

Figure 4.21 – Excitatory Coupling, Bihemispheric Sleep
Synchronization indices for left (black line) and right (blue line) hemisphere VLPO. Both VLPO regions exhibit similar synchronization indices throughout the simulation, suggesting high correlation between the hemispheres and consistent with BHS. Parameters are $g_A = -0.0000275$, $g_{CA} = 0.00115$, $g = 0.000045$, $g_V = -0.0000425$, $g_{CV} = -0.0019$, $g_{V_{LtR}} = 0.000025$, $g_{V_{RtL}} = 0.000025$, and $I = 2.50$, with 4 neurons per region.

4.2.1. Excitatory Connection Between Hemispheres. While they occur more frequently with inhibitory connections, chimera states can nonetheless be found with excitatory coupling between groups (Tinsley *et al*. 2012, Glaze *et al*. 2016). Indeed, the chimera states described above in Section 3.3. all occur for excitatory coupling between hemispheres. This implies that UHS may be found in this model with excitatory interhemispheric coupling. Here, I show results with symmetrical excitatory interhemispheric connections corresponding to both asymmetric and unihemispheric sleep.

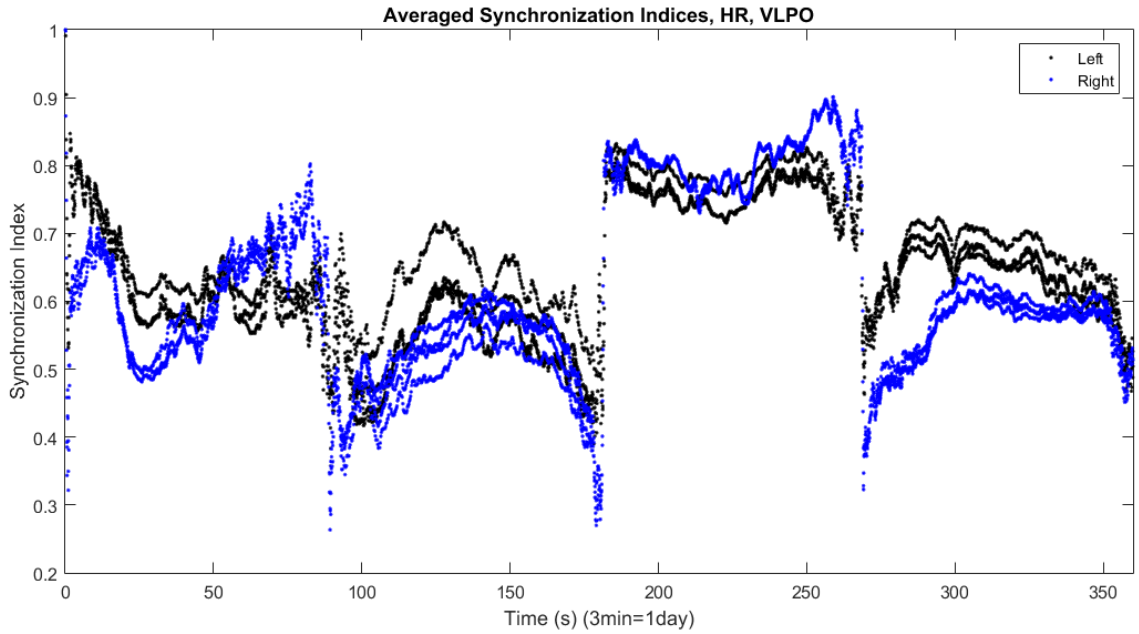

Figure 4.22 – Excitatory Coupling, Asymmetric Sleep
Synchronization indices for left (black line) and right (blue line) hemisphere VLPO, showing asymmetric sleep. The second night shows a distinct gap between left and right hemisphere VLPO synchronization indices. The gap is small, and does not last the entirety of the night, consistent with asymmetric sleep. Parameters are $g_A = -0.0000275$, $g_{CA} = 0.00115$, $g = 0.000045$, $g_V = -0.0000425$, $g_{CV} = -0.0019$, $g_{V_{LtR}} = 0.00002$, $g_{V_{RtL}} = 0.00002$, and $I = 2.00$, with 4 neurons per region.

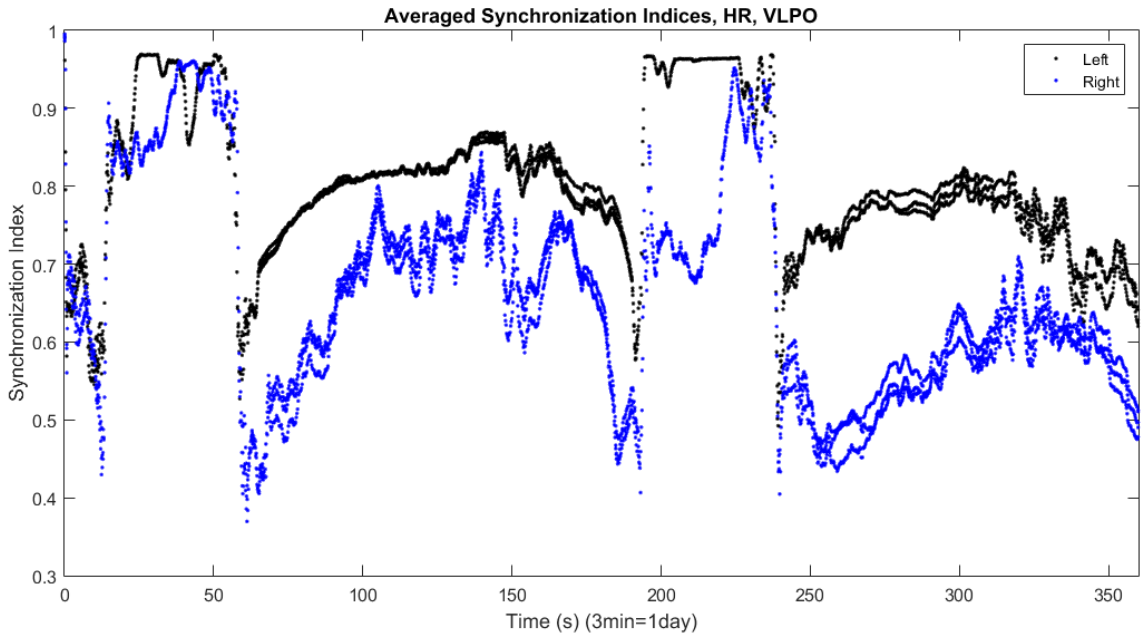

Figure 4.23 – Excitatory Coupling, Asymmetric and UHS
Synchronization indices for left (black line) and right (blue line) hemisphere VLPO, showing asymmetric sleep (night one) and UHS (night two). Parameters are $g_A = -0.0000275$, $g_{CA} = 0.00115$, $g = 0.000045$, $g_V = -0.0000425$, $g_{CV} = -0.0019$, $g_{V_{LtR}} = 0.000025$, $g_{V_{RtL}} = 0.000025$, and $I = 1.75$, with 4 neurons per region.

Kedziora *et al*. (2012) found bihemispheric sleep (BHS) when utilizing excitatory interhemispheric coupling in their model. In a computational model of BHS, one would expect both hemispheres to be, as the name suggests, asleep at the same time and synchronized with each other. An example of nearly identical synchronization of VLPO regions from each hemisphere is shown in Figure 4.21. For this value of the input current ($I = 2.50$), HR neurons are deep in the bursting regime. Consequently, the synchronization of each region changes rapidly numerous times throughout the simulation. However, the significant overlap between the left and right VLPO through these abrupt shifts in

synchronization show that the regions are well synchronized to one another, inducing during sleep states.

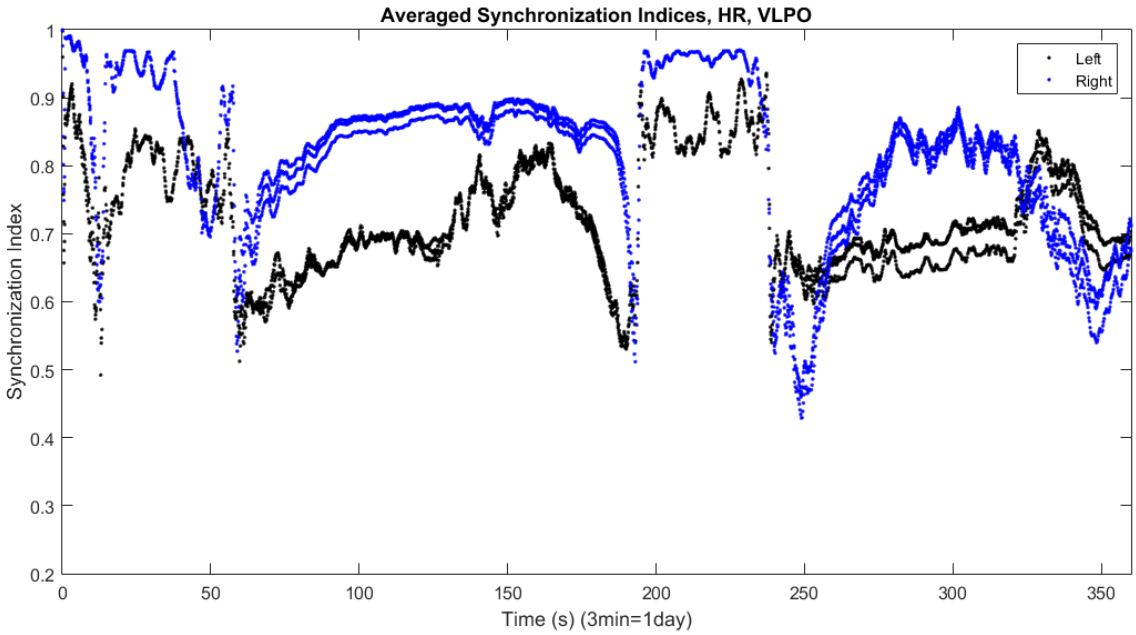

Figure 4.24 – Excitatory Coupling, Dominant Hemisphere Switching
Synchronization indices for left (black line) and right (blue line) hemisphere VLPO, showing dominant hemisphere switching. Parameters are $g_A = -0.0000275$, $g_{CA} = 0.00115$, $g = 0.000045$, $g_V = -0.0000425$, $g_{CV} = -0.0019$, $g_{V_{LtR}} = 0.00004$, $g_{V_{RtL}} = 0.00004$, and $I = 1.75$, with 4 neurons per region.

Figure 4.22 shows the synchronization of two VLPO regions from the left and right hemispheres, for a different set of parameter values. While over the first night the regions have similar degrees of synchronization, there is a slight gap between synchronization indices of the left and right VLPO for most of the second night. This gap indicates that the left hemisphere is more synchronized than the right hemisphere. Slight asymmetry between

the hemispheres, like that shown in Figure 4.22, occurs in the human brain during the first night effect and as a result of sleep apnea (Section 1.3.1.2.).

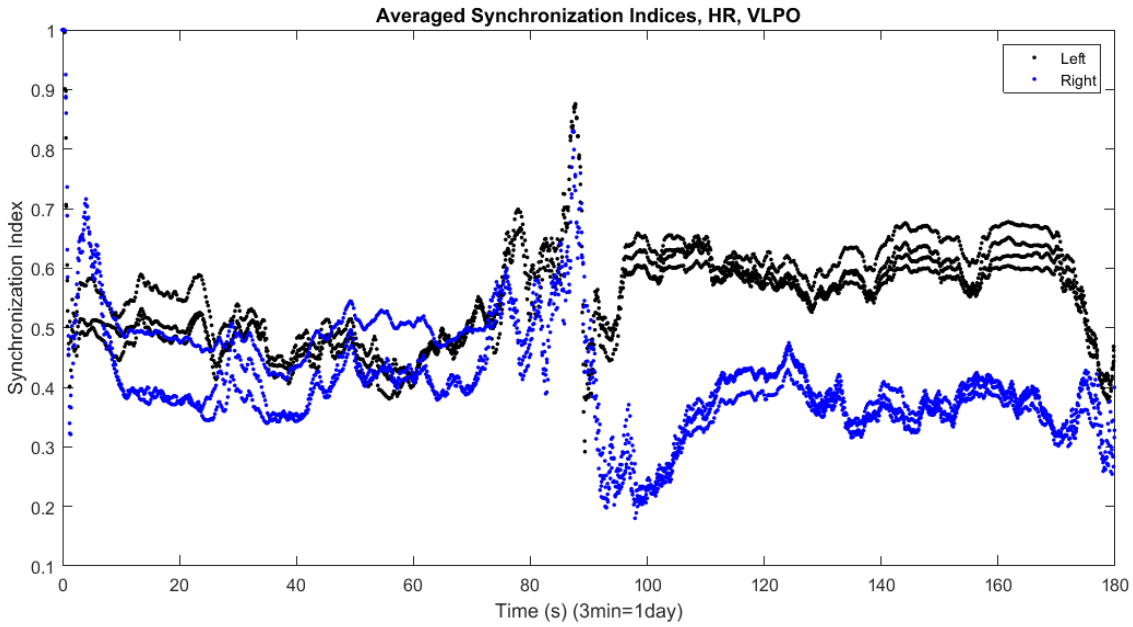

Figure 4.25 – UHS in Phase-Cluster Chimera Data
Synchronization indices for left (black line) and right (blue line) hemisphere VLPO, showing UHS, from data in Figure 3.13 (phase-cluster chimera state). Parameters are $g_A = -0.0000075$, $g_{CA} = 0.00115$, $g = 0.000045$, $g_V = -0.0000425$, $g_{CV} = -0.0019$, $g_{V_{LtR}} = 0.00002$, $g_{V_{RtL}} = 0.00002$, and $I = 2.00$, with 4 neurons per region.

Asymmetry is also present for the first night in Figure 4.23. In this case, there is a distinct gap between left and right VLPO throughout the entire night. At several times during the night, the gap in the synchronization index is as large as 0.2. A similar gap is seen in Figure 2.36, indicating the difference between an active (comparatively desynchronized) and a resting (comparatively synchronized) region. The first night in Figure 4.23 can be interpreted as either asymmetric sleep or UHS, depending on the

difference in synchronization indices selected as a cutoff between the two states. The second day in this figure, however, shows a larger gap, maintained through the better half of the night, and indicative of UHS.

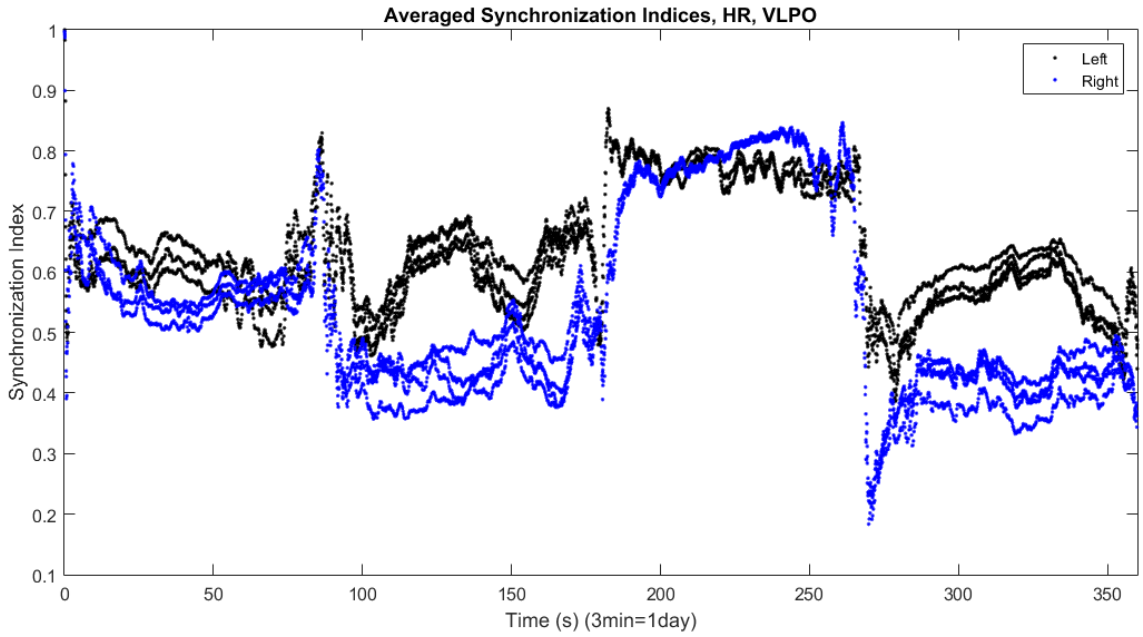

Figure 4.26 – Inhibitory Coupling, Asymmetric Sleep
Synchronization indices for left (black line) and right (blue line) hemisphere VLPO, showing asymmetric sleep. Parameters are $g_A = -0.0000275$, $g_{CA} = 0.00115$, $g = 0.000045$, $g_V = -0.0000425$, $g_{CV} = -0.0019$, $g_{V_{LtR}} = -0.00002$, $g_{V_{RtL}} = -0.00002$, and $I = 2.00$, with 4 neurons per region.

Asymmetric sleep is present in Figure 4.24 over both nights. This figure illustrates another key feature of UHS – hemispheric switching. In biological UHS, once one hemisphere has slept for a time, it wakes so that the other hemisphere can sleep, and this alternating process repeats numerous times over the night (see Section 1.3.2.). This is

precisely what occurs in Figure 4.24, where the left and right hemisphere VLPO regions switch which is more synchronized. The presence of this aspect of UHS demonstrates that this model can exhibit additional key properties of UHS beyond simple hemispheric synchronization asymmetry.

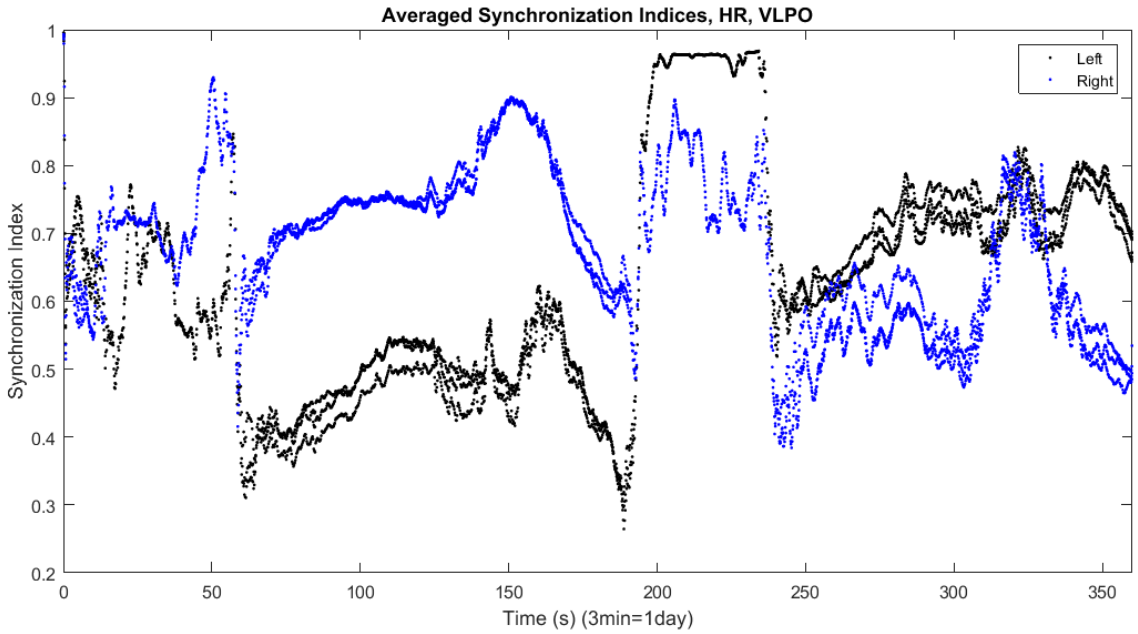

Figure 4.27 – Inhibitory Coupling, UHS and Asymmetric, Apneic Sleep
Synchronization indices for left (black line) and right (blue line) hemisphere VLPO. Night one exhibits a large gap between left and right hemisphere VLPO synchronization, indicative of UHS. Night two shows asymmetric sleep with a brief collapse into symmetric BHS before a return to asymmetry, reminiscent of the shifts known to occur in patients with sleep apnea. Parameters are $g_A = -0.0000275$, $g_{CA} = 0.00115$, $g = 0.000045$, $g_V = -0.0000425$, $g_{CV} = -0.0019$, $g_{V_{LtR}} = -0.000035$, $g_{V_{RtL}} = -0.000035$, and $I = 1.75$, with 4 neurons per region.

Strong interhemispheric asymmetries were observed in the phase-cluster chimera state shown in Figure 3.13. Given the parallel between chimera states and UHS, the

synchronization indices of the VLPO regions from Figure 3.13 are shown in Figure 4.25. This data is consistent with UHS, showing a distinct gap between the synchronization indices of the left and right hemisphere.

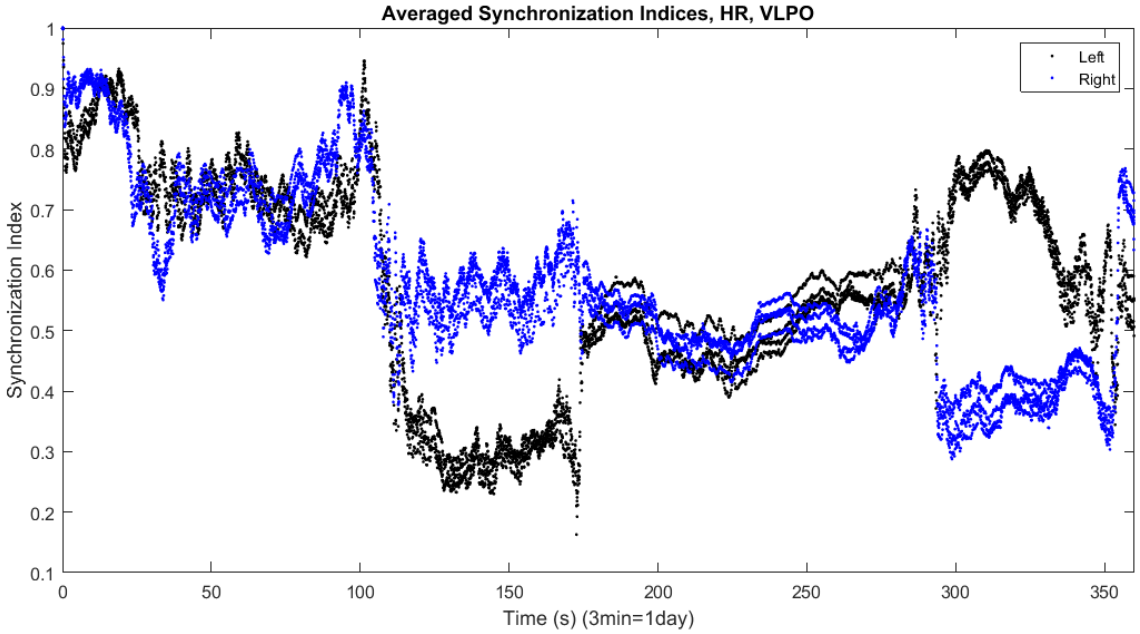

Figure 4.28 – Inhibitory Coupling, UHS and Dominant Hemisphere Switching Synchronization indices for left (black line) and right (blue line) hemisphere VLPO, showing UHS. Each night shows a different hemisphere exhibiting higher synchronization, though both have a large gap indicative of UHS. Parameters are $g_A = -0.0000275$, $g_{CA} = 0.00115$, $g = 0.000045$, $g_V = -0.0000425$, $g_{CV} = -0.0019$, $g_{V_{LtR}} = -0.000025$, $g_{V_{RtL}} = -0.000025$, and $I = 2.25$, with 4 neurons per region.

4.2.2. Inhibitory Connection Between Hemispheres. Asymmetric sleep can be observed with an inhibitory connection between the VLPO regions, as shown in Figure 4.26. Here, each night shows asymmetric sleep, with the left (black line) hemisphere being the more synchronized during both nights. This figure has equivalent parameters to Figure

4.22, save that the interhemispheric connection strength is negative (inhibitory) rather than positive (excitatory). As may be expected from the inhibitory connection, which is more likely to produce chimera states, both nights exhibit asymmetric sleep, in contrast to the one night of asymmetric sleep shown in Figure 4.22.

Figure 4.27 reveals both UHS and asymmetric sleep in the non-bursting region of parameter space ($I = 1.75$). The first night exhibits a large gap between left and right VLPO synchronization indices, indicative of UHS. On the other hand, the second night shows a smaller gap which can be interpreted as asymmetric sleep, punctuated by a brief period of symmetric BHS. Switching between asymmetric and symmetric sleep is known to occur in apneic patients, (see Section 1.3.1.2.). During normal breathing in sleep, apneic patients exhibit asymmetry in their sleep, but return to symmetric sleep when they enter an apneic episode (paused breathing). This instance of apnea-like sleep demonstrates that the model is able to simulate not only UHS and asymmetric sleep, but also changes in sleep state associated with a sleep disorder.

UHS occurs deep in the bursting regime, as seen in Figure 4.28. Both nights exhibit UHS, through the right hemisphere is synchronized during the first night, while the left hemisphere dominates during the second. While not the same as switching hemispheres multiple times in one night so that each side gets a chance to rest, this interesting detail leads to the question of what determines which hemisphere sleeps which night, or at least which hemisphere gets to sleep first. This night-by-night switching was not present in any of the examined runs with excitatory interhemispheric coupling (Section 4.2.1.) but was present in two of the three figures analyzed in this section for inhibitory coupling (Figures

4.27 and 4.28). Whether this is a product of the inhibitory coupling, noise, or other factors remains to be explored in future work.

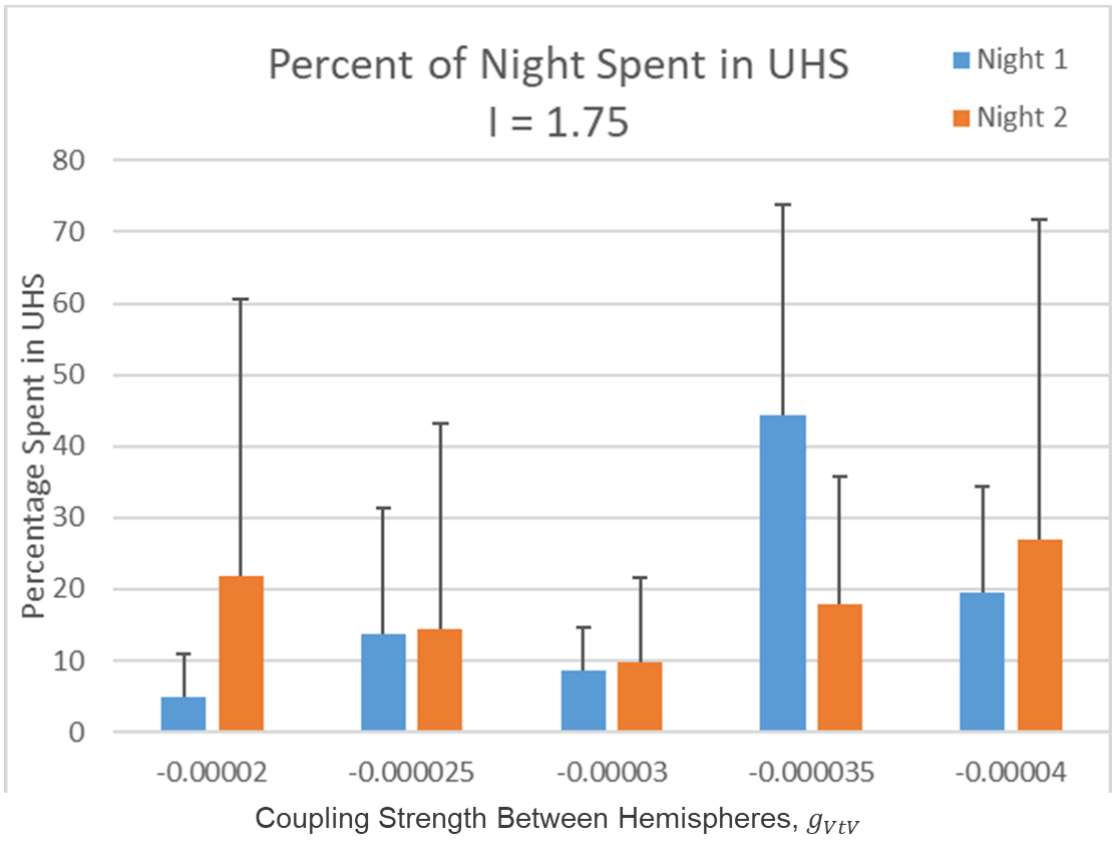

Figure 4.29 – Percent of Night Spent in UHS
Histogram of the percentage of each night spent in UHS. Colored bars (blue for night 1, orange for night 2) denote the percentage of the night the difference in synchronization between hemispheres was greater than a threshold (0.18). Night 1 is about 60 s to 190 s, and night 2 is about 235 s to 360 s. The error bars denote the standard deviation.

To explore the reproducibility of these UHS, four runs were conducted for each of the values $g_{VtV} = -0.00002, -0.000025, -0.00003, -0.000035,$ and -0.00004. The

sliding synchronization was found for each run using a window size of 70 spikes, and the synchronization indices of one hemisphere subtracted from the other. If the magnitude of the difference between the hemispheres was greater than 0.18 at any time during night 1 (about 60s to 195s) or night 2 (about 235s to 360s), the system was considered in UHS. From this the percentage of time the system was in UHS each night was compiled, averaged over the four runs and shown in Figure 4.29. The highest colored bars and error bars appear for larger values of coupling strength between hemispheres (g_{VtV}), with the exception of night 2 for the smallest coupling strength (-0.00002). This suggests that higher coupling strengths are more likely to produce UHS, while the error bars imply that UHS is not a guarantee. There is no distinct correlation between a specific night and the appearance of UHS.

4.3. CONCLUSIONS

The results for both jet lag and unihemispheric sleep are reviewed below.

4.3.1. Jet Lag. While the jet lag results described above are still preliminary, they nonetheless provide a good idea of the model's reaction to circadian changes, even if these are not completely biologically accurate. It should be remembered that in the results above, the day and night portions of the circadian cycle have equal lengths. Future modifications of the model will include a more realistic 8-hour/16-hour night/day cycle.

Some of jet lag results show difficulty with state transitions after a change in the circadian drive, while others exhibit no discernable change from the reciprocal synchronization relationship seen in the control case for these parameters (Figure 2.36). The degree to which state transitions were affected varied as a function of the applied

circadian disturbance. The system was more stable in response to circadian delays than to circadian perturbation, and the system was more stable in response to backwards than to forward phase shifts.

As for the DST specific runs, the autumn end of DST, or the backward shift, had runs that were moderately less disturbed than the spring DST, or the forward shift. This is consistent with experimental results showing that the sleep disruptions from DST increases instances of heart attacks, strokes, and traffic accidents, as mentioned above (Sections 4.1.2.1. and 4.1.2.2.).

The inclusion of a homeostatic drive may give a better indication of the impact of circadian rhythm disruptions due to jet lag. A combination of a delay or perturbation with a phase shift may provide results more consistent with other real-world scenarios, such as various lengths of flights that land at varying values of CD. Changing the constant value of CD during delays and perturbations will also provide a wider variety of results. Increasing the length of the simulation, particularly for the parameters where no clear recovery occurred, may reveal more of the impact of the circadian disturbance. Isolating the disturbance caused by changes in CD will be made simpler by using longer simulations, allowing the system to run through an entire daily cycle before the perturbation is introduced. The impact of noise on the results presented here, specifically with respect to the inconsistency between the multiple runs, should also be addressed. Lastly, future work will involve the development of a means of quantifying the effect of circadian disruptions; for example, by measuring the deviation of the AMIN and VLPO synchronization indices from their expected control values.

4.3.2. Unihemispheric Sleep. In the model, BHS, asymmetric sleep, and UHS were found using both excitatory and inhibitory interhemispheric coupling. The model also exhibited a couple of distinct characteristics. Interhemispheric switching, which occurs in UHS to allow the hemispheres to take turns resting, was displayed, both within a single night (Figure 4.24) and with night-by-night switching (Figure 4.28). Asymmetric sleep with brief forays into BHS was shown by the model as well (Figure 4.27), a result evocative of the changes in synchronization seen in patients with sleep apnea.

Perhaps most vitally, data that showed a phase-cluster chimera state in Section 3.2.4.3. also displayed synchronization differences characteristic of UHS. The common attributes of UHS and the chimera state have been noted, and the possibility of a relation between these states discussed. Here, a possible link may have been found; further study may reveal more connections between UHS and the chimera state.

5. CONCLUSIONS

5.1. SUMMARY

A computational model of sleep dynamics has been developed, using two different neural models (Huber-Braun and Hindmarsh-Rose). The model has been developed in both a single-hemisphere and a two-hemisphere form, with clusters of neurons representing the sleep-promoting (VLPO) and wake-promoting (AMIN) regions.

With the single hemisphere and Huber-Braun neurons, the synchronization of the simulated wake-promoting and sleep-promoting regions has a reciprocal relationship: AMIN has higher synchronization than VLPO during the daytime, and VLPO has higher synchronization than AMIN during the nighttime (Sections 2.2.4.2. and 2.2.4.3.). Burst synchronization analysis showed that VLPO may have higher synchronization during the day than shown by the spike-by-spike phase synchronization (Section 2.3.4.). Both VLPO and AMIN exhibit burst-firing during their downtimes and rapid, single spikes during their active times (Figures 2.12 and 2.13).

When Hindmarsh-Rose neurons are used instead, the synchronization relationship seen with HB neurons is reversed, with synchronization highs occurring during a region's downtime (daytime for VLPO, nighttime for AMIN, Figure 2.36). Each region exhibits burst firing throughout the simulation, with the number of spikes per burst increasing during active times and decreasing during downtimes.

In the two-hemisphere version of the model, chimera states and phase-cluster chimera states were found (Sections 3.2.4.2.-3.2.4.4.). These were all found with excitatory

coupling between hemispheres, rather than the inhibitory connection which typically produces chimera states (Tinsley *et al*. 2012).

The two-hemisphere model also simulated asymmetric sleep and UHS using both excitatory interhemispheric coupling (Figure 4.23) and inhibitory coupling (Figures 4.26 and 4.27). It also exhibited interhemispheric switching (Figure 4.24), which occurs during UHS, and asymmetric sleep with brief forays into BHS (Figure 4.27), similar to the changes in synchronization seen in patients with sleep apnea. Finally, and far from being the least, data that showed a phase-cluster chimera state in Section 3.2.4.3. also displayed an interhemispheric synchronization gap indicative of UHS (Figure 4.25).

The jet lag results, while preliminary, showed a variety of reactions to changes in the circadian drive, including difficulty in changing states. The system showed greater resistance to changes in synchronization with circadian delays and backwards phase shifts and experienced a greater effect from the circadian perturbations and forward phase shifts. Particularly, the daylight-saving time (DST) results (Figures 4.12 and 4.17) revealed synchronization disruptions that are reminiscent of the sleep disturbances caused by DST, reported to increase the risk of traffic accidents and medical issues such as heart attacks and strokes (Janszky *et al*. 2012, Harrison 2013, Sipilä *et al*. 2016, Manfredini *et al*. 2019). Future changes and additions to the model will help shed light on the results found here, as discussed below (Section 5.3).

5.2. APPLICATIONS

The model presented here can be used to simulate various aspects of sleep dynamics, including changes in synchronization within and between regions or

hemispheres (Sections 2.2.4. and 2.3.2. – 2.3.4.), chimera states (Section 3.3.), and jet lag and unihemispheric or asymmetric sleep (Section 4.2.). While the jet lag results (Section 4.1.) remain preliminary, the model has simulated a range of phenomena including unihemispheric sleep, bihemispheric sleep, asymmetric sleep (Section 4.2), changes in regional synchronization, response to unusual sleep environments (first night effect, Section 1.3.1.2.), and circadian disturbances (jet lag, daylight savings, Section 4.1.). It may also be applied to the investigation of other aspects of sleep, including the effects of lesions (which could be simulated by decreasing the coupling strengths between certain regions) and sleep deprivation.

Each of these aspects of sleep are important topics of future investigation, not least because of the health implications of sleep disturbances. Healthy human sleep occurs bihemispherically, yet hemispheres can become slightly desynchronized (Section 1.3.1.2.) as a reaction to environmental cues (first night effect), or as a result of a sleep disorder (sleep apnea). Jet lag (Sections 1.5.4.2. and 4.1.) and sleep deprivation (Section 1.4.) feel dreadful and repeated exposures can lead to negative health effects. The symptoms of each of these have been studied, though not yet at the level of individual neural synchronization. The model presented here provides insights into the possible behavior of neurons in sleep-related regions of the brain during these sleep instances through the synchronization within and between each region and hemisphere. An expanded version of the model with more neurons per region could be used to develop predictive hypotheses as to local synchronization changes that accompany sleep disturbances. These hypotheses could conceivably be tested in vivo in animal models and might eventually form the basis for the design of possible clinical interventions.

5.3. FUTURE RESEARCH

There are still a wealth of studies that can be performed with this model, especially with further refinement.

5.3.1. Circadian Rhythm Changes. The circadian rhythm provides ample possibilities for further study. In future, the model presented here can be modified to consider changes to the circadian drive. Projections from other regions of the brain back to the SCN can provide a more detailed interaction between the regions in the model and changes in the circadian drive. Allowing other inputs to impact the circadian rhythm, such as non-photic elements (St. Hilaire *et al*. 2007) or even the wavelength of the entraining light (Duffy & Czeisler 2009), will provide new aspects to explore in the model. Alongside this, creating an internal circadian rhythm for the "subject" in the model and a separate circadian drive (external entrainment) will make differentiating the study of external and internal circadian perturbations much clearer and allow study of circadian misalignment (Fischer *et al*. 2016).

Within the current model, the coupling strength from the circadian drive to each region is constant, while the value of CD changes over the day. Another aspect to study would be to change the value of g_C during the course of the day, whether proportionally (as g_{CA} increases, g_{CV} decreases and vice versa), with the change in activity of certain regions, or some other variant. This may be equated to something changing the effectiveness of circadian entrainment, such as caffeine keeping a person awake, or melatonin supplements helping a person sleep.

The preliminary jet lag simulations described in Section 4.1. yielded various anomalous results. Perturbations late in the day had more impact than perturbations early

in the day, and longer perturbations often appeared to have little to no effect on the system's synchronization, while small perturbations ended with the system failing to switch states, or even ending in an undeterminable state with overlapping synchronization. These results are not conclusive, due to the small sample size.

More simulations can be run, and further changes for the study of jet lag can be implemented. A larger region of parameter space should be explored with varying changes to the circadian drive, to see how different coupling values may change how the circadian perturbation impacts the synchronization. The value at which the circadian drive is held constant may also be changed, rather than simply holding at the current value. This would allow study of the impact of sudden darkness (dropping from a high value of CD to a low value) or bright light in late evening or night (increasing form low value of CD to a high value), along with the impact due to the timing and duration of these changes.

A combination of the preliminary jet lag simulations reviewed above (Section 4.1.) may also allow study of more detailed and varied versions of jet lag, such as a delay (CD held at a constant value) leading into a phase shift. This specifically would more accurately simulate traveling in a plane at a set light value (delay) for a period of time before landing in a new time zone (phase shift). Examining jet lag in the two-hemisphere model would also lend another layer of complexity and realism to the results. Light level shifts analogous to the darkening of the lights on a plane for a truncated night during an eastward trans-Atlantic flight could also be modeled. Additional simulations will be needed in all cases in order to assess the repeatability of the responses to these perturbations. Size effects of larger neural ensembles also remain to be investigated. Development of a measure to *quantify* the effect of the time perturbation on the reciprocal synchronization between

AMIN and VLPO would be invaluable in assessing the intensity and repeatability of the simulated effects.

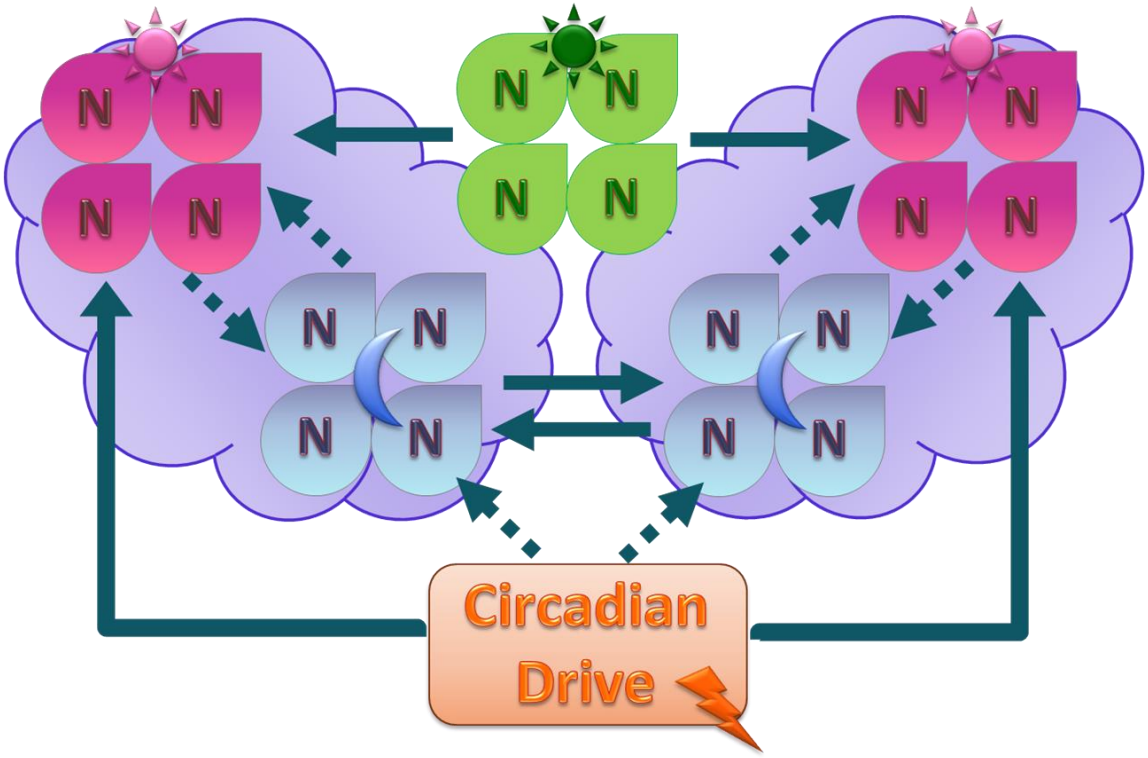

Figure 5.1 – Two-Hemisphere Model with Orexin
Schematic of the two-hemisphere model with the inclusion of neurons representing orexin (ORX). Solid arrows represent excitatory connections, and dashed arrows represent inhibitory connections. Pink regions with suns represent AMIN, blue with moons represent VLPO, and green with a sun represent ORX.

5.3.2. Additional Regions and Drives. An additional wake-promoting region can shift the dynamics of the model; specifically, the addition of orexinergic (ORX) neurons from the lateral hypothalamic area (LHA). These neurons release the neurotransmitter orexin (also called hypocretin), a crucial element of sleep-wake regulation. Lack of orexin

can cause narcolepsy (see Section 1.5.1.; Sakurai 2007, Schwartz & Kilduff 2015). ORX is present in many models of sleep, including the UHS model developed by Kedziora *et al*. (2012) and the sleep/wake flip-flop model by Rempe *et al*. (2010). The ORX neurons of LHA interact with both VLPO and AMIN (Saper & Lowell 2014), the two key regions of the presented model. The addition of ORX neurons can strengthen and stabilize the wake state, especially in the two-hemisphere version of the model, where the VLPO regions stimulate each other. A schematic of how ORX would be incorporated into the two-hemisphere model is shown in Figure 5.1.

Additional sleep-promoting regions can also change the dynamics of the model. The median preoptic nucleus (MnPO), also located in the hypothalamus, promotes the transition from wake to sleep while the VLPO consolidates the sleep state and regulates the depth of sleep (Gvilia *et al*. 2006). Firing ahead of the switch to sleep, MnPO may add to sleep pressure (Saper *et al*. 2010). It also inhibits the LHA, promoting the wake-to-sleep transition (Suntsova *et al*. 2007), balancing the addition of ORX.

Another key region in sleep regulation is the extended ventrolateral preoptic nucleus (eVLPO). This region inhibits the REM-off regions in the brain, allowing the transition from NREM to REM sleep (Lu *et al*. 2006, Rempe *et al*. 2010). The eVLPO exists in a flip-flop switch with both AMIN (which inhibits REM-on regions) and the VLPO (to regulate the switching between NREM and REM sleep) (Rempe *et al*. 2010). This region also projects to the LC (where the AMIN neurons from this model reside) and is inhibitory (Saper *et al*. 2010). The addition of the eVLPO to the model would allow for the transition into REM sleep, and the synchronization of all included regions during this state can be analyzed.

Working in conjunction with the circadian drive, the homeostatic drive builds up sleep pressure as time spent awake accumulates and decreases sleep pressure with time spent asleep. This relationship between these two processes was put forward by Borbély (1982) and modeled by Daan *et al*. (1984), whose Process C, or circadian drive, was used in the present model. Besides the circadian rhythm, the homeostatic drive has been proposed to be regulated by neurons in the VLPO and MnPO (Gvilia *et al*. 2006), as well as by ORX (Postnova *et al*. 2009). The homeostatic drive interacts with many of the proposed elements of the model, adds a new input and robustness to the circadian drive, and its addition to the model would create another driving force. It would also allow the study of sleep debt (Borbély *et al*. 2016).

5.3.3. Miscellaneous. Besides the above listed, other future changes can be made to improve the model and obtain more results. Additional neurons per region may add to the complexity of the model's behavior. Using HB, results were inconclusive with no discernable change with an increase in neurons (Section 2.2.2.4.), and with HR, small improvements in the smoothness and consistency of the synchronization index curves were observed (Section 2.2.4.3.). More significant system size increases, including in expanded versions of the model, may have a greater impact. This may be explored with the HR versions of the model, and, once developed, the two-hemisphere HB version of the model. Simpler oscillator models such as integrate-and-fire neurons could be used as well, in order to reduce the computational time while increasing the number of oscillators per region.

Extension of the simulation time, along with further expansion of the time compression, may yield new information. This was seen to an extent in the HB results, in the difference between the one-minute day results (Figures 2.39 and 2.40) and the three-

minute day results (Figures 2.20 and 2.37). The impact of noise on the model may also be explored for both HB and HR. While noise provides an aspect of biological realism and acts as a catalyst for some dynamical behavior (such as driving the voltage of a neuron above the firing threshold during sub-threshold oscillations), it may also create difficulties in being able to reliably replicate results without performing a very large number of simulations for each set of parameters.

To further investigate the range of dynamical behavior for both the HR and HB versions of the model, further exploration of parameter space should be conducted. The differences between in Figure 2.6 and Figure 2.14 for HB with different coupling strengths, and between Figures 2.22 and 2.23 for HR with different input current (I) strengths, shows how the parameters impact the activity of the model. Parameter-space plots showing the regions in which certain phenomena (such as UHS and chimera states) can be generated. Particular parameters of interest would be the temperature and various coupling strengths in the HB model, and the input current and coupling strengths in the HR model. Choices of parameter regions of particular interest will also be informed by single-unit recordings from sleep-regulating brain regions in vivo and in vitro, such as the recent work by Takahashi *et al*. (2008) in orexin and non-orexin waking-active neurons, Takahashi *et al*. (2010) in the locus coeruleus, and Sakai (2014) in the SCN.

APPENDIX A.

CONSTANTS OF HUBER-BRAUN MODEL

Table A. Constants of the Huber-Braun Model

Conductances $\left(\frac{ms}{cm^2}\right)$	$g_d = 1.5$ $g_l = 0.1$ $g_r = 2.0$ $g_{sd} = 0.25$ $g_{sr} = 0.4$
Half Activation (mV)	$V_{0d} = -25$ $V_{0r} = -25$ $V_{0sd} = -40$
Membrane Capacitance $\left(\frac{\mu F}{cm^2}\right)$	$C_M = 1$
Reversal Potentials (mV)	$V_d = 50$ $V_l = -60$ $V_r = -90$ $V_{sd} = 50$ $V_{sr} = -90$

Table A. Constants of the Huber-Braun Model (Cont.)

Steepness (mV^{-1})	$S_d = 0.25$ $S_r = 0.25$ $S_{sd} = 0.09$
Time Constants (ms)	$\tau_d = 0.1$ $\tau_r = 2$ $\tau_{sd} = 10$ $\tau_{sr} = 20$
Other Parameters	$T_0 = 25℃$ $\eta = 0.012$ $k = 0.17$ $D = 100\ A^2/s$

APPENDIX B.

CONSTANTS OF HINDMARSH-ROSE MODEL

Table B. Constants of the Hindmarsh-Rose Model

Noise Amplitude (A^2/s)	$D = 0.005$
Equilibrium Point	$x_1 = -1.6$
Other Constants	$a = 1$ $b = 3$ $c = 1$ $d = 5$ $r = 0.003$ $s = 4$

BIBLIOGRAPHY

Abel, T., R. Havekes, J.M. Saletin, and M.P. Walker. 2013. Sleep, Plasticity and Memory from Molecules to Whole-Brain Networks. *Current Biology* 23 (17): R774-R788.

Abeyratne, U.R., V. Swarnkar, C. Hukins, and B. Duce. 2010. Interhemispheric Asynchrony Correlates with Severity of Respiratory Disturbance Index in Patients with Sleep Apnea. *IEEE Transactions on Bio-Medical Engineering* 57 (12): 2947-2955.

Abrams, D.M. and S.H. Strogatz. 2004. Chimera States for Coupled Oscillators. *Physical Review Letters* 93 (17): 174102.

Abrams, D.M., R. Mirollo, S.H. Strogatz, and D.A. Wiley. 2008. Solvable Model for Chimera States of Coupled Oscillators. *Physical Review Letters* 101 (8): 084103.

Achermann, P., T. Rusterholz, R. Dürr, T. König, and L. Tarokh. 2016. Global Field Synchronization Reveals Rapid Eye Movement Sleep as Most Synchronized Brain State in the Human EEG. *Royal Society Open Science* 3 (10): 160201.

Aguilay-Roblero, R., L.P. Morin, and R.Y. Moore. 1994. Morphological Correlates of Circadian Rhythm Restoration Induced by Transplantation of the Suprachiasmatic Nucleus in Hamsters. *Experimental Neurology* 130 (2): 2250-260.

Allada, R., and J.M. Siegel. 2008. Unearthing the Phylogenetic Roots of Sleep. *Current Biology* 18 (15): R670-R679.

Andreassi, K. 2012. Venus the Two-Faced Cat a Mystery. *National Geographic* https://news.nationalgeographic.com/news/2012/08/120831-venus-two-faced-cat-genetics-animals-science/.

Anton, S.J., and E.D. Herzog. 2005. Come Together, Right… Now: Synchronization of Rhythms in a Mammalian Circadian Clock. *Neuron* 48 (4): 531-534.

Aserinsky, E. and N. Kleitman. 2003. Regularly Occurring Periods of Eye Motility, and Concomitant Phenomena, During Sleep. 1953. *Journal of Neuropsychiatry and Clinical Neuroscience* 15 (4): 454-455.

Ashenheim, L. 1841. On Sleep: With Arguments in Favour of the Doctrine of Afflux of Blood to the Brain During This State. *Provincial Medical & Surgical Journal* 2 (33): 137-138.

Banks, S., and D.F. Dinges. 2007. Behavioral and Physiological Consequences of Sleep Restriction. *Journal of Clinical Sleep Medicine* 3 (5): 519-528.

Barnett, M.W., and P.M. Larkman. 2007. The Action Potential. *Practical Neurology* 7 (3): 192-197.

Bayne, T. 2008. The Unity of Consciousness and the Split-Brain Syndrome. *The Journal of Philosophy* 105 (6): 277-300.

Berg, P., D. Baltimore, H.W. Boyer, S.N. Cohen, R.W. Davis, D.S. Hogness, D. Nathans, R. Roblin, J.D. Watson, S. Weissman, and N.D. Zinder. 1974. Potential Biohazards of Recombinant DNA Molecules. *Science* 185 (4148): 303.

Bick, C., M. Sebek, and I.Z. Kiss. 2017. Robust Weak Chimeras in Oscillator Networks with Delayed Linear and Quadratic Interactions. *Physical Review Letters* 119 (16): 168301.

Booth, V. and C.G. Diniz Behn. 2012. A Fast-Slow Analysis of the Dynamics of REM Sleep. *SIAM Journal of Applied Dynamical Systems* 11 (1): 212-242.

Booth, V., and C.G. Diniz Behn. 2014. Physiologically-Based Modeling of Sleep-Wake Regulatory Networks. *Mathematical Biosciences* 250: 54-68.

Borbély, A.A. 1982. A Two Process Model of Sleep Regulation. *Human Neurobiology* 1 (3): 195-204.

Borbély, A.A., and P. Achermann. 1992. Concepts and Models of Sleep Regulation: An Overview. *Journal of Sleep Research* 1 (2): 63-79.

Borbély, A.A., S. Daan, A. Wirz-Justice, and T. Deboer. 2016. The Two-Process Model of Sleep Regulation: A Reappraisal. *Journal of Sleep Research* 25 (2): 131-143.

Bosch, T.C.G., A. Klimovich, T. Domazet-Lošo, S. Gründer, T.W. Holstein, G. Jékely, D.J. Miller, A.P. Murillo-Rincon, F. Rentzsch, G.S. Richards, K. Schröder, U. Technau, and R. Yuste. 2017. Back to the Basics: Cnidarians Start to Fire. *Trends in Neurosciences* 40 (2): 92-105.

Branch, A.F., W. Navidi, S. Tabuchi, A. Terao, A. Yamanaka, T.E. Scammell, and C. Diniz Behn. 2016. Progressive Loss of the Orexin Neurons Reveals Dual Effects on Wakefulness. *Sleep* 39 (2): 369-377.

Braun, A.R., T.J. Balkin, N.J. Wesenten, R.E. Carson, M. Varga, P. Baldwin, S. Selbie, G. Belenky, and P. Herscovitch. 1997. Regional Cerebral Blood Flow Throughout the Sleep-Wake Cycle: An H2(15)O PET Study. *Brain* 120 (Pt 7): 1173-1197.

Braun, H.A., M.T. Huber, M. Dewald, K. Schafer, and K. Voigt. 1998. Computer Simulations of the Neuronal Signal Transduction: The Role of Nonlinear Dynamics and Noise. *International Journal of Bifurcation and Chaos* 8 (5): 881-889.

Buysse, D.J. 2013. Insomnia. *JAMA* 309 (7): 706-716.

Cajavilca, C., J. Varon, and G.L. Sternbach. 2009. Luigi Galvani and the Foundations of Electrophysiology. *Resuscitation* 80 (2): 159-162.

Corsi-Cabrera, M., R. Ondarza, V. Martinez-Gutiérrez, Y. del Río-Portilla, M.A. Guevara, and J. Ramos-Loyo. 2006. Role of Corpus Callosum in Interhemispheric Coherent Activity During Sleep. *Clinical Neurophysiology* 117 (8): 1826-1835.

Cortelli, P., P. Gambetti, P. Montagna, and E. Lugaresi. 1999. Fatal Familial Insomnia: Clinical Features and Molecular Genetics. *Journal of Sleep Research* 1: 23-29.

Czeisler, C.A., and J.J. Gooley. 2007. Sleep and Circadian Rhythms in Humans. *Cold Spring Harbor Symposia on Quantitative Biology* 72: 579-597.

Daan, S., D.G.M. Beersma, and A.A. Borbély. 1984. Timing of Human Sleep: Recovery Process Gated by a Circadian Pacemaker. *The American Journal of Physiology* 246 (2 Pt 2): R161-83.

de Andrés, I., M. Garzón, and F. Reinoso-Suárez. 2011. Functional Anatomy of Non-REM Sleep. *Frontiers in Neurology* 2: 70.

De Los Angeles, A., I. Hyun, S.R. Latham, J.D. Elsworth, and D.E. Redmond Jr. 2019. Human-Monkey Chimeras for Modeling Human Disease: Opportunities and Challenges. *Methods in Molecular Biology* 20005: 221-231.

Diekelmann, S., and J. Born. 2010. The Memory Function of Sleep. *Nature Reviews Neuroscience* 11 (2): 114-126.

Diniz Behn, C.G., E.N. Brown, T.E. Scammell, and N.J. Kopell. 2007. Mathematical Model of Network Dynamics Governing Mouse Sleep-Wake Behavior. *Journal of Neurophysiology* 97: 3828-3840.

Dudai, Y., A. Kami, and J. Born. 2015. The Consolidation and Transformation of Memory. *Neuron* 88 (1): 20-32.

Duffy, J.F., and C.A. Czeisler. 2009. Effect of Light on Human Circadian Physiology. *Sleep Medicine Clinics* 4 (2): 165-177.

Edgar, D.M., W.C. Dement, and C.A. Fuller. 1993. Effect of SCN Lesions on Sleep in Squirrel Monkeys: Evidence for Opponent Processes in Sleep-Wake Regulation. *Journal of Neuroscience* 13 (3): 1065-1079.

Fehilly, C.B., S.M. Willadsen, and E.M. Tucker. 1984. Interspecific Chimaerism Between Sheep and Goat. *Nature* 307 (5952): 634-636.

Feudel, U., A. Neiman, X. Pei, W. Wojtenek, H. Braun, M. Huber, and F. Moss. 2000. Homoclinic Bifurcation in a Hodgkin-Huxley Model of Thermally Sensitive Neurons. *Chaos* 10: 231-239.

Finke, C., J.A. Freund, E. Rosa, P.H. Bryant, H.A. Braun, and U. Feudel. 2011. Temperature-Dependent Stochastic Dynamics of the Huber-Braun Neuron Model. *Chaos* 21: 047510.

Finkelstein, G. 2015. Mechanical Neuroscience: Emil du Bois-Reymond's Innovations in Theory and Practice. *Frontiers in Systems Neuroscience* 9: 133.

Fischer, D., C. Vetter, and T. Roenneberg. 2016. A Novel Method to Visualize and Quantify Circadian Misalignment. *Scientific Reports* 6: 38601.

Fosse, R., R. Stickgold, and J.A. Hobson. 2001. The Mind in REM Sleep: Reports of Emotional Experience. *Sleep* 24 (8): 947-955.

Fox, R.F., I.R. Gatland, R. Roy, and G. Vemuri. 1988. Fast, Accurate Algorithm for Numerical Simulation of Exponentially Correlated Colored Noise. *Physical Review. A, General Physics* 38 (11): 5938-5940.

Friborg, O., J.H. Rosenvinge, R. Wynn, and M. Gradisar. 2014. Sleeping, Chronotype, Mood, and Behavior at an Artic Latitude (69° N). *Sleep Medicine* 15 (7): 798-807.

Gallopin, T., P. Fort, E. Eggermann, B. Cauli, P.H. Luppi, J. Rossier, E. Audinat, M. Mühlethaler, and M. Serafin. 2000. Identification of Sleep-Promoting Neurons *in vitro*. *Nature* 404 (6781): 992-995.

Gambetti, P. and E. Lugaresi. 1998. Conclusions of the Symposium. *Brain Pathology* 8 (3): 571-575.

García-Moreno, F., and Z. Molnár. 2015. Subset of Early Radial Glial Progenitors That Contribute to the Development of Callosal Neurons Is Absent from Avian Brain. *Proceedings of the National Academy of Sciences of the USA* 112 (36): E5058-E5067.

Glaze, T.A. 2015. Neural Chimeras in the Huber-Braun Model with Abrams-Strogatz and Kuramoto Coupling Schemes. *Master's Thesis* Retrieved from https://irl.umsl.edu/thesis/277/

Glaze, T.A., S. Lewis, and S. Bahar. 2016. Chimera States in a Hodgkin-Huxley Model of Thermally Sensitive Neurons. *Chaos* 26 (8): 083119.

Guo, J.H., W.M. Qu, S.G. Chen, X.P. Chen, K. Lv, Z.L. Huang, and Y.L. Wu. 2014. Keeping the Right Time in Space: Importance of Circadian Clock and Sleep for Physiology and Performance of Astronauts. *Military Medical Research* 1: 23.

Gvilia, I., F. Xu, D. McGinty, and R. Szymusiak. 2006. Homeostatic Regulation of Sleep: A Role for Preoptic Area Neurons. *Journal of Neuroscience* 26 (37): 9426-9433.

Hagan-Brown, A., M. Favaretto, and P. Borry. 2017. Newspaper Coverage of Human-Pig Chimera Research: A Qualitative Study on Select Media Coverage of Scientific Breakthrough. *Xenotransplantation* 24 (4): e12317.

Hagerstrom, A.M., T.E. Murphy, R. Ry, P. Hövel, I. Omelchenko, and E. Schöll. 2012. Experimental Observation of Chimeras in Coupled-Map Lattices. *Nature Physics* 8: 658-661.

Harrison, Y. 2013. The Impact of Daylight Saving Time on Sleep and related Behaviours. *Sleep Medicine Reviews* 17 (4): 285-292.

Herxheimer, A. 2014. Jet Lag. *BMJ Clinical Evidence* 2014: 2303.

Hindmarsh, J.L. and R.M. Rose. 1982. A Model of the Nerve Impulse Using Two First-Order Differential Equations. *Nature* 296 (5853): 162-164.

Hindmarsh, J.L. and R.M. Rose. 1984. A Model of Neuronal Bursting Using Three Coupled First Order Differential Equations. *Proceedings of the Royal Society of London Series B, Biological Sciences* 221 (1222): 87-102.

Hizanidis, J., V.G. Kanas, A. Bezerianos, and T. Bountis. 2014. Chimera States in Networks of Nonlocally Coupled Hindmarsh-Rose Neuron Models. *International Journal of Bifurcation and Chaos* 24: 1450030.

Hobson, J.A. and E.F. Pace-Schott. 2002. The Cognitive Neuroscience of Sleep: Neuronal Systems, Consciousness and Learning. *Nature Reviews Neuroscience* 3 (9): 679-693.

Hodgkin, A.L. 1937. Evidence for Electrical Transmission in Nerve: Part 1. *Journal of Physiology* 90 (2): 183-210.

Hodgkin, A.L. and A.F. Huxley. 1952. A Quantitative Description of Membrane Current and Its Application to Conduction and Excitation in Nerve. *Journal of Physiology* 117 (4): 500-544.

Janszky, I., S. Ahnve, R. Ljung, K.J. Mukamai, S. Gautam, L. Wallentin, and U. Stenestrand. 2012. Daylight Saving Time Shifts and Incidence of Acute Myocardial Infarction – Swedish Register of Information and Knowledge About Swedish Heart Intensive Care Admissions (RIKS-HIA). *Sleep Medicine* 13 (3): 237-242.

Jouvet, M., and F. Michel. 1959. Electromyographic Correlations of Sleep in the Chronic Decorticate and Mesencephalic Cat. *Comptes rendus des Seances de la Societe de Biologie et de ses Filiales* 153 (3): 422-425.

Kazamel, M., and P.P. Warren. 2017. History of Electromyography and Nerve Conduction Studies: A Tribute to the Founding Fathers. *Journal of Clinical Neuroscience* 43: 54-60.

Kedziora, D.J., R.G. Abeysuriya, A.J.K. Phillips, and P.A. Robinson. 2012. Physiologically Based Quantitative Modeling of Unihemispheric Sleep. *Journal of Theoretical Biology* 314: 109-119.

Khan, Z., and P.C. Bollu. 2018. Fatal Familial Insomnia. *StatPearls*.

Knight, J. 2003. GloFish Casts Light on Murky Policing of Transgenic Animals. *Nature* 426 (6965): 372.

Kronauer, R.E., C.A. Czeisler, S.F. Pilato, M.C. Moore-Ede, and E.D. Weitzman. 1982. Mathematical Model of the Human Circadian System with Two Interacting Oscillators. *American Journal of Physiology* 242 (1): R3-R17.

Krueger, J.M., D.M. Rector, S. Roy, H.P. Van Dongen, G. Belenky, and J. Panksepp. 2008. Sleep as a Fundamental Property of Neuronal Assemblies. *Nature Reviews Neuroscience* 9 (12): 910-919.

Kumar, R., A. Bose, and B.N. Mallick. 2012. A Mathematical Model Towards Understanding the Mechanism of Neuronal Regulation of Wake-NREMS-REMS States. *PLoS One* 7 (8): e42059.

Kunz, H., and P. Achermann. 2003. Simulations of Circadian Rhythm Generation in the Suprachiasmatic Nucleus with Locally Coupled Self-Sustained Oscillators. *Journal of Theoretical Biology* 224 (1): 63-78.

Kuramoto, Y. and D. Battogtokh. 2002. Coexistence of Coherence and Incoherence in Nonlocally Coupled Phase Oscillators. *Nonlinear Phenomena in Complex Systems* 5: 380-385.

Lesku, J.A., and L.M.T. Ly. 2017. Sleep Origins: Restful Jellyfish Are Sleeping Jellyfish. *Current Biology* 27 (19): R1060-R1062.

Levine, S., and L. Grabel. 2017. The Contribution of Human/Non-Human Animal Chimeras to Stem Cell Research. *Stem Cell Research* 24: 128-134.

Lewis, P.R., and Lobban, M.C. 1957. Disassociation of Diurnal Rhythms in Human Subjects Living on Abnormal Time Routines. *Quarterly Journal of Experimental Physiology and Cognate Medical Sciences* 42 (4): 371-386.

Lima, S.L., N.C. Rattenborg, J.A. Lesku, and C.J. Amlaner. 2005. Sleeping Under the Risk of Predation. *Animal Behavior* 70: 723-736.

Lu, J., D. Sherman, M. Devor, and C.B. Saper. 2006. A Putative Flip-Flop Switch for Control of REM Sleep. *Nature* 441 (7093): 589-594.

Lugaresi, E., R. Medori, P. Montagna, A. Baruzzi, P. Cortelli, A. Lugaresi, P. Tinuper, M. Zucconi, and P. Gambetti. 1986. Fatal Familial Insomnia and Dysautonomia with Selective Degeneration of Thalamic Nuclei. *New England Journal of Medicine* 315 (16): 997-1003.

Lugaresi, E., I. Tobler, P. Gambetti, and P. Montagna. 1998. The Pathophysiology of Fatal Familial Insomnia. *Brain Pathology* 8 (3): 521-526.

Lühken, G., H.W. Wagner, D. Seichter, W. Hecht, and G. Erhardt. 2009. Genetic Characterization of a Sheep-Dwarf Goat Hybrid. *Cytogenetic and Genome Research* 125 (2): 158-161.

Luo, J.J., A.L. Truant, Q. Kong, and W.Q. Zou. 2012. Sporadic Fatal Insomnia with Clinical, Laboratory, and Genetic Findings. *Journal of Clinical Neuroscience* 19 (8): 1188-1192.

Lyamin, O.I., L.M. Mukhametov, and J.M. Siegel. 2004. Relationship Between Sleep and Eye State in Cetaceans and Pinnipeds. *Archives Italiennes de Biologie* 142 (4): 557-568.

Madan, V., and S.K. Jha. 2012. Sleep Alterations in Mammals: Did Aquatic Conditions Inhibit REM? *Neuroscience Bulletin* 28 (6): 746-758.

Mahler, S.V., D.E. Moorman, R.J. Smith, M.H. James, and G. Aston-Jones. 2014. Motivational Activation: A Unifying Hypothesis of Orexin/Hypocretin Function. *Nature Neuroscience* 17 (10): 1298-1303.

Mahlios, J., A.K. De la Herrán-Arita, and E. Mignot. 2013. The Autoimmune Basis of Narcolepsy. *Current Opinion in Neurobiology* 23 (5): 767-773.

Majhi, S., B.K. Bera, D. Ghosh, and M. Perc. 2019. Chimera States in Neuronal Networks: A Review. *Physics of Life Reviews* 28: 100-121.

Manfredini, R., F. Fabbian, R. Cappadona, A. De Giorgi, F. Bravi, T. Carradori, M.E. Flacco, and L. Manzoli. 2019. Daylight Saving Time and Acute Myocardial Infarction: A Meta-Analysis. *Journal of Clinical Medicine* 8 (3): E404.

Martens, E.A., S. Thutupalli, A. Fourrière, and O. Hallatschek. 2013. Chimera States in Mechanical Oscillator Networks. *Proceedings of the National Academy of Sciences of the USA* 110 (26): 10563-10567.

Mascetti, G.G. 2016. Unihemispheric Sleep and Asymmetrical Sleep: Behavioral, Neurophysiological, and Functional Perspectives. *Nature and Science of Sleep* 8: 221-238.

Massimini, M., F. Ferrarelli, R. Huber, S.K. Esser, H. Singh, and G. Tononi. 2005. Breakdown of Cortical Effective Connectivity During Sleep. *Science* 309 (5744): 2228-2232.

McGinty, D., and R. Szymusiak. 2000. The Sleep-Wake Switch: A Neuronal Alarm Clock. *Nature Medicine* 6 (5): 510-511.

Meng, L., A.J. Ward, S. Chun, C.F. Bennett, A.L. Beaudet, and F. Rigo. 2015. Towards a Therapy for Angelman Syndrome by Targeting a Long Non-coding RNA. *Nature* 518 (7539): 409-412.

Montagna, P., P. Gambetti, P. Cortelli, and E. Lugaresi. 2003. Familial and Sporadic Fatal Insomnia. *Lancet Neurology* 2 (3): 167-176.

Moore, R.Y., and V.B. Eichler. 1972. Loss of a Circadian Adrenal Corticosterone Rhythm Following Suprachiasmatic Lesion in the Rat. *Brain Research* 42 (1): 201-206.

Moore, R.Y., and N.J. Lenn. 1972. A Retinohypothalamic Projection in the Rat. *Journal of Comparative Neurology* 146 (1): 1-14.

Nakao, M., A. Karashima, and N. Katayama. 2007. Mathematical Models of Regulatory Mechanisms of Sleep-Wake Rhythms. *Cellular and Molecular Life Sciences* 64: 1236-1243.

Nath, R.D., C.N. Bedbrook, M.J. Abrams, T. Basinger, J.S. Bois, D.A. Prober, P.W. Sternberg, V. Gradinaru, and L. Goentoro. 2017. The Jellyfish Cassiopea Exhibits a Sleep-Like State. *Current Biology* 27 (19): 2984-2990.

Nauta, W.J. 1946. Hypothalamic Regulation of Sleep in Rats; An Experimental Study. *Journal of Neurophysiology* 9: 285-316.

Nielsen, T., J. Montplaisir, and M. Lassonde. 1992. Sleep Architecture in Agenesis of the Corpus Callosum: Laboratory Assessment of Four Cases. *Journal of Sleep Research* 1 (3): 197-200.

Nofzinger, E.A., C. Nissen, A. Germain, D. Moul, M. Hall, J.C. Price, J.M. Miewald, and J.D. Buysse. 2006. Regional Cerebral Metabolic Correlates of WASO During NREM Sleep in Insomnia. *Journal of Clinical Sleep Medicine* 2 (3): 3116-322.

Omelchenko, I., O.E. Omel'chenko, P. Hövel, and E. Schöll. 2013. When Nonlocal Coupling Between Oscillators Becomes Stronger: Patched Synchrony or Multichimera States. *Physical Review Letters* 110 (22): 224101.

Patriarca, M., S. Postnova, H.A. Braun, E. Hernandez-Garcia, and R. Toral. 2012. Diversity and Noise Effects in a Model of Homeostatic Regulation of the Sleep-Wake Cycle. *PLoS Computational Biology* 8 (8): e1002650.

Peever, J. and P.M. Fuller. 2017. The Biology of REM Sleep. *Current Biology* 27 (22): R1237-R1248.

Phillips, A.J., and P.A. Robinson. 2007. A Quantitative Model of Sleep-Wake Dynamics Based on the Physiology of the Brainstem Ascending Arousal System. *Journal of Biological Rhythms* 22 (2): 167-179.

Phillips, A.J., B.D. Fulcher, P.A. Robinson, and E.B. Klerman. 2013. Mammalian Rest/Activity Patterns Explained by Physiologically Based Modeling. *PLoS Computational Biology* 9 (9): e1003213.

Piccolino, M. 1997. Luigi Galvani and Animal Electricity: Two Centuries After the Foundation of Electrophysiology. *Trends in Neurosciences* 20 (10): 443-448.

Pikovsky, A., M. Rosenblum, and J. Kurths. 2001. *Synchronization: A Universal Concept in Nonlinear Sciences*. Cambridge University Press.

Polzin, V.J., D.L. Anderson, G.B. Anderson, R.H. BonDurant, J.E. Butler, R.L. Pashen, M.C. Penedo, and J.D. Rowe. 1987. Production of Sheep-Goat Chimeras by Inner Cell Mass Transplantation. *Journal of Animal Science* 65 (1): 325-330.

Postnova, S., K. Voigt, and H.A. Braun. 2009. A Mathematical Model of Homeostatic Regulation of Sleep-Wake Cycles by Hypocretin/Orexin. *Journal of Biological Rhythms* 24 (6): 523-535.

Puckeridge, M., B.D. Fulcher, A.J.K. Phillips, and P.A. Robinson. 2011. Incorporation of Caffeine into a Quantitative Model of Fatigue and Sleep. *Journal of Theoretical Biology* 273 (1): 44-54.

Ralph, M.R., R.G. Foster, F.C. Davis, and M. Menaker. 1990. Transplanted Suprachiasmatic Nucleus Determines Circadian Period. *Science* 247 (4945): 975-978.

Rattenborg, N.C., S.L. Lima, and C.J. Amlaner. 1999. Half-Awake to the Risk of Predation. *Nature* 397 (6718): 397-398.

Rattenborg, N.C., C.J. Amlaner, and S.L. Lima. 2000. Behavioral, Neurophysiological and Evolutionary Perspectives on Unihemispheric Sleep. *Neuroscience and Behavioral Reviews* 24 (8): 817-842.

Rattenborg, N.C. 2017. Sleeping on the Wing. *Interface Focus* 7 (1): 20160082.

Rattenborg, N.C., J. van der Meij, G.J.L. Beckers, and J.A. Lesku. 2019. Local Aspects of Avian Non-REM and REM Sleep. *Frontiers in Neuroscience* 13: 567.

Reimer, M.A., and W.W. Flemons. 2003. Quality of Life in Sleep Disorders. *Sleep Medicine Reviews* 7 (4): 335-349.

Rempe, M.J., J. Best, and D. Terman. 2010. A Mathematical Model of the Sleep/Wake Cycle. *Journal of Mathematical Biology* 60: 615-644.

Rial, R.V., M.C. Nicolau, A. Gamundí, M. Akaârir, S. Aparicio, C. Garau, P. Barceló, and S. Estaban. 2012. REM Sleep Could Have No Adaptive Value. *Sleep Medicine Reviews* 16 (1): 109.

Rial, R., J. González, L. Gené, M. Akaârir, S. Esteban, A. Gamundí, P. Barceló, and C. Nicolau. 2013. Asymmetric Sleep in Apneic Human Patients. *American Journal of Physiology. Regulatory, Integrative, and Comparative Physiology* 304 (3): R232-R237.

Robinson, E. S., and S.O. Herrmann. 1922. Effects of Loss of Sleep. *Journal of Experimental Psychology* 5: 93-100.

Sack, R.L., D. Auckley, R.R. Auger, M.A. Carskadon, K.P. Wright Jr, M.V. Vitiello, I.V. Zhdanova, and American Academy of Sleep Medicine. 2007A. Circadian Rhythm Sleep Disorders: Part I, Basic Principles, Shift Work and Jet Lag Disorders. An American Academy of Sleep Medicine Review. *Sleep* 30 (11): 1460-1483.

Sack, R.L., D. Auckley, R.R. Auger, M.A. Carskadon, K.P. Wright Jr, M.V. Vitiello, I.V. Zhdanova, and American Academy of Sleep Medicine. 2007B. Circadian Rhythm Sleep Disorders: Part II, Advanced Sleep Phase Disorder, Delayed Sleep Phase Disorder, Free-Running Disorder, and Irregular Sleep-Wake Rhythm. An American Academy of Sleep Medicine Review. *Sleep* 30 (11): 1484-14501.

Sakai, K. 2014. Single Unit Activity of the Suprachiasmatic Nucleus and Surrounding Neurons During the Wake-Sleep Cycle in Mice. *Neuroscience* 260: 249-264.

Sakurai, T. 2007. The Neural Circuit of Orexin (Hypocretin): Maintaining Sleep and Wakefulness. *Nature Reviews Neuroscience* 8 (3): 171-181.

Saper, C.B., T.C. Chou, and T.E. Scammell. 2001. The Sleep Switch: Hypothalamic Control of Sleep and Wakefulness. *Trends in Neurosciences* 24 (12): 726-731.

Saper, C.B., P.M. Fuller, N.P. Pedersen, J. Lu, and T.E. Scammell. 2010. Sleep State Switching. *Neuron* 68 (6): 1023-1042.

Saper, C.B., and B.B. Lowell. 2014. The Hypothalamus. *Current Biology* 24 (23): R1111-R1116.

Scammell, T.E. 2015. Narcolepsy. *New England Journal of Medicine* 373 (27): 2654-2662.

Schmidt, M.H. 2014. The Energy Allocation Function of Sleep: A Unifying Theory of Sleep, Torpor, and Continuous Wakefulness. *Neuroscience and Behavioral Reviews* 47: 122-153.

Schwabedal, J.T., M. Riedl, T. Penzel, and N. Wessel. 2016. Alpha-Wave Frequency Characteristics in Health and Insomnia During Sleep. *Journal of Sleep Research* 25 (3): 278-286.

Schwartz, M. D., and T.S. Kilduff. 2015. The Neurobiology of Sleep and Wakefulness. *Psychiatric Clinics of North America* 38 (4): 615-644.

Sethia, G.C., A. Sen, and F.M. Atay. 2012. Clustered Chimera States in Delay-Coupled Oscillator Systems. *Physical Review Letters* 100 (14): 144102.

Shein-Idelson, M., J.M. Ondracek, H.P. Liaw, S. Reiter, and G. Laurent. 2016. Slow Waves, Sharp Waves, Ripples, and REM in Sleeping Dragons. *Science* 352 (6285): 590-595.

Sherin, J.E., P.J. Shiromani, R.W. McCarley, and C.B. Saper. 1996. Activation of Ventrolateral Preoptic Neurons During Sleep. *Science* 271 (5246): 216-219.

Siegel, J.M. 2001. The REM Sleep-Memory Consolidation Hypothesis. *Science* 294 (5544): 1058-1063.

Siegel, J.M. 2003. Why We Sleep. *Scientific American* 289 (5): 92-97.

Siegel, J.M. 2011. REM Sleep: A Biological and Psychological Paradox. *Sleep Medicine Reviews* 15 (3): 139-142.

Siegel, J.M. 2012. REM Sleep Must Have an Adaptive Value. *Sleep Medicine Reviews* 16: 111.

Simon, G.E., and M. VonKorff. 1997. Prevalence, Burden, and Treatment of Insomnia in Primary Care. *American Journal of Psychiatry* 154 (10): 1417-1423.

Sipilä, J.O., J.O. Ruuskanen, P. Rautava, and V. Kytö. 2016. Changes in Ischemic Stroke Occurrence Following Daylight Saving Time Transitions. *Sleep Medicine* 27-28: 20-24.

Skeldon, A.C., A.J. Phillips, and D.J. Dijk. 2017. The Effects of Self-Selected Light-Dark Cycles and Social Constraints on Human Sleep and Circadian Timing: A Modeling Approach. *Scientific Reports* 7: 45158.

Sperry, R.W. 1961. Cerebral Organization and Behavior: The Split Brain Behaves in Many Respects like Two Separate Brains, Providing New Research Possibilities. *Science* 133 (3466): 1749-1757.

St. Hilaire, M.A., E.B. Klerman, S.B. Khalsa, K.P. Wright Jr, C.A. Czeisler, and R.E. Kronauer. 2007. Addition of a Non-Photic Component to a Light-Based Mathematical Model of the Human Circadian Pacemaker. *Journal of Theoretical Biology* 247 (4): 583-599.

Stickgold, R., J.A. Hobson, R. Fosse, and M. Fosse. 2001. Sleep, Learning, and Dreams: Off-Line Memory Reprocessing. *Science* 294 (5544): 1052-1057.

Stickgold, R. 2007. Of Sleep, Memories, and Trauma. *Nature Neuroscience* 10 (5): 540-542.

Strogatz, S.H. 1987. Human Sleep and Circadian Rhythms: A Simple Model Based on Two Coupled Oscillators. *Journal of Mathematical Biology* 25: 327-347.

Suntsova, N., R. Guzman-Marin, S. Kumar, M.N. Alam, R. Szymusiak, and D. McGinty. 2007. The Median Preoptic Nucleus Reciprocally Modulates Activity of Arousal-Related and Sleep-Related Neurons in the Perifornical Lateral Hypothalamus. *Journal of Neuroscience* 27 (7): 1616-1630.

Szymusiak, R., N. Alam, T.L. Steininger, and D. McGinty. 1998. Sleep-Waking Discharge Patterns of Ventrolateral Preoptic/Anterior Hypothalamic Neurons in Rats. *Brain Research* 803 (1-2): 178-188.

Takahashi, K., J.S. Lin, and K. Sakai. 2008. Neuronal Activity of Orexin and Non-Orexin Waking-Active Neurons During Wake-Sleep States in the Mouse. *Neuroscience* 153 (3): 860-870.

Takahasi, K., Y. Kayama, J.S. Lin, and K. Sakai. 2010. Locus Coeruleus Neuronal Activity During the Sleep-Waking Cycle in Mice. *Neuroscience* 169 (3): 1115-1126.

Tamaki, M., J.W. Bang, T. Watanabe, and Y. Sasaki. 2016. Night Watch in One Brain Hemisphere During Sleep Associated with the First-Night Effect in Humans. *Current Biology* 26 (9): 1190-1194.

Timofeev, I., and S. Chauvette. 2017. Sleep Slow Oscillation and Plasticity. *Current Opinion in Neurobiology* 44: 116-126.

Tinsley, M.R., S. Nkomo, and K. Showalter. 2012. Chimera and Phase-Cluster States in Populations of Coupled Chemical Oscillators. *Nature Physics* 8: 662-665.

Tononi, G., and C. Cirelli. 2014. Sleep and the Price of Plasticity: From Synaptic and Cellular Homeostasis to Memory Consolidation and Integration. *Neuron* 81 (1): 12-34.

Tovar-Moll, F., M. Monteiro, J. Andrade, I.E. Bramati, R. Vianna-Barbosa, T. Marins, E. Rodrigues, N. Dantas, T.E. Behrens, R. de Oliveira-Souza, J. Moll, and R. Lent. 2014. Structural and Functional Brain Rewiring Clarifies Preserved Interhemispheric Transfer in Humans Born Without the Corpus Callosum. *Proceedings of the National Academy of Sciences of the USA* 111 (21): 7843-7848.

Uhlhaas, P.J., and W. Singer. 2006. Neural Synchrony in Brain Disorders: Relevance for Cognitive Dysfunctions and Pathophysiology. *Neuron* 52 (1): 155-168.

Vorster, A.P., and J. Born. 2015. Sleep and Memory in Mammals, Birds and Invertebrates. *Neuroscience and Behavioral Reviews* 50: 103-119.

Vyazovskiy, V., P. Achermann, A.A. Borbély, and I. Tobler. 2004. Interhemispheric Coherence of Sleep Electroencephalogram in Mice with Congenital Callosal Dysgenesis. *Neuroscience* 124 (2): 481-488.

Weihberger, O., and S. Bahar. 2007. Frustration, Drift and Antiphase Coupling in a Neural Array. *Physical Review E* 76: 011910.

Welsh, D.K., D.E. Logothetis, M. Meister, S.M. Reppert. 1995. Individual Neurons Dissociated from Rat Suprachiasmatic Nucleus Express Independently Phased Circadian Firing Rhythms. *Neuron* 14 (4): 697-706.

Wenk, R.E. 2018. A Review of the Biology and Classification of Human Chimeras. *Transfusion* 58 (8): 2054-2067.

Wickramasinghe, M., and I.Z. Kiss. 2013. Spatially Organized Dynamical States in Chemical Oscillator Networks: Synchronization, Dynamical Differentiation, and Chimera Patterns. *PLoS One* 8 (11): e80586.

Wickramasinghe, M., and I.Z. Kiss. 2014. Spatially Organized Partial Synchronization Through the Chimera Mechanism in a Network of Electrochemical Reactions. *Physical Chemistry Chemical Physics* 16 (34): 18360-18369.

Wolfrum, M., and O.E. Omel'chenko. 2011. Chimera States are Chaotic Transients. *Physical Review E, Statistical, Nonlinear, and Soft Matter Physics* 84 (1 Pt 2): 015201.

Wu, L.Y., S.Q. Zhan, Z.Y. Huang, B. Zhang, T. Wang, C.F. Liu, H. Lu, X.P. Dong, Z.Y. Wu, J.W. Zhang, J.H. Zhang, Z.X. Zhao, F. Han, Y. Huang, J. Hu, S. Gauthier, J.P. Jia, and Y.P. Wang. 2018. Expert Consensus on Clinical Diagnostic Criteria for Fatal Familial Insomnia. *Chinese Medical Journal (English)* 131 (13): 1613-1617.

Xie, L., H. Kang, Q. Xu, M.J. Chen, Y. Liao, M. Thiyagarajan, J. O'Donnell,, D.J. Christensen, C. Nicholson, J.J. Iliff, T. Takano, R. Deane, and M. Nedergaard. 2013. Sleep Drives Metabolite Clearance from the Adult Brain. *Science* 342 (6156): 373-377.

VITA

Tera Ashley Glaze was born in Illinois. She received her Bachelor of Science with Honors in Physics from the University of Missouri – St. Louis in December 2012. In the summer of 2015, she earned her Master of Science in Physics from the same university. She received her Doctor of Philosophy in Physics in December 2019 through the co-operative program between the University of Missouri – St. Louis and Missouri University of Science and Technology.

She published a peer-reviewed paper in the journal Chaos and presented her research at several conferences.